INVESTIGATION OF LATERAL PERFORMANCE OF AN ATV TIRE ON

NATURAL, DEFORMABLE SURFACES

Except where reference is made to the work of others, the work described in this thesis is my own or was done in collaboration with my advisory committee. This thesis does not include proprietary or classified information.

_____

Darrell R. Krueger

Certificate of Approval:

_____	_____
Timothy McDonald Assistant Professor Biosystems Engineering	Peter Jones, Chair Associate Professor Mechanical Engineering
_____	_____
David Bevly Assistant Professor Mechanical Engineering	Robert Jackson Assistant Professor Mechanical Engineering

_____

George T. Flowers
Interim Dean
Graduate School

INVESTIGATION OF LATERAL PERFORMANCE OF AN ATV TIRE ON NATURAL, DEFORMABLE SURFACES

Darrell R. Krueger

A Thesis

Submitted to

the Graduate Faculty of

Auburn University

in Partial Fulfillment of the

Requirements for the

Degree of

Master of Science

Auburn, Alabama
December 17, 2007

INVESTIGATION OF LATERAL PERFORMANCE OF AN ATV TIRE ON

NATURAL, DEFORMABLE SURFACES

Darrell R. Krueger

_____

Signature of Author

_____

Date of Graduation

THESIS ABSTRACT

INVESTIGATION OF LATERAL PERFORMANCE OF AN ATV TIRE ON NATURAL, DEFORMABLE SURFACES

Darrell R. Krueger

Master of Science, December 17, 2007
(B.S., Auburn University, 2005)

235 Typed Pages

Directed by Peter Jones

A study is undertaken to discover links between soil-rubber interface strength, camber, pressure and lateral performance of a front ATV tire. New tire and soil test rigs are also designed and fabricated for the support of this research. The tire is tested at various geometries and inflation pressures on cohesive and frictional soils. Lateral, longitudinal and vertical forces are recorded with an electronic data logging system.

Using the results from the tire tests, an exponential tire model is fit to the tire data. Coefficients of the model are then compared to the inflation pressures, camber angles, and soil data. The effects on tire performance trends are observed. Data from these experiments can be used to aid in the programming of autonomous unmanned ground vehicles, or to create better vehicle dynamics models for small off-road vehicles.

ACKNOWLEDGEMENTS

This work is dedicated to all the men and women of War Eagle Motorsports. It is dedicated to those who believed in me as a freshman, teaching, mentoring, and motivating me to stick with engineering, and develop the Auburn work ethic.

This work is dedicated to my teammates who gave their all and more throughout the ups and downs of Baja racing at Auburn, who sacrificed their grades and spare time for the smell of gasoline, the buzz of the welder, burn of the grinder, and the sight of the checkered flag.

To Dr. Peter Jones, infinite thanks. He listened to my proposal, believed in it, found funding, and gave support. As the advisor for War Eagle Motorsports, he has contributed so much of his time and energy to building great engineers with the right balance of practical experience and book knowlege.

To Taylor Owens and Marc Jarmulowicz, I give thanks. They are great friends and great engineers who can solve anything over a plate of barbecue. Marc and Taylor's friendship and encouragement through the years have been nothing short of outstanding.

To Randy Whitehead, I thank for numerous discussions of engineering, racing, Christianity, and life after college, especially when enjoying lunch at Hamilton's.

A thousand thanks go to the College of Engineering. To Larry Benefield, for his bold vision and action in making the College the best it can be. To Jim Killian and Cheryl Cobb for showcasing all the great things that happen within the College, and to Buzz

Powell and his great staff at the National Center for Asphalt Technology. Without their support and involvement, this research would have been painfully difficult.

And finally, I would like to thank all of my amazing friends and family, including my parents, Donna and Mark, and brother Christopher, who never doubted my ability, and encouraged me every step of the way to completion. I could not have done it without your love and support.

Style of journal used:

ASME Journal of Dynamic Systems, Measurement and Control

Computer software used:

Microsoft Word

TABLE OF CONTENTS

LIST OF TABLES

LIST OF FIGURES

NOMENCLATURE

$a_{y,}$	[G]	Lateral Acceleration
a	[in]	Horizontal distance from CG to front axle
A	[-]	Exponential tire model coefficient
b	[in]	Horizontal distance from CG to rear axle
b	[in]	Pressure plate diameter
B	[1/deg]	Exponential tire model coefficient
c	[-]	Exponential tire model coefficient
c	[lbf/in^2]	Cohesion
C	[1/deg]	Exponential tire model coefficient
C_α	[lbf/deg]	Tire cornering stiffness
C_γ	[lbf/deg]	Tire camber stiffness
D	[1/deg]	Exponential tire model coefficient
F_x	[lbf]	Longitudinal tire force
F_y	[lbf]	Lateral tire force
F_z	[lbf]	Vertical tire force
h	[in]	CG height above ground
h'	[in]	CG distance from roll axis
j	[in]	Soil shear displacement
K	[lbf/in]	Soil shear deformation modulus
k_φ	[lbf/in^{n+2}]	Frictional sinkage parameter
k_c	[lbf/in^{n+1}]	Cohesive sinkage parameter
m	[-]	Exponent for Metz exponential model
M_z	[lbf-in]	Moment about vertical (z) axis
n	[-]	Sinkage exponent
p	[lbf/in^2]	Pressure
s	[lbf/in^2]	Shear stress
s_{max}	[lbf/in^2]	Maximum shear stress
t	[in]	Track width
V	[in/s]	Velocity
z	[in]	Sinkage into soil
α	[deg]	Tire slip angle
β	[deg]	Vehicle slip angle
γ	[deg]	Tire camber angle
δ	[deg]	Tire steer angle
σ	[lbf/in^2]	Normal stress
τ	[lbf/in^2]	Shear stress
φ	[deg]	Friction angle

CHAPTER 1

INTRODUCTION

1.1 Motivation and Intent

Tire lateral forces are forces generated by the interaction of the tire and surface in the ground plane that seek to steer the vehicle and thus induce motion about the yaw axis and change direction of the vehicle. Lateral forces are particularly important to ground vehicles as they govern how well the vehicle handles, maneuverability, and the stability of a vehicle. Design of high performance vehicles (especially autonomous vehicles) requires significant knowledge of the tire-soil interaction in order to ensure as-designed operation in all conditions considered.

Tire lateral force information is used by designers for vehicle dynamics simulations and calculations to assess the handling and maneuvering capabilities of a vehicle before it is built. By looking at plots of the lateral force data, or using a tire model, the designer can assess the relative sensitivity to steering input, vertical load, and the maximum lateral force generated under various conditions of inflation pressure, camber angle, and operating surface strength.

The intent of the following research is to update the knowledge base regarding lateral force performance (and some limited longitudinal knowledge) of an ATV tire when varying camber, inflation pressure, and draw links to the influence of operating surface normal and shear strength. Furthermore, the data are applied to a tire model to

assess the influence of inflation, camber, and operating surface on the coefficients of the tire model.

Only one other study of this nature was conducted before, and so happened to be in the late 1980's at the University of Maryland [25]. However, no quantitative data on surface, inflation pressure, or camber information was collected. While conducting experiments similar to those conducted by those at UMD, additional experiments were conducted on the shear and normal strength of the operating surfaces, also along with the use of D.A. Crolla's exponential tire model [15] to compare the performance changes between surface, inflation pressure, and camber.

An assessment of the problem of measuring ATV tire forces specified a need to record the several operational variables of the tire as it will be placed in service. Also required would be strength data of the rubber-soil interface as to make surface comparisons with. Using the UMD study for initial guidance, a towed test rig designed and fabricated for use over natural surfaces. In addition, a bevameter was designed and fabricated for use in testing the strength of the rubber-soil interface. Both pieces of equipment were outfitted with sensors and transducers as to interface with an interchangeable data logging system.

Upon processing the data from numerous runs on the tire test rig, lateral, vertical, and longitudinal forces can be plotted against each other or against slip angle. A basic understanding of the operational characteristics of ATV tires is sought, yet further investigation can lead to more knowledge of the effects of different operating surfaces and operational parameters of the tire like camber and inflation pressure. By using the D.A. Crolla's exponential tire model, one can perform curve fits to the gathered data and

deduce coefficients of the tire model. Then the coefficients can be used by vehicle designers to account for camber, pressure, and operating surface in their vehicle dynamics simulations with ATV tires, which was previously unavailable.

1.2 Background and Literature Review

Tires are arguably the most important component in a vehicle system. The tires of a wheeled vehicle are the only link from the body of the vehicle to the ground. All of the forces required to support, propel, stop, and steer a vehicle are transferred to the surface through the interface between the tire and surface (except aerodynamic forces). Figure 1 details the Society of Automotive Engineers (SAE) vehicle axis system, while Figure 2 presents the schematic of an uncambered tire as indicated by Pacejka [20]

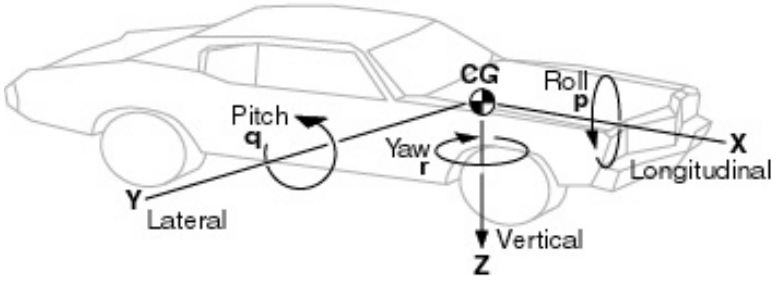

Figure 1.1 – SAE Vehicle Axis System [19]

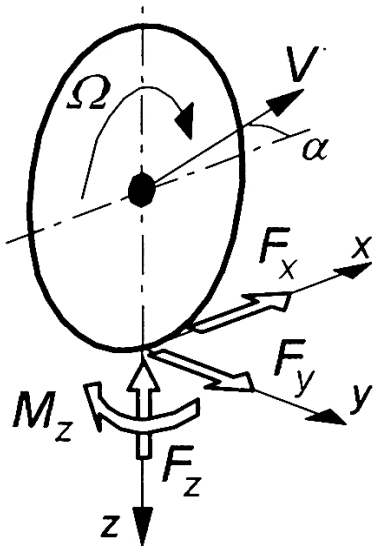

Figure 1.2 – Schematic of tire and forces acting on it [20]

Tires are made to be deformable such that they can assume the shape of the surface they are in contact with. This deformability provides some level of isolation between the operator and the environment. The interface is a complex region in which adhesion and slip occur simultaneously on the microscopic level [20]. Also given the large monolithic tread blocks of off-road tires, there is mechanical interlocking between the terrain and these tread elements, provide lateral and longitudinal traction on a macroscopic level.

While it has been established that the tire is the only link for forces to be imparted to the vehicle from the ground, just how are these forces used to maneuver a vehicle? Other key vehicle subsystems are well defined and designers have much information in specifying their construction and use, including, but not limited to the suspension, steering, and powertrain subsystems. The tire, and specifically in our interest, the ATV tire is severely lacking information. To date, only one study regarding lateral forces of ATV tires has been conducted [25].

This study created a test rig to measure tire forces in the lateral, longitudinal, and vertical directions [25]. The researchers at the University of Maryland only proceeded up to fifteen degrees of slip angle, and also no terrain measurement was conducted, only basic descriptions of the surface were made. [25]

1.2.1 Vehicle Dynamics

A simple vehicle model known as the bicycle model can be used to illustrate how lateral and longitudinal forces are imparted to a vehicle. The bicycle model is shown in Figure 1.3 as described by Pacejka [20].

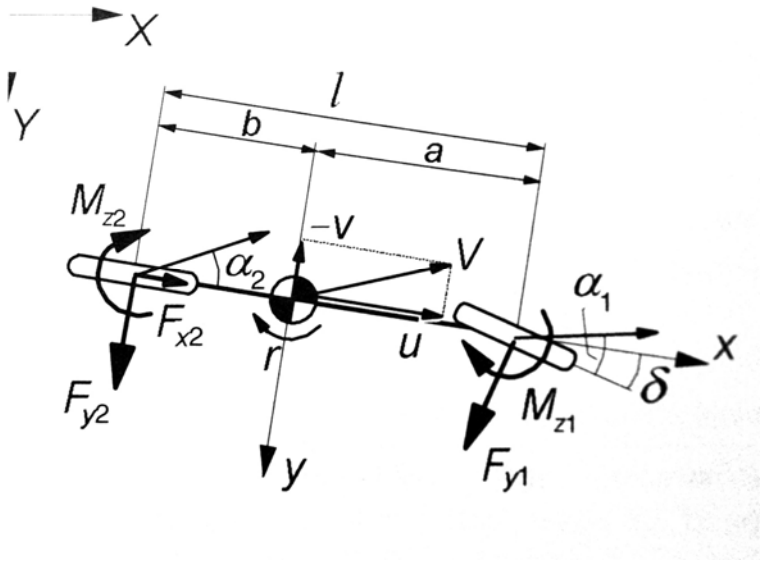

Figure 1.3 – Schematic of simple vehicle model [19]

There are some assumptions Milliken [19] stresses about the bicycle model that must be made clear before going any further.

- No lateral load transfer
- No longitudinal transfer

- No roll or pitch motion
- Linear tire behavior
- Constant forward velocity
- No chassis stiffness
- No aerodynamic loads

First taking the assumption that the tires are linear, an expression can be formed for the front and rear tire forces with cornering stiffness and geometric parameters.

$$Y_f = C_f(\beta + \frac{ar}{V} - \delta) \tag{1.1}$$

$$Y_r = C_r(\beta + \frac{br}{V}) \tag{1.2}$$

The equations described in 1.1 and 1.2 assume the linear tire model, where the product of the cornering stiffness and the slip angle equal a tire force in the lateral direction. The expression within the parenthesis equals the slip angle, by geometric means. Equation 1.1 has a provision to add steer angle into the calculation of lateral forces.

Moments can also be summed about the center of gravity (CG) by multiplying the tire forces by the respective wheelbase dimensions, a and b. The total moment equation becomes the following equation.

$$N = (aC_f - bC_r)\beta + \frac{1}{V}(a^2C_f + b^2C_r)r - aC_f\delta \tag{1.3}$$

Milliken [19] then describes vehicle movement in derivative notation, where the forces and moments are, respectively:

$$Y = f(\beta, r, \delta) = \left(\frac{\partial Y}{\partial \beta}\right)\beta + \left(\frac{\partial Y}{\partial r}\right)r + \left(\frac{\partial Y}{\partial \delta}\right)\delta \tag{1.4}$$

$$N = f(\beta, r, \delta) = \left(\frac{\partial N}{\partial \beta}\right)\beta + \left(\frac{\partial N}{\partial r}\right)r + \left(\frac{\partial N}{\partial \delta}\right)\delta \tag{1.5}$$

Furthermore, Milliken describes various stability derivatives that can be calculated.

$$Y_\beta = C_f + C_r \tag{1.6}$$

$$Y_r = \left(\frac{1}{V}\right)\left(aC_f - bC_r\right) \tag{1.7}$$

$$Y_\delta = -C_f \tag{1.8}$$

$$N_\beta = aC_f - bC_r \tag{1.9}$$

$$N_r = \left(\frac{1}{V}\right)\left(a^2C_f + b^2C_r\right) \tag{1.10}$$

$$N_\delta = -aC_f \tag{1.11}$$

The full derivative notation of the equations of motion is presented by Milliken as the following:

$$I_z\dot{r} = N_\beta\beta + N_r r + N_\delta\delta \tag{1.12}$$

$$mV(r + \dot{\beta}) = Y_\beta\beta + Y_r r + Y_\delta\delta \tag{1.13}$$

While this model is simple and workable, one must recall the assumptions placed on the model. As a tire's cornering ability changes with normal load and slip angle, an

effective model must take this into account. The vertical loads imparted on tires in the off road world can change significantly, and is thusly another reason to add vertical load effects to the model. The bicycle model is a good starting point for modeling vehicle behavior, however further improvements can be made without sacrificing simplicity. These improvements can be found in the four wheel tire model, and using nonlinear tire models.

Another improvement to the model is changing the tire forces from their current linear form to a nonlinear model. The nonlinear model more accurately depicts the force generation trends and can allow greater slip angles to be simulated. Nonlinear tire models predict the shape of the transition region, and the shape of the saturation region, which is where high slip angles occur, and where lateral force either becomes constant or trails off with increasing slip angle.

Recall that lateral forces are governed in part by the normal load on the tire. The simple bicycle model assumed that the normal load on the tire was constant. In realistic conditions, however, there are suspensions which allow for roll motion which in turn place differing normal loads on each tire of the vehicle. By characterizing the suspensions roll effects, one can provide a normal load to a tire model or look-up table in a simulation to generate the required lateral force values.

Observe Figure 1.4 where Milliken provides a look into the forces on a vehicle when viewed from the front or rear.

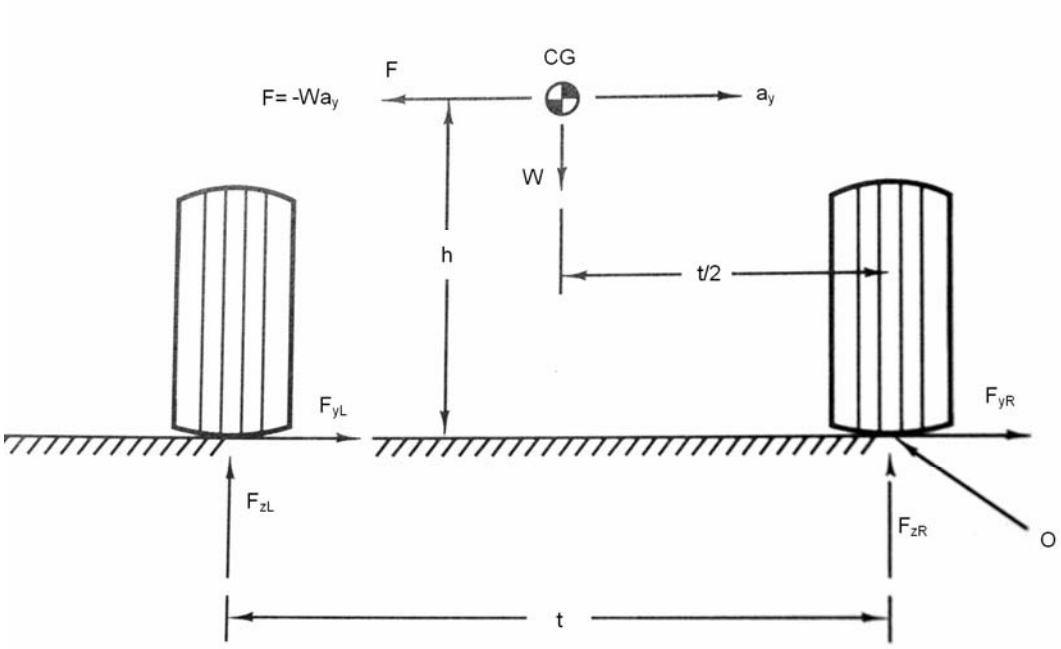

Figure 1.4 – Load transfer due to cornering [19]

Note that the centrifugal force that is acting to the left is opposite the direction of the lateral acceleration which is created by the forces at the tire-surface interface. Also note that the CG is at a height above the ground and acts as a moment arm for the centrifugal force to induce a roll moment. If one sums the moments about point *O* listed in the figure, they will have:

$$W_L = \frac{W}{2} + \frac{WA_y h}{t} \tag{1.14}$$

Finding the change in weight transfer, one then has:

$$\Delta W = W_L - \frac{W}{2} = \frac{WA_y h}{t} \tag{1.15}$$

Note how no suspension parameters for roll motion have been introduced. This is to highlight that load transfer can occur even with a very stiff or no suspension

whatsoever. Observe Figure 1.5 from Pacejka [20] that depicts a schematic of a simple, four-wheeled vehicle.

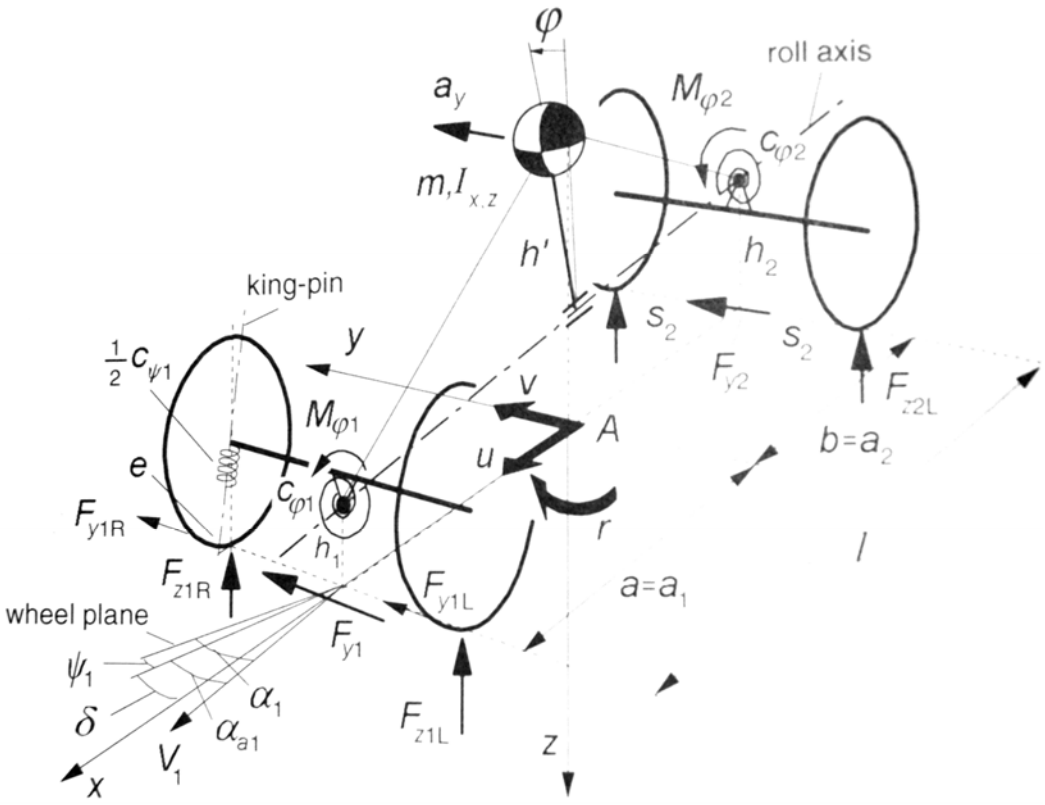

Figure 1.5 – Four wheel vehicle model [20]

There is a roll axis (also known as the neutral roll axis) defined as a line passing through the front and rear roll centers. Also, there is a perpendicular distance, *h'*, that the CG is located away from the roll axis. The motion of the CG about this axis during cornering gives rise to roll moments which are resisted by roll stiffness' of the front and rear suspension setup [19]. The moment about the roll axis created by the motion of the CG is,

$$M = -W_s h'(A_y - \phi) \tag{1.16}$$

where the angle φ is the roll angle of the chassis. One can then equate the roll moment to the roll stiffness and see that:

$$\frac{\phi}{A_y} = \frac{-W_s h'}{K_f + K_R - W_s h'} = K_\phi \tag{1.17}$$

Using all information that Milliken and Pacejka have provided so far, full load transfer equations for the front and rear can be seen as:

$$\frac{\Delta W_f}{A_y} = \frac{W_s}{t_f}\left[\frac{h' K_{f'}}{K_f + K_r - W_s h'} + \frac{\ell - a_s}{\ell} z_{RF}\right] + \frac{W_{uF}}{t_F} z_{WF} \tag{1.18}$$

$$\frac{\Delta W_r}{A_y} = \frac{W_s}{t_r}\left[\frac{h' K_{r'}}{K_f + K_r - W_s h'} + \frac{a_s}{\ell} z_{RR}\right] + \frac{W_{uR}}{t_R} z_{WR} \tag{1.19}$$

Again, recall that these load transfer equations give rise to the changing normal loads that the tire experiences. Simulations need these normal loads along with slip angle to look up the lateral forces that will be generated by the tire-soil interface.

The last missing piece of information to the vehicle model presented is that of the lateral forces generated by the tires. One may pick an acceleration, and backtrack to find what will be expected of the tires, however it is this acceleration we wish to find for a given vehicle setup. By knowing how the tires behave we can then put together simulations by Equations 1.12 and 1.13 that find the acceleration, which can then be integrated to find velocity, and integrated twice to find position.

Seeing that these simulations need lateral tire data, how does one acquire the sought information? One way would be to provide the simulation of look-up tables created by data from experimentation. Generating these tables for every condition a particular tire can be put into is time consuming, and the computer storage space required is tremendous.

An easier way to provide data to a simulation would be with a tire model. A tire model is a mathematical expression, or set of expressions that, when the proper data is applied, will return a lateral force. Many tire models exist, however each has their own advantages and disadvantages. While details of specific tire models will be discussed in subsequent chapters, the idea is that a tire model is easier and cheaper to implement than look-up tables.

It is the goal of this research to generate enough empirical data such that tire force trends in the lateral, vertical, and horizontal directions can be observed and recorded. Then, a tire model is selected that can appropriately match the experimental results. This will allow designers to create more effective designs with less physical testing, and thusly save time and cost.

1.2.2 Tires

To simulations, tire lateral force is simply a value that is fed to equations of motion. How do tires physically generate these forces? What are the mechanisms that provide grip? How are tires characterized? One must first step back and understand that it is not the tire that is simply generating forces, but it is the interaction of the tire with its

operating surface. Both the tire and the operating surface have measurable characteristics that give insight as to what performance one can expect.

Simplistically, tire lateral force is a function of normal load and slip angle. For a given lateral load, one can expect the shape of a tire curve to look similar to that of Figure 1.6.

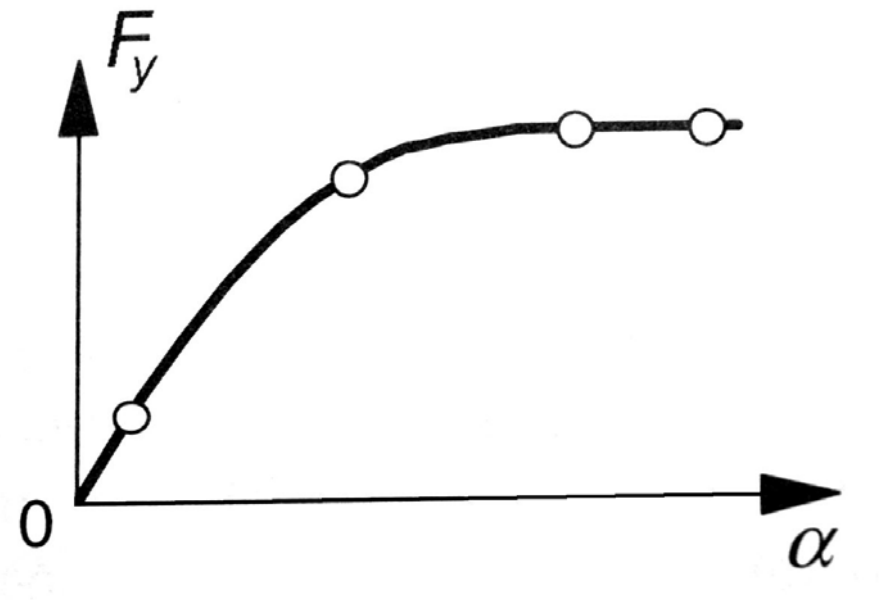

Figure 1.6 – Sample plot of lateral force v. slip angle [20]

One will observe a linear trend at low slip angles, then entering a transition phase, and finally to a saturated level, where addition of more slip angle results in no further lateral force being generated. The saturated region depends on the coefficient of friction [19], while the linear region is important in comparing the cornering abilities between tires [19]. The slope of the linear region at zero slip angle is known as the cornering stiffness [3].

$$C_\alpha = \left.\frac{\partial F_y}{\partial \alpha}\right|_{\alpha=0} \tag{1.20}$$

The shape of this lateral force – slip angle relationship is governed by several physical variables, not only of the tire, but of the surface as well. Two main tire variables to observe are that of the inflation pressure, and the camber angle. The operating surface has many other variables onto it, and will be discussed further in the text.

Inflation pressure is arguably the easiest thing to change on a vehicle. The pressure of a tire has several effects on the longitudinal and lateral performance of a vehicle. Inflation pressure can change the cornering stiffness of a vehicle, i.e. the elastic properties [19]. A slight increase in pressure can give a slight increase in lateral force [19]. This knowledge can be used in vehicles to fine tune the balance of a vehicle for certain conditions [19].

Recall that performance at high slip angles is governed by the effective friction coefficient. If one reduces inflation pressure, they will realize a larger contact area and thus a larger friction coefficient. This effect must be balanced such that the inflation pressure allows the center of the tread and the tire carcass sidewalls to carry a proportional amount of the vehicle load on that tire [19].

Another effect of altering tire pressure is how the pressure change affects the motion resistance forces on a vehicle. A decreased pressure will allow a lower spring rate, and thusly more deformation of the tire [19]. More deformation at speed translates to more energy going into deforming the tire. This energy is then changed to heat and at

great levels, may damage a tire. A higher pressure will produce less deformation, and thus less motion resistance and increased tire life.

Camber angle also has a significant effect on the performance of a tire. Adding camber to a tire means that the tire is tilted about an axis that lies in the ground plane, and is oriented longitudinally to the vehicle. Figure 1.7 depicts this arrangement. Positive camber is defined as the tilting of the tire such that the top of the tire is moved in the direction of the lateral force generated by the tire.

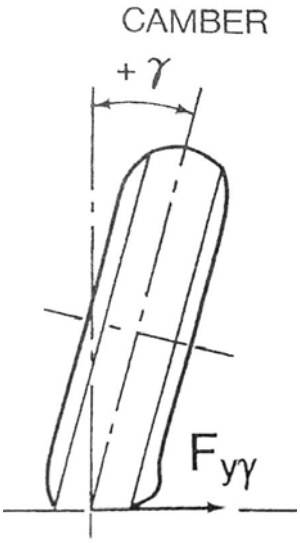

Figure 1.7 – A cambered tire [20]

The increased angle of tilt generates a thrust force in the contact patch. Much like cornering stiffness, there exists camber stiffness. Camber stiffness is the measure of the slope of the camber thrust curve at zero slip angle [3].

$$C_\gamma = \left.\frac{\partial F_{y\gamma}}{\partial \gamma}\right|_{\gamma=0} \tag{1.21}$$

Camber stiffness is generally less than cornering stiffness, and Milliken reports that it is around five or six times less than that of cornering stiffness [19]. Furthermore, Milliken indicates that in wide racing tires, camber effects tend to trail off after about five degrees [19]. Motorcycle tires however, generate effective lateral force to upwards of fifty degrees of camber [19]. Other factors influencing the amount of camber a suspension designer can put into a suspension is the packaging of the vehicle, and the extra stresses put on wheel set components due to the increased camber angle.

1.2.3 Operating Surfaces

While tire properties have an effect on lateral force generation, the operating surface also has a large hand in generating lateral forces. The shearing of a soil generates lateral and longitudinal tractive forces. Normal response of a soil has an effect on the motion resistance and the vertical support of vehicular loads. Several methods for evaluating the various soil properties for vehicle operations have been developed over the last 75 years with some producing more useful results than others. The field of terramechanics has been devoted to characterizing soil mechanics in relation to vehicular operations.

The informal beginnings of terramechanics can be linked to World War I where British Officers walking sticks were reportedly used to prod the ground and determine if it was safe for passage. These walking sticks are also rumored to be the basis for the cone penetrometer [2]. Around 1913, Russian scientists proposed an equation relating the

sinkage of a plate in soil with a uniformly distributed load. The equation took the following form:

$$p = kz^n \tag{1.22}$$

Where, static sinkage (displacement into soil) is measured by z, and pressure under the pressure plate by p. Deformation modulus k, and deformation exponent n, was to be determined by experiment [1]. In that same time frame, Bernstein used a deformation exponent of n=1/2 in his works on motion resistance of wheels [1]. Goriatchkin and Bernstein tried to surmount the difficulties seen in using k as a deformation modulus (as it was directly related to the plate size), however their attempts did not turn the result they hoped [1]. Many years later, M.G. Bekker would find a way to improve the pressure-sinkage relationship in his development of the bevameter [27].

Originally, soil measurement has its roots in civil engineering knowledge, and some soil measurement techniques from civil engineering were imported to be used for vehicular travel. There are several methods for measuring soil from a civil engineering approach, and each test must be used carefully in reference to the problem at hand. The dominant approaches are the vane shear test, tri-axial test, and direct shear test [26].

A vane shear test (Figure 1.8) involves forcing a four-bladed vane into the soil or a core sample obtained at the test site. It is then rotated at a constant angular velocity and the torque is recorded [8].

Figure 1.8 – Vane shear apparatus

Care must be used if using vane shear tests as the strength indicated is a function of angular velocity. This is due to the presence of pore water pressure that may not dissipate quickly enough based on the grain sizes of the soil and thus fail the soil at a lower stress. [9]. Note that ground vehicles will apply varying shear rates to the soil, and not necessarily under the soil, but rather on the top, especially in the case of medium UGVs, where sinkage is small related to the diameter of the tire.

Direct shear tests (Figure 1.9) comprise of a cylindrical sample of soil placed between two rings, and a normal load is applied. Then a shear force is applied across the rings, and then each test is plotted against its normal load to obtain a Mohr-Coulomb failure envelope [10].

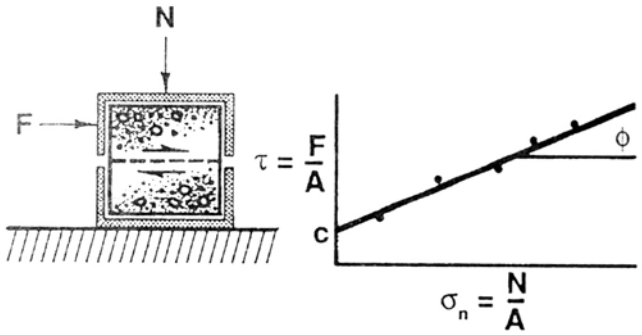

Figure 1.9 – Schematic of a direct shear test [10]

The test specimens are core samples taken from a particular site and then the test is performed in the lab. On the fastest setting obtainable, the staff at CRREL (Cold Regions Research and Engineering Laboratory) could only obtain a shear rate of 0.8 cm/s, wheras the typical shear rate of a traction generating tire is between 10 and 40cm/s [10].

While Shoop and her colleagues have pointed out that there is a discrepancy between actual and required shear rates for the direct shear test [10], Okello stated, "The authors concluded, very uncommittedly, that it may be suspected that the shearing mechanism of the direct shear test is most closely allied to that of a soil under a vehicle…" [8] The uncertainty regarding direct shear leads one away from using this test. Also, like the vane shear test, it indicates the shear stress within a soil, and not at the interface between a vehicles tire and the soil.

The third and final civil engineering approach to soil measurement for vehicular travel is the tri-axial test (Figure 1.10). Like the direct shear test, a core sample is prepared for use in the laboratory. The sample is encased in a rubber membrane with caps on the top and bottom. It is then placed on a pedestal in a chamber that is filled with water and a confining pressure is applied to the sample. The pedestal is then set in motion and normal reaction forces are recorded [8].

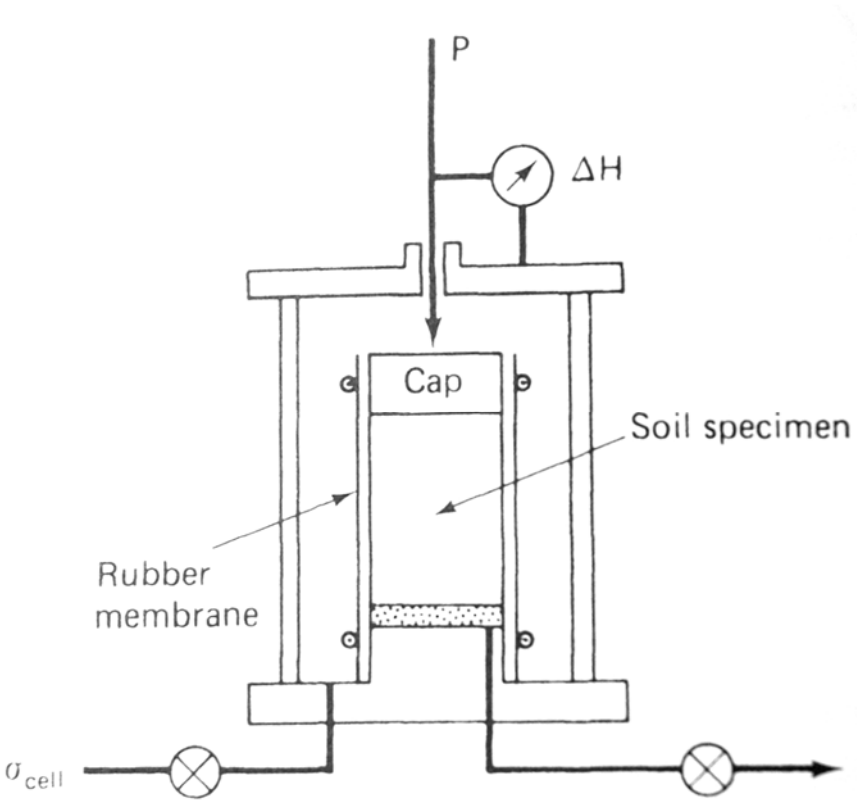

Figure 1.10 - Schematic of Tri-axial soil testing apparatus [26]

Tests are then compiled by varied normal loads and the Mohr-Coulomb failure envelope can then be developed [10]. Unfortunately the soil can not be measured in-situ, nor can the whole field be measured due to the extremely slow and costly nature of the tri-axial test [8].

While there are several methods available to measure soil, two methods have found significant support in the field of terramechanics. The cone penetrometer is a simple, lightweight device which provides limited information, while the bevameter is a larger, more complex apparatus, yet provides significant insight into the strength properties of the terrain for vehicular travel.

Developed by the Waterways Experiment Station (WES) for the U.S. Military, the cone penetrometer would originally be used to provide a “go/no-go” decision on soil strength for military commanders in the field [3]. The cone penetrometer (Figure 1.11) is a 30-degree right-circular cone having a ½” base area [3]. The Cone Index is a measure of force per unit cone base area. At the top is a proving ring or load cell to measure penetration resistance at various depths when the cone is forced into the ground at 1 cm/s [3], [4].

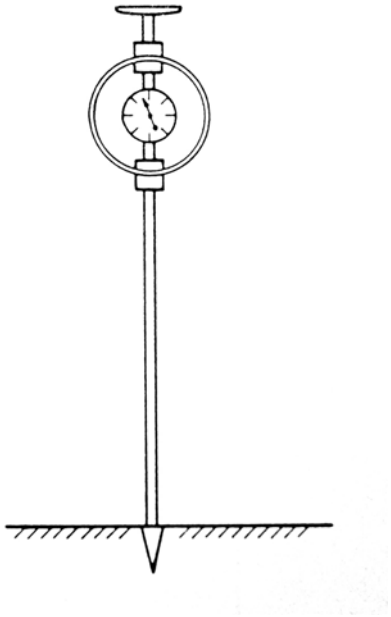

Figure 1.11 – Cone penetrometer [3]

Despite its relative user friendliness and widespread use within the agriculture world, the cone penetrometer’s effectiveness has been questioned on its ability to deliver accurate results in mobility studies [5].

While several versions of Turnage’s Mobility number are available (a number created by dimensional analysis that relates various contact dimensions but only works at

zero slip angle), Gee-Cough and Sommer [32] state that “broadly speaking” the Turnage Mobility numbers may be used to model the coefficient of side force if soil friction angle was constant and the cone index was a measure of soil cohesion [29]. With that being said, however, the “validity of using soil cone index value to represent soil condition has always been questionable” and that the soil cone index is “a compound parameter which is a function of several soil properties” including soil friction angle and cohesion [18].

The bevameter, also known as the Bekker Value Meter, was developed by M.G. Bekker in the 1950’s seeing that soil-vehicle properties should be measured under conditions as close to those presented by a vehicle [3]. The premise is that vehicles apply normal and shear loads to the soil and therefore soil should be measured when subjected to normal and shear loads. This is the soil testing apparatus used in this study of ATV tires. Specifics regarding the bevameter used for the study can be found in subsequent chapters. The bevameter (Figure 1.12) consists of a two part apparatus with one measuring normal load response, and the other measuring shear load response. For normal loading, penetration plates are forced into the ground and the pressure-sinkage behavior is recorded. The second part is a shear test, typically in the form of an annulus which measures traction-slip performance [3]. These two tests are indicators of the strength of a soil for vehicular travel (i.e. rubber-soil friction angle).

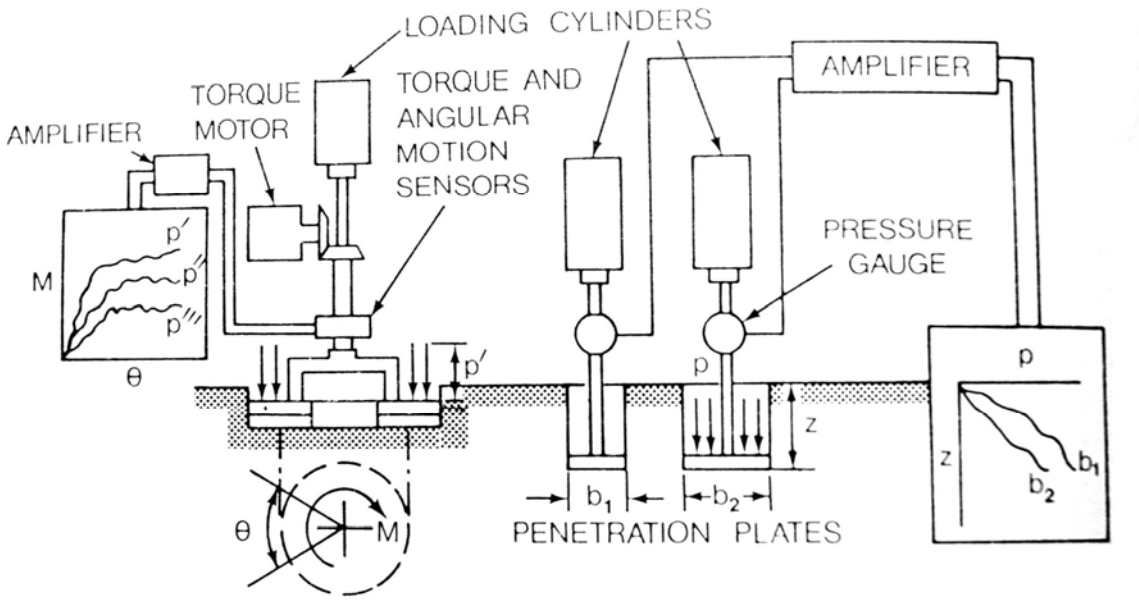

Figure 1.12 – Schematic of a Bevameter [3]

As the bevameter characterizes a soil's strength for vehicular travel, it must be characterized in such a way that can be connected to existing work. The bevameter generates data such that a Mohr-Coulomb failure envelope can be generated for a particular surface. The Mohr-Coulomb failure envelope is a principle used extensively in soil-mechanics, and much has been written about it. One must be reminded that the bevameter's results represent the strength of a soil for vehicular travel.

Before looking into the bevameter parameters, one must have a brief understanding of the Mohr-Coulomb soil failure envelope, and thus a slice of classic soil mechanics.

Soils can be viewed as frictional, cohesive, or a combination of both. Frictional soils (i.e. sand) gain their strength from the intergranular friction forces. The greater the confinement force, the greater the intergranular friction, and thus a stronger element of

soil. Cohesive soils have intermolecular bonds, originating from the positive and negative electric charges imparted on them [26]. Please note that cohesive soils have much smaller particle sizes than frictional soils [26]. This small grain size is what allows the intermolecular forces to dominate the strength of the soil [26].

Both cohesion and friction can be quantified from the Mohr-Coulomb failure envelope. Normal stresses are plotted on the x-axis, and shear stresses plotted on the y-axis. A line is laid tangent to the Mohr circles, and the y-intercept is measured as cohesion, in units of stress, while the angle of the line is the friction angle, in units of degrees. See Figure 1.13 for a representation of the Mohr-Coulomb envelope.

The Mohr-Coulomb failure theory for soils, states (as reported by Liang, et. al. in [33]) that the soil at a point will fail if the shear stress meets the conditions of Equation 1.23.

$$\tau = c + \sigma \tan \phi \tag{1.23}$$

For Equation 1.23, c is the cohesion, measured in units of stress, σ is the normal stress on an element of soil, τ is the shear stress experienced on that element of soil, and φ is the internal friction angle. Equation 1.23 shows that under conditions of normal and shear stress, cohesion and friction angle govern the strength of the soil [33]. This can be used with vehicular studies, as vehicles apply shear and normal loads to the surface of a soil. While the internal friction angle is used for soil mechanics, the rubber-soil friction angle is used for vehicular studies as the stress is being applied via the tire in this study, which is rubber.

In the words of Karl Terzaghi, cohesion and friction angle can be quantified as follows: “If we dig into a bed of dry or of completely immersed sand, the material at the

sides of the excavation slides towards the bottom. This behavior indicates the complete absence of a bond between the individual sand particles. The sliding material does not come to rest until the angle of inclination of the slopes becomes equal to a certain angle known as the angle of repose. The angle of repose of dry sand as well as that of completely immersed sand is independent of the height of a slope. On the other hand a trench 20 to 30 feet deep with unsupported vertical sides can be excavated in stiff plastic clay. This fact indicates the existence of a firm bond between the clay particles. However, as soon as the depth of the trench exceeds a certain value, dependant upon the intensity of the bond between clay particles, the sides of the trench fail and the slope of the debris which covers the bottom of the cut after failure is far from vertical. The bond between the soil particles is called cohesion. No definite angle of repose can be assigned to a soil with cohesion, because the steepest slope at which such a soil can stand decreases with increasing height of the slope. Even sand, if it is moist, has some cohesion." [13]

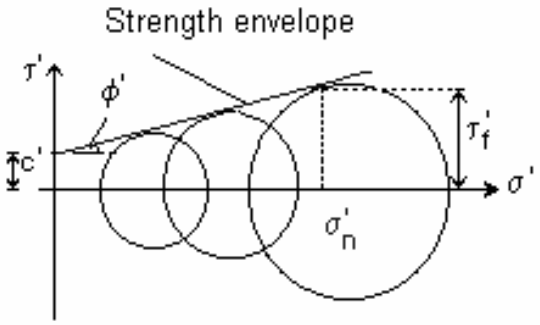

Figure 1.13 – Mohr-Coulomb strength envelope

One must note however that the strength envelope is not linear throughout its entirety. Particularly associated with granular soils, confinement, and normal stresses can

become so great that grain crushing can occur, and thus lower the strength envelope seen in Figure 1.14 [26]. At the bottom line however, we can see that there are two mechanisms governing soil strength, cohesion, and friction.

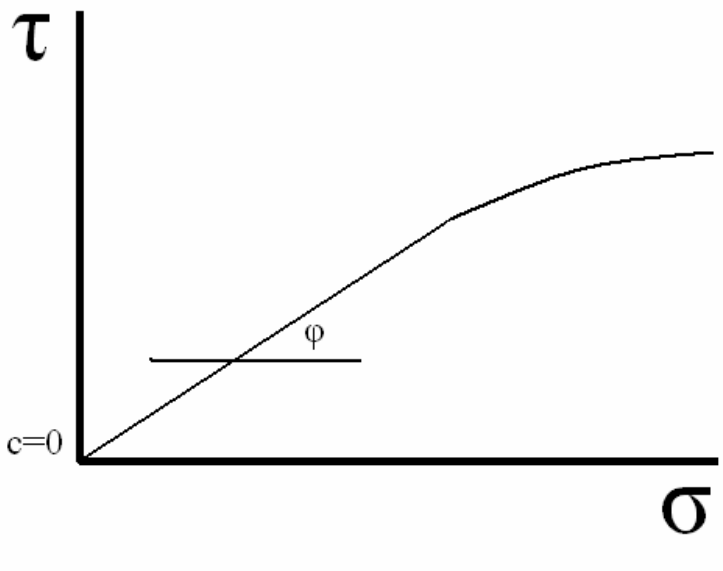

Figure 1.14 – Nonlinearities of Mohr-Coulomb envelope at high normal stresses

Another soil value that the bevameter can produce is that of the shear deformation modulus. The shear deformation modulus measures the amount of shear displacement needed for the development of the maximum shear stress. Denoted by the letter *K*, the shear deformation modulus is used in Equation 1.24, where *j* is the measure of linear displacement.

$$\frac{s}{s_{\max}} = 1 - \exp\left(\frac{-j}{K}\right) \tag{1.24}$$

While the bevameter method has a shear strength component, there is an associated normal component. This normal component characterized the relationship

between normal (vertical) loadings and the associated sinkage (displacement) into the terrain.

Bekker used the work of Karl Terzaghi for soil bearing capacity in order to develop a pressure-sinkage relationship [1]. Following the form of the Bernstein equation, Bekker developed the following equation:

$$p = (\frac{k_c}{b} + k_\phi)z^n \tag{1.25}$$

The variables within Equation 1.23 have p as pressure, b as the width or diameter of the penetration plates, z as the sinkage, and k_φ, k_c, and n are soil properties. Properties k_φ, and k_c, are related to friction angle and cohesion, respectively. The sinkage exponent is n. As indicated by Wong, significant manipulation of the test data must be performed in order to generate these properties [3]. First the data must be plotted on a log-log scale, then, a straight line is fit to the data. No standard method for the fit is observed, and is generally fit by eye [3].

It must be noted once more that while the bevameter measures various soil properties, these properties are only of use to vehicular studies. These properties are only used in describing the strength of a soil for the movement of a vehicle. Soil properties that are familiar to civil engineers such as void ratio, liquid limit, and water content all play roles in the values of the bevameter properties, however their effects are complicated, but manifest themselves in the various values listed previously, and are not within the scope of this research.

While there were little physical improvements to bevameter equipment over the years (besides computerization), the use of the data obtained would undergo changes,

particularly in the pressure-sinkage relationship. Bekker's original pressure-sinkage relations would be modified by A.R. Reece to suggest that pressure increases linearly with the width of the sinkage plate for a given value of sinkage divided by width [7]. Reece's work would make the two sinkage coefficients dimensionless and independent of the sinkage exponent. The new equation was backed up by significant testing, and also fit into soil behavior that could be predicted by classical soil mechanics as described by Karl Terzaghi [7].

$$p = (ck_c^{'} + \gamma bk_\phi^{'})(z/b)^n \tag{1.26}$$

In addition to the pressure-sinkage issues, the bevameter came under fire by Karafiath and Notazwiki, indicating that the true failure surface of a soil did not occur at the surface of the shear head, but rather on oblique planes due to the lack of lateral confinement of the soil [11]. This lack of lateral confinement around the shear also allows the large shear displacements to in turn allow large vertical displacements, known as slip-sinkage. To alleviate this, Janosi and Karafiath suggest the application of a surcharge to prevent the shear head from continually sinking [12]. (Note: A surcharge is the application of an identical normal load to that of what is being applied by a shear head. This is meant to ensure that the soil immediately outside of that which is being sheared has the same confining stress as that of adjacent soil.)

J. Okello noted the bevameter method and the cone penetrometer method to be the most appropriate for vehicular studies as the measurements were made in-situ. He further states a potential drawback to the use of the bevameter, as it only characterizes the soil on the surface and does not allow for penetration plates or shear heads to be of the same contact area as the vehicles under question [23].

While these issues of size and depth may seem detrimental to the further use of the bevameter, these issues are not present in small vehicle studies. This can be realized by the fact that sinkage of ATV's or medium sized UGV's is not enough to cause a significant change in confinement stress. Okello further notes that the size of the body in a bevameter is more important than the shape, and should "reproduce those of the vehicle ground contact area" [23].

1.3 Purpose of Thesis and Contribution

As described in the preceding text, there are several methods for collecting data on tire performance and soil strength. Trends in tire pressure and camber changes are known qualitatively, and changes in performance from a surface change are also qualitatively known. This research will measure, through load cells and accelerometers, forces generated by the tire. These forces will be reduced by equations derived from the geometry of the test rig, or calculated directly in the case of accelerometer data. Soil data will be measured via bevameter techniques that characterize soil-rubber shear stress response and soil normal stress response. Soil properties of cohesion, friction angle, and shear modulus are reduced from the displacement and moment data from the bevameter. Tire lateral force information is still needed to generate accurate vehicle dynamics simulations and improve tire performance models. By building test apparatus and using a tire model for vehicle dynamics, one can gain insight as to how tire parameters, such as camber, and inflation pressure, and operating surface properties, such as cohesion, shear modulus, and friction angle, affect the performance of a vehicle. This insight leads to understanding the links and relationships such that tire model parameters can be

formulated, and alleviate the need to do substantial guessing during the design process or make several expensive performance tests. This work seeks to measure tire forces and apply a tire model at different settings of camber, pressure, and surface to observe their effects on the exponential tire models coefficients.

CHAPTER 2

RESEARCH TOOLS

The research tools presented in this chapter represent the items used by the author to either generate or analyze the test data. Much time was invested in the design and fabrication of the test rigs as nothing meeting the specific need is available commercially. Chapter 2 will highlight the design and use of these tools in the generation of tire and soil data.

2.1 Bevameter

As described in Chapter 1, the bevameter is a device which measures the shear and normal strength of a soil in relation to vehicular travel. Dozens of bevameters have been built since M.G. Bekker first built them in the 1950's, and the progression of technology has certainly aided the effectiveness of the bevameter over time. Highlighted in this section are some of the more successful designs and their benefits, the goals and requirements of the bevameter for this study, and the as-built result.

2.1.1 Bevameter Development

The design and development of a bevameter includes a look at existing designs, highlighting the advantages of each design, and specifying goals for a new design. Existing bevameter designs were reviewed in order to fine tune design goals for this work. The result is a field-portable bevameter capable of one-man operation.

Bekker's work at the Land Locomotion Laboratory produced several small, man-portable bevameters and eventually a large mobile bevameter mounted on a tracked vehicle [27]. Upon observation, most of the shear heads on Bekker's bevameters are those which have grousers (teeth) attached to them. This would seem to indicate testing that is more for tracked vehicle research than that for wheeled vehicle research.

Several authors indicate the great importance that the pressure plate and shear head contact area should closely represent those of the vehicle in question [23]. While this may seem a simple goal to achieve, many of the off-road vehicles studied by Bekker and Wong were so large that substantial structures to hold the apparatus were required [27]. This condition limited the mobility of the bevameter that matched pressure plate and shear head area to the vehicle that was studied.

Shoop, of the U.S. Army Cold Regions Research and Engineering Laboratory (CRREL) reports on a bevameter shear head designed by Stafford and Tanner (Figure 2.1) [29].

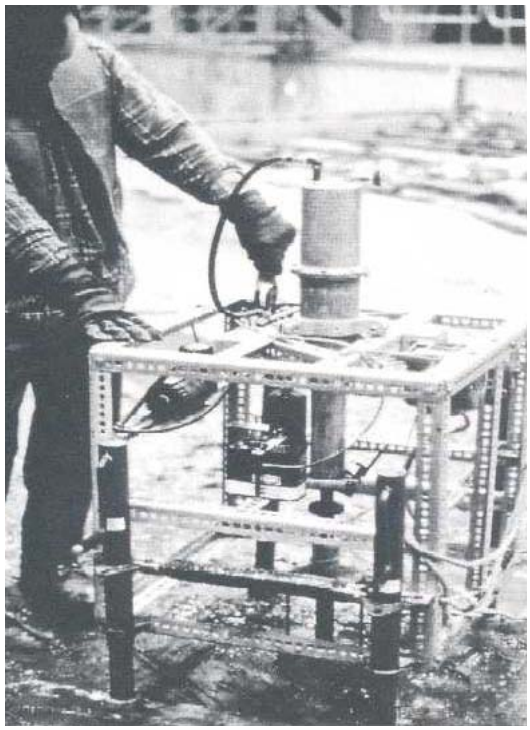

Figure 2.1 – Bevameter shear-head as described by CRREL [10]

While man-portable and easy to use, the shear head did not match the contact area of the vehicles generally studied by CRREL [10]. The advantage of studying ATV tires is that the contact area is small, and a bevameter can be designed to be vehicle portable on a platform that is not excessive in size.

The bevameter constructed by Wong made use of a substantial transport platform, and electronic sensors [3]. Collecting this data was facilitated by the use of a personal computer and specifically written software to alleviate the manual data reduction of earlier strip charts [3] [14].

Figure 2.2 – Bevameter as designed by Wong [3]

In Figure 2.2, note the shear head by the vehicles right track, and the pressure-sinkage apparatus near the center of the vehicle, closest to the operator. Figure 2.3 shows a schematic of the shear head.

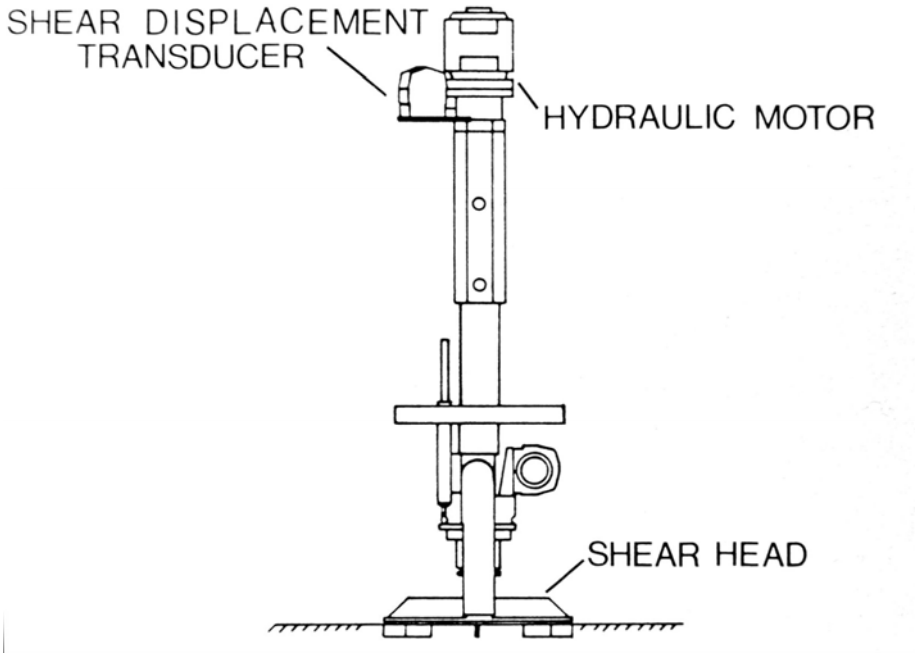

Figure 2.3 – Details of shear head instrumentation and control [3]

Note that Wong also makes use of hydraulic actuation methods, easily supported by the transportation platform.

Looking at the systems previously built, three things are clear. First, the bevameter should have contact areas similar to the vehicle studied. Second, a bevameter should be portable, either by human, or vehicle. Third, a bevameter should use electronic sensors with computers to reduce data reduction workload and reduce chances of error.

For the bevameter constructed at Auburn University for this project, all three design goals were tied into a fourth goal of maintaining low cost. In order to ensure the proper contact area, a KT 821 tire (the tire used in the study) had its lug-tips coated with a marking compound (Figure 2.4). The tire was then placed on a vehicle, with the tire on a piece of paper to depict the contact pattern. Approximately 300 lbf vertical load was applied, and the tread pattern marked.

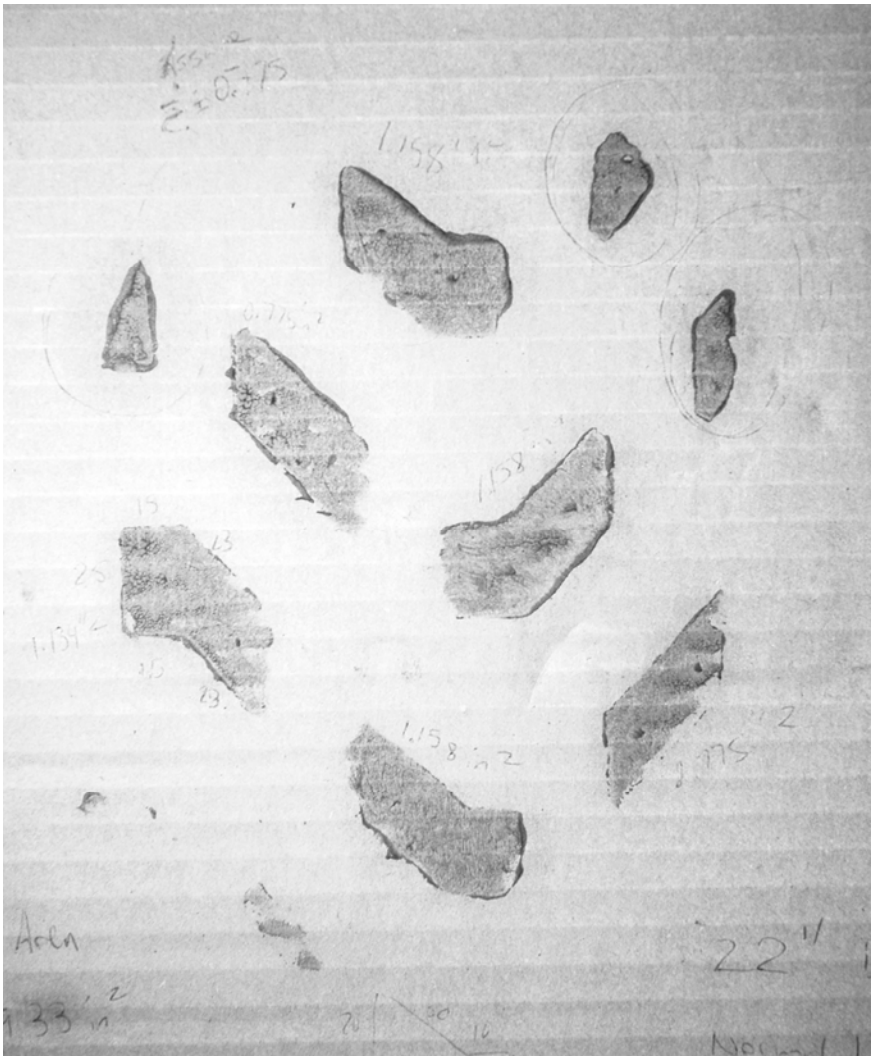

Figure 2.4 – KT 821 lug contact area

Each lug marking was measured, and an area for each was calculated. The sum of the areas totaled 6.933 sq. in. Other tires were tested, and their results were factored into the decision to make the shear head have a 5 in. outside diameter, and a 3 in. inside diameter. This results in a 12.5 sq. in. Also, the shear head would be coated in silicone rubber of the same durometer hardness as the KT 821 tire.

The decision to make the shear head to be 12.5 sq. in. stems from larger contact patterns from other tires, and also assuming that the KT 821 could sink into the soil

beyond than the lug height, with the tire carcass making contact, and effectively doubling the 6.933 sq. in. contact area by the lug tips.

The pressure plates used for the pressure-sinkage tests were sized to span the area difference between the lug tips, and the entire carcass making contact. Four inch and three inch pressure plates were fabricated providing 12.56 sq. in. and 7.06 sq. in. of contact area, respectively.

As the contact areas were sized to emulate those of ATV tires, the normal loads must be of a similar magnitude as well. Looking at the man-portable models, carrying around enough weight to provide a normal load typical to an ATV tire would be quite cumbersome. According to Weir and Zellner, a typical ATV can have an overall weight near 600 lbf [28]. Assuming an equally divided weight to all four wheels, this would result in 150 lbf of normal load at a static condition.

Figure 2.5 – Bevameter as attached to Yamaha Rhino

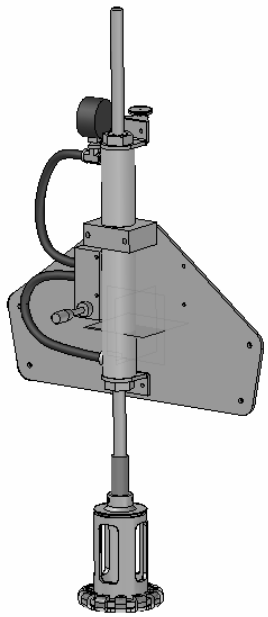

Figure 2.6 – Bevameter as designed in CAD

In order to provide the significant normal loads to the shear head and pressure plates, the bevameter is mounted to a Yamaha Rhino side-by-side ATV (Figure 2.5, 2.6). The Rhino weighs approximately 1,000 lbf, and with the bevameter mounted on one end, the Rhino can provide well in excess of 300 lbf of normal load. By looking at Equation 1.5, the load transfer equation, this would generate well over 1 G of lateral acceleration, which is above the range expected for ATV's and UGV's especially on soil surfaces.

Allowing the normal load to be changed as required in experiments, a pneumatic cylinder was employed to provide the varying normal loads to the pressure plates and the shear head. A double ended pneumatic cylinder was selected so that applying torque to the shear head would be easier to control than a hydraulically or pneumatically actuated system. This manually actuated (torque applied by operator's strength) system significantly reduced cost over a hydraulic or pneumatic actuation system.

Lastly, to fulfill the goal of simplification of data collection, electronic sensors were used on the shear test portion of the bevameter. Normal load tests were conducted (Figure 2.7) by recording the pressure reading on the cylinder, and the displacement into the soil via a dial indicator.

Figure 2.7 – Details of normal load test apparatus

The use of the dial indicator allowed much accuracy for the small displacements found in the stiff test soils. For the shear tests, a torque cell was placed between the pneumatic cylinder shaft and the breaker bar used by the operator. Displacement was recorded by a rotary potentiometer as seen just behind the pressure gauge in Figure 2.8.

Figure 2.8 – Elements of shear head data acquisition system

Using design elements from previous, successful bevameters, a custom bevameter is built for application to ATV tires. Included in the design is field mobility, low cost, proper sizing, and semi-automated data acquisition.

2.1.2 Operations

Operating the bevameter to collect field data requires some basic knowledge of soils, computers, and electronics, while also requiring a steady hand. Upon meeting these requirements, gathering soil data can be completed with relative ease.

As the bevameter is mounted to an ATV, several sites can be tested over a particular area due to the mobility of the vehicle. Once a particular site is selected, the vehicle is parked in as a level of a condition as possible to get the best results. Even if the terrain is not perfectly level at the location, a universal joint mounted between the shear head and cylinder shaft can allow for slight misalignment.

Once positioned, the bevameters compressed gas source is connected to the cylinder, and the appropriate attachment affixed to the cylinder shaft, be it a pressure plate or shear head. For the pressure-sinkage tests, the pressure plates are affixed, and the dial indicator attached. Pressure is applied to the cylinder, and sinkage is measured. Repeat measurements are taken with higher cylinder pressures.

For the shear head tests, the data acquisition system is initialized, and sensors are zeroed. A normal load is applied to the shear head by increasing cylinder pressure to the desired level. The operator then applies a torque about the cylinder shaft, rotating the shear head through approximately 180 deg. of angular displacement, while the data recorder collects torque and displacement data. The experiment is repeated with increasing normal loads.

The operation of the bevameter is convenient due to the mounting on a transportation platform. A single operator can then collect data from either a normal load test or a shear head test with relative ease due to the use of a data acquisition system.

2.1.3 Assessment

As any other mechanical device, the bevameter must be evaluated to see that useful, acceptable results are being generated. Since several bevameters have been built over the years, there is plenty of data to use for comparisons.

Shear head tests produced data whose shape fit that of equations provided by Wong [3], and filtered data from Yu [30].

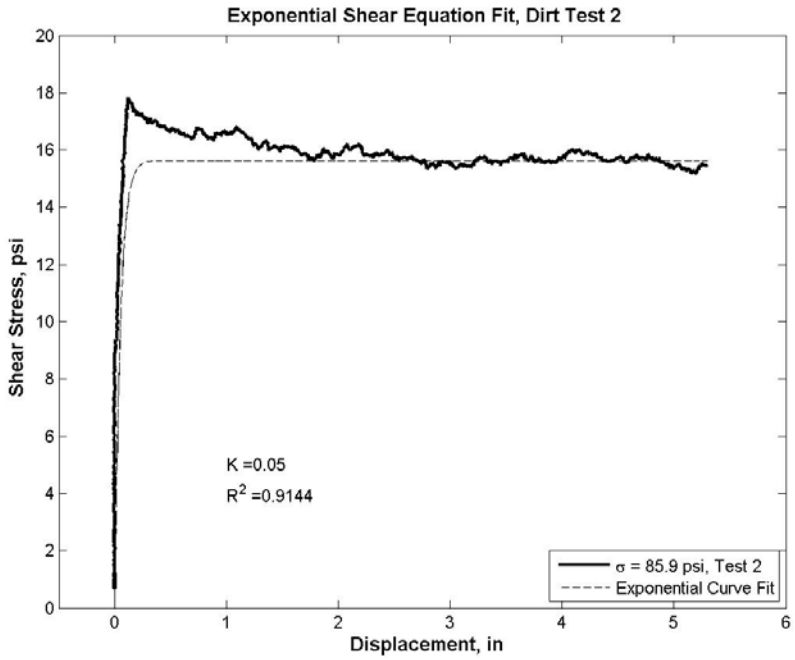

Figure 2.9 – Shear head data with curve fit from Equation 1.23

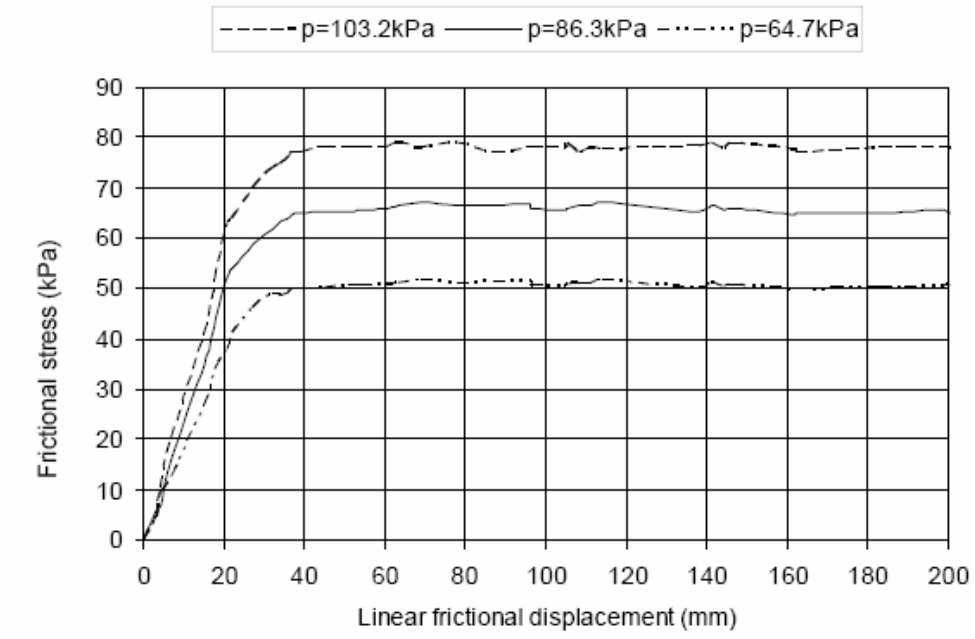

Figure 2.10 – Shear test data from University of Pretoria [30]

As one can see, Figure 2.9 shows good agreement between the equation presented by Wong [3] and the data collected for this study. Also, one will see that this data is of the same shape that was presented by Yu in tests conducted for the University of Pretoria in Figure 2.10 [30]. Note that the linear displacement is the displacement around the circumference of the center of the shear head.

Normal load tests also showed the similar trends as recorded previously by Yu. These trends show an increasing pressure for a proportional increase in sinkage. The tests conducted by the author used circular pressure plates, while Yu utilized rectangular plates [30]. The difference of shape is not of concern, as the Bekker equations for sinkage (Equation 18), do not use an area, but the radius for a circular plate, and the smaller dimension of a rectangular plate. Figure 2.11 shows Yu's data, while Figure 2.12 shows data collected by the author.

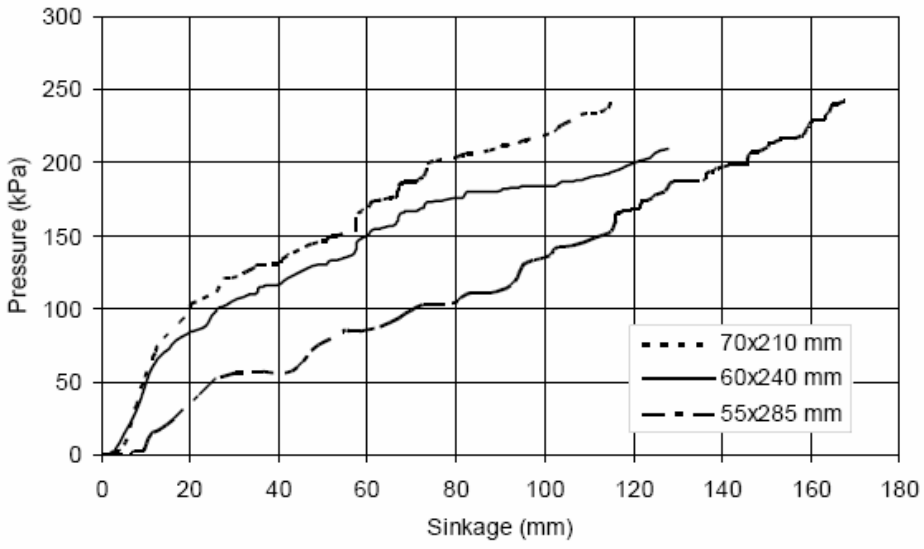

Figure 2.11 – Penetration test data from University of Pretoria [30]

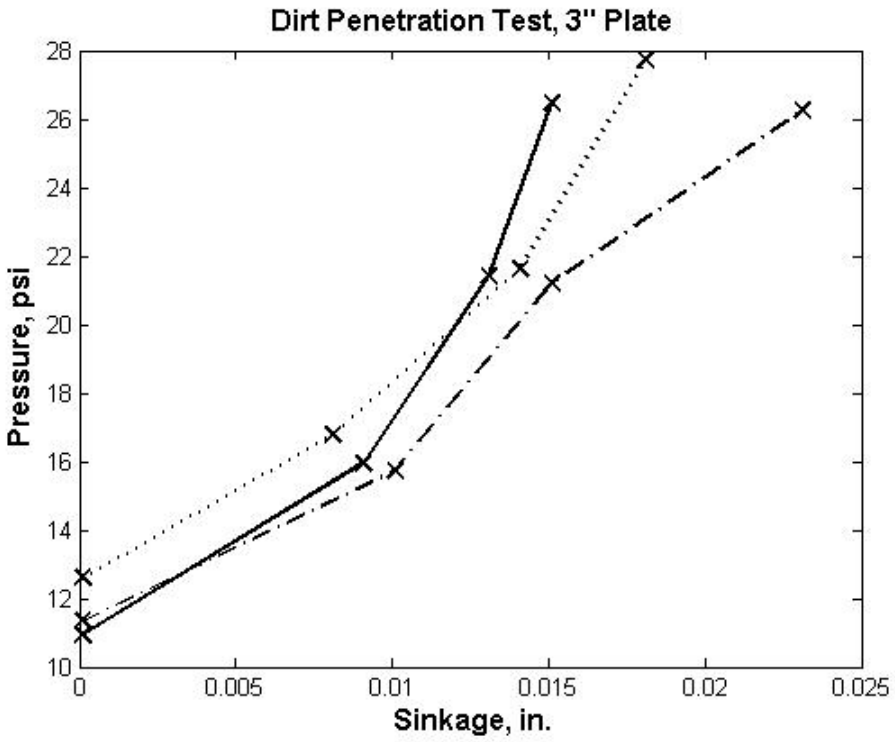

Figure 2.12 – Penetration test data collected by author

2.2 Tire Test Rig

2.2.1 Introduction

Just as important collecting soil data, is collecting tire data for the understanding of the tire-terrain interface. Several methods for testing tires are available, including rolling drum rigs, belted test rigs, and towed test rigs. Each has their own benefits, yet the towed test rig is the method of choice for this study for its simplicity, cost, mobility, and ability to collect field data.

2.2.2 Development

Upon studying the several methods for testing tires, three methods were considered. These methods included a rolling drum apparatus, an MTS Flat-Trac (rolling roadway) machine, and developing a towed test rig specifically for this study.

Rolling drum test rigs have an advantage of being less complicated than a Flat-Trac machine, however they are typically used only in longitudinal studies. A major disadvantage of the rolling drum test rigs is that soil cannot be directly tested. Drums are usually made of steel and are much more rigid than soil. While less costly and less complicated than an Flat-Trac, the rolling drum simply cannot deliver the required data.

Utilization of an MTS Flat-Trac test rig would generate significantly more useful results than the rolling drum tests, as the Flat-Trac is designed specifically to test tires in cornering performance and longitudinal performance. The machines themselves are of tremendous cost and require much care and maintenance. Furthermore, the rolling roadway utilized is not a soil. The roadway is a belt that is much like sand-paper that has a given friction coefficient. Vertical stiffness of the roadway can be simulated by

changing properties of the water bearing under the belt under the contact patch, and the tension in the belt, however this still does not mimic the actual conditions in the field.

The lack of being able to simulate field conditions in the laboratory forces the researcher to develop a test rig to be towed by either a trolley (in soil bins) or by a vehicle over terrain found in the field. As indicated before, there has been one previous study that has tested the lateral performance of ATV tires [25]. The researchers at the University of Maryland constructed an instrumented test rig, towed by a vehicle over various surfaces [25]. The test rig allowed steer angle, camber angle, and braking slip to be adjusted.

Furthermore the UMD rig had fabricated proving-ring load cells at the reaction points where the test rig attached to the tow vehicle [25]. These sensors fed into the data acquisition system where their output was recorded to strip charts. Vehicle speed was measured by an un-driven wheel, while actual wheel-speed of the test tire was recorded to gather slip values [25]. Again, this data was fed to the data acquisition system for recording on strip charts [25].

Normal load was applied through weights which were mounted at a point just ahead of the contact patch of the tire. Their reaction forces were measured from two load cells measuring in the vertical direction at the reaction points on the tow vehicle [25].

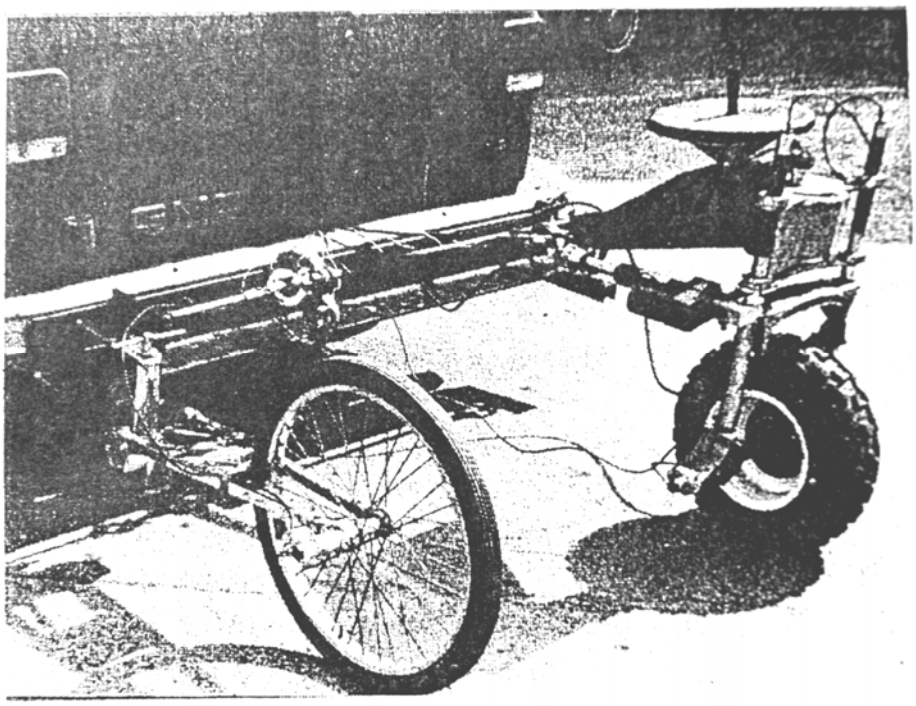

Figure 2.13 – Test rig designed by University of Maryland [25]

The core design in for the UMD test rig (Figure 2.13) was utilized by the author for this study. Several improvements were made such that more accurate and reliable data could be gathered. Improvements included the addition of a fully electronic data acquisition system, elimination of vertical load cells (and replacement with an accelerometer at the tire), and an inclinometer to observe true camber angle.

The data acquisition system is centered on a Dataq 710 8-channel data logger. Fed into the Dataq are lines from three load cells, two measuring longitudinal force, and one measuring lateral (See Figures 2.14 and 2.15). Also, an accelerometer is mounted under the weights which are situated directly above the contact patch of the tire.

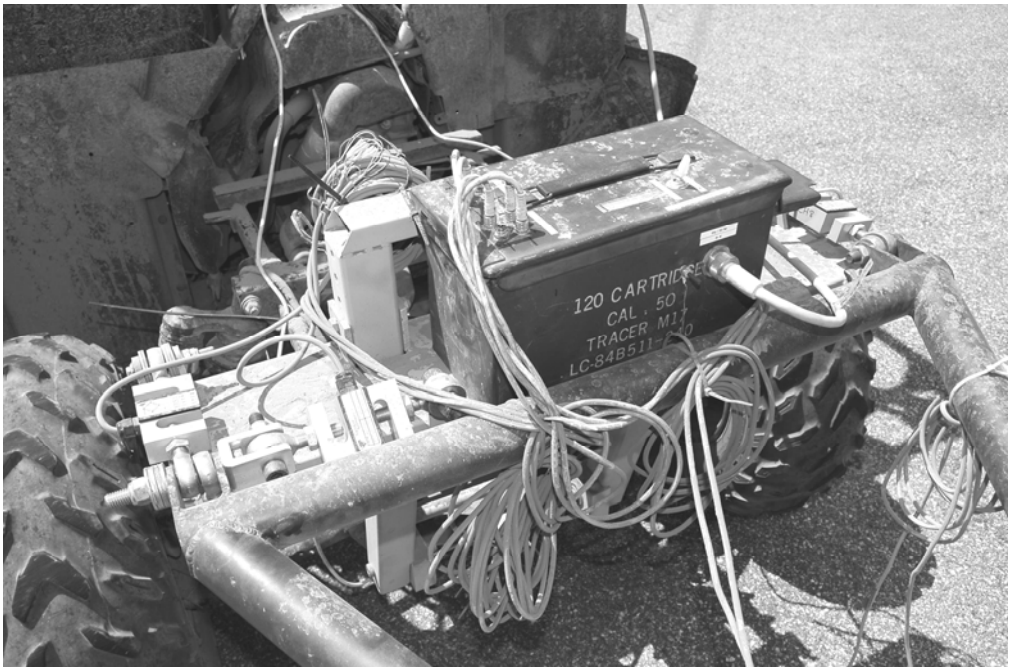

Figure 2.14 – Details of data acquisition box and load cells

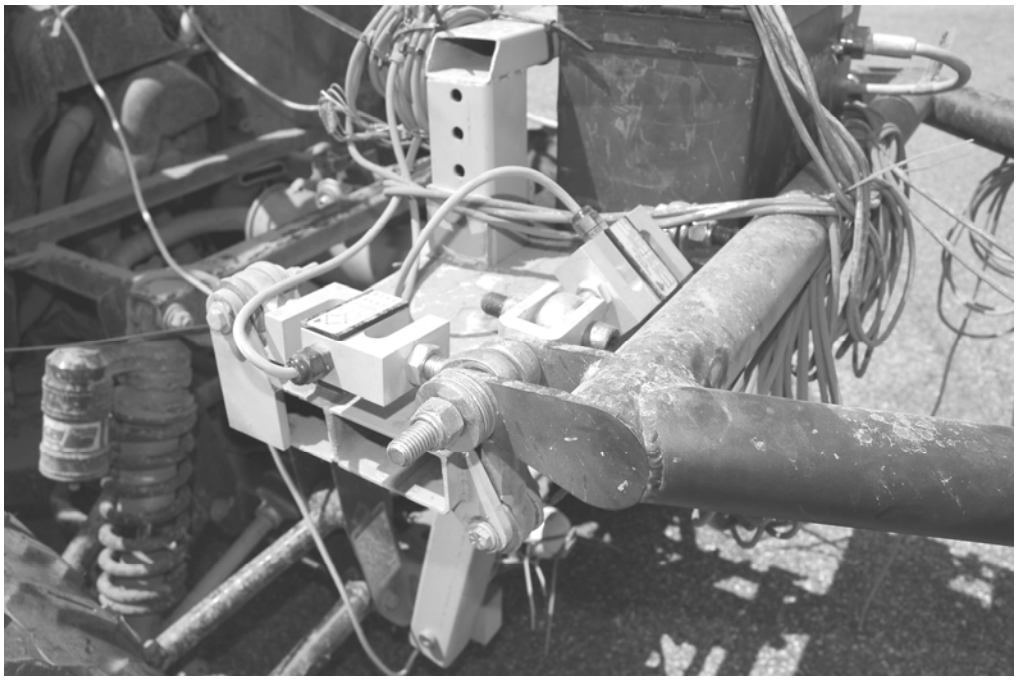

Figure 2.15 – Details of load cells

Mechanical and structural considerations for the test rig (Figure 2.16) were made such that sufficient camber and steer angle for various sized tires could be induced while attempting to minimize deflection. CAD software was utilized to design the layout of the test rig such that it could be affixed to the Yamaha Rhino tow vehicle, and allow 22 in. to 26 in. diameter tires. Limited FEA was conducted to ensure that no major deflections of the test rig would occur due to significant lateral and vertical loads.

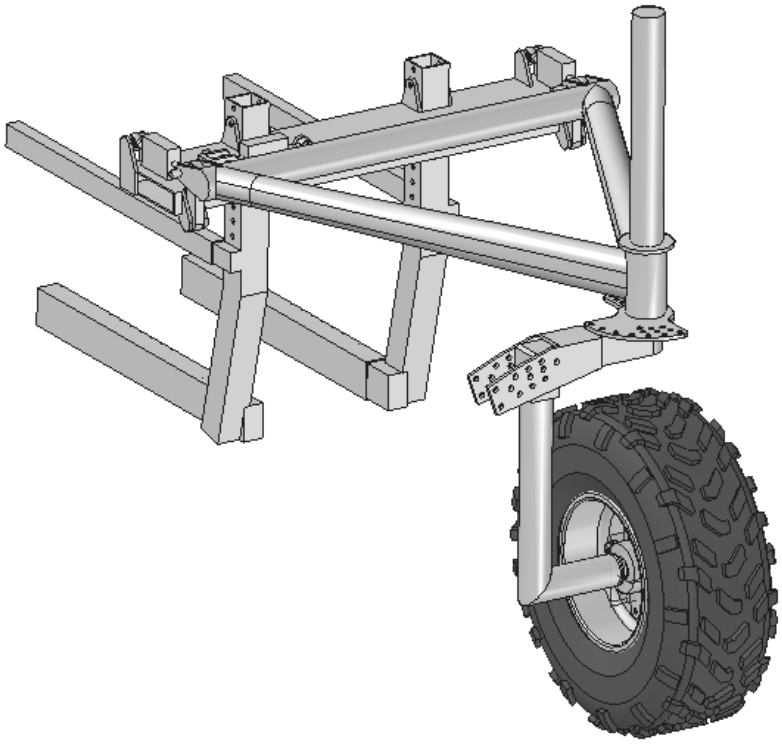

Figure 2.16 – 3D model of tire test rig in CAD

The towed test rig is designed in three parts: vehicle mount, triangle, and hook. The vehicle mount allows bolt-on capabilities to the Yamaha Rhino while allowing the vehicle to be returned to normal use when testing is complete. The mount (Figure 2.17) also has several settings such that tires of various diameters can be accommodated. The

triangle is the simplest part of the test rig, as it is a structural element, bridging the gap between the separately calibrated load cells and the hook. The triangle also includes the sector plate, where slip angle selections can be made. The final part of the test rig is the hook. While the triangle oriented parallel to the ground plane, the hook is in a vertical plane, which rotates about the z-axis through a bearing hole on the triangle. The hook also has a tab such that when the hook is rotated within the triangle, a stop-pin can be inserted when the desired slip angle has been set.

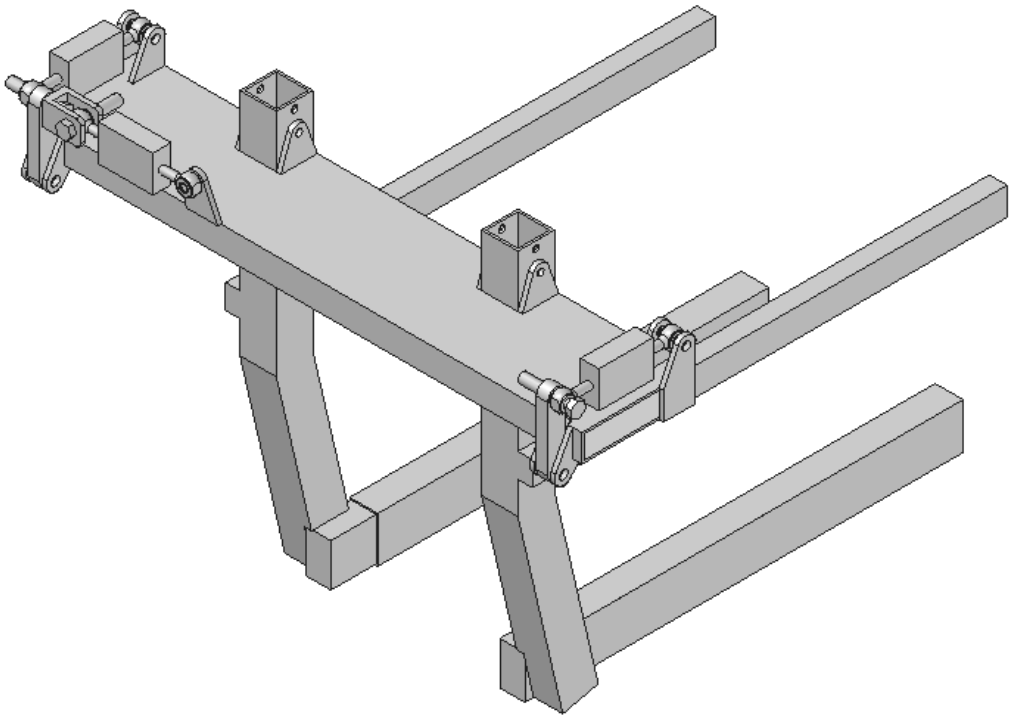

Figure 2.17 – 3D model of tire test rig mounting system

Camber adjustment is made on the hook, where camber angles from zero degrees to eight degrees are possible (Figure 2.18). The arc which the camber adjustment follows is centered about the contact patch of the tire, such that major displacements of the center

of vertical loading are avoided. Finally, the hook terminates at a spindle, where a hub and brake disc mount to the test rig. Since the hook only supports the tire from one side, changing tires is a short task. The one sided support does raise structural questions, however.

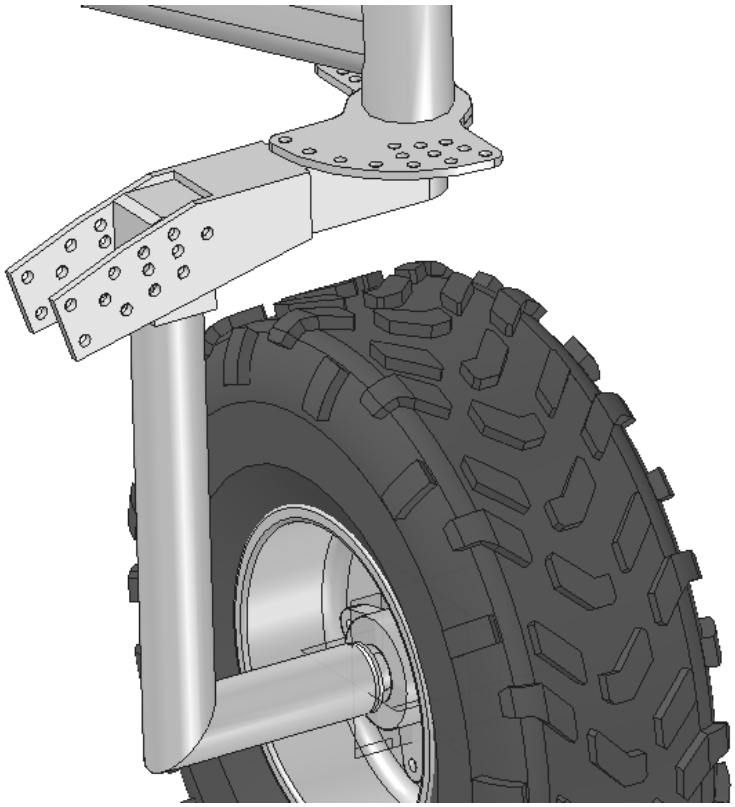

Figure 2.18 – Details of camber and slip angle adjustment

In order to allow tires of various diameters and widths, the hook must be of a certain geometry. Supporting the tire from only one side with this geometry and a maximum of 300 lbf of static load (and subsequently higher dynamic loads) requires that proper materials of proper dimensions be employed.

Two design goals were set to limit the flexure of the hook when loaded by forces seen at the spindle. First, the slip angle must not exceed half of a degree through flexure of the hook. Second, the camber angle must not exceed one degree through flexure of the

hook. With these goals in mind, FEA was applied in order to specify the proper diameter tubing to make up the hook.

A simple FEA was conducted in ALGOR with a basic beam-truss analysis. The hook was modeled by x, y, z coordinates, and various properties were changed to model commonly available tubing sizes. One-and-a-half inch tubing was determined to be structurally acceptable; however, a decision was made to use 2 in. diameter tubing with a 0.125 in. wall thickness. Two inch tubing of the mentioned wall thickness is a very commonly available arrangement, and for much less cost than the 1.5 in. diameter tubing. The use of the 2 in. tubing in the designed arrangement holds the camber angle to 0.5 deg. and the slip angle to 0.27 deg. The loaded condition is assumed to be a 600 lbf normal load, and a 300 lbf lateral load, which is a worst-case scenario.

Other sources of possible deflection include play at the load cell mounting points, frame-to-vehicle mounts, and play within the slip angle adjuster. These locations were checked for excessive movement, and since significant care was taken during construction, no play of any concern was recorded.

2.2.3 Operations

Like the bevameter, the tire test rig is capable of being run by only one operator. Operations for collecting data on a particular tire include involvement with the data acquisition system, mechanical settings on the test rig, and proper driving techniques with the tow vehicle. Careful observation of all three areas during a test ensure the generation of useful data.

A tire to be tested is affixed to the test rig and the desired camber set into the hook. The desired weights are then applied to the top of the hook. The operator then positions the tow vehicle such that a run of approximately 30 to 40 yards can be taken. Before proceeding, the operator then manually sets the steer angle between the triangle and the hook. A final check is made to ensure that fasteners are properly tightened and the proper settings are applied.

Once the settings have been confirmed, the operator accelerates the vehicle to the test speed, which is nominally 10 mph. Once a steady-state speed is reached, the operator starts logging data to the computer. Before the end of the run, and decelerating the tow vehicle, the operator stops data collection. A loop is then made back to the starting point where runs are repeated to generate enough data to create statistically significant results.

2.2.4 Assessment

Before the test data can be used, the data must be checked to see that acceptable results are being generated. Checking for acceptable results requires referencing the data generated by the previous ATV tire lateral force study conducted by the University of Maryland [25]. Lateral Force and longitudinal force curves are compared for shape and the magnitudes of forces are compared.

Expectant lateral force data takes on the form of what is presented in Figure 2.19.

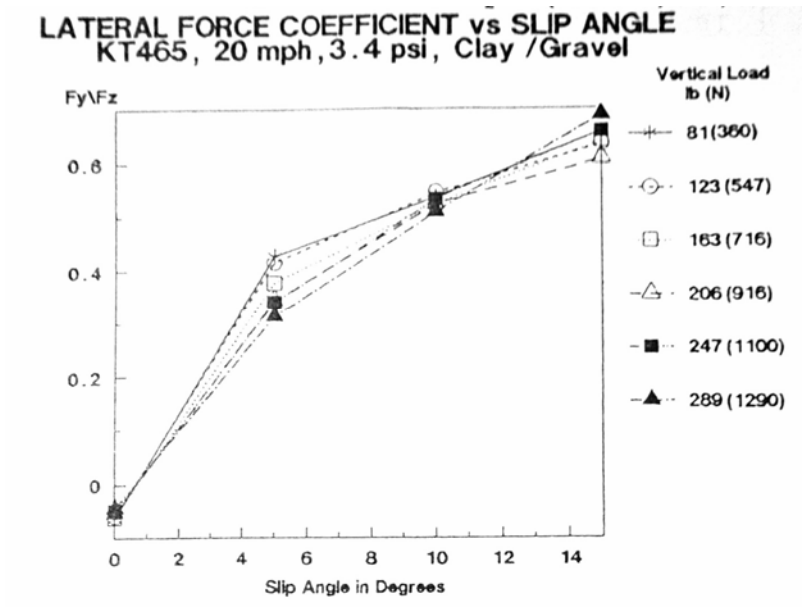

Figure 2.19 – Lateral force coefficient data from UMD study [25]

Observe no distinct peak to the data, and how it gradually approaches a constant value for large slip angles. Also note how slip angles to only 15 degrees were tested. Figure 2.20 shows longitudinal force data from the UMD study.

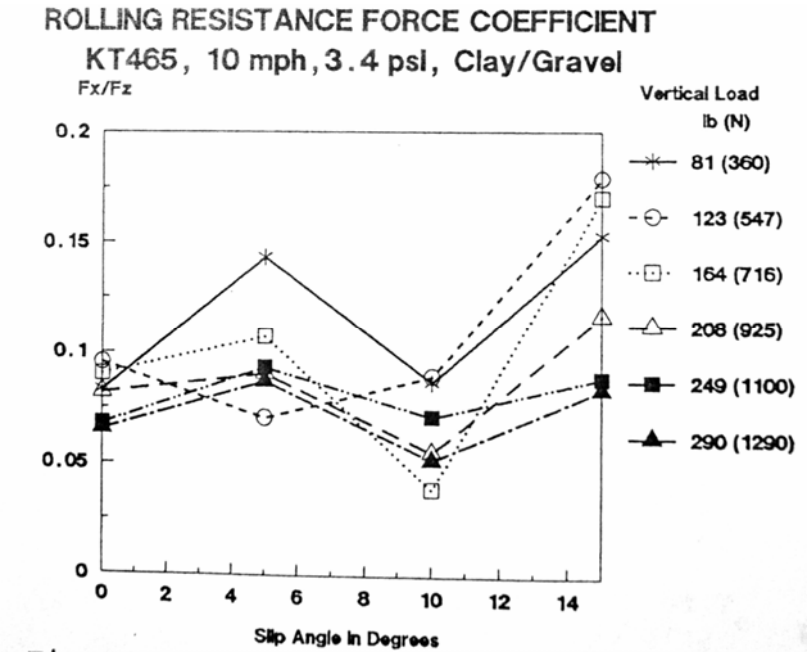

Figure 2.20 – Rolling resistance coefficient from UMD [25]

Note on the rolling resistance coefficient, it generally increases as slip angle increases. This is expected as the longitudinal component of the lateral force increases with increasing slip angle. Also note the rough grouping of data and how it seems to fluctuate between 0.05 and 0.15.

Lateral and longitudinal force data generated by the tire test rig can be seen in Figure 2.21. Normalized lateral force (also known as Lateral Force Coefficient, LFC) is shown on the y-axis. Like the data generated in [25], note the same trends are present, and the magnitudes of lateral and longitudinal force data are consistent.

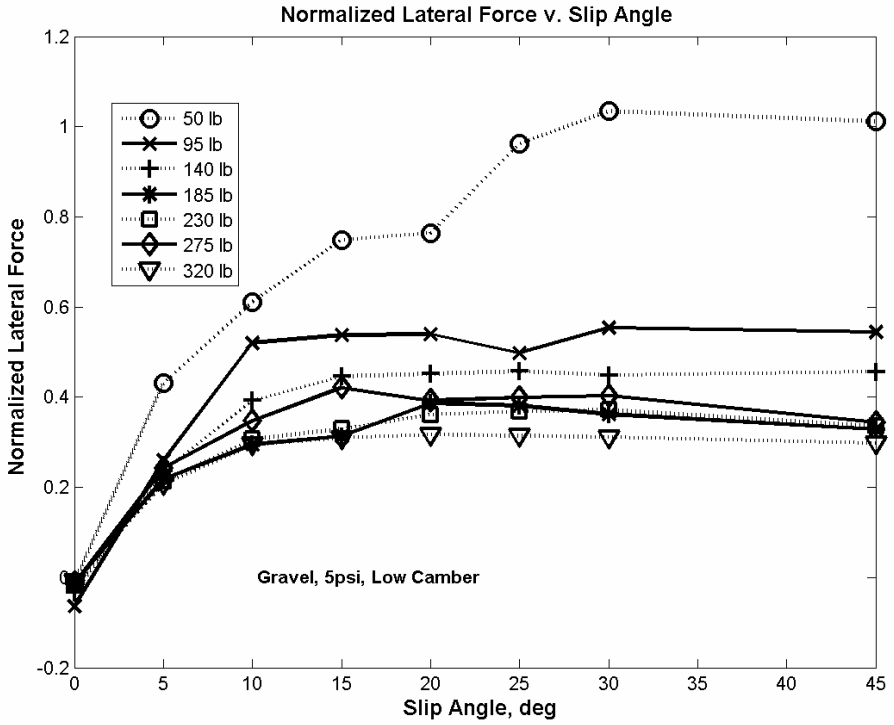

Figure 2.21 – Example lateral force data generated by the author

2.3 Tire Model

2.3.1 Introduction

In order to draw connections between the soil and tire performance, a tire model, a mathematical representation of tire performance, must be employed. Models have various coefficients which can be linked to variables like tire pressure, camber angle, and various properties of the operating surface. Several tire models have been developed over the last few decades, and some are more applicable than others.

According to Metz, there are five basic tire models: Linear, Bi-Linear, Exponential, Polynomial, and Modified Sinusoidal (Pacejka) [31]. Each model has their own marks of merit, and shortcomings. This study employs the use of the exponential tire model as it closely represents off road tire data as observed by Crolla, et. al. [15]

2.3.2 Tire Models

The linear tire model presented by Metz is a mathematically simple model relying only on cornering stiffness; $C\alpha$. Calculations are very easy for mathematics packages. This model is useful only in situations where small slip angles are encountered, and it is known that the tire is operating in the linear range (Equation 2.1) [31].

$$F_{Lateral} = C_{y\alpha}\alpha \tag{2.1}$$

A bi-linear model is an improvement upon the linear tire model. While retaining the linear portion, a limiting value is imposed on lateral force. The line of the limiting value has zero slope and presents a constant lateral force above a particular transition slip angle. This model can accurately model the linear portions of the tire for low slip angles, and the saturated region for high slip angles for some tires (Equation 2.2) [31]. The

transition region is poorly represented, and has a discontinuous slope, which can be numerically problematic for vehicle handling simulations.

$$\begin{aligned} F_{Lateral} &= C_{y\alpha}\alpha, F_{Lateral} < F_{Lateral,Max} \\ F_{Lateral} &= F_{Lateral,Max}, F \geq F_{Lateral,Max} \end{aligned} \tag{2.2}$$

The polynomial tire model (Equation 2.3) is an improvement in accuracy over the bi-linear and linear models. There are, however, some numerical instabilities and a lack of camber effect. The coefficients of the polynomial model also do not have any physical meaning [31].

$$\begin{aligned} F_Y &= b_0 + b_1\alpha + b_2\alpha^2 + b_3\alpha^3 \\ b_n &= c_0 + c_1F_z + c_2F_z^{\,2} \end{aligned} \tag{2.3}$$

The model with the most accurate fit is the Pacejka Modified Sinusoidal tire model. This model accepts vertical load effects and camber effects, combining them into a very smooth curve fit. Disadvantages include the fact that the model has six more equations to compute just to arrive at a lateral force, and the said equations require significant data for curve fitting [31]. The Pacejka Modified Sinusoidal tire model is as follows in Equation 2.4.

$$\begin{aligned} F_Y &= D\sin(1.3\arctan(B\phi)) + S_z' \\ \phi &= (1-E)(\alpha + S_x') + (E/B)\arctan(B(\alpha + S_x')) \\ D &= a_1F_y^2 + a_2F_y \\ E &= a_6F_z^2 + a_7F_z \\ S_x' &= a_9\Gamma \\ S_z' &= (a_{10}F_z^{\,2} + a_{11}F_z)\Gamma \\ B &= \frac{[a_3\sin(a_4\arctan(a_5F_z))]}{1.3D}(1 - a_{12}\Gamma) \end{aligned} \tag{2.4}$$

Lastly, the exponential model is presented in Equation 2.5. This is the model that will be utilized in the remainder of the study. The exponential tire model enjoys the benefits of having vertical load effect, having a continuous slope, and most importantly, the coefficients have physical meaning. Seeing that the soil shear stress–shear displacement relationship is of an exponential form, a tire's behavior on soil assuming an exponential form should not be surprising. The exponential tire presented by Crolla [15] and Metz [31] does not, however, include effects for camber. This does raise a question as to how the coefficients of the exponential model are affected by changes in camber.

$$F_y = F_z A(1 - \exp(-B\alpha)) \tag{2.5}$$

One may note the simplicity of the equation developed by Crolla [31]. This allows for hand calculations to be performed in the requirement of a quick answer. The simplicity also lends itself to shorter processor times when compared to the Pacejka model when utilized in vehicle dynamics calculations.

While Crolla presents the simple model in Equation 2.5, Metz offers a hypothesized improvement on modeling the effect of normal load variations in Equation 2.6 [31]. Metz shows how the "B" coefficient in the exponential tire model may be affected by normal loads [31].

$$B = (C / A)(F_{z,ref} / F_z)^m + D / A \tag{2.6}$$

There are several variable additions to the expanded exponential model. $F_{z,ref}$ is a reference vertical load, and the tire rated vertical load is suggested by Metz to serve as this value. *C, D*, and *m* are all empirical exponents from fit data. While the expanded exponential model seems to provide an added degree of accuracy, it is the goal of this study to obtain the basic relationships between soil properties, tire settings, and just the

basic *A* and *B* coefficients of the exponential tire model. Further analysis of Equation 2.6 may be conducted in subsequent studies.

2.3.3 Assessment

As the exponential tire model was selected for its similarity to soil-rubber shear characteristics, and ease of implementation in computer models, the true test of any model is how well it predicts a process or phenomenon. Since tire data collected from the towed rig was determined to be acceptable and on order with the previous ATV tire study [25], the data collected would be used to judge how well the exponential model would fit. Figure 2.22 depicts the application of the tire model on a clay surface. Then, Figure 2.23 shows comparison for a gravel surface. One will note R-squared values exceeding 0.80, indicating an acceptable fit.

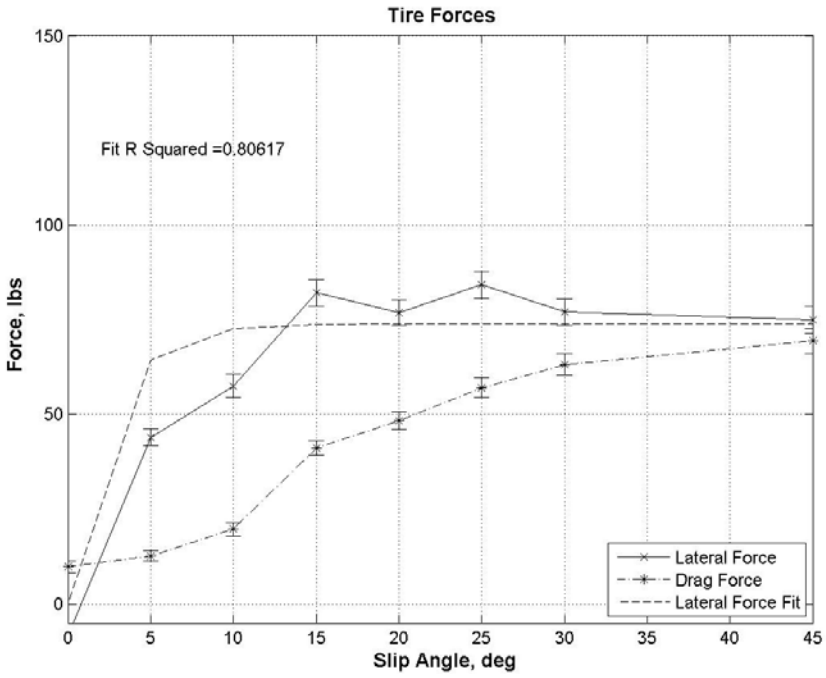

Figure 2.22 – Sample output data. Clay, 10 psi, low camber, 185 lb normal load

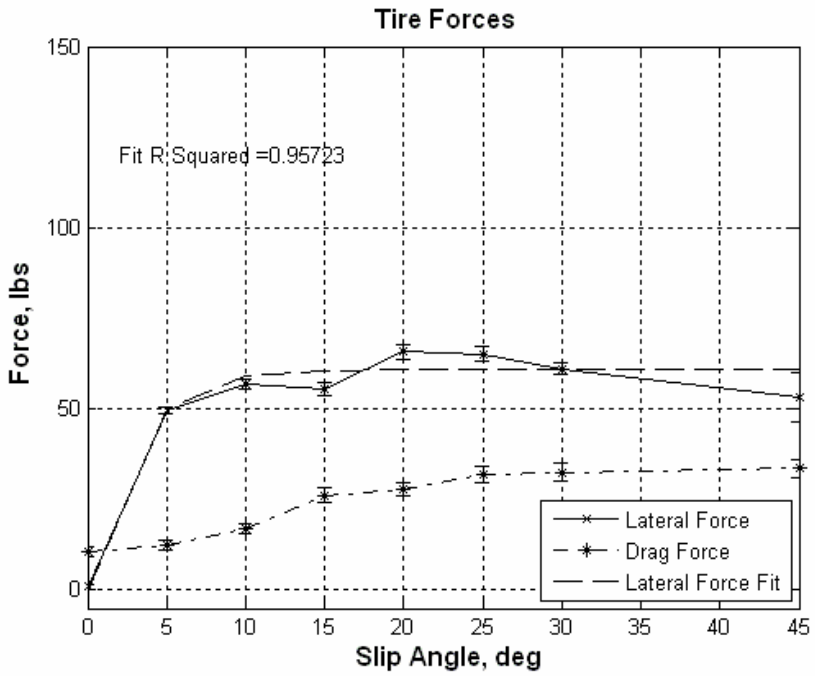

Figure 2.23 – Sample output data, Gravel, 10psi, low camber, 185 lb normal load

CHAPTER 3

RESULTS

3.1 Introduction

After satisfactory test equipment were constructed, electronics and data recording equipment debugged, and several trial runs completed, reliable and repeatable experiments could be conducted. Presented in the following section are the results from bevameter tests, empirical tire data, and the curve fits from exponential tire models. Also included are basic effects of bevameter parameters on key tire performance numbers.

3.1.1 Test Surfaces

Natural surfaces (snow, peat, or soil) can have their mechanical strength described by two parameters, cohesion and friction angle. Cohesive soils rely on intermolecular bonds between the particles of the soil. In layman's terms, it is a measure of the "stickiness" of the soil. Frictional soils do not have this bond, and their strength is a function of the confining stress and thus intergranular friction. A soil can be purely frictional, purely cohesive, or a combination of both. An example of a frictional soil would be dry sand, whereas a cohesive soil would be a type of clay. The test surfaces for experimentation were selected to be as close to a purely frictional and purely cohesive soil as possible. The surfaces have proved to meet requirements, and exhibit the behavior expected from a frictional and a cohesive soil.

Both test surfaces are located at the National Center for Asphalt Technology (NCAT) on land prepared for use by the 2006 Baja SAE competition hosted by Auburn University. The terrain is clear of trees, graded nearly level, and grass was planted on most of the area, while gravel was spread along the approach road and in front of storage buildings used by NCAT. Photographs of the test lanes can be found in the appendix. While the gravel, or frictional, surface needed little preparation, the cohesive surface was to be the clay under the grass. Numerous vehicle passes were made in the early summer by the test vehicle at various lateral offsets to clear a uniform lane through the grass and onto the clay surface below.

The frictional surface exists on a lane approximately twenty feet wide, and approximately thirty to forty yards in length. The loose gravel on top consisted of No. 2 limestone gravel. This upper layer of loose stone ranged in thickness between one and two inches. Finer particles, resembling the size of beach sand grains found their way to the bottom layer, which all sat on top of a very stiff layer of compacted fines from the stones abrading on each other, atop the clay subsoil.

The cohesive test surface shared the same length of thirty to forty yards as the frictional surface. The lane is approximately twelve to fifteen feet wide, and again, like the frictional surface was nearly level. During the summer months when testing occurred, the cohesive soil was hard, dry, and brittle. Care was taken to ensure that the soil was sun dried for at least three days after a rain so that moisture content would not be a factor in keeping the soil as uniform between runs as possible. The hard clay surface was also selected such that it did not allow the tire lugs to penetrate the surface such that bulldozing forces created by lug interlocking would not affect test data. Allowing the lugs

to penetrate the surface would turn the soil much like a disk harrow and alter the soil strength after each run. This situation would cause the strength to be variable between runs and would thus negatively affect the experiments certainty. It must also be noted that a very fine clay dust would continually coat the upper surface of the clay which would be created by the abrasive action of the tire on the hard, brittle clay soil.

3.1.2 Test Tire

Upon completion of construction of the test rig and soil testing apparatus, it became clear that hundreds of extensive experiments would necessary on each tire to gather the data necessary. As this study seeks to gain a general understanding of how bevameter values affect the lateral performance of small (22" to 26"), off-road tires, and not tire tread effects, it was decided that one front, steered tire be tested for the sake of time and uniformity.

The test matrix includes making three runs at each specified normal load and slip angle combination. The test matrix is seen in Table 3.1.

	0°	5°	10°	15°	20°	25°	30°	45°
50 lbf	3	3	3	3	3	3	3	3
95 lbf	3	3	3	3	3	3	3	3
140 lbf	3	3	3	3	3	3	3	3
185 lbf	3	3	3	3	3	3	3	3
230 lbf	3	3	3	3	3	3	3	3
275 lbf	3	3	3	3	3	3	3	3
320 lbf	3	3	3	3	3	3	3	3

Table 3.1 – Tire rig test matrix indicating three runs per setting

Table 3.1 shows three runs for a 7x8 matrix. This yields 168 runs per unique tire setup. These 168 tests are repeated for two camber settings, two inflation pressures, and two surfaces. In order to reduce some of the number of runs, camber and inflation pressure were tested on the gravel surface only. This results in 840 individual passes down a test surface.

The tire selected for use is the Dunlop KT 821. The KT 821 is a 22 inch diameter by 8 inch wide front tire designed for use on sport ATV's. The KT 821 shown in Figure 3.1 accepts 10 inch diameter wheels.

Figure 3.1 – Dunlop KT 821 ATV tire

Other tires were considered for use in this study; however the KT821 was ultimately selected as the best solution. The author has over five years experience with the KT 821 as used on several Baja SAE racing vehicles designed and created by Auburn University. Numerous test sessions altering camber, inflation pressure, and toe-out angle

were conducted over the years, and thus the qualitative performance changes are well understood. In addition, the 821 is a relatively inexpensive and lightweight tire, fitting well into the research budget.

Finally, there are several tires of varying states of wear available to observe what to expect even before any of the tests commenced. The wear of the tire is significant in initial stages, but settles to a consistent lug shape quickly. The KT 821's lugs have sharp, squared edges which deteriorate quickly to a radiused edge of approximately $1/8^{th}$ of an inch. This radius is maintained through the majority of the life of the tire, whereas the wear is seen on the tops of the lugs rather than on the edges as seen in the beginning stages. This consistent wear pattern allowed for the same tire to be used in all tests. No "chunking" of the lugs occurred, and the tire maintained its integrity throughout the tests. Seeing as sinkage is insignificant due to the stiff terrains, lug interlocking is also not a factor in the certainty of lateral force results.

3.2 Bevameter

With the substantial amount of information available regarding bevameter operations, few issues arose with testing the soil. The vehicle-mounted bevameter proved to be effective in producing useful data that can be applied to the study at hand. The most difficult issue to overcome was the wear and structural integrity of the rubber coating on the shear head. This limited amount of surface testing due to structural concerns of the shear head do not have negative effects on the data, as it shares the same trends as found in [3] and [30] Also, the shear rate was on the low end of the range presented by Shoop that which is acceptable for vehicular studies [10]. Faster shear rates are attainable with a

human operator, but the consistency decreases, and risk of tearing the rubber from the shear head increases. Furthermore, the cost of adapting a motor drive to provide an appropriate shear rate would be out of range for the budget on this project. Nevertheless, the bevameter designed for this project has put forth acceptable data to help unlock knowledge about soil-vehicle interaction.

3.2.1 Shear Response

The shear response of the test surfaces were tested at various points along the lanes in order to provide overall response characteristics and not soil-rubber properties in localized spots. Data collected resembles that of other data collected in previous terramechanics studies. Key values collected from the shear data include shear deformation modulus, residual shear stress, normal stress, and thusly cohesion and rubber-soil friction angle.

Frictional Terrain

The frictional terrain proved to be the surface with the most variation in shear stress. In addition the rocks which made up the soil were sharp and easily gouged and/or scored the rubber on the shear head. This damage allowed only two test sites on the gravel surface, however the results were very similar and it was determined that further tests on gravel not be made as to allow for potentially more testing on the cohesive (clay) surface.

Unfiltered shear stress versus shear displacement is presented in Figure 3.2. Note the nearly vertical initial slope, indicating a very stiff terrain. After the initial slope and throughout the displacement of the shear head, the shear stress changes dramatically. This

can be attributed to the sharp rocks interlocking, digging into the substrate and the soft shear head, failing (releasing), then building up again. The test data does however match the general trends found by Shoop [10] and Wong [3].

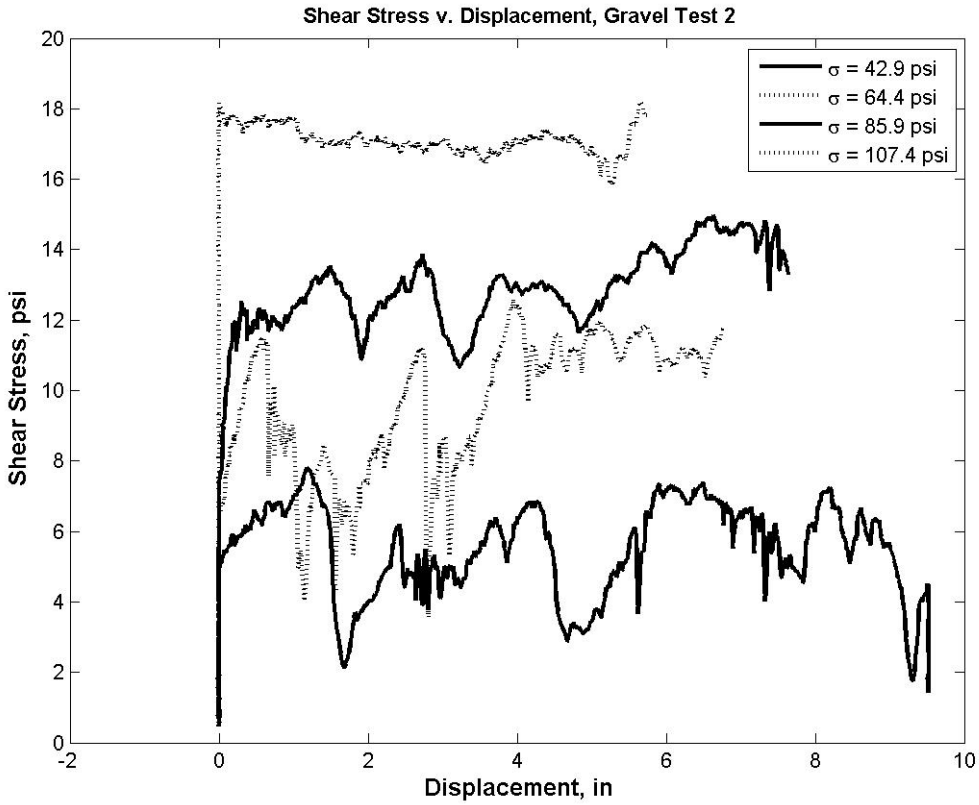

Figure 3.2 – Shear stress v. linear displacement on frictional soil

Residual shear stresses were determined to be the average of the last 1300 data points. For comparison, 1800 data points make up each data set, and the time step is 0.002084 s, making for tests around three to four seconds in length. The residual stresses are collected and stored for use in creating the Mohr-Coulomb failure envelope. The residual stresses are plotted against their associated normal stresses found under the shear head. From the Mohr-Coulomb failure envelope, one can determine friction angle, and

cohesion (which one would expect to be zero). Figure 3.3 shows the Mohr-Coulomb envelope associated with Gravel test number two.

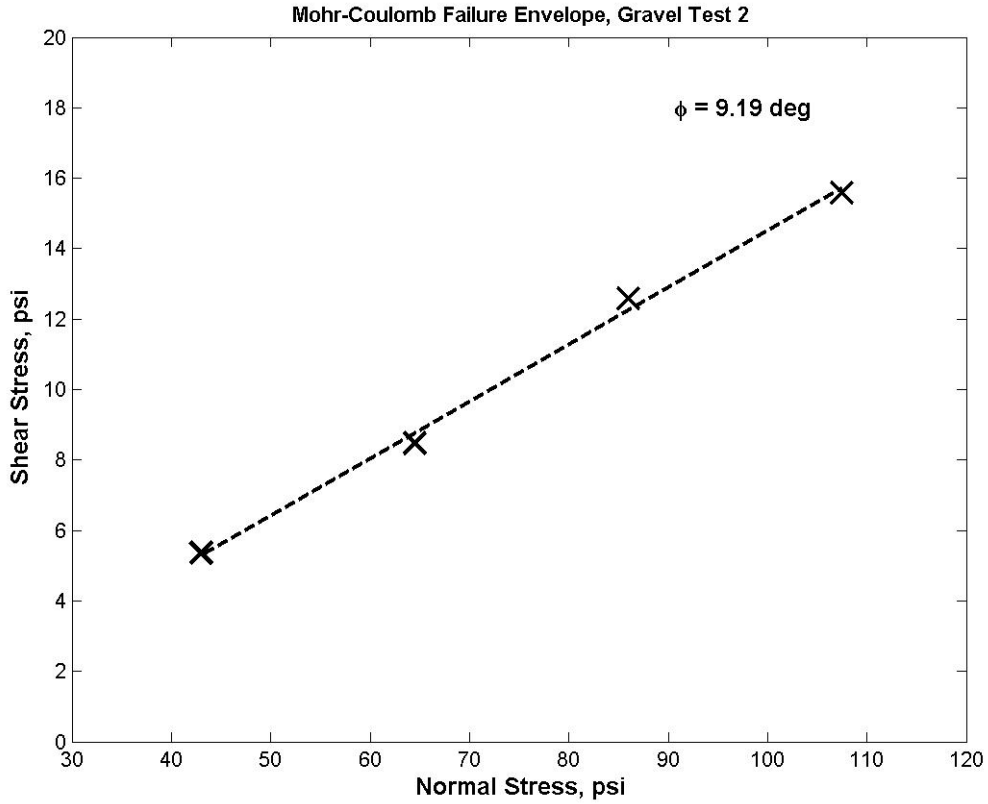

Figure 3.3 – Mohr-Coulomb failure envelope for frictional soil

Data points for the Mohr-Coulomb failure envelope were plotted in MATLAB and then the *polyfit* and *polyval* functions were used to obtain a linear curve fit. As one can see the fit matches the data quite well. Upon measurement from the slope, a soil-rubber friction angle of 9.19 degrees is measured. Gravel Test 1 provided a slightly larger friction angle of 12.16 degrees. This difference could be attributed to the highly irregular nature of the gravel surface as evidenced in Figure 3.2.

Cohesion in the Mohr-Coulomb plots for both Gravel tests as calculated from the failure envelope are indicated to be -4.57 psi for Gravel Test 1 and -1.66 psi for Gravel

Test 2. While not exactly zero cohesion as one would expect from non-bonded stones, the apparent negative cohesion is desired more than seeing a positive cohesion for this situation. Had a positive cohesion been present on a dry, frictional soil, that condition would cause concern as to the quality of the test being conducted, as there is no physical bond between particles, as described in [13]. Simply, the gravel tests have proven to be in-line with expected cohesion values.

As the bevameter designed for this project is human powered, questions of shear-rate repeatability arise. The human powered shear test has the operator manually apply a moment to the shear head through a moment arm (i.e. Craftsman cheater bar). Shown in Figure 3.4 are shear-rate data taken from the Gravel Tests.

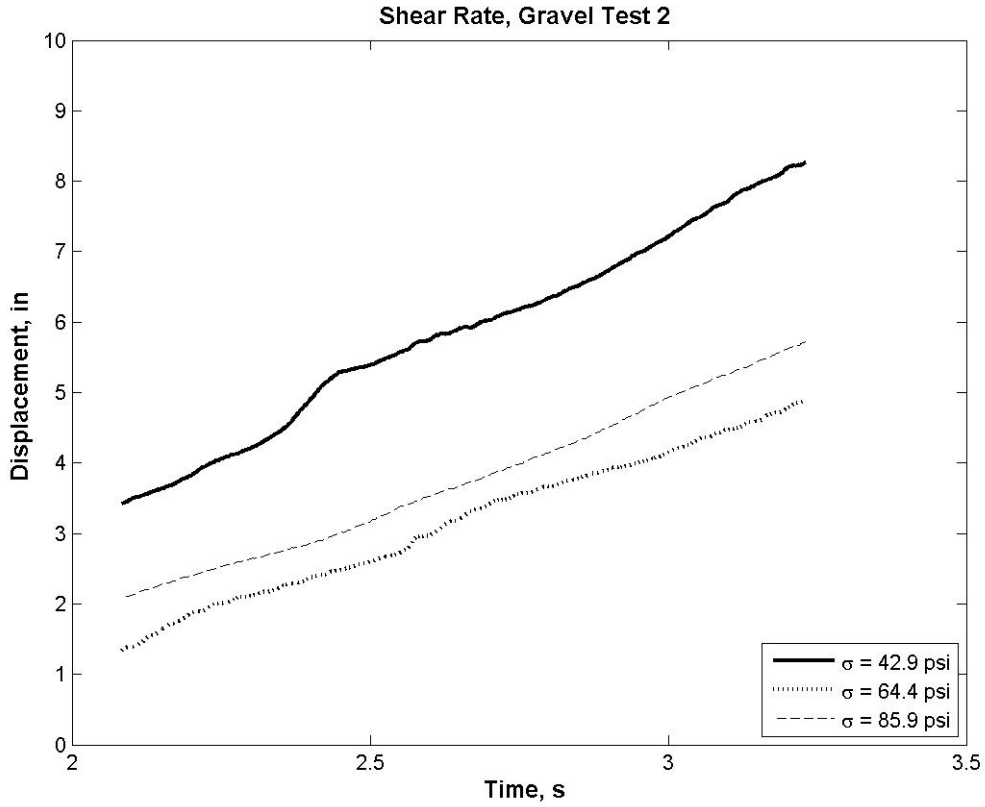

Figure 3.4 – Shear rate for Gravel Test 2

Upon first glance, one notices that the data is linear, and of a similar slope between the three different tests presented. The lines do not overlap due to the difference in actual start times of rotation versus start times of data recording. The slope of the lines is the important parameter in Figure 3.4. The author notes that he was the only one that conducted the shear response tests; therefore variance due to different operators is not a factor. Shear rates from Gravel Test 2 can be seen in Table 3.1.

Normal Stress, psi	Shear Rate, Test 1	Shear Rate, Test 2
42.9 psi	3.367 in/s	4.181 in/s
64.4 psi	2.976 in/s	3.000 in/s
86.9 psi	3.322 in/s	3.217 in/s

Table 3.2 – Gravel surface shear rates

As one can see, the shear rates average 3.34±0.179 in/s, indicating a very consistent shear rate conditions for the shear response experiments on the frictional surface. The shear rate of approximately 3.34 in/s is close to double the shear rate of the CRREL bevameter; however it is on the bottom end of the range of the rate produced by the CRREL Instrumented Vehicle [10]. The shear rate of the human-actuated bevameter could be increased; however repeatability and consistency significantly decrease.

Finally, as friction angle, cohesion, and residual shear stresses are determined, the final task is to find the shear deformation modulus, which will be represented by K. One may note that the raw data from the shear stress versus shear displacement graph in

Figure 3.2 all shared a very similar initial slope. In Figure 3.5, one may see Equation 1.22 as presented by Wong [3] being fit to shear stress-shear displacement data.

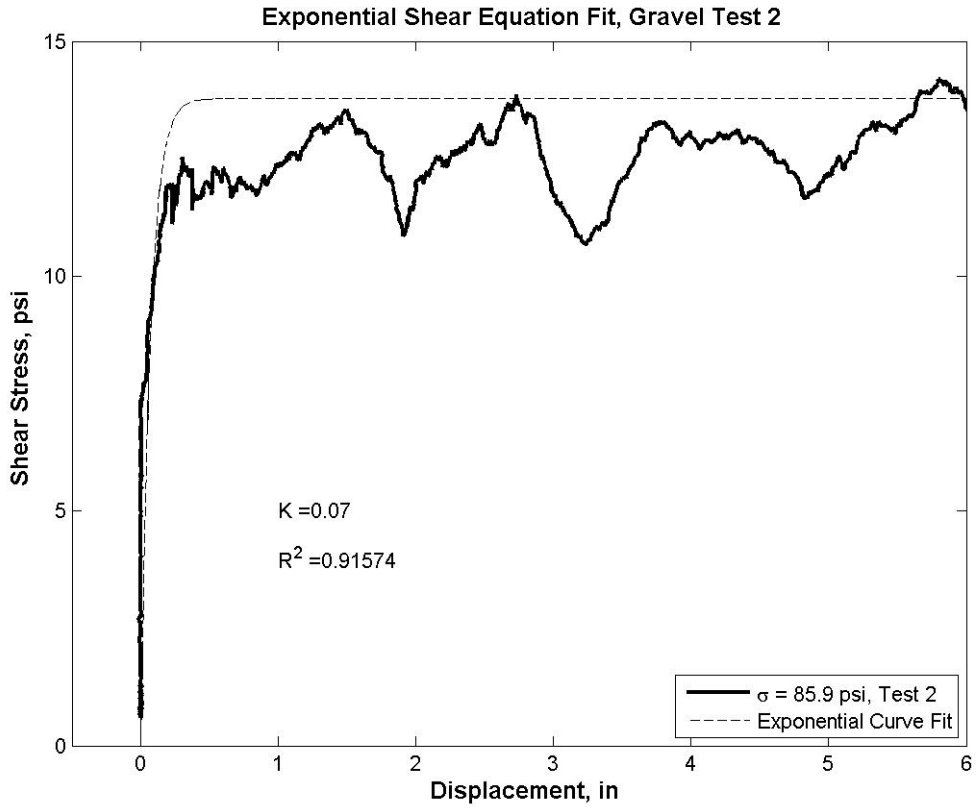

Figure 3.5 – Exponential shear stress equation fit to shear data

The fit to the shear stress data was generated by creating an array of possible *K* values between 0.01 and 0.99. Each value was plugged into a fit equation, and an R-squared value was calculated. For the largest R-squared value, the index of the *K* value was noted, and referenced at the end of the code to display the *K* value for the best fit. Note that the residual force in the curve fit is the midpoint between the average true residual stress and the maximum value of shear stress. This was applied to every fit in this study. In Figure 3.6, one may see what "messier" data looks like with this curve fit.

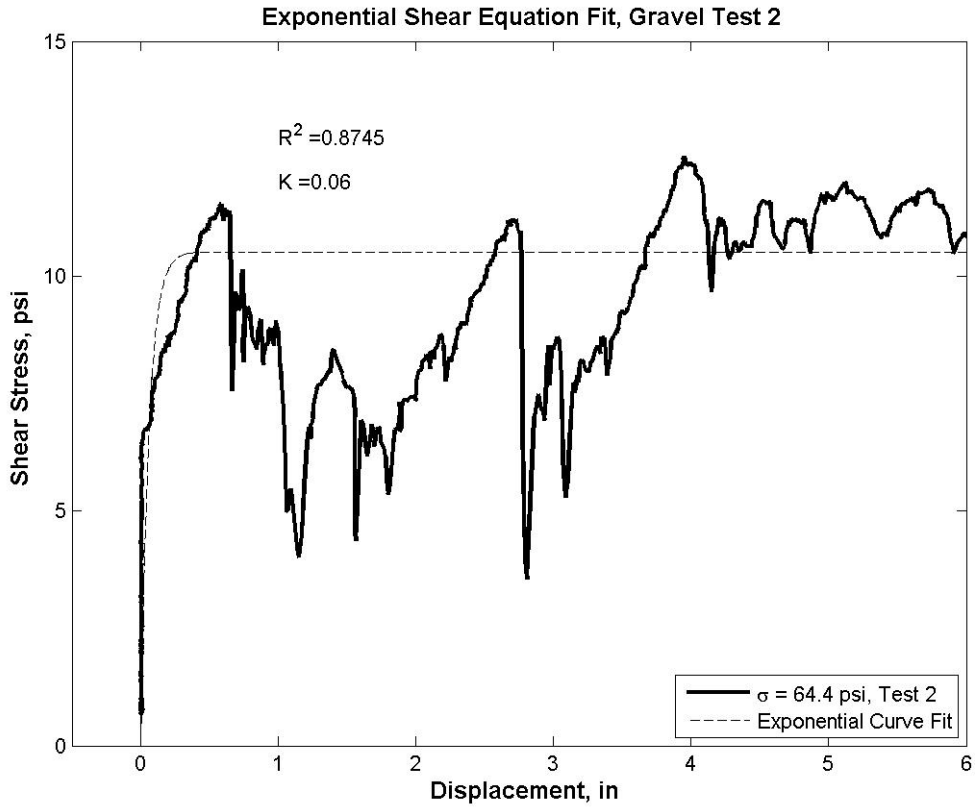

Figure 3.6 – Exponential shear stress equation fit to shear data

As one can see, there is considerable variation in the shear stress, as noted before, due to the climbing and falling of the stones in the gravel test surface upon each other. Recall from Equation 1.22 that was used to fit these equations that there is the shear modulus parameter. As noted before, all tests were fit with the method of checking all possible *K* values for the greatest R-squared value, and the shear modulus values were recorded and plotted against normal stress, as seen in Figure 3.7, and another test in Figure 3.8.

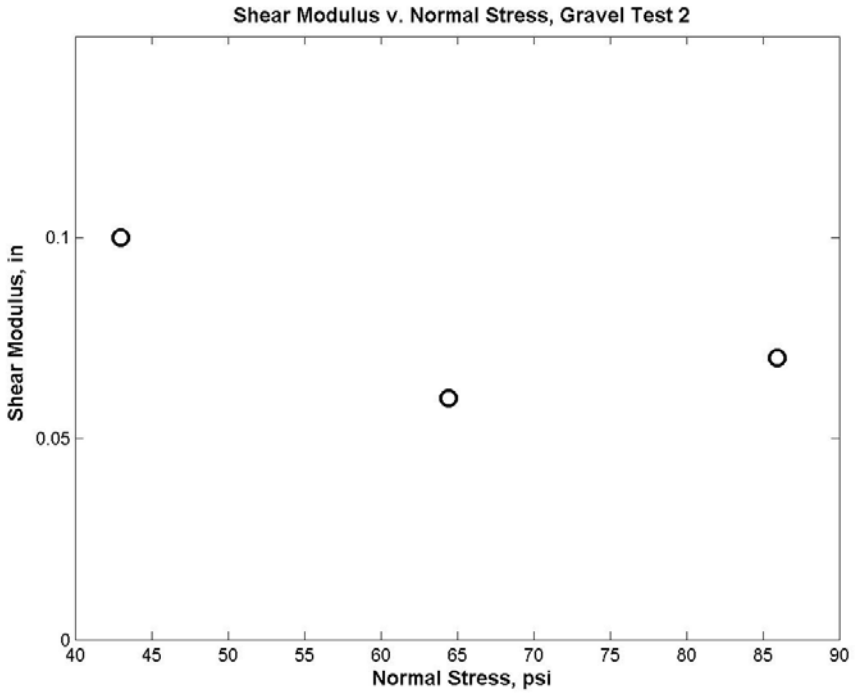

Figure 3.7 – Shear modulus v. normal stress, Gravel test 2

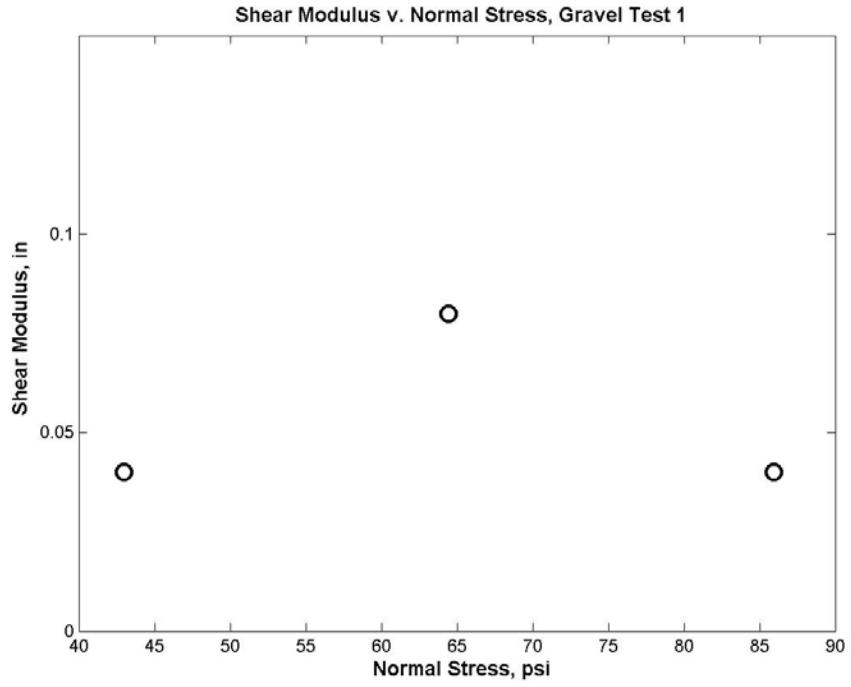

Figure 3.8 – Shear modulus v. normal stress, Gravel Test 1

Upon further inspection, one can see that the values tend to group about a *K*-value of 0.05 in. This indicates that the frictional soil is very stiff and begins to support substantial shear force with rubber after approximately 0.05 in of displacement.

Despite the significant of fluctuation of shear stress due to stones sliding up and over each other, consistent shear rates and closely grouped values for shear deformation modulus were obtained. Values of soil-rubber friction angle ranged between 9 and 12 degrees, yet the cohesion was listed as negative. It is highly improbable for a dry, frictional soil to have a negative cohesion, especially with no physical bond between particles. It could be arranged to add an extra data point at the origin for inclusion in the curve fitting, however the friction angle itself is much more important than cohesion for this frictional soil, and as long as the cohesion is near zero stress (as has been found) it is not of concern. Complete results for the frictional terrain may be found in the Appendix.

Cohesive Terrain

As the frictional terrain generated acceptable data, the cohesive data has proven to be much smoother and easier to fit curves to. The data is not as "choppy" as the frictional terrain data as the particles in the cohesive terrain are orders of magnitude smaller and have a more fluid motion as they slide across each other. The presence of these small particles also resulted in no damage to the rubber surface on the shear head. Figure 3.9 shows some of the raw data from tests on the cohesive soil.

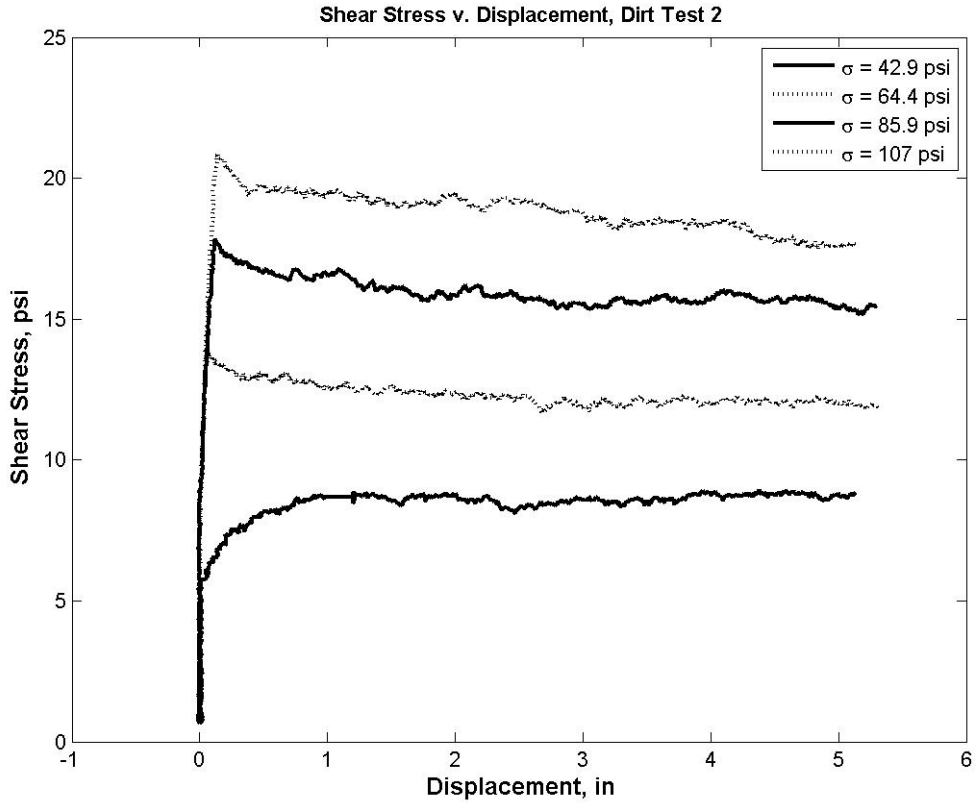

Figure 3.9 – Shear stress v. shear displacement, Clay soil test 2

After a first glance, notice how tightly grouped the data is in comparison to the highly variable shear stress values from the rocky frictional terrain. This indicates the smooth movement of the shear head across the terrain, as the particle size is smaller, so are the jumps in the graph. Also like the frictional terrain, the cohesive terrain fits the exponential response described by Wong [3] more closely.

$$s = s_{\max}(1 - e^{-j/k}) \tag{3.1}$$

In the same fashion that the frictional terrain was analyzed, the last 1300 points of the 1800 point data set were averaged and saved as the residual stress. This residual stress was then used in the construction of the Mohr-Coulomb failure envelope. These residual stresses are plotted against their associated normal stresses, and line is fit to the data. For

Figure 3.10, the soil-rubber friction angle was calculated to be 7.9 degrees, and cohesion of 0.95 psi. Both values are expected, as a cohesive soil will have a larger cohesion and a smaller friction angle than a frictional terrain.

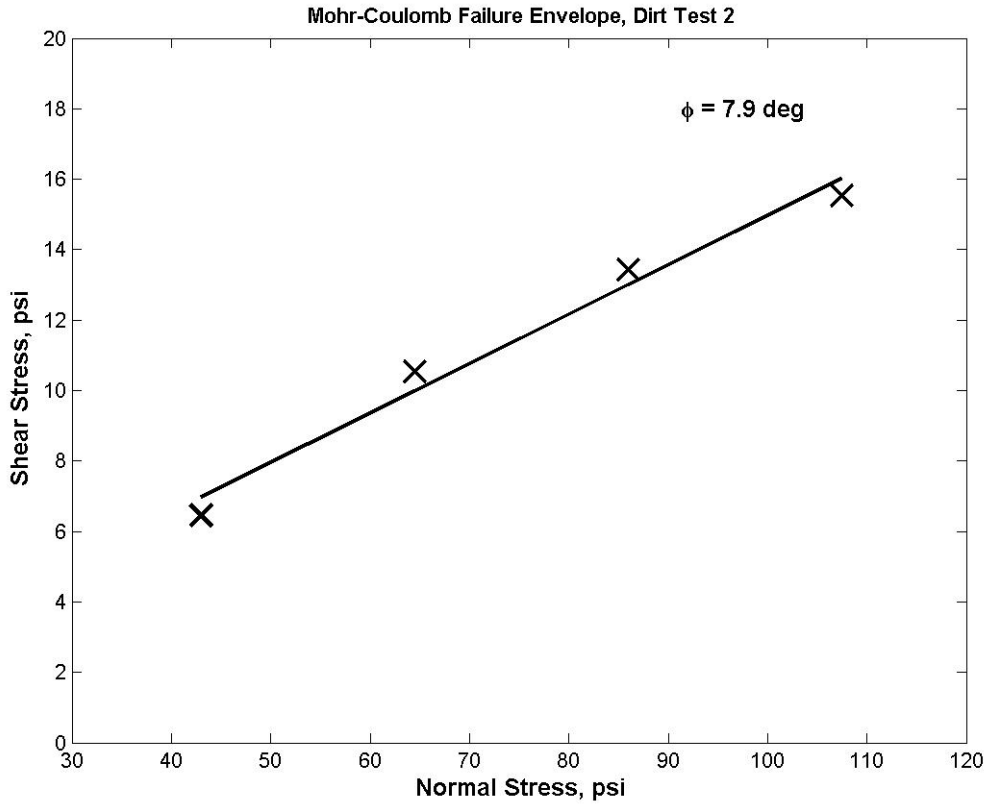

Figure 3.10 – Mohr-Coulomb failure envelope

The other tests made on the cohesive terrain yielded 6.2 degrees and 3.77 psi of cohesion for the second test, while the third test provided values of 4.30 degrees friction angle and 5.91 psi of cohesion.

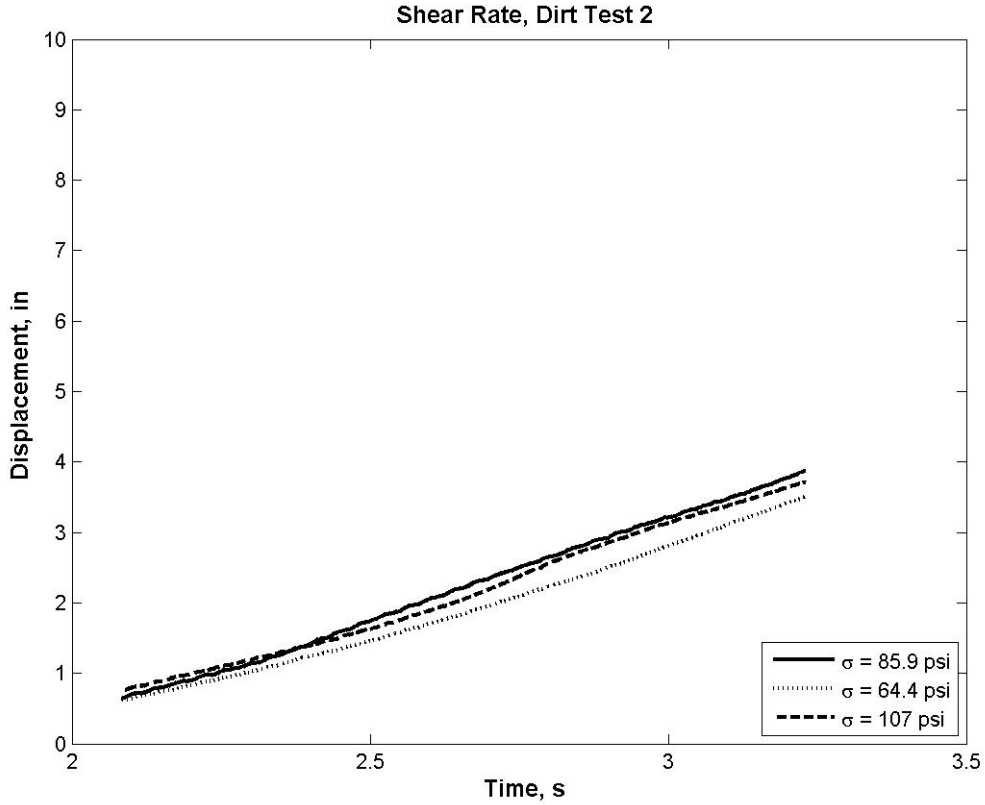

Figure – 3.11 Shear Rate, Clay soil test 2

Following in the path of the frictional terrain tests, the cohesive terrain allowed for very consistent shear rates. Table 3.1 shows data (from Figure 3.11) from the second shear test on the cohesive terrain.

Normal Stress, psi	Shear Rate, in/s
64.4 psi	2.540 in/s
85.9 psi	2.885 in/s
107 psi	2.704 in/s

Table 3.3 – Shear rates, Clay soil

These shear rates, averaging 2.70±0.09 in/s, are consistent with those of the other tests showing that they are very close to those seen during the frictional terrain shear

testing, and still above the speed that the CRREL bevameter provided, yet on the low end of shear rates seen by the CRREL Instrumented Vehicle, which were around 3.8 cm/s [10].

Furthermore, as other parameters are identified, the shear deformation modulus (K) is determined by a calculating fits for a table of K values, then calculating R-squared values, the maximum R-squared value is chosen along with the associated K value. These curves maximum value are set directly between the maximum shear stress value seen, and the residual stress recorded for use in the Mohr-Coulomb failure envelope. Figure 3.12 depicts a typical fit seen for the cohesive surface.

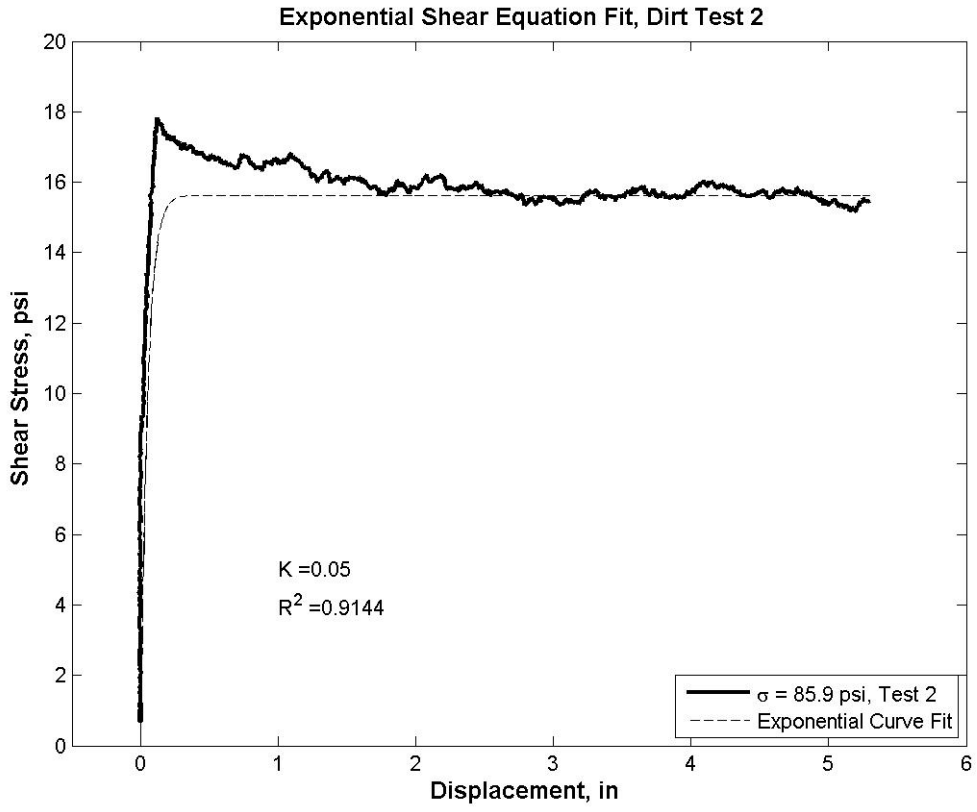

Figure 3.12 Exponential shear stress equation fit to shear data, Clay test 2

For the three tests conducted on the cohesive surface, the shear modulus values were found from running curve fits with *K* values between 0.01 and 0.99, recording the R-squared value, then based on the maximum R-squared value, the corresponding *K* value was selected. Figure 3.13 shows these *K* values.

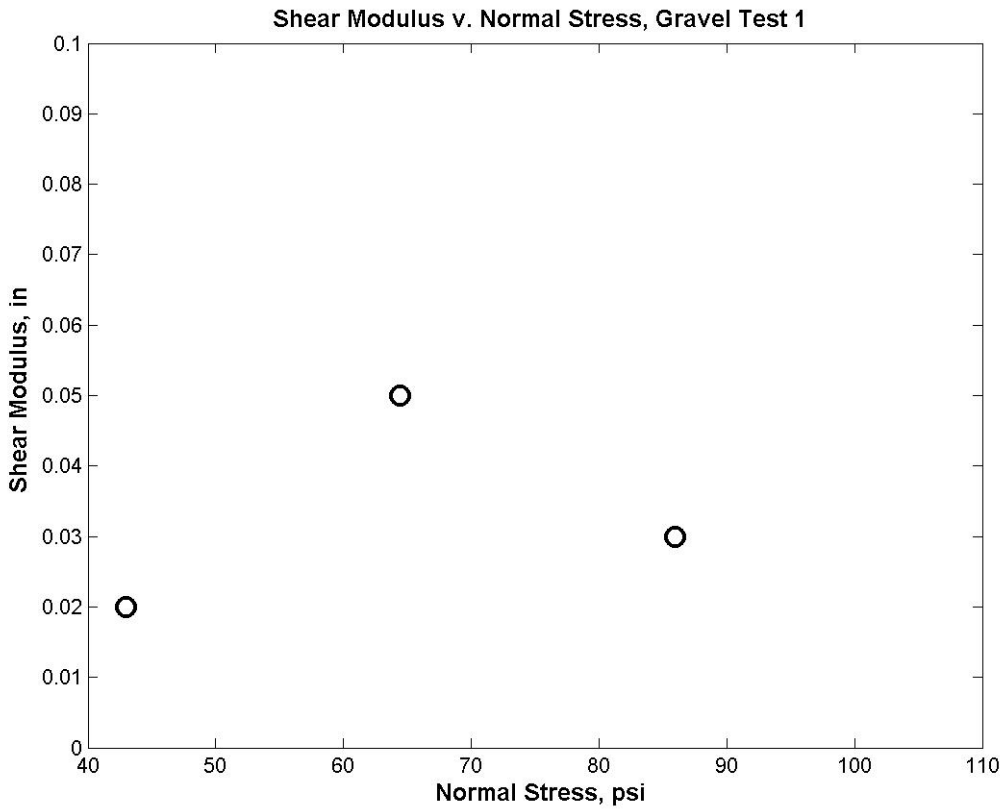

Figure 3.13 – Shear modulus v. normal stress, Gravel test 1

From this plot, one can see that the *K*-value seems to hover about 0.03 in. Recall that the frictional terrain supported significant shear stresses in approximately twice the cohesive surface's *K*-value. This can be attributed to the larger cohesion values seen in the cohesive terrain, ultimately do to the strong bonds between each soil particle.

One final point must be noted regarding shear stress – shear displacement data. When the shear stress is normalized with the associated normal stress, it can be seen in

Figure 3.14 that the plots collapse upon each other. In the data shown for Dirt Test 2, the coefficient of normalized shear stress averages 0.185, when using the second half of the data.

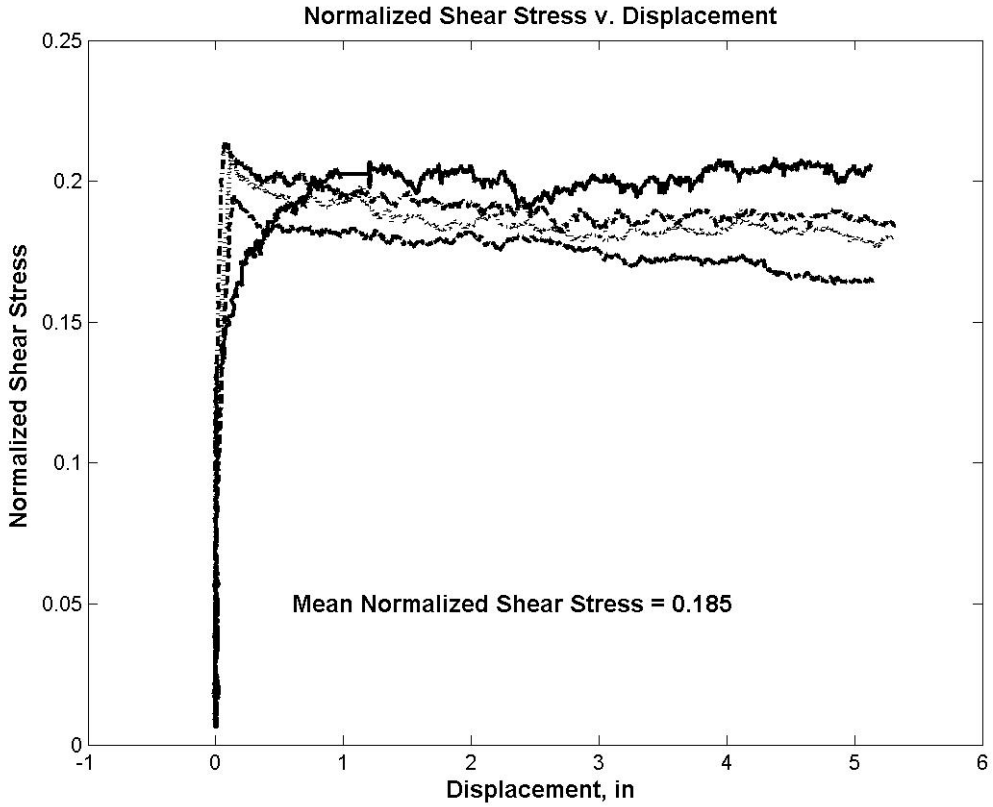

Figure 3.14 – Normalized shear stress v. displacement

The cohesive terrain has proven to provide much cleaner data than the rough, rocky, frictional surface shown earlier. Cohesion and friction angle values fit what is to be expected of a cohesive surface compared to a frictional surface, higher cohesion values for the cohesive soil and thus lower friction angles on the cohesive soil were present. Cohesion values ranged between approximately 1 and 6 psi, while soil-rubber friction angle was between 4.3 and 7.9 degrees. The remainder of the cohesive surface

data, full results can be found in the Appendix. Final data from the bevameter is listed in Table 3.4.

	Gravel Surface	Clay Surface
Average Friction Angle φ, degrees	10.68°	6.13°
Average Cohesion c, lb/in^2	0 lb/in^2	4.8 lb/in^2
Shear Deformation Modulus, K, lb/in	0.06 lb/in	0.05 lb/in

Table 3.4 – Average values for various soil-rubber interface properties

3.2.2 Normal Response

Normal load tests were conducted in conjunction with the shear-head tests. The normal load tests were performed manually, recording displacement from a dial indicator and pressure from the pressure gauge on the pneumatic cylinder. While results were not as well grouped as the shear tests, appropriate trends were observed that matched what to expect of the surfaces.

The following plots (Figures 3.15 - 3.18) are the raw data recorded from the tests. As noted in Chapter 2, they follow trends (increasing sinkage for increasing pressure) observed by Yu [30].

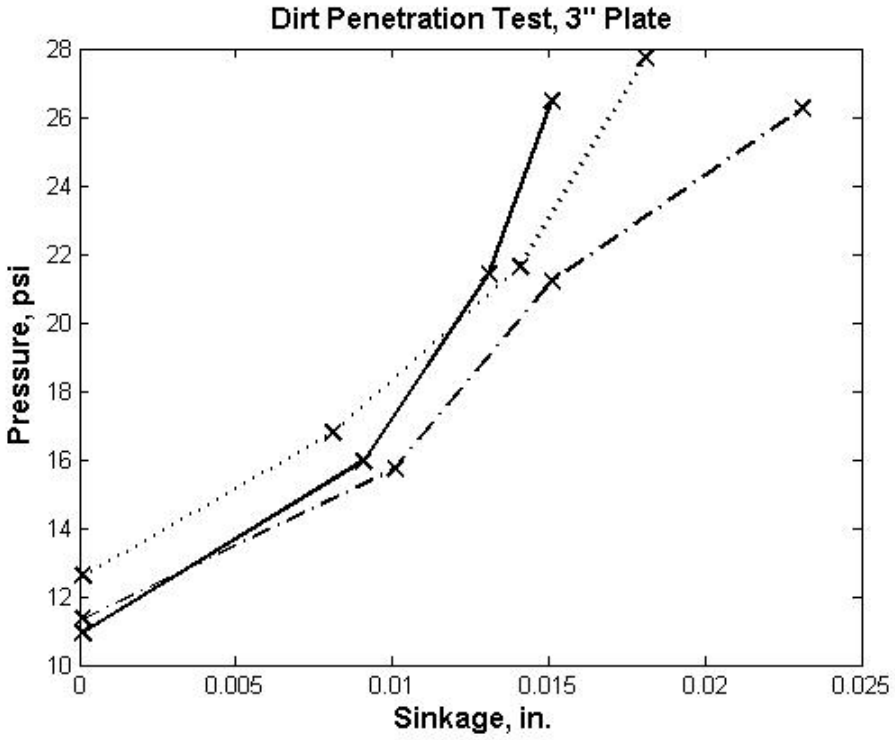

Figure 3.15 – Cohesive soil 3” plate penetration test

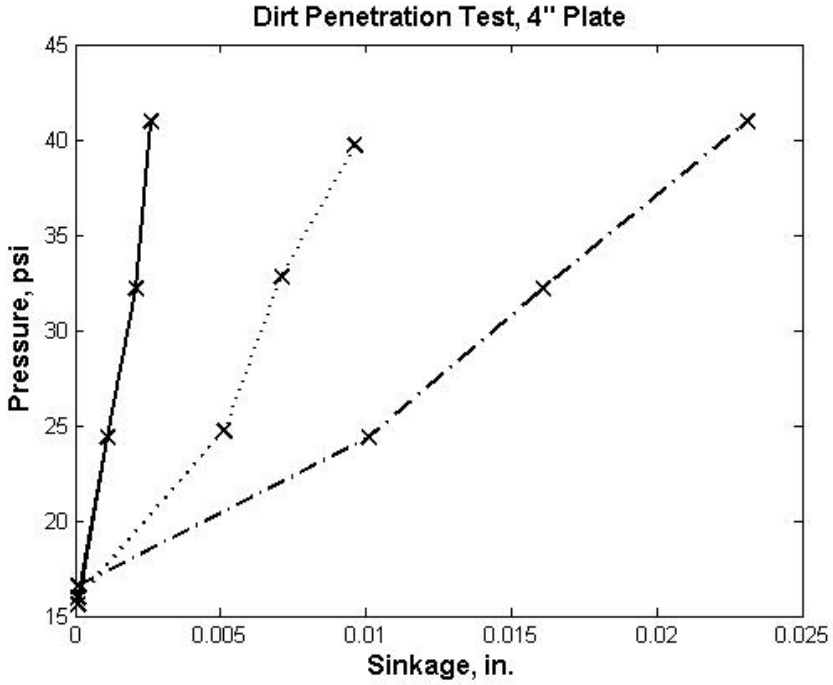

Figure 3.16 Cohesive Soil 4” plate penetration test

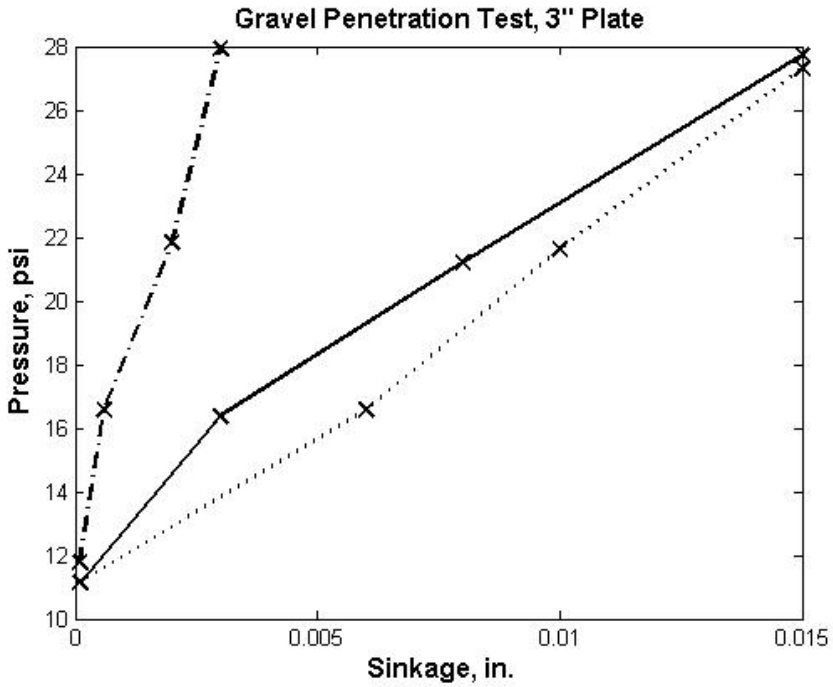

Figure 3.17 – Frictional Soil 3” plate penetration test

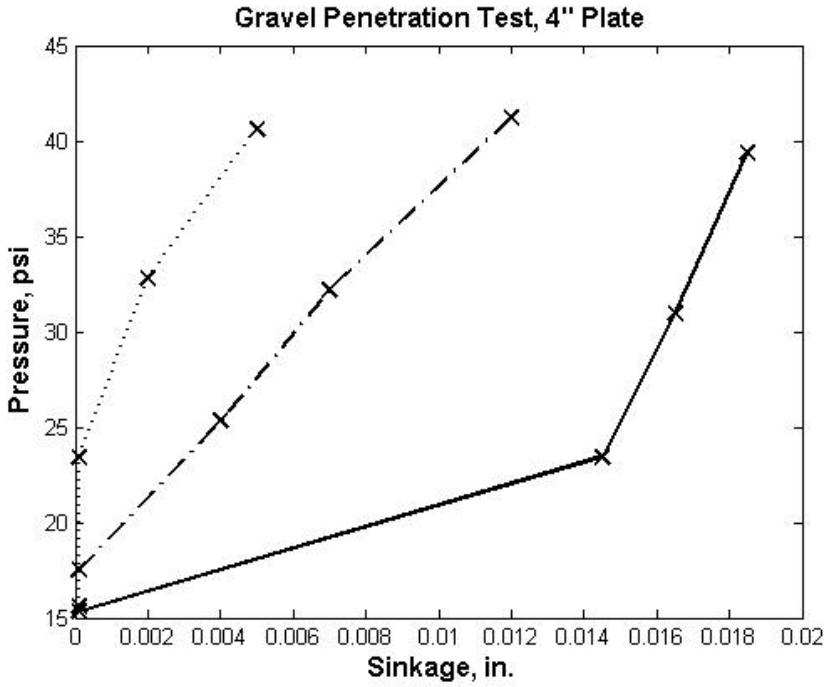

Figure 3.18 – Frictional Soil 4” plate penetration test

Looking at the very small displacements on the x-axis, one can immediately discern that the soil is very stiff. This stiffness does not allow for any appreciable sinkage, and thusly does not allow lug interlocking. The lack of lug interlocking allows the tire measurements to be tread-pattern independent, and focus on the soil-rubber interface. It must be noted that during the normal load tests on gravel, the top layer was not penetrated by the plates.

Evaluating the bevameter data as per [34] and [3], the surface normal properties are shown in Table 3.2

	Gravel (Frictional Surface)	Clay (Cohesive Surface)
Sinkage Exponent, n	6.08	2.89
k_{φ}, lb/in^{n+2}	44.667	39.33
k_c, lb/in^{n+1}	0.0	14

Table 3.5 – Bekker bevameter sinkage properties

Further analysis with A.R. Reece's methods were not deemed important, as the soil was found to be very stiff and thus any sinkage would not give extra lateral force at the tire-soil interface. This is indicated by the large sinkage exponent found on both soils, and their stiffness confirmed by numbers compiled by Wong [7].

3.3 Tire Test Rig

A test rig constructed at Auburn University was used to gather raw operational data of the KT 821 tire in various configurations. Static normal load, static slip angle, and static camber angle are all set by the operator while dynamic normal load, dynamic

camber angle along with reaction forces were recorded by the Dataq model 710 data recorder through associated sensors. Despite the noisy nature of off-road data, useable data could be obtained on the effect on lateral performance of camber, tire pressure, and vehicle-soil interface strength.

Raw data is collected from two accelerometers and three load cells on a typical run. Other special runs have been made with the inclinometer to measure camber throughout passes on the test surfaces. In Figure 3.19 is a sample plot of raw data as it comes from the Dataq 710 to simply illustrate the frequently fluctuating loads imparted onto the tire. The small voltages coming from the load cells can be seen tightly grouped against the x-axis.

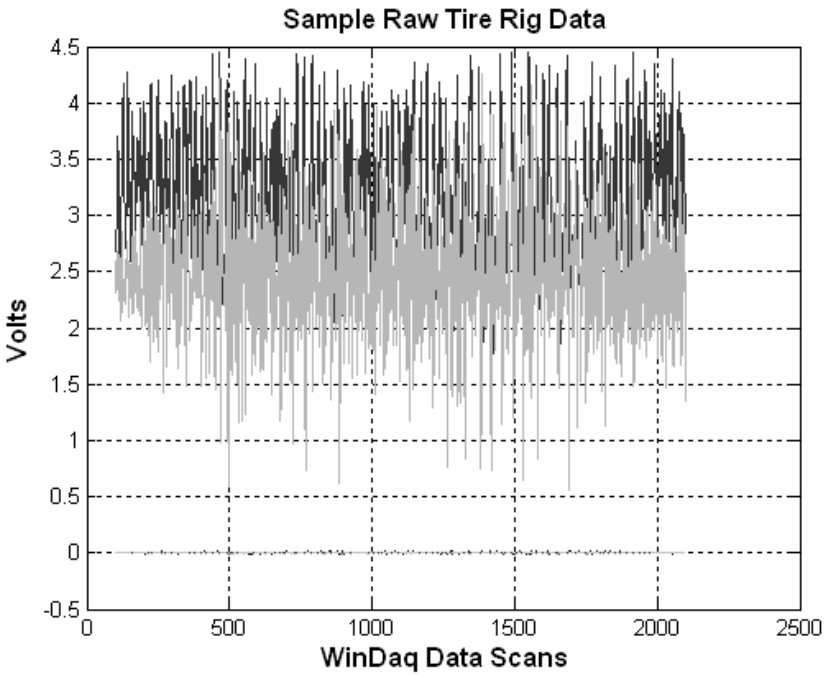

Figure 3.19 – Sample raw data from tire test rig

Once processed, several forms of data can be presented. Typical formations of tire data can be presented as (but not limited to):

1) A 3-dimensional plot of Normal Force, Lateral Force, and Slip Angle, also known as a “Carpet Plot”
2) A 3-dimensional plot of Normal Force, Longitudinal Force, and Slip Angle. Also a “Carpet Plot”
3) Peak Longitudinal Force(in this case, drag force) versus Normal Load
4) Peak Lateral Force versus Normal Load
5) Lateral Force Coefficient (LFC) versus Slip Angle
6) Drag Force Coefficient (DFC) (also can be listed as COT, coefficient of traction) versus Slip Angle
7) Cornering Stiffness (C_α, lb/deg) versus Normal Load

A note must be made regarding the uncertainty of the values presented by these plots. Before going into the uncertainty, insight into the data processing methodology is required. Once all testing is complete, all runs for a particular configuration are combined into one data file. Recall that the acceleration and deceleration portions are not part of the data, so combining the data does not have any ill effects. Three load cells and two accelerometers are read into the data acquisition system. Once adjusted through the calibration curves, lateral, longitudinal, and vertical forces can then be deduced.

Vertical load is determined through the accelerometer attached just below the dead weights. By knowing the acceleration and the mass, a vertical force can be calculated. As the terrain fluctuates greatly, this can cause wildly fluctuating normal loads. The software written for this study incorporates a filter that only processes lines of data where the normal load is within ten percent of nominal. This process manually sets the uncertainty

of the vertical load. Brief experiments were conducted to reduce this tolerance, however further reductions in tolerance significantly limited the number of data points for analysis. As this is the first excursion into the uncertainty of ATV tire forces it was determined that a ten percent tolerance was an acceptable starting point, as no analysis of this type has been conducted.

As data points are accepted by their meeting normal load tolerance, the program begins calculating lateral and longitudinal forces through the schematic of the tire rig, presented in Figure 3.20. Lateral and longitudinal forces are calculated as follows:

$$\begin{aligned} F_x &= f_{Ch.6}\sin(\alpha) + f_{Ch.7}\cos(\alpha) + f_{Ch.8}\cos(\alpha) \\ F_y &= -f_{Ch.6}\cos(\alpha) + f_{Ch.7}\sin(\alpha) + f_{Ch.8}\sin(\alpha) \end{aligned} \tag{3.4}$$

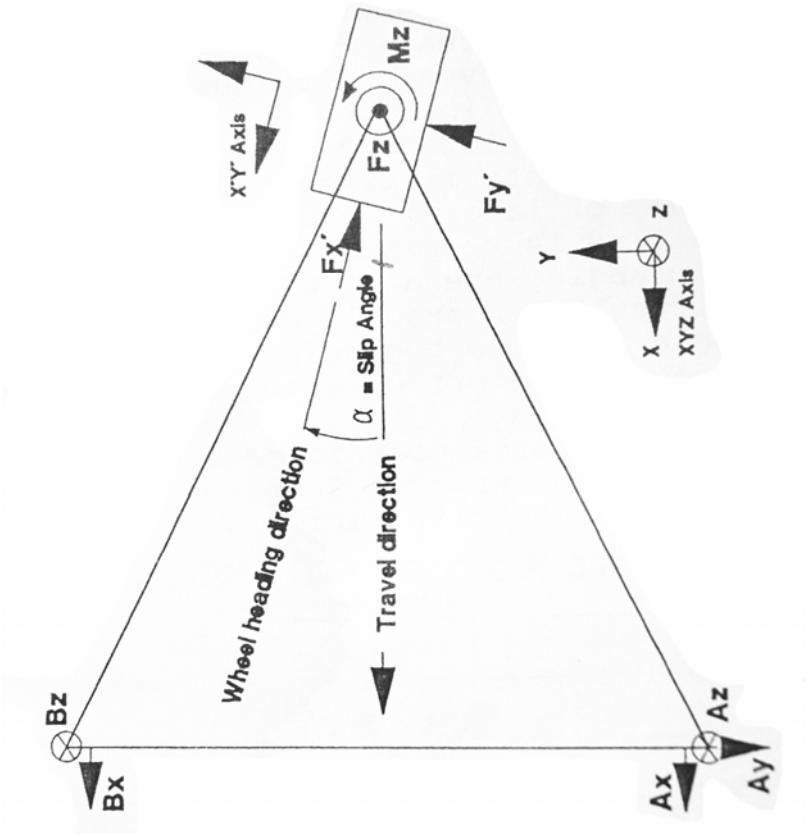

Figure 3.20 – Schematic for tire test rig

This process generates lateral and longitudinal force vectors that are associated with normal loads that are within ten percent of the nominal normal load for that run. As the vehicle has been driven over as a consistent and level surface as possible, the mean of these vectors is taken. This average value is then saved as the lateral and longitudinal forces for that particular run. Standard deviations are also computed for both vectors.

Given the standard deviation, and the number of samples, the standard error of the mean can be calculated for these mean values of lateral force.

$$S_E = \hat{\sigma} / \sqrt{n} \tag{3.5}$$

For most of the data presented in this paper, standard errors for lateral force and longitudinal force are approximately ±4 lbs.

The same approach was applied to camber data collected with an inclinometer. Slow speed tests over each test surface were recorded, and the camber uncertainty was found to be between around ±5 degrees. Camber values can change even on "zero" camber runs, and therefore creates the need to label camber data as "high" and "low" camber. Intermediate values were not fully tested as the statistical difference could not be detected until the camber in the test rig was placed at the maximum camber value.

The information provided by the plots within this section can allow a vehicle designer to specify appropriate spring rates as to not saturate the tire, or design for the least longitudinal resistance for maximum efficiency.

The first plot to be presented is the lateral force carpet plot. It can help put the tire's "operational map" in perspective.

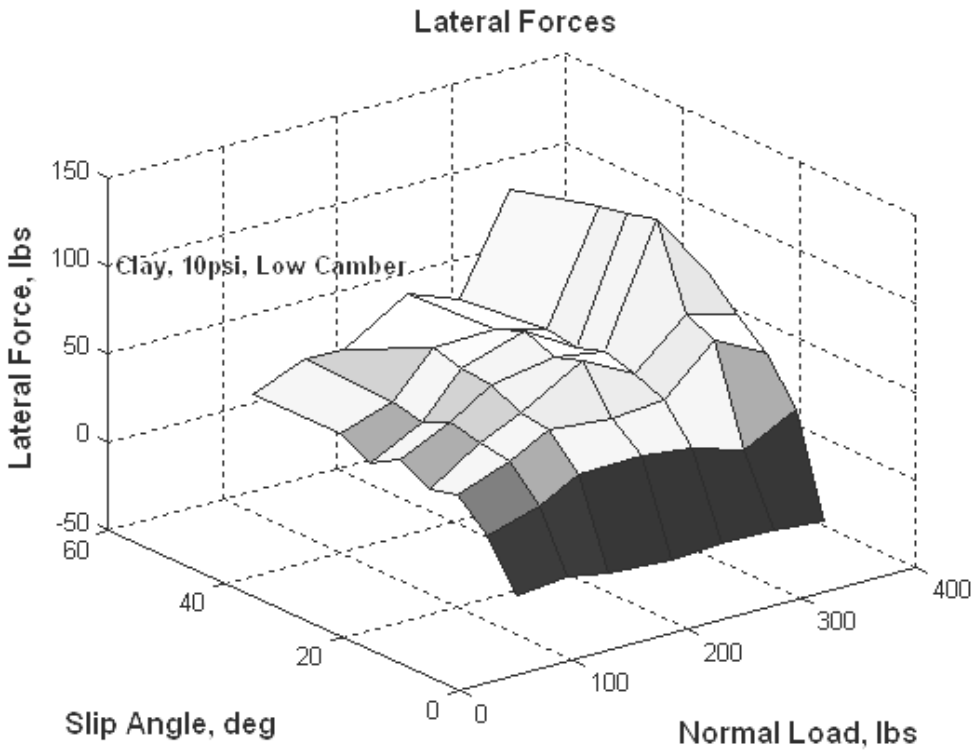

Figure 3.21 – Sample carpet plot of lateral tire data

One will notice the trough at 185 lbf. nominal normal load in Figure 3.21. At the 185 lbf. normal load, and 10 psi inflation pressure, an oscillation developed while towing the tire. The tire can be modeled as a spring-mass system, and a natural frequency calculated. This natural frequency seemed to be excited by the ten miles-per-hour tow speed, and the test surfaces. An analysis of tire spring rate and natural frequency can be found in the Appendix. While the vertical spring rate does not directly correlate to the towing frequency of the tire, there are other flexibilities of the tire that may contribute to the oscillations. It is hypothesized that a mechanism very much like the mechanism that gives rise to relaxation length in tires is causing the trough on Figure 3.21.

Relaxation length is the length a tire rolls between when a step steering input is applied, and when the tire generates its maximum force for that given slip angle and normal load.

Since the terrain has a highly variable vertical profile, it is hypothesized that there is a time between when the appropriate normal load is rapidly applied and when the actual force associated is generated. This may be in part due to the deformable nature of the operating surface, where on pavement, it is very rigid in comparison to a vehicle tire. The trough can be seen in other carpet plots, and may vary in size depending on the surface, inflation pressure, and small fluctuations in the towing speed. Since the data reduction software written for this study used on all of the data only allows a narrow band of normal loads about the nominal normal load, the lateral force generated may lag the application of the normal load by a small amount of time, and thus be rejected by the selection process in the code. Further exploration of this phenomenon may offer more insight into the operation of off-road tires on deformable surfaces.

Another version of the carpet plot can be generated with longitudinal forces. Seen in Figure 3.22, is the same trough about 185 lbf. normal load. As the lateral and longitudinal forces are derived from the same sensors, the phenomenon described above will make its way into the longitudinal carpet plot.

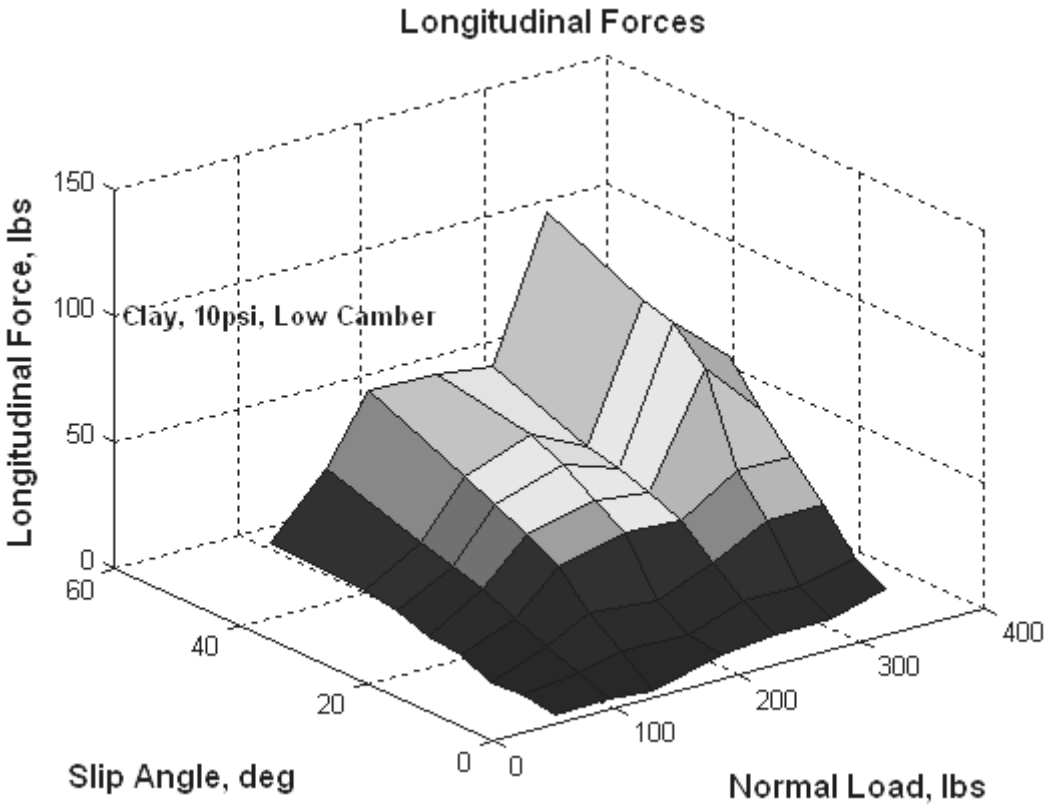

Figure 3.22 – Sample carpet plot of longitudinal tire data

Seen in Figure 3.23, while loosely grouped, the relationship between longitudinal force and slip angle may be linearized within a small band of normal loads.

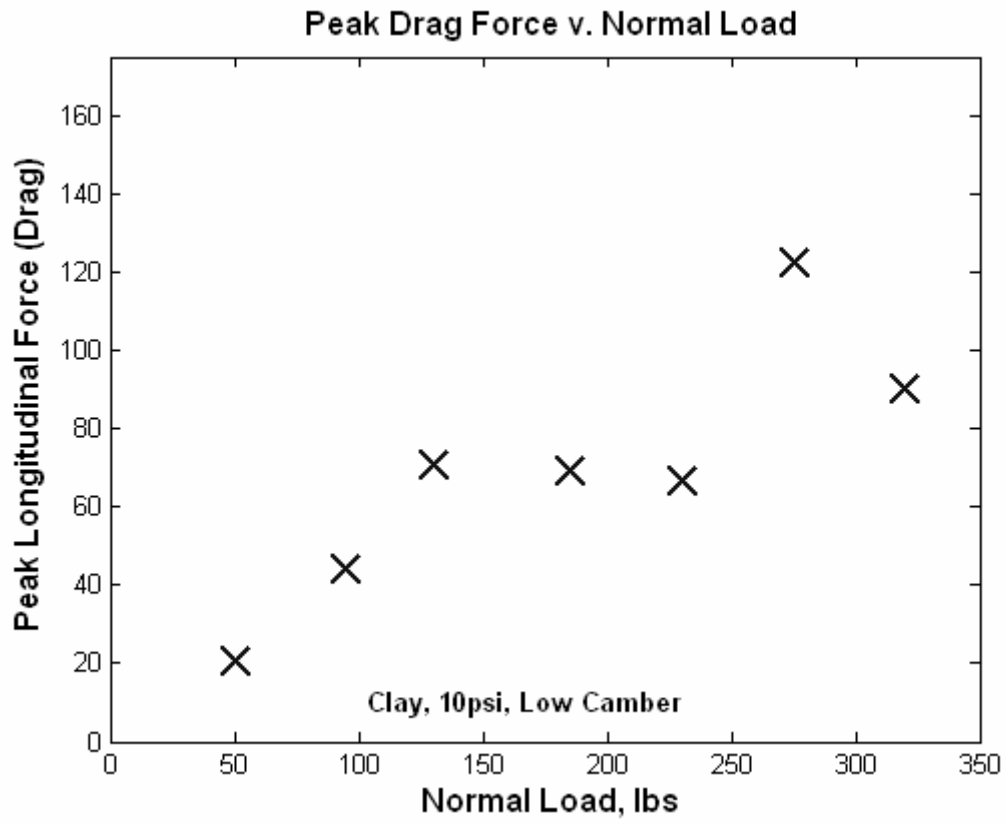

Figure 3.23 – Peak drag force v. normal load

Another way of visualizing this data is normalizing it with respect to the nominal normal load imparted on the tire. Shown in Figure 3.24, the first linear section can be seen, however at increasing normal loads (near 320 lbf. normal load), the curve shape shifts to that of an exponential form, which matches that presented by Crolla, et al [15].

$$COT = COT_{\max}(1 - e^{-Ks}) \tag{3.2}$$

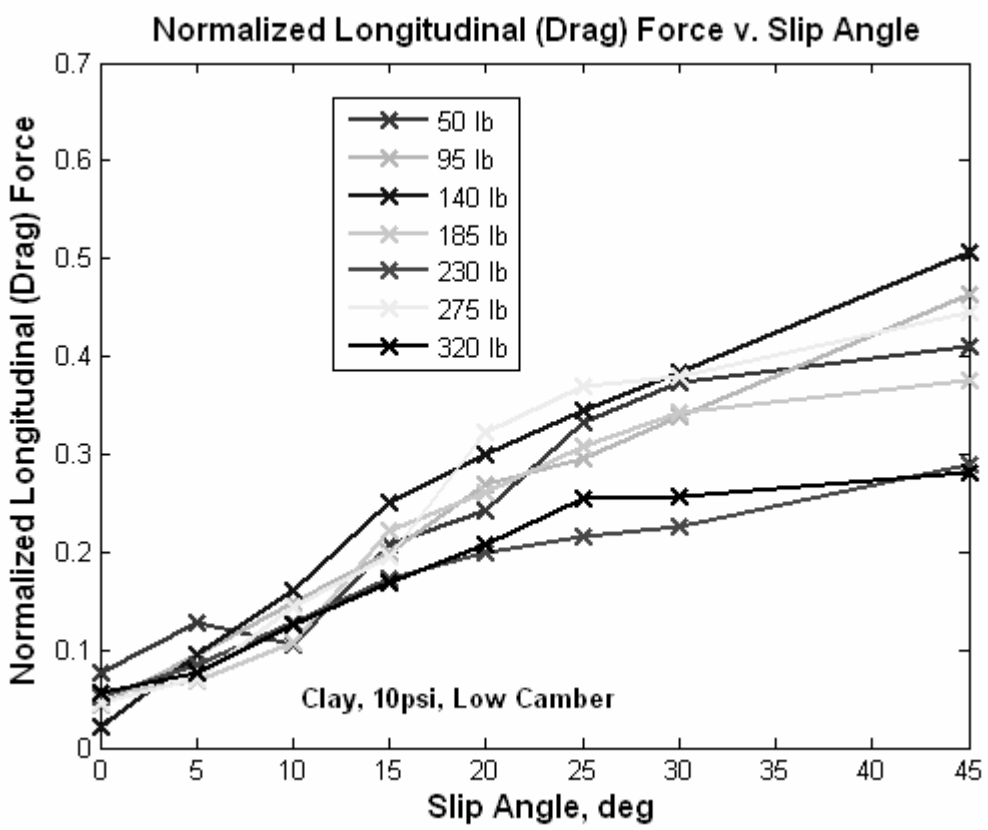

Figure 3.24 – Sample Normalized longitudinal force v. slip angle

Similar to Figure 3.24 is the plot of the LFC. Instead of showing longitudinal force which is normalized, the normalized lateral force is plotted against slip angle for various normal loads. Normalization is performed by dividing the lateral force by the nominal normal load for that set of data. Figure 3.25 represents a typical LFC plot.

Note in the LFC plot that the curves do not collapse upon each other. This showcases what is called tire load sensitivity. Tire load sensitivity has a major effect on the balance of a vehicle. Breakaway characteristics are also affected, as some tires lateral force capability may diminish smoothly, whereas some may suddenly drop off. [19].

Another entity of note is the data points for 50 lbf. normal load. The lightly loaded tire at high slip angles found a "slip-then-grip" mode causing the data points to be less accurate than for the immediately following normal loads.

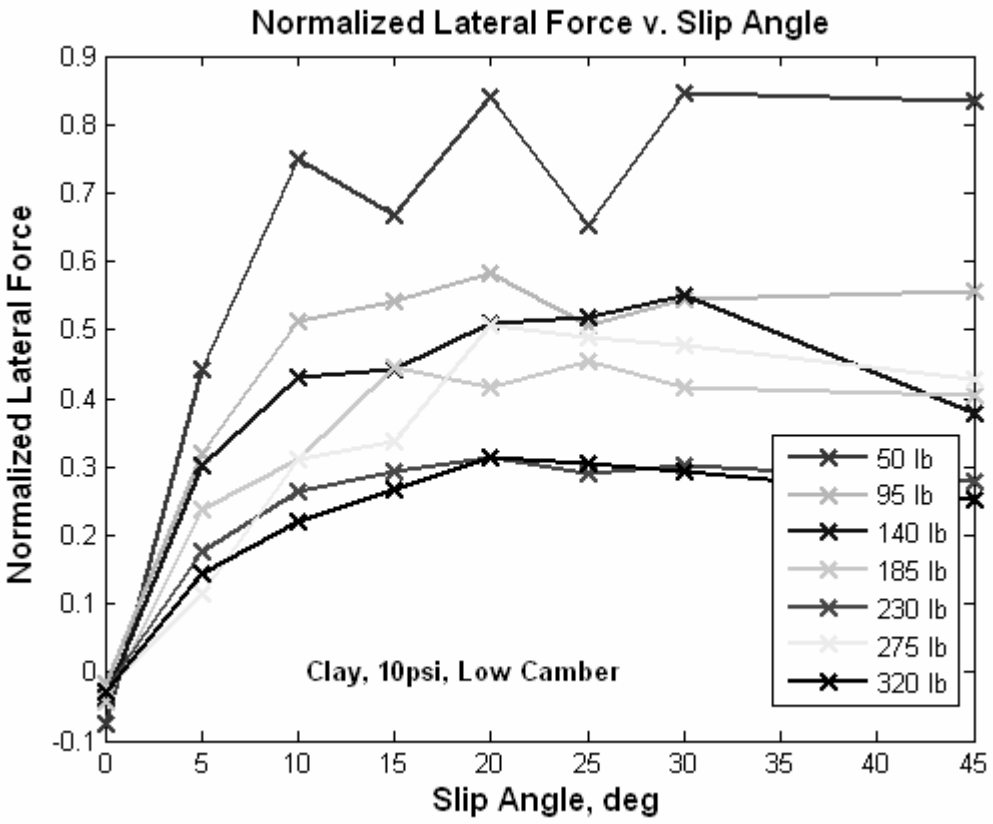

Figure 3.25 – Sample Normalized lateral force v. slip angle

A related plot to Figure 3.25 is that of cornering stiffness, denoted by C_α, versus normal load (Figure 3.26). Cornering stiffness is the slope of the linear region of the lateral force versus slip angle plot, and measured in units of lbs/deg. Seen in Figure 3.25, there is a trend to have increasing $C\alpha$ with normal load. The values of Cα were generated by the second data point in a lateral force versus slip angle data set, and the origin of the plot. For example, if the data point at five degrees slip angle is 30 lbf, then the associated

$C\alpha$ value is thirty divided by five, and thusly 6 lbf/deg. They follow a general trend similar to that shown by Pacejka [20].

Cornering stiffness is important in understanding how much slip angle, (indirectly, steer input), must be provided before the vehicle will generate peak cornering forces for a given normal load. A balance must be struck between excessive steering sensitivity and the time and speed required to steer from center to lock.

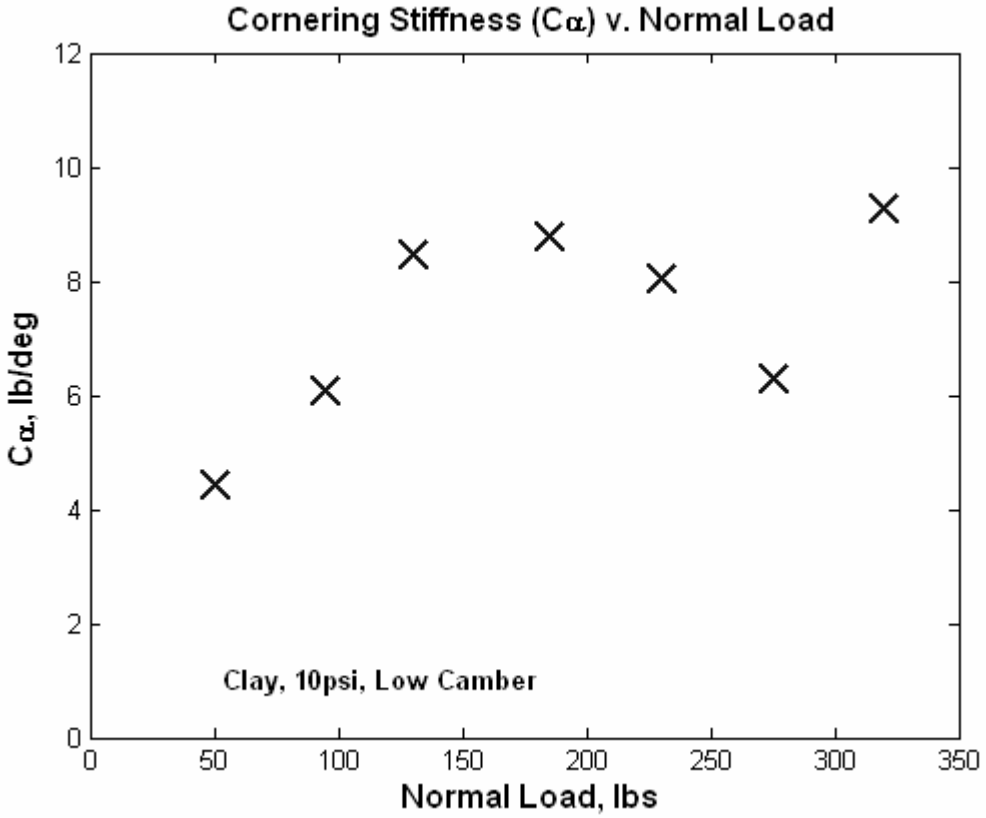

Figure 3.26 – Cornering stiffness v. normal load

A similar plot (which was shown before with longitudinal force) is shown as Figure 3.27, illustrating how peak lateral force changes with increasing normal load.

The trend for this type of data will be to increase linearly into a transition period, where the tire starts to become overloaded vertically and will not produce any more lateral force.

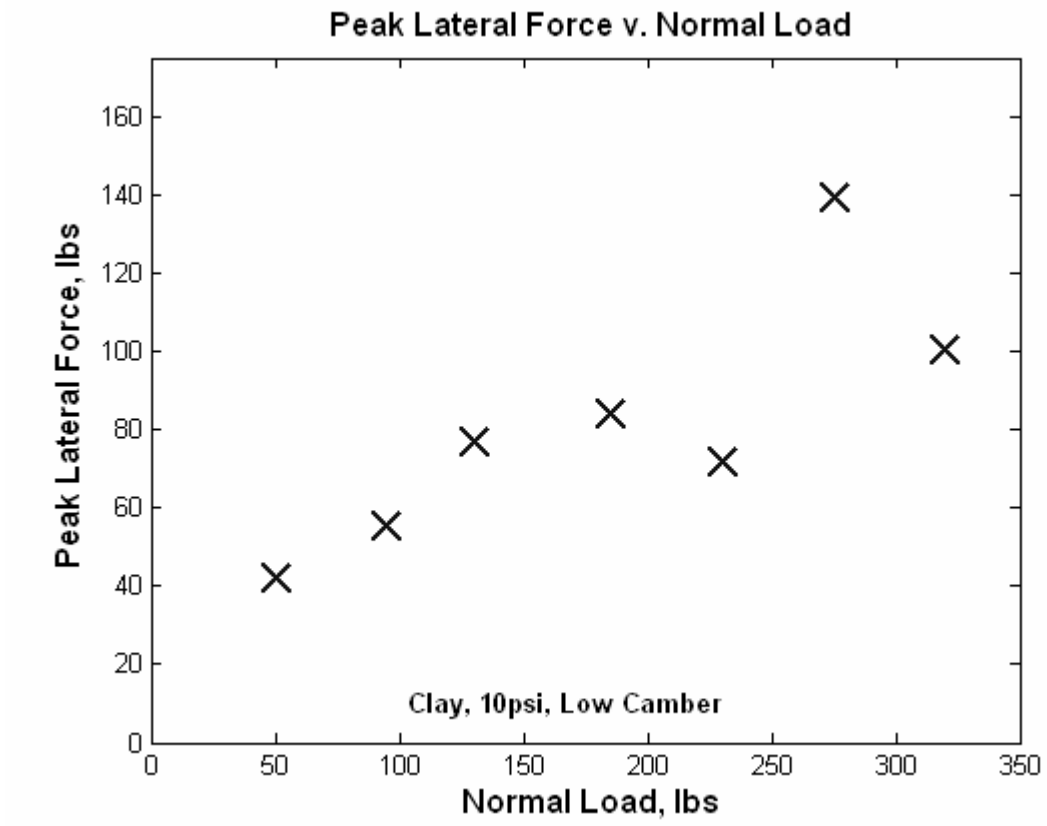

Figure 3.27 – Peak lateral force v. normal load

Through the information presented in Figure 3.27, adequate methods have been used in order to collect and present relevant tire data. These plots can be used to compare tire performance between the changes in camber, inflation pressure and operating surface. The following sections will highlight the results of the specific camber, pressure, and surface tests. One may note that normalizing the values in 3.27 will yield a sort of "effective friction coefficient" of the tire based on normal load.

3.3.1 Inflation Pressure

Utilizing the inflation pressure first in the presentation of results allows the comparison of trends to other trends observed when pressure was altered. The most notable change with inflation pressure tends to be that of cornering stiffness, as inflation pressure directly affects carcass stiffness. Inflation pressure also has an influence on peak force by way of coefficient of friction, yet is less easily understood [19].

First presented are the carpet plots for both high and low inflation pressures of 10 and 5 pounds per square inch, respectively. As a note, the lateral force carpet plots (Figure 3.28) all share the same axes for ease of comparison, as do the longitudinal force carpet plots.

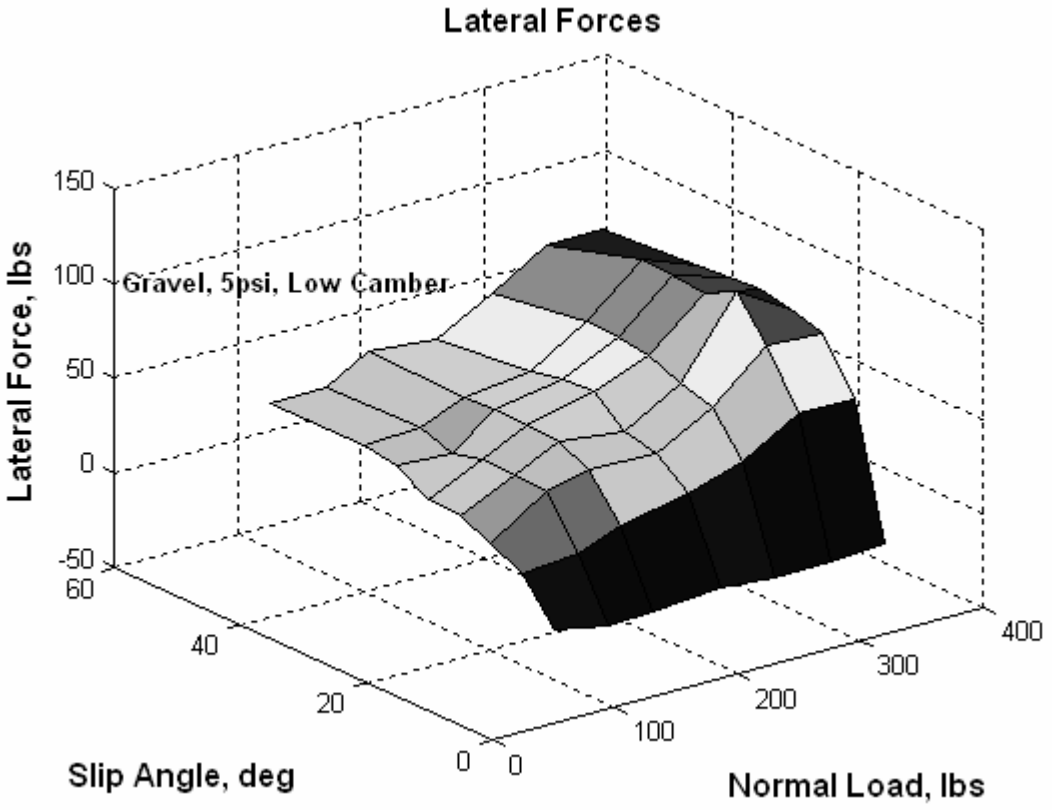

Figure 3.28 – Lateral force carpet plot for Gravel, 5 psi, Low camber

Figure 3.28 depicts shows the relation of slip angle, normal load, and lateral force generated in a three-dimensional format for an operating pressure of 5 psi. Note as slip angle increases, the lateral force exponentially increases to a more or less constant value as described by Crolla [18]. Figure 3.29, shows the three-dimensional representation of longitudinal force in relation to slip angle and normal load. Note now as normal load increases, the longitudinal force increases exponentially, whereas increasing slip angle has a semi-linear to exponential relationship with longitudinal force.

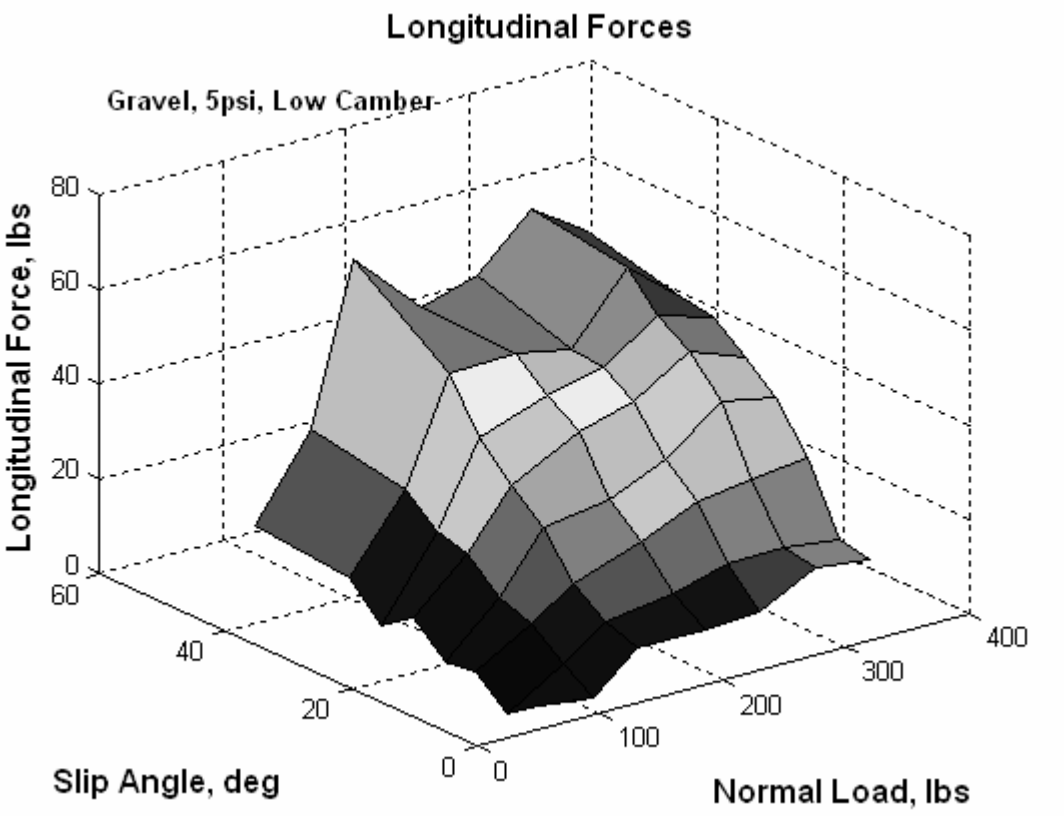

Figure 3.29 – Longitudinal force carpet plot for gravel, 5 psi, low camber

Increasing tire inflation pressure alters the carcass stiffness and the contact patch with the operating surface. Figure 3.30 showcases the carpet plot for lateral force data, while Figure 3.31 shows the longitudinal data.

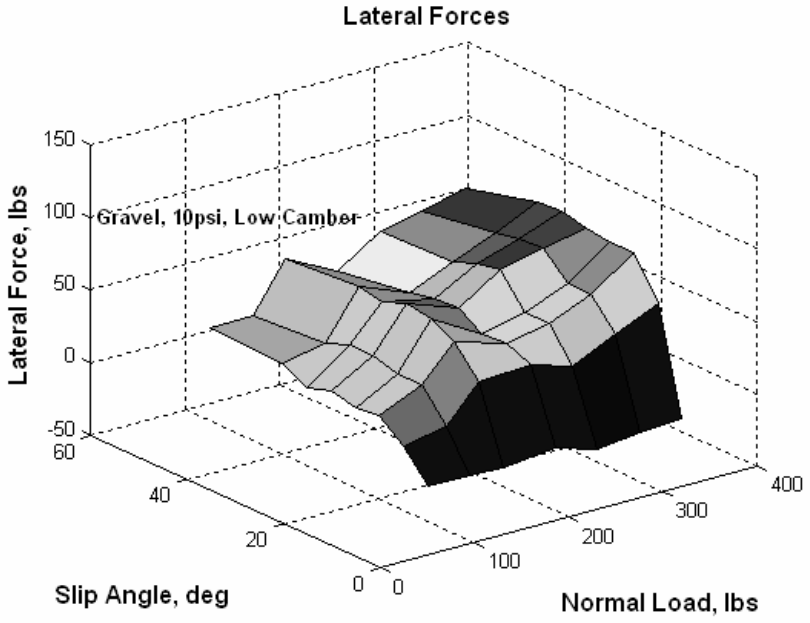

Figure 3.30 – Lateral force carpet plot for gravel, 10 psi, low camber

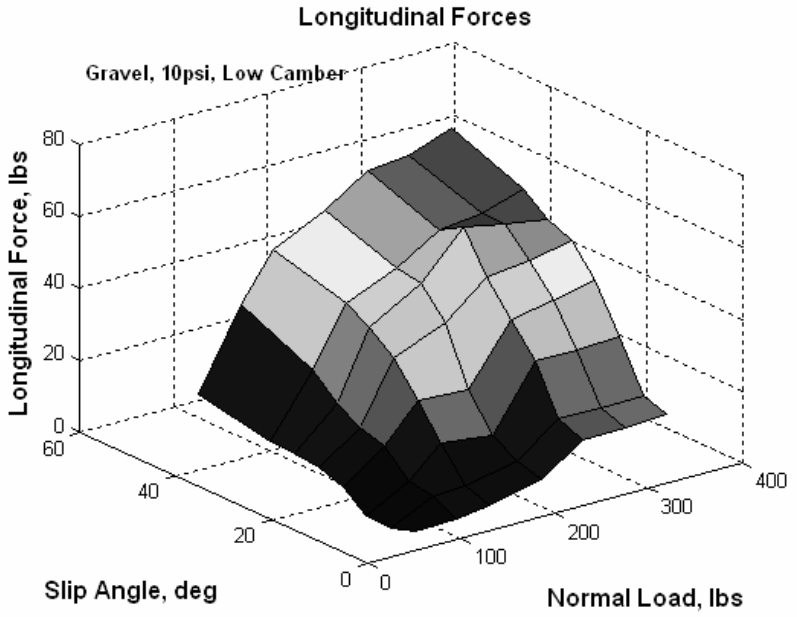

Figure 3.31 – Longitudinal force carpet plot for gravel, 10 psi, low camber

As was noticed with the low pressure experiment, the same trend of exponential rise to lateral force with addition of slip angle occurs. The shape of the longitudinal force carpet plot matches that of the 5 psi tests as well.

One may note a distinct ridge for the 140 lbf normal load plot on the lateral force carpet plot. Each value is consistently above those of larger and smaller normal loads. By changing the inflation pressure of the tire, one increases vertical spring rate. Based on oscillations observed during that particular test, it is believed that the phenomenon explained previously where there is a lag time between load application and actual realization of force is taking place. Further work to alleviate potential problems with unwanted oscillations may focus efforts on the application of a damper to the rig, properly instrumented as to record the forces at the attachment point of the frame.

As the carpet plots have been presented to align one with the general operating map of the tire, the following plots compare various data such as peak force in the lateral and longitudinal direction, cornering stiffness, and normalized lateral force versus slip angle.

Presented first is the plot of cornering stiffness with respect to normal load in Figure 3.32. One will note that the 5 psi change (rather large in the scope of ATV tires) has little effect on the cornering stiffness. Qualitative assessments from KT 821 testing in a race setting found that inflation pressures below 5 psi negatively affected the handling of the test vehicle, and added unnecessary rolling resistance to the system. Typical inflation pressures for the KT 821 are between 5 psi and 10 psi hence the tests were conducted with these conditions in mind.

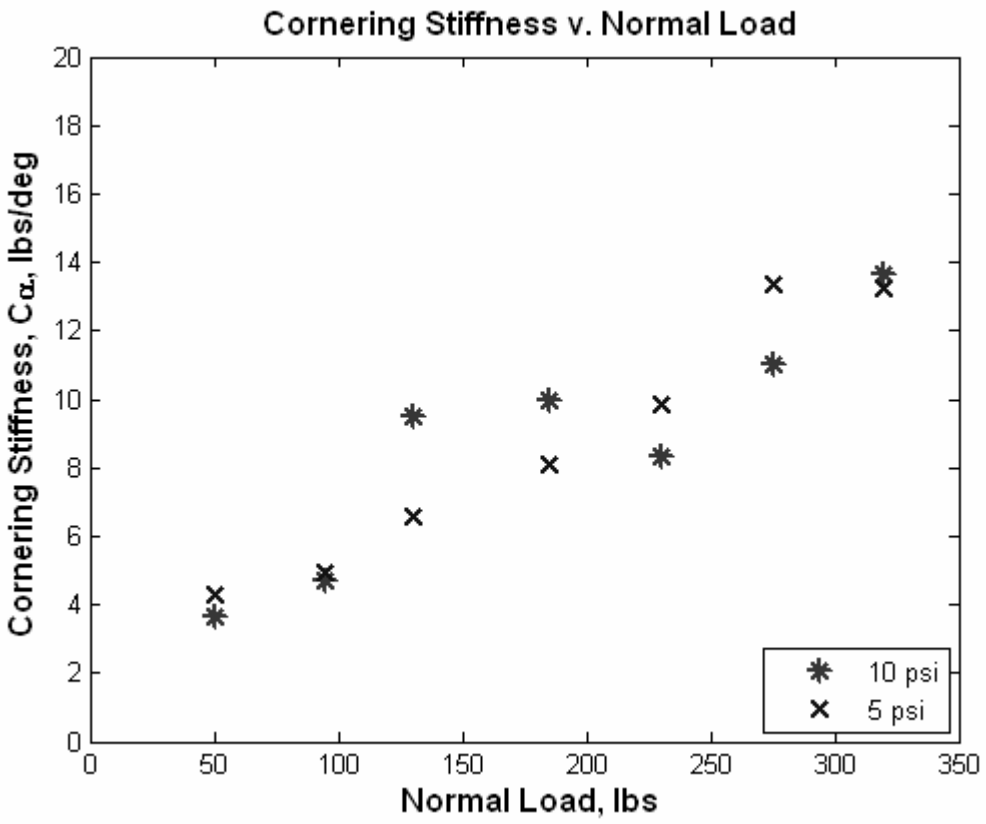

Figure 3.32 – Cornering stiffness comparison between pressures on gravel

Note that the closely grouped data sets follow a linear trend, increasing cornering stiffness with normal load. This relationship allows the KT 821 to undergo pressure changes due to operating environment change, or from extended use, and not adversely affect the performance of the vehicle. Controllers do not have to be greatly adjusted, nor would a driver have to deal with significant changes in the handling of the vehicle. It must be noted however, that this is only for the linear portion of the tire performance curve. Peak lateral force may be different between two operating pressures, even if the cornering stiffness does not change.

That said, Figure 3.33, and Figure 3.34 show how peak longitudinal and lateral forces are affected by inflation pressure.

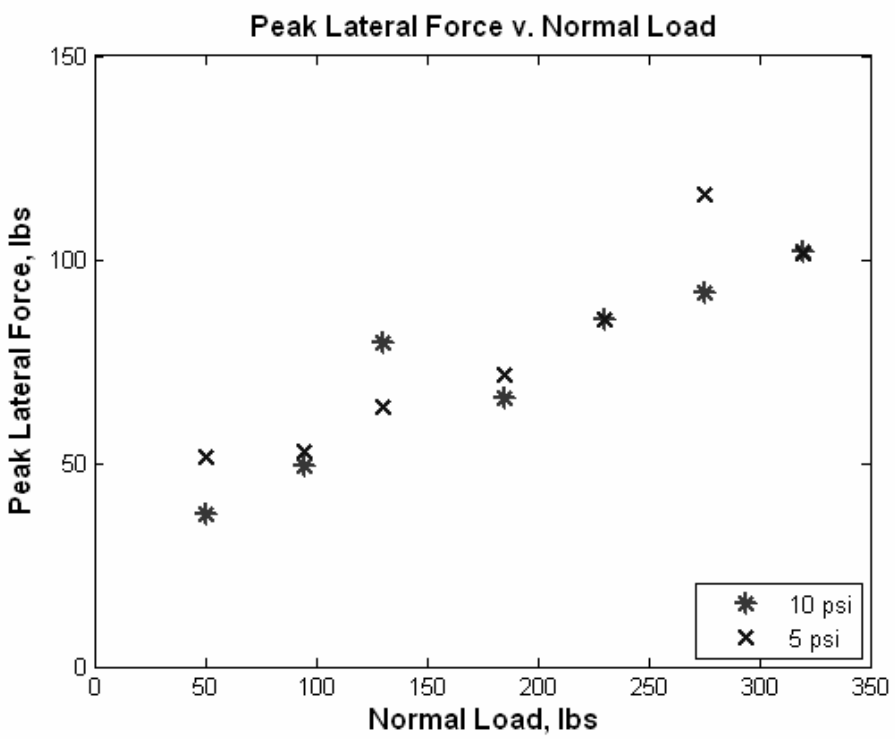

Figure 3.33 – Peak lateral force comparison between pressures on gravel

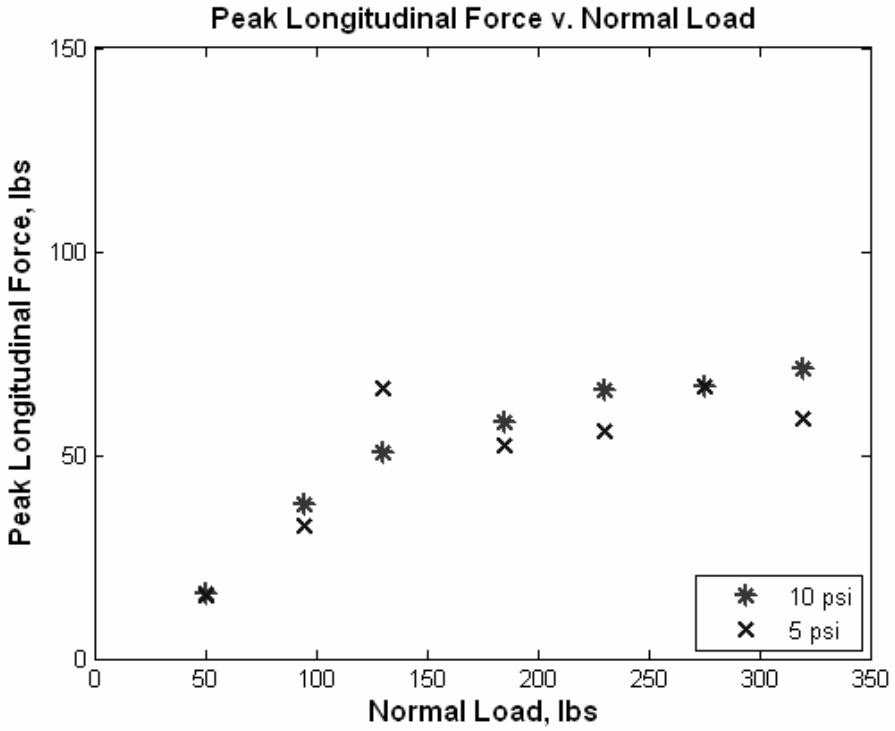

Figure 3.34 – Peak longitudinal force comparison between pressures on gravel

Much like the results found in cornering stiffness, there does not seem to be any appreciable change in peak lateral and peak longitudinal force between 10 psi and 5 psi of inflation pressure. Any small differences would be within the error range of the data. The first analysis of error in ATV lateral performance studies can be found in the Appendix.

Another way of visualizing the cornering stiffness and peak force data is to observe these trends from the normalized force plots. Shown in Figures 3.35 – 3.40 are comparisons of high and low inflation pressure for the 90, 140, 185, 230, 275, and 320 lbf tests.

One may note that the slope of a line fit to the data in 3.33 will be less than one. This indicates that lateral force does not increase proportional to normal load.

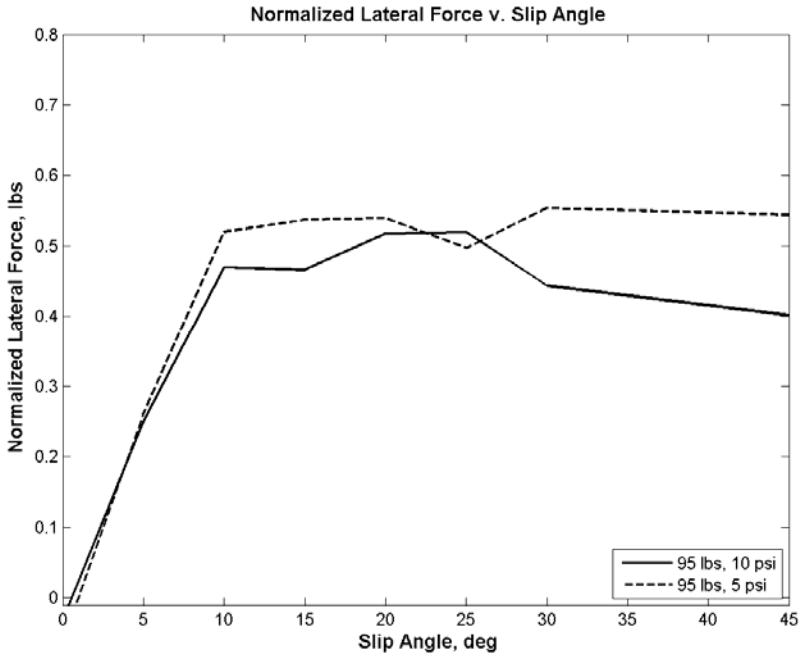

Figure 3.35 –Normalized lateral force comparison between pressures at 95 lbf normal load, gravel

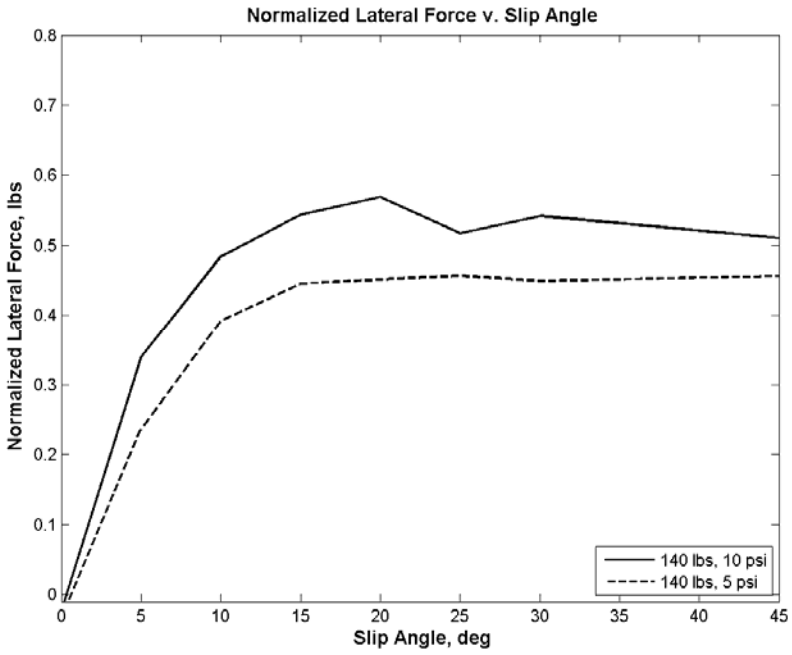

Figure 3.36 – Normalized lateral force comparison between pressures at 140 lbf normal load, gravel

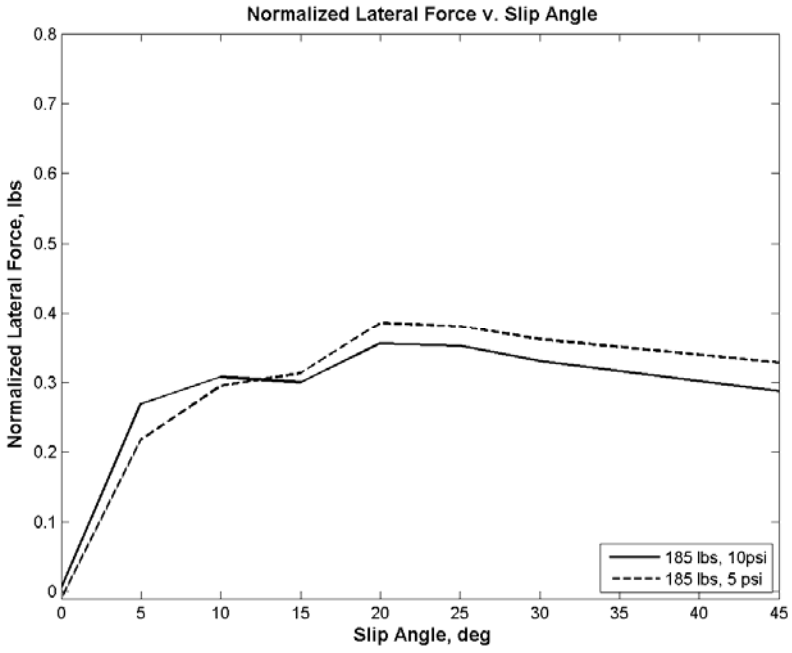

Figure 3.37 – Normalized lateral force comparison between pressures at 185 lbf normal load, gravel

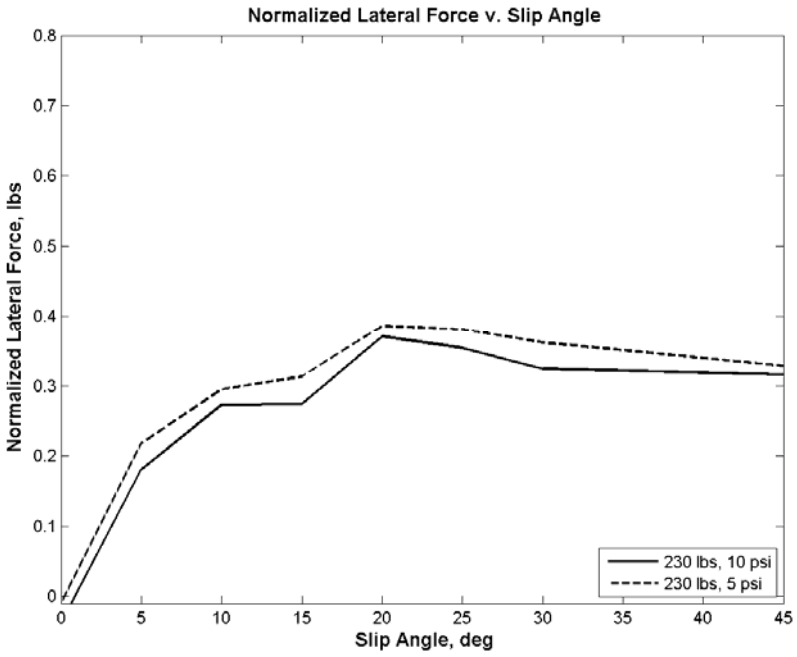

Figure 3.38 – Normalized lateral force comparison between pressures at 230 lbf normal load, gravel

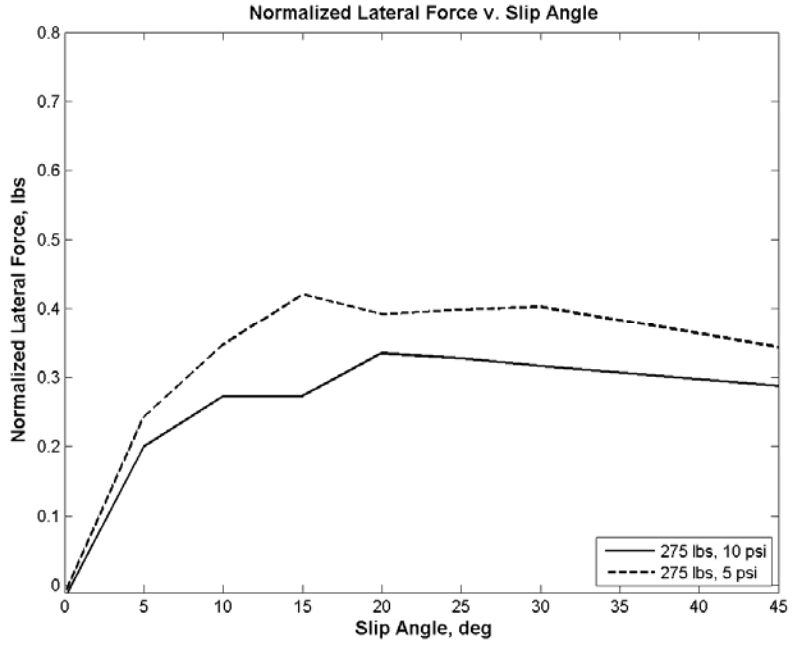

Figure 3.39 – Normalized lateral force comparison between pressures at 275 lbf normal load, gravel

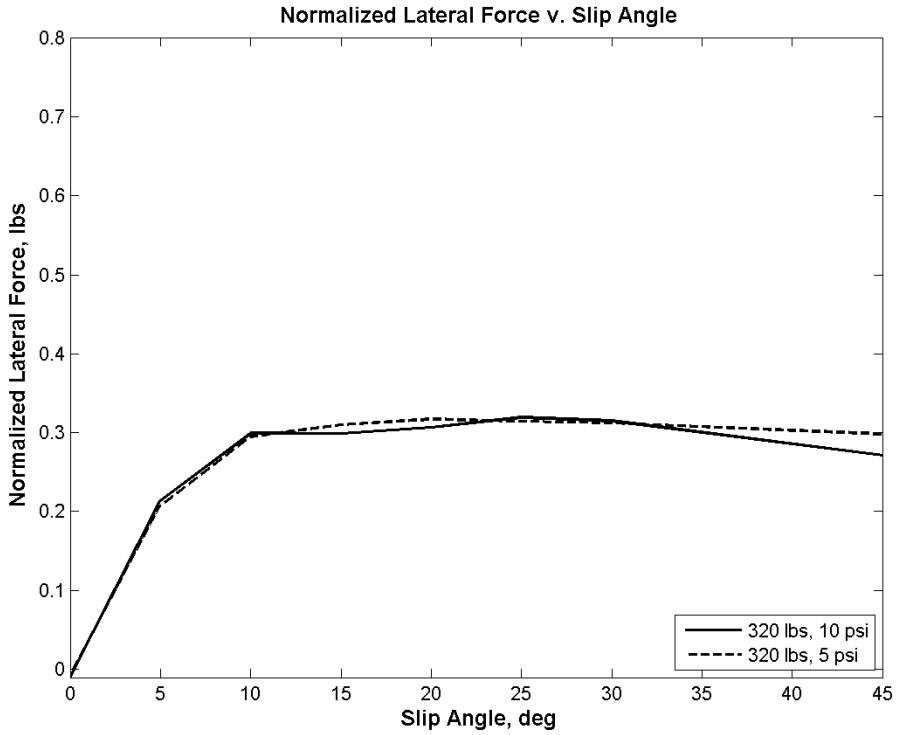

Figure 3.40 – Normalized lateral force comparison between pressures at 320 lbf normal load, gravel

Note in all figures how the initial slope of each plot is very similar, and the peak forces between high and low inflation pressure for a given normal load do not change significantly either. This insensitivity to inflation pressure may prove beneficial to designers working on control systems for UGV's, and designers designing vehicles that do not require intensive driver training or high maintenance requirements to keep check on air pressure.

3.3.1 Camber

As described in Chapter 2, camber refers to the inclination of the tire if rotated about the x (longitudinal) axis. Negative camber values are present when the tops of the

tires are angled inward, and positive when angled outward. This angle is changed by static adjustments in the suspension, or by the dynamics of the linkages within a suspension. Camber is used to fine tune a vehicles performance, and the addition of negative camber can manifest itself in more lateral force available for cornering [19].

Tests were conducted at varying camber levels to determine the effects on the generation of tire lateral forces, and longitudinal drag forces. Early tests at each camber setting (0, 2, 4, 6, and 8 degrees) revealed that differences in camber addition could only be realized between the 0 and 8 degree settings. This condition, in conjunction with the camber uncertainty for the given terrains forced "high" (nominal -8 degrees) and "low" (nominal 0 degrees) values to be used in the data gathering process.

A first comparison between both camber settings in Figure 3.41 places a light on that of the effect of camber on cornering stiffness, C_{α}.

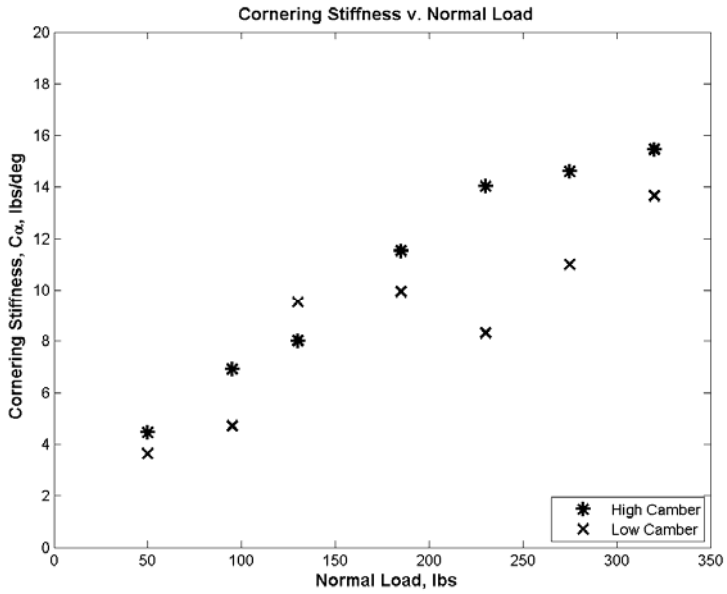

Figure 3.41 – Comparison of cornering stiffness v. normal load for camber angle on gravel

Observing Figure 3.41, one sees that increasing camber produces a slight increase in cornering stiffness. Camber's effect on peak lateral and longitudinal forces can be seen in the following Figures, 3.42 and 3.43.

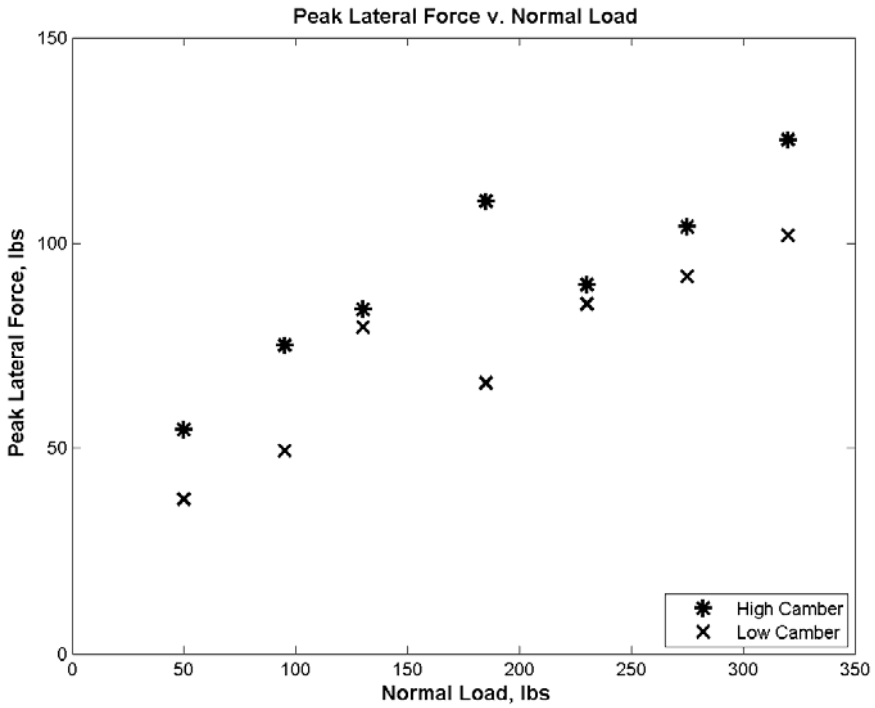

Figure 3.42 – Comparison of peak lateral forces for camber angle, on gravel

The trends presented in the peak lateral force versus normal load graphs are the same as noted by Pacejka [20]. The curve is concave down, however the data gathered in this study did not extend far enough to capture the full trend that Pacejka discusses.

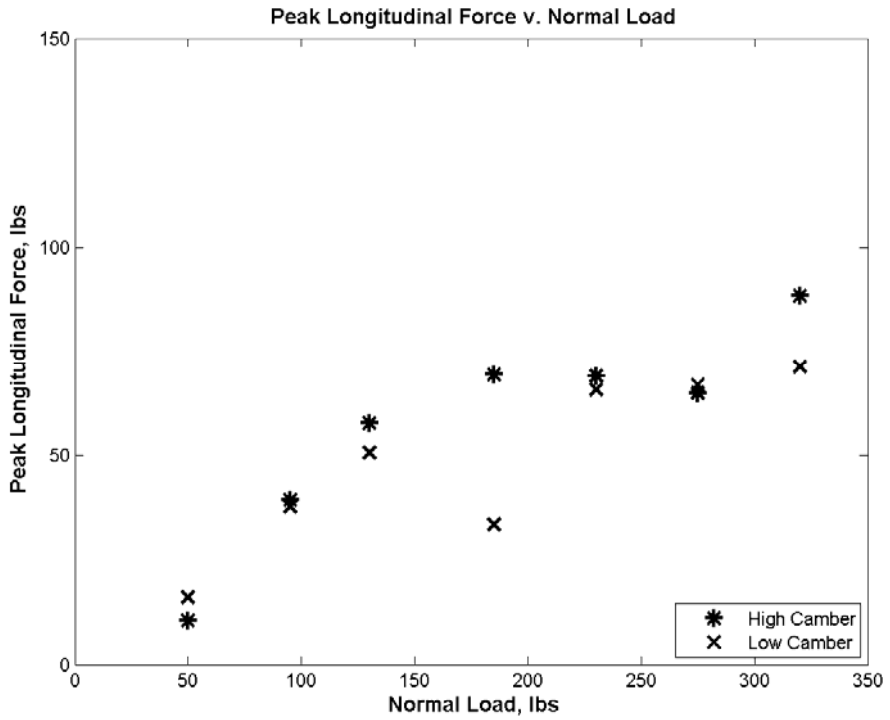

Figure 3.43 – Comparison of peak longitudinal forces for camber angle, on gravel

From the plots in Figures 3.42 and 3.43, one can deduce that a slight increase in peak lateral force can be gained for seemingly little increase in peak longitudinal force.

Presented in Figures 3.44 – 3.49 are comparisons of the high and low cambered tires at increasing normal loads, and their lateral force versus slip angle plots.

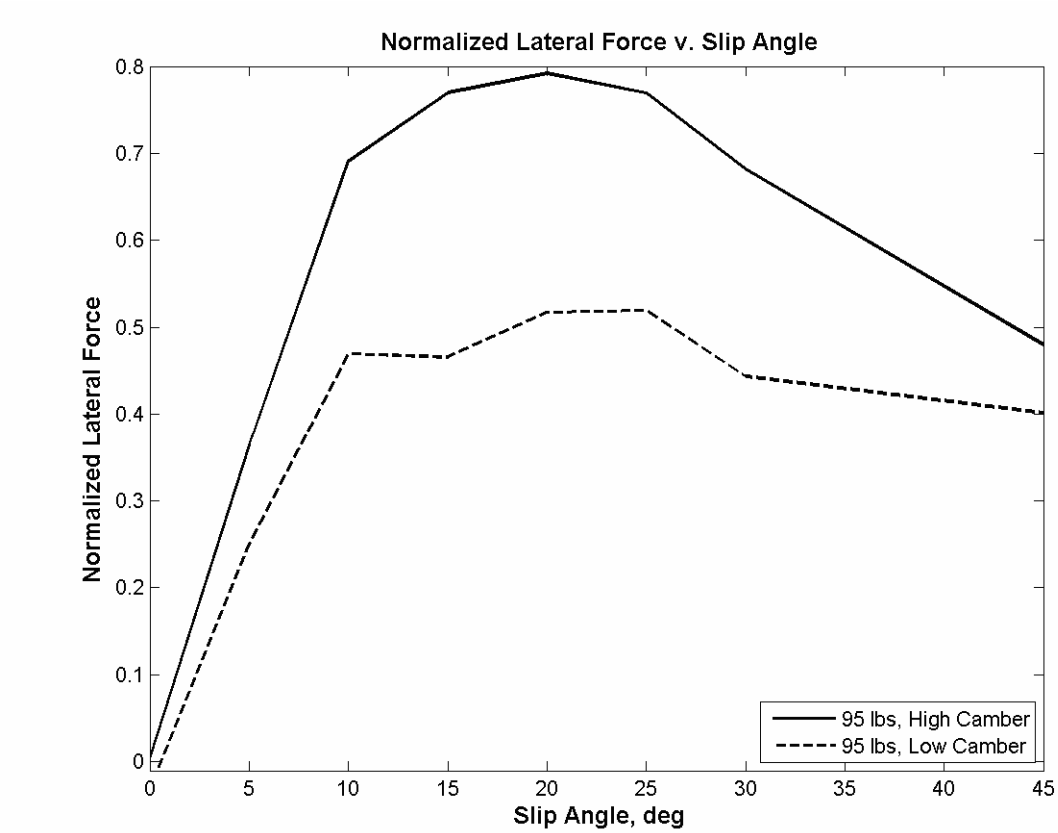

Figure 3.44 – Comparison of cambered tire lateral forces at 95 lbf normal load, on gravel

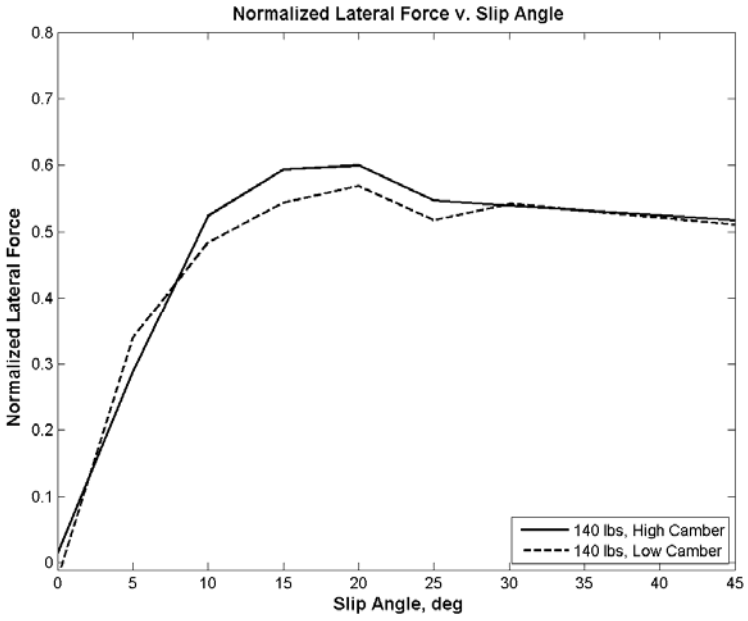

Figure 3.45 – Comparison of cambered tire lateral forces at 140 lbf normal load, on gravel

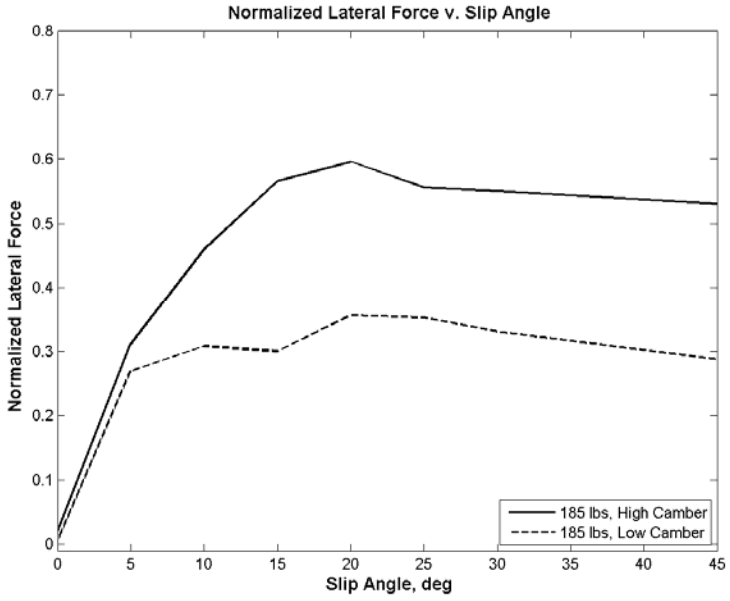

Figure 3.46 – Comparison of cambered tire lateral forces at 185 lbf normal load, on gravel

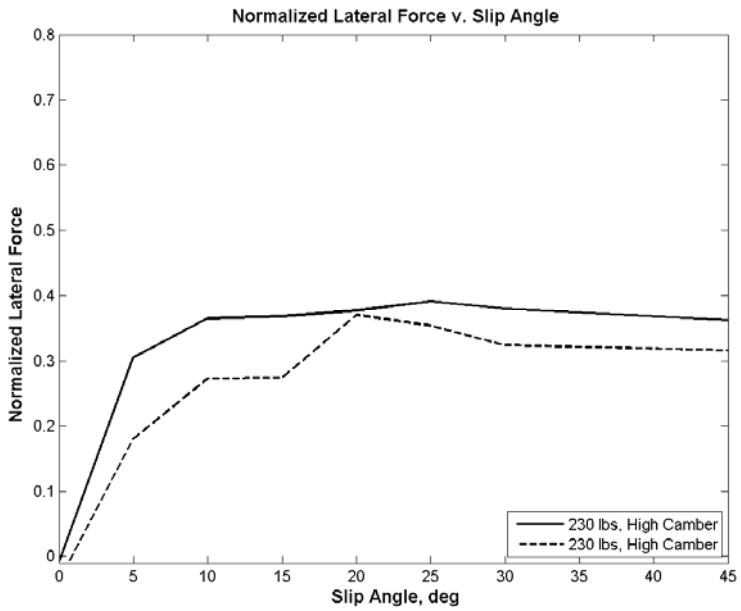

Figure 3.47 – Comparison of cambered tire lateral forces at 230 lbf normal load, on gravel

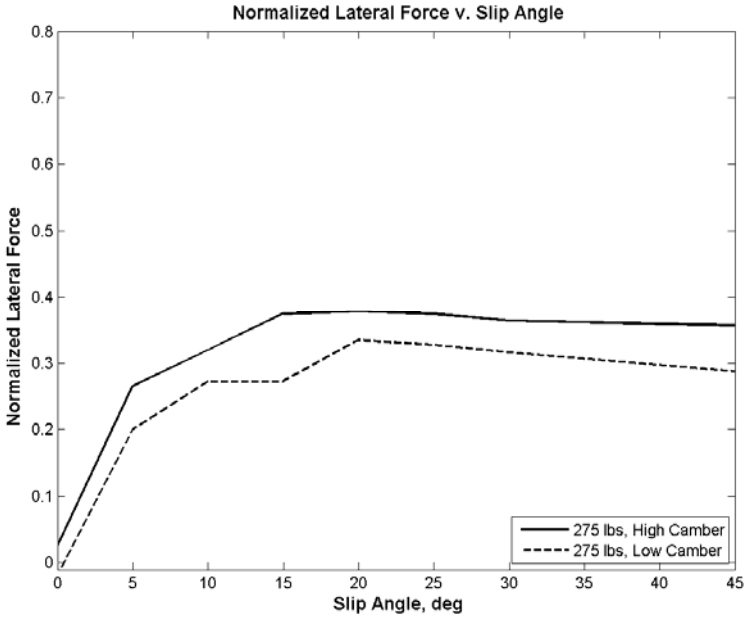

Figure 3.48 – Comparison of cambered tire lateral forces at 275 lbf normal load, on gravel

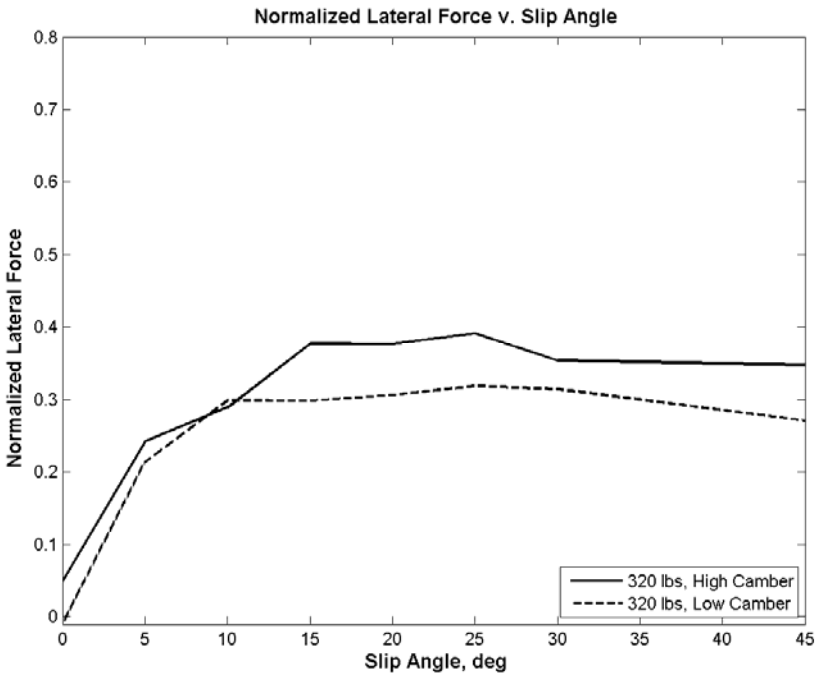

Figure 3.49 – Comparison of cambered tire lateral forces at 320 lbf normal load, on gravel

One will note that the linear region did not change much between high and low camber, however amongst the lower normal loads (those that are less than static); the available lateral forces to the vehicle were higher.

3.3.3 Operating Surface

The operating surface of a tire while off-road has just as much as an affect on the performance of a vehicle as the tire selected to be on the vehicle. The interface between the surface and the tire is what generates the forces required for propelling and steering a vehicle. If a typically well performing tire traverses soil which is not strong, it will not perform well at all. Significant sinkage and / or understeer could occur. As seen from the bevameter section of the results chapter, both operating surfaces tested were significantly

stiff, such that appreciable sinkage would not occur. This allows the rubber-soil interface to be isolated and studied further.

The first plot on operating surface effects is that of C_α versus normal load.

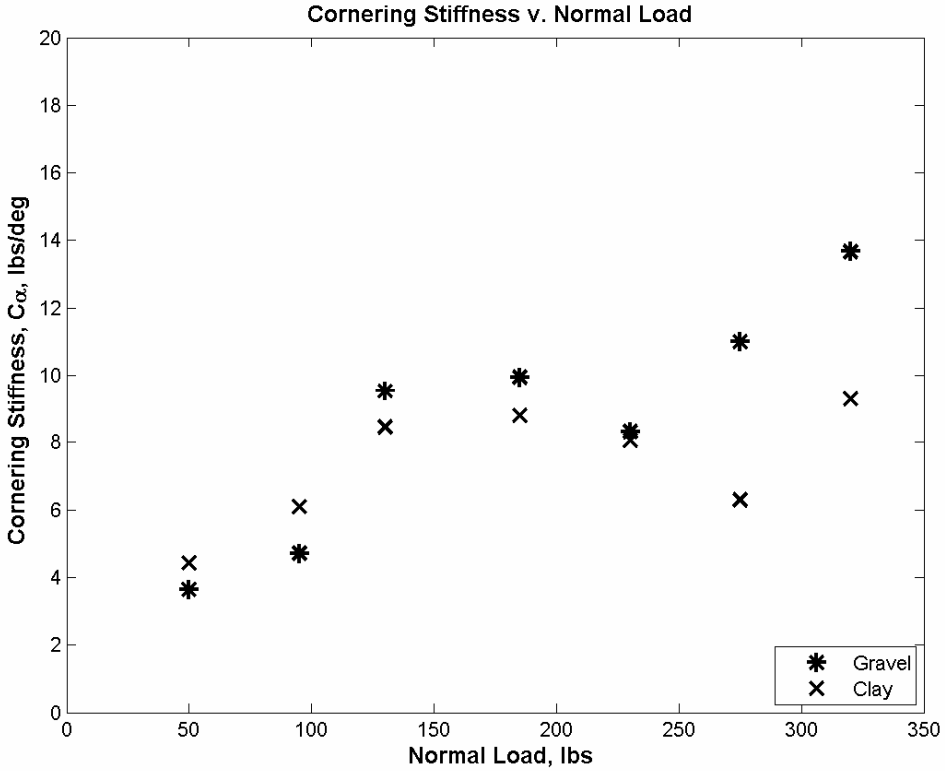

Figure 3.50 – Comparison of cornering stiffness v. normal load for different surfaces

One can observe good agreement up to about 275 lbf, and then the data diverges, yet retains the same slope at the higher normal loads.

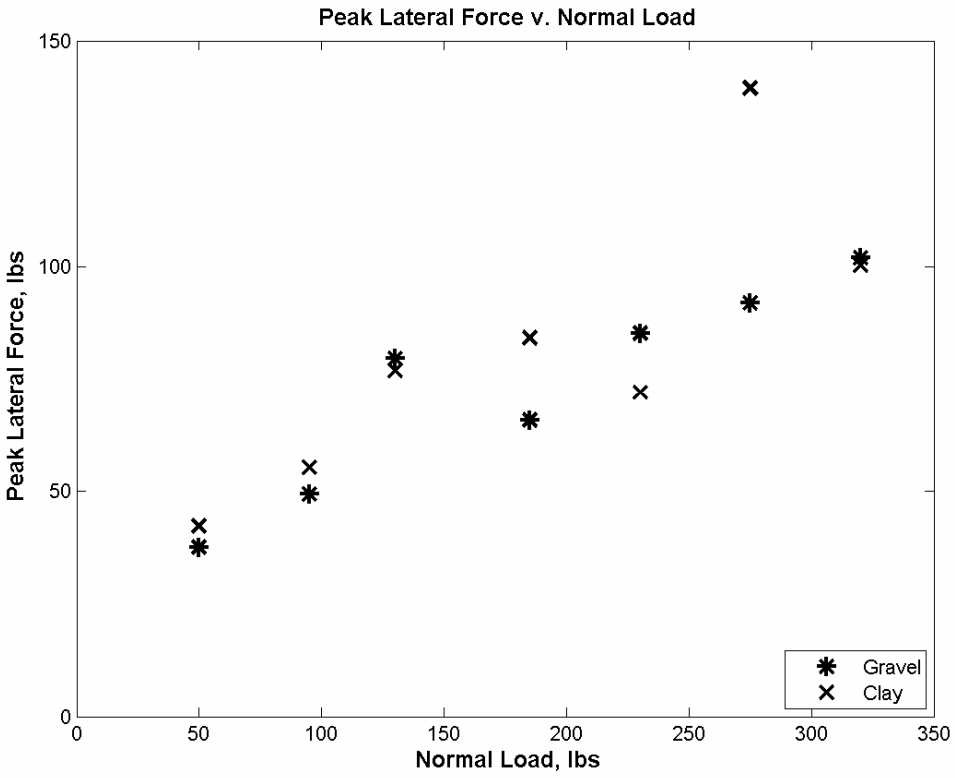

Figure 3.51 – Comparison of peak lateral force v. normal load for different surfaces

As with the previous plot, the peak lateral force of the tire between the two surfaces does not change much across the frictional and clay surfaces.

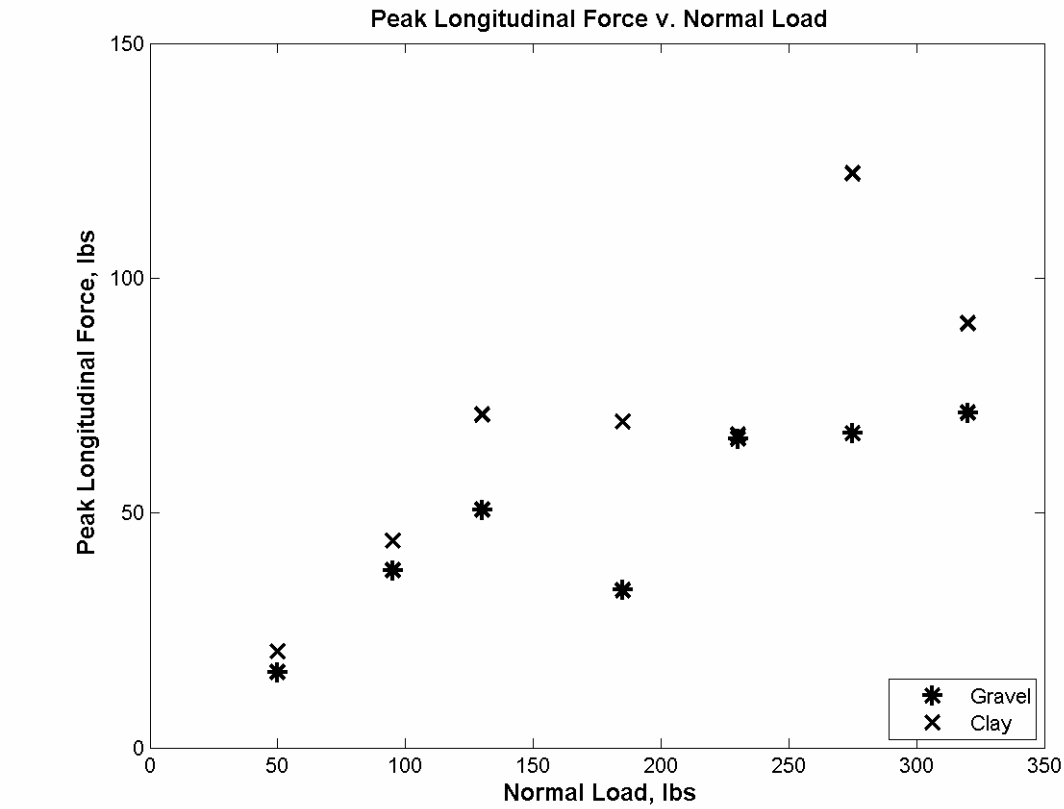

Figure 3.52 – Comparison of peak longitudinal forces v. normal load for different surfaces

This plot of peak longitudinal force shows more scatter after about 95 lbf of normal load.

The following family of plots tracks the lateral force coefficient for the range of normal loads while comparing between both clay and gravel surfaces.

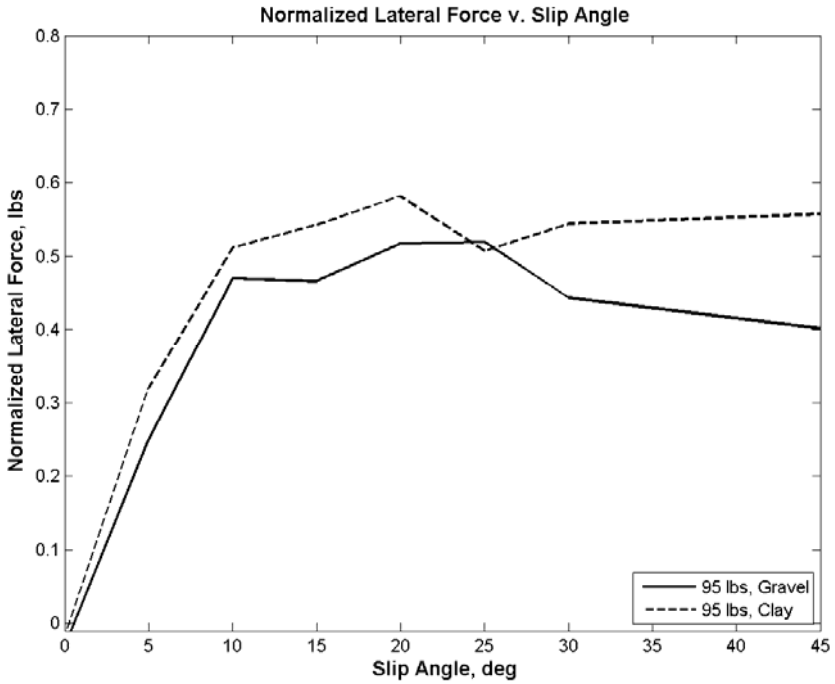

Figure 3.53 – Comparison of lateral forces on different surfaces at 95 lbf normal load

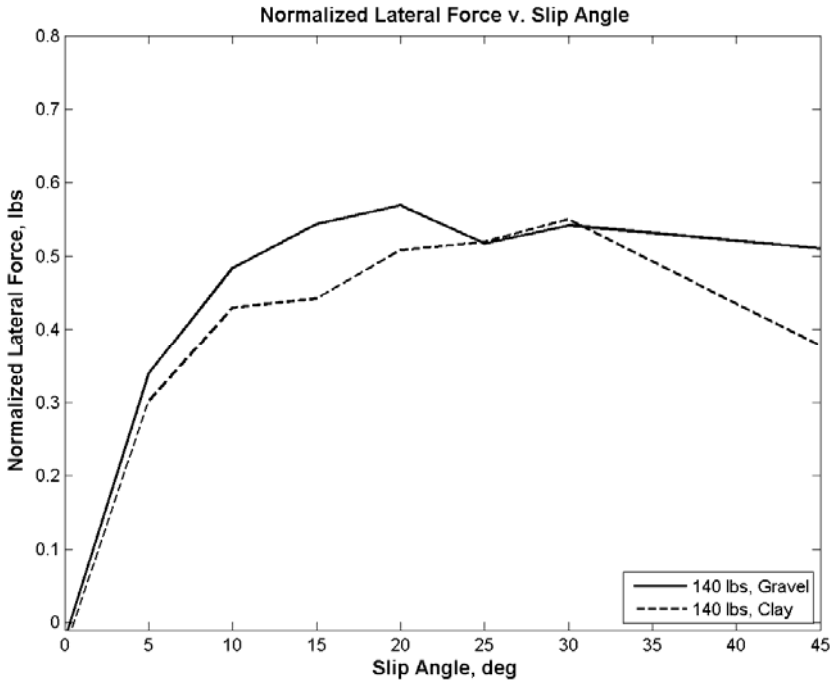

Figure 3.54 – Comparison of lateral forces on different surfaces at 140 lbf normal load

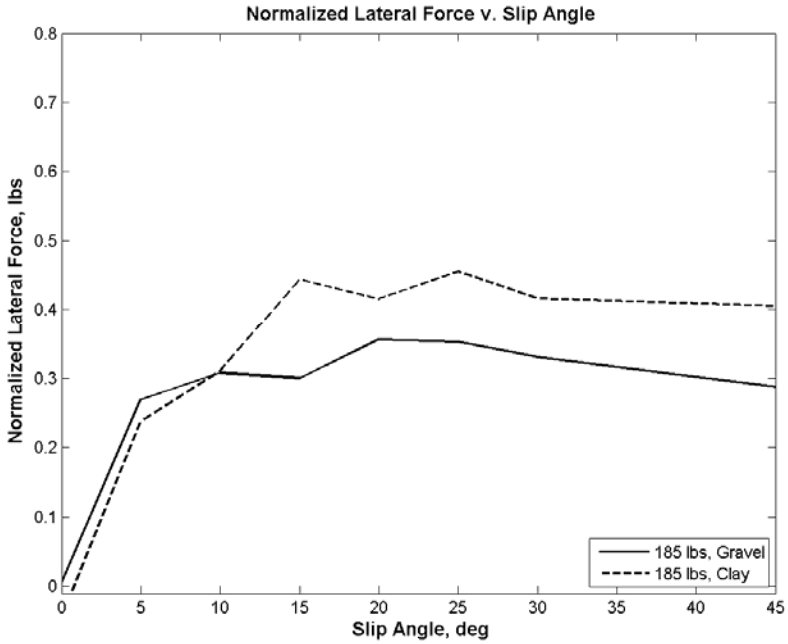

Figure 3.55 – Comparison of lateral forces on different surfaces at 185 lbf normal load

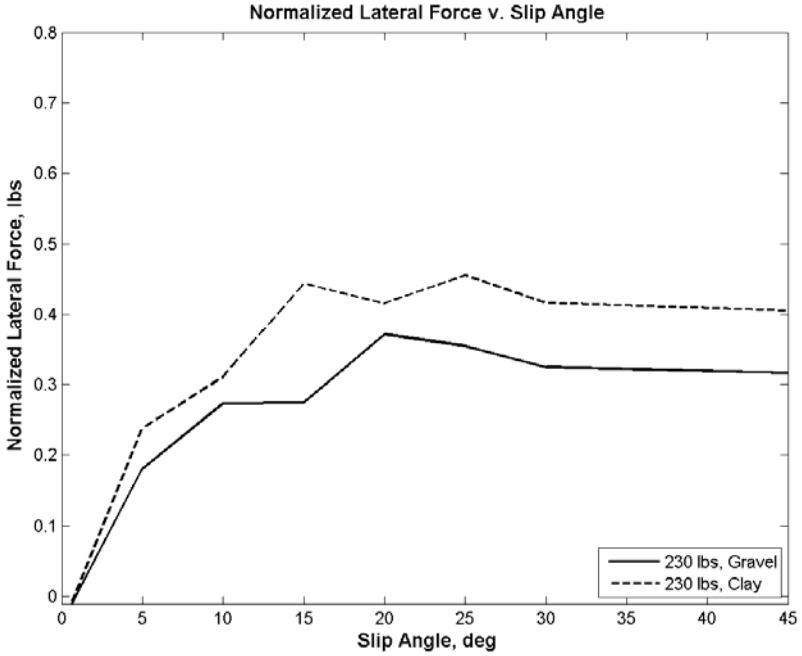

Figure 3.56 – Comparison of lateral forces on different surfaces at 230 lbf normal load

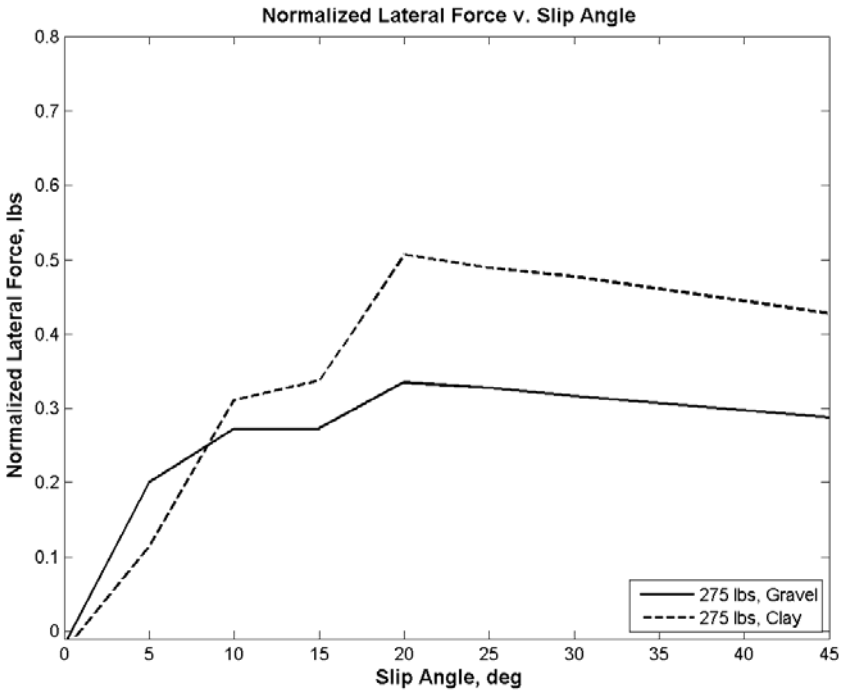

Figure 3.57 – Comparison of lateral forces on different surfaces at 275 lbf normal load

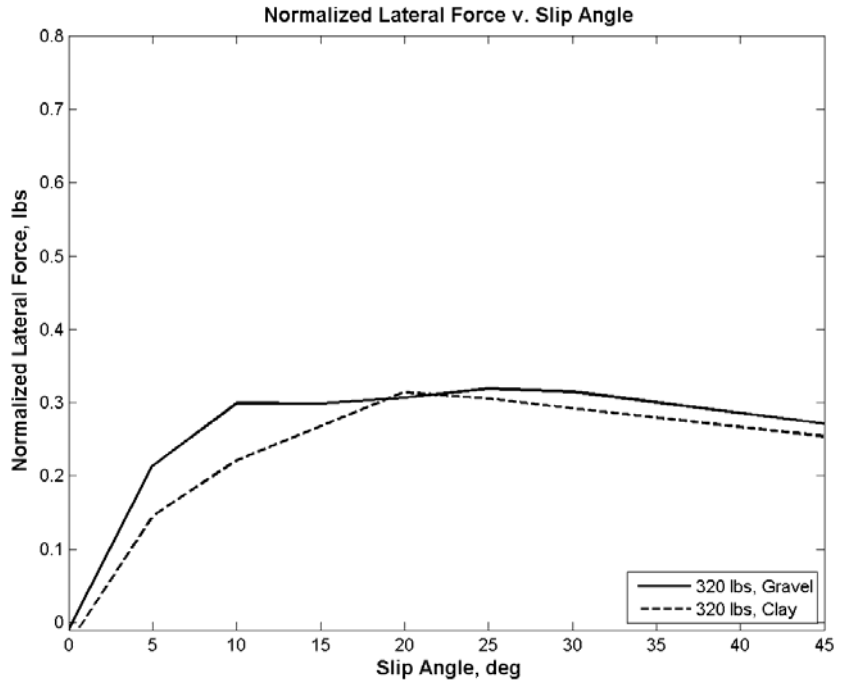

Figure 3.58 – Comparison of lateral forces on different surfaces at 320 lbf normal load

These plots confirm the findings of the cornering stiffness and peak lateral and longitudinal force plots. No appreciable difference between the surfaces could be seen. One may note again, the deterioration of cornering stiffness on the clay surface as higher normal loads are attainted. This might be explained by the top layer of the soil being crushed slightly, and adding to the fine dust on top of the clay surface. This barrier between the structurally sound soil and the tire might delay the tire from building up force as fast as would be done on gravel.

3.4 Exponential Tire Model

As data have been collected on the strength of soils for vehicular travel, and tire data collected from the towed test rig, the influence of the two can be tied together by fitting curves to the tire data with the exponential model. Then, the coefficients of the model can then be compared to the soil properties to see how the coefficients are affected. Recall the exponential tire model form as described in Equation 3.3.

$$F_y = F_z A(1 - \exp(-B\alpha)) \tag{3.3}$$

Curve fitting the exponential tire model to the data generated by the towed test rig is done by maximizing the R-squared value of a particular fit. An array of possible values for the A and B coefficients of the tire model are generated. Possible situations for A and B values are run through the exponential tire model. For each pass, an R-squared value is calculated and stored with an index. The highest R-squared value is selected, and the associated index is used to retrieve the A and B values for that particular fit. While not computationally efficient, the speeds of modern computers and the low volume of data processing do not hinder the process of data reduction.

One interesting thing to note is that for every single run through checking for the best R-squared value, the values for *A* and *B* came out to be exactly the same. The cause of this phenomenon is unknown, and may be the basis of a further study. Subsequent plots will illustrate this phenomenon.

The following plots (Figure 3.59, 3.60) are representative of those found for each run on a particular slip angle, normal load, surface, camber, and inflation pressure.

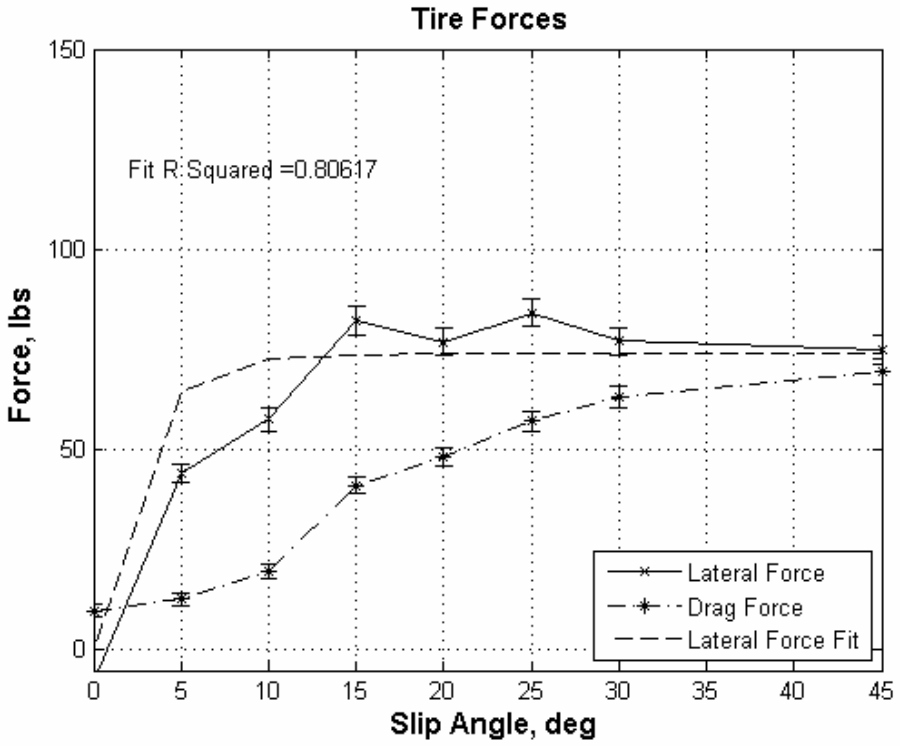

Figure 3.59 – Example of exponential model fit to data on Clay, at 10 psi, low camber, and 185 lbf normal load

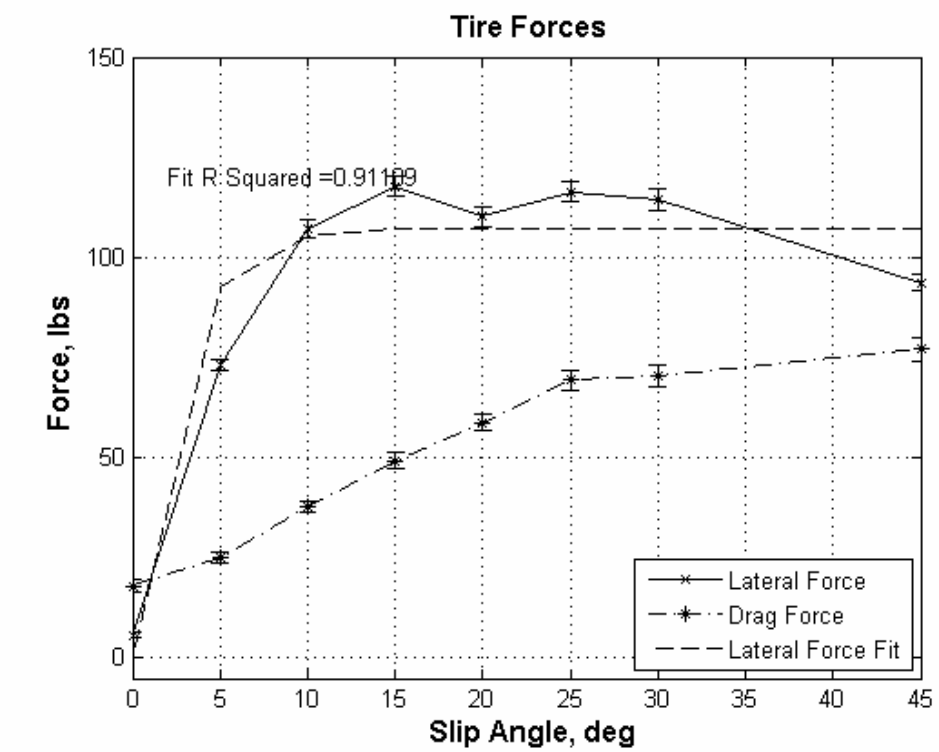

Figure 3.60 – Example of exponential fit for tire data on gravel, 5 psi, high camber, 275 lbf normal load

An inspection of the plots will show a fit curve by a purely dashed line. The R-squared value is listed directly in Figure 3.60. Error bars calculated from the standard error of the mean are found at each data point for lateral and longitudinal data. Dozens of tests like these were run, and the associated *A* and *B* coefficients calculated.

As mentioned previously, the plots for finding the best R-squared value are shown in Figures 3.60 and 3.61. Note that the index that the x-axis is referring to is that within the array which stores thousands of combinations of *A* and *B* values for fitting to the data. Many plots assume the shape of Figure 3.60, while the few instances of low R-squared values take on the shape of Figure 3.61.

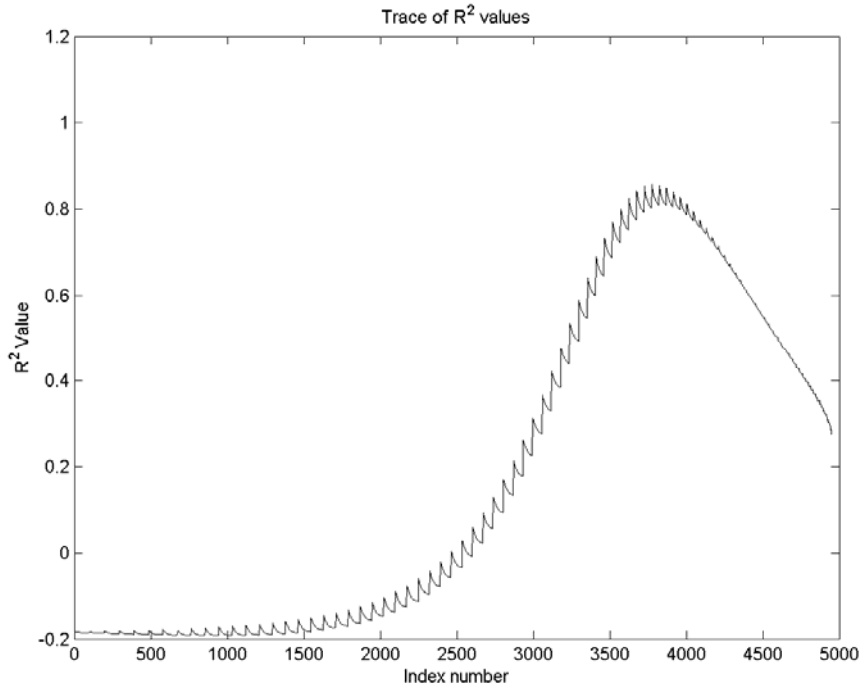

Figure 3.61 – Trace of R-squared values for data on gravel, 5 psi, high camber, 275 lbf normal load, High R^2 value

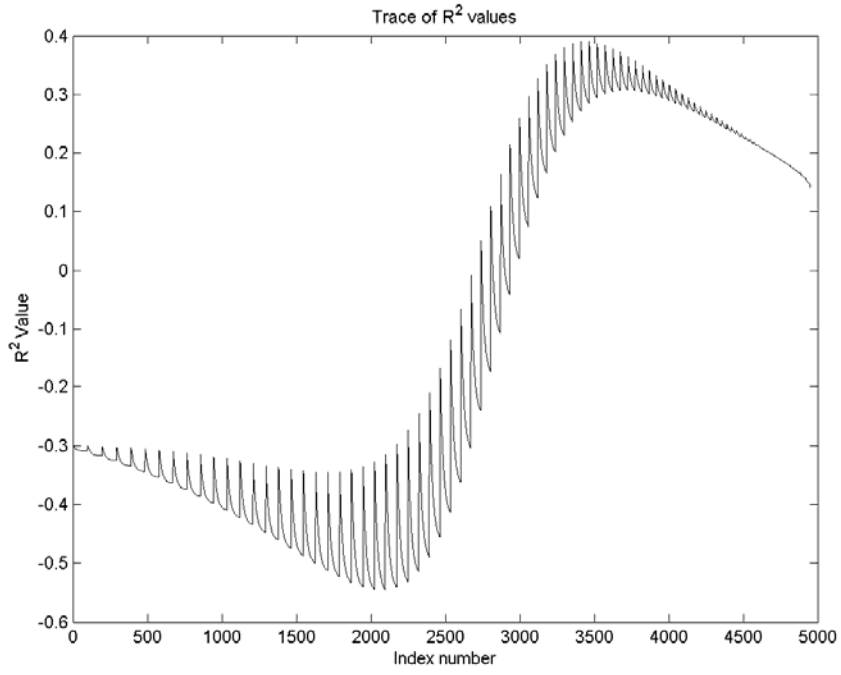

Figure 3.62 – Trace of R-squared values for data on clay, 10 psi, low camber, 90 lbf normal load. Low R^2 value

The key data, however, for this section is that of the *A* and *B* values versus normal loads. The shape of these curves confirms Metz's suggestion that the *B* coefficient should be exponential in nature when comparing to normal loads. Note, values of *A* and *B* of zero indicate the lack of computable data due to corrupt data.

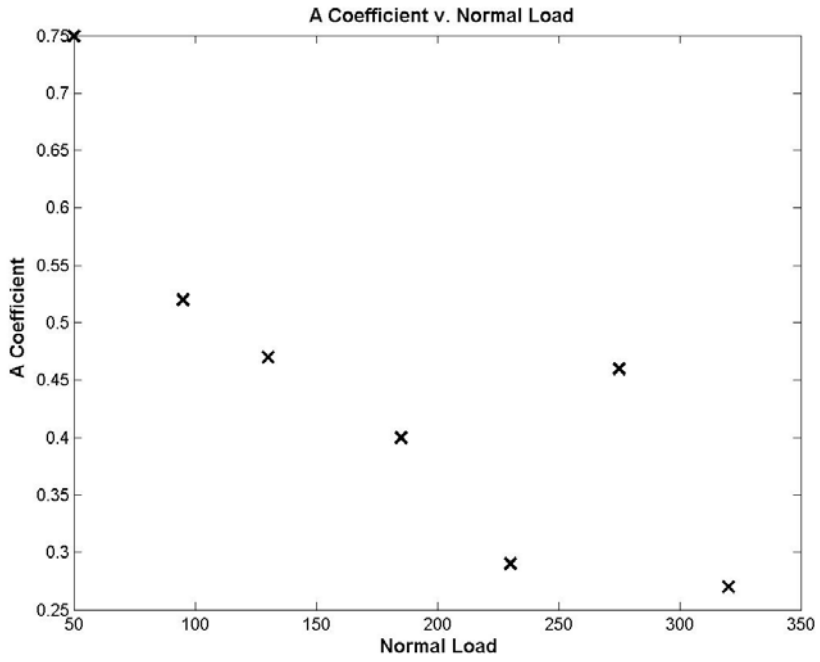

Figure 3.63 – A Coefficient plot v. normal load for clay, 10 psi, low camber

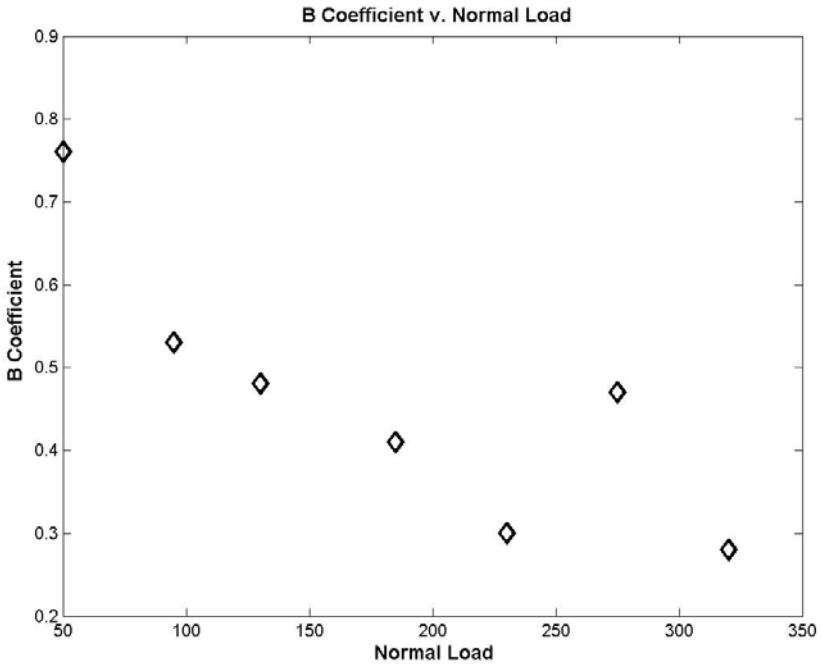

Figure 3.64 – B Coefficient plot v. normal load for clay, 10 psi, low camber

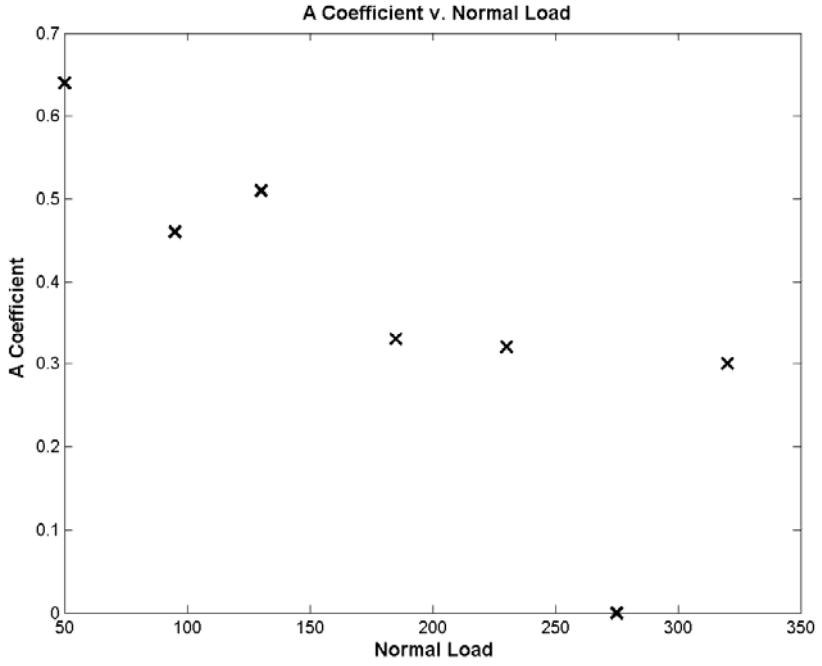

Figure 3.65 – A coefficient v. normal load for gravel, 10 psi, low camber

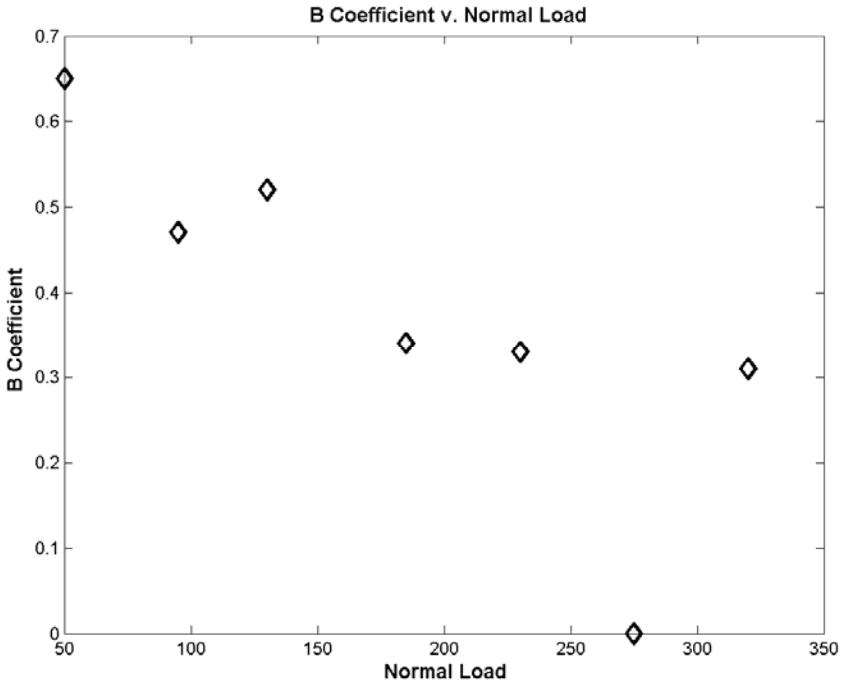

Figure 3.66 – B coefficient v. normal load for gravel, 10 psi, low camber

A careful look at these graphs for the gravel and clay surfaces will see the *A* and *B* coefficients converge to around 0.3 for higher normal loads.

Noting that the data for *A* and *B* coefficients (which have been found to be identical, *A=B*), fall off and assume a relatively constant value with increasing normal load, one can begin to apply curve fits to this data to uncover the relationship between model coefficient and normal load. After experimenting with various curve fits, the following equation provided the most appropriate fits.

$$A = B = cF_z^{\,m} \tag{3.2}$$

This Equation 3.2 was applied to fit the data for *A* and *B* coefficients that were presented in Figures 3.64 and 3.65. Very good agreement was reached with R-squared values ranging from 0.72 to 0.97.

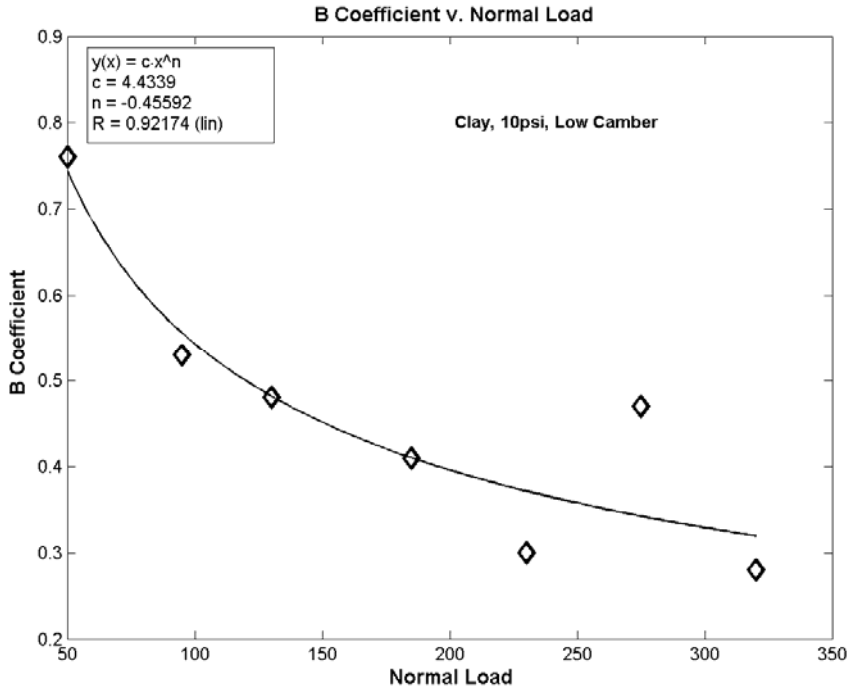

Figure 3.67 – Curve fit to B coefficient data for Clay, 10 psi, low camber

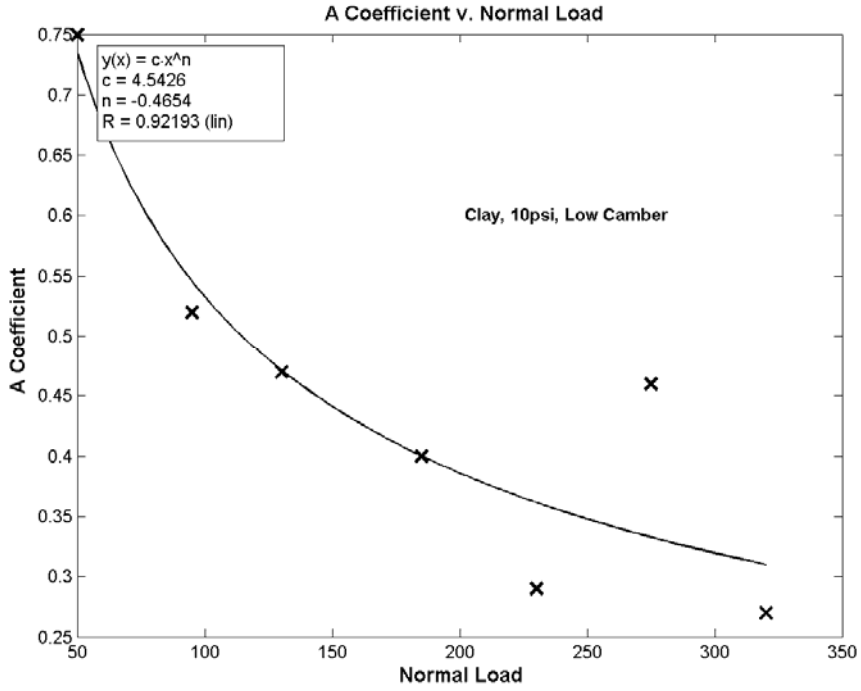

Figure 3.68 – Curve fit to A coefficient data for Clay, 10 psi, low camber

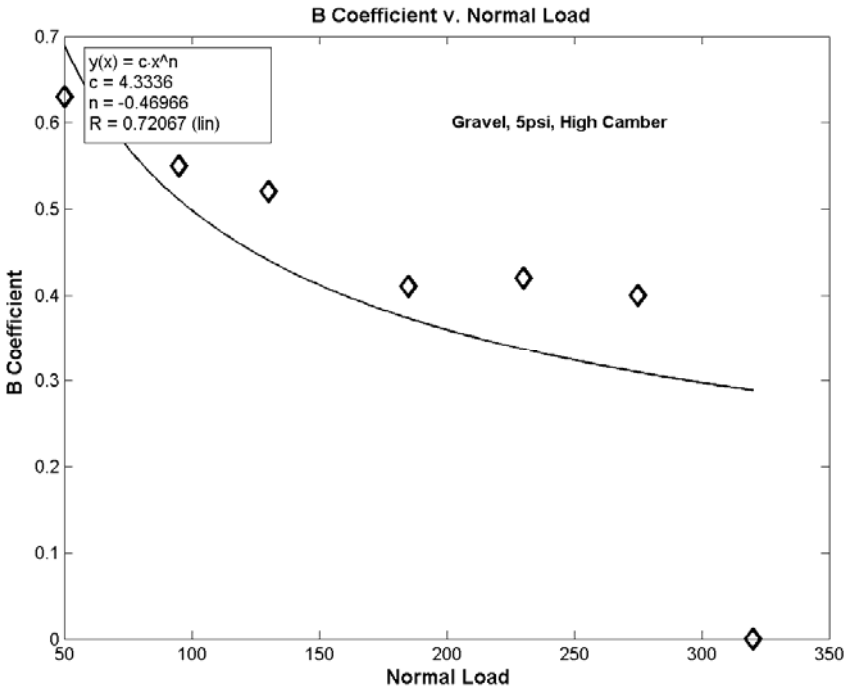

Figure 3.69 – Curve fit to B coefficient data for Gravel, 5 psi, high camber

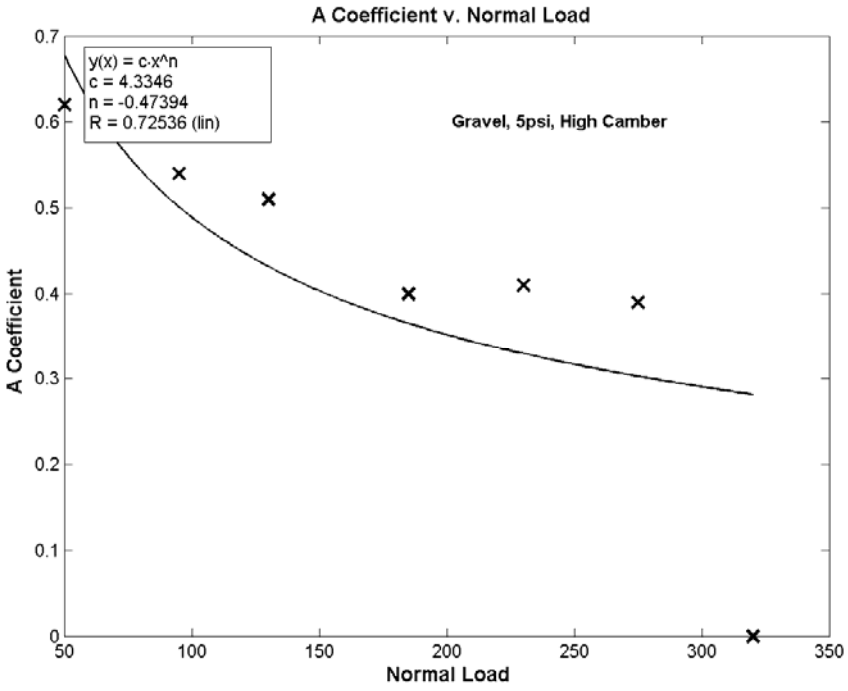

Figure 3.70 – Curve fit to A coefficient data for Gravel, 5 psi, high camber

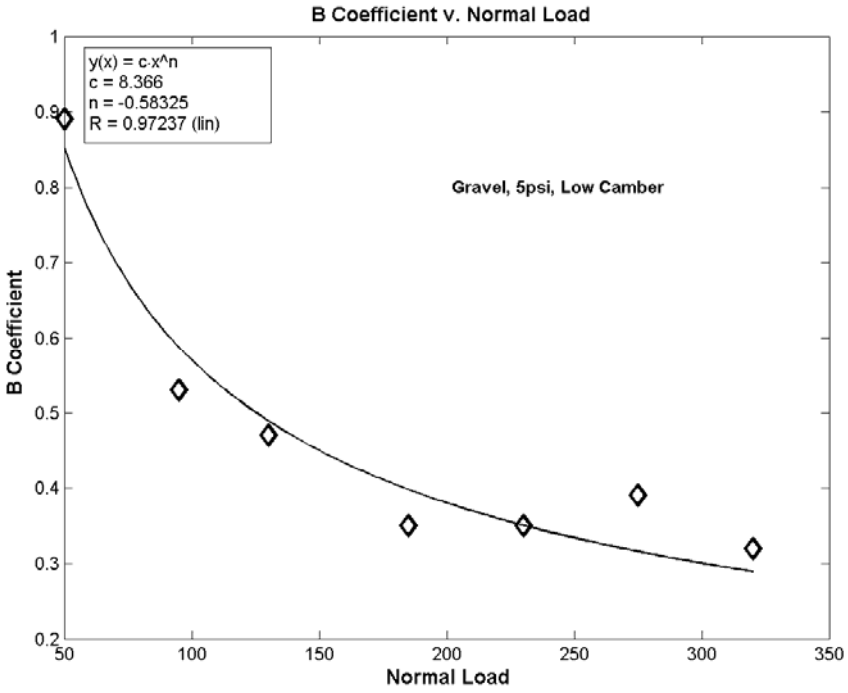

Figure 3.71 – Curve fit to B coefficient data for Gravel, 5 psi, low camber

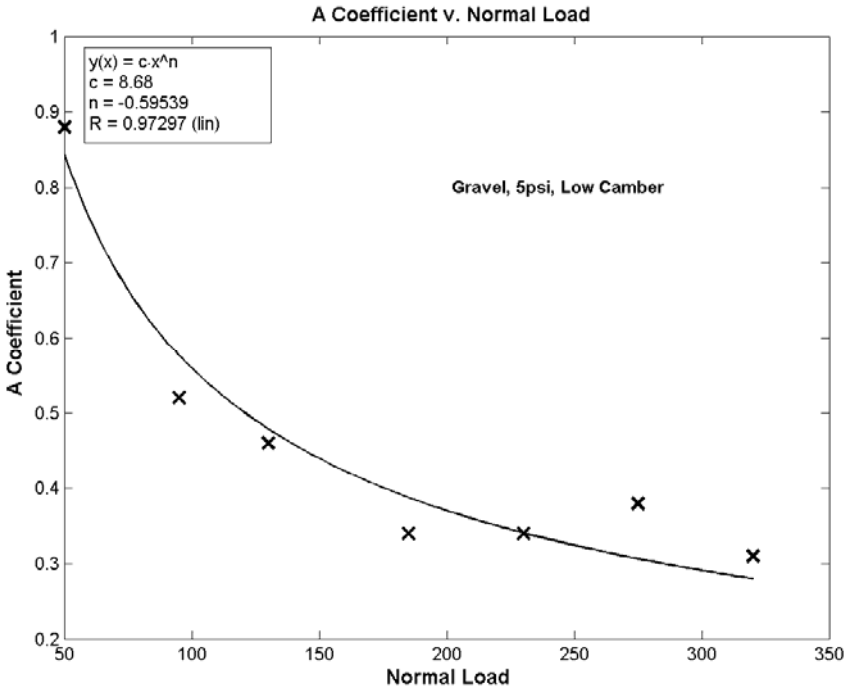

Figure 3.72 – Curve fit to A coefficient data for Gravel, 5 psi, low camber

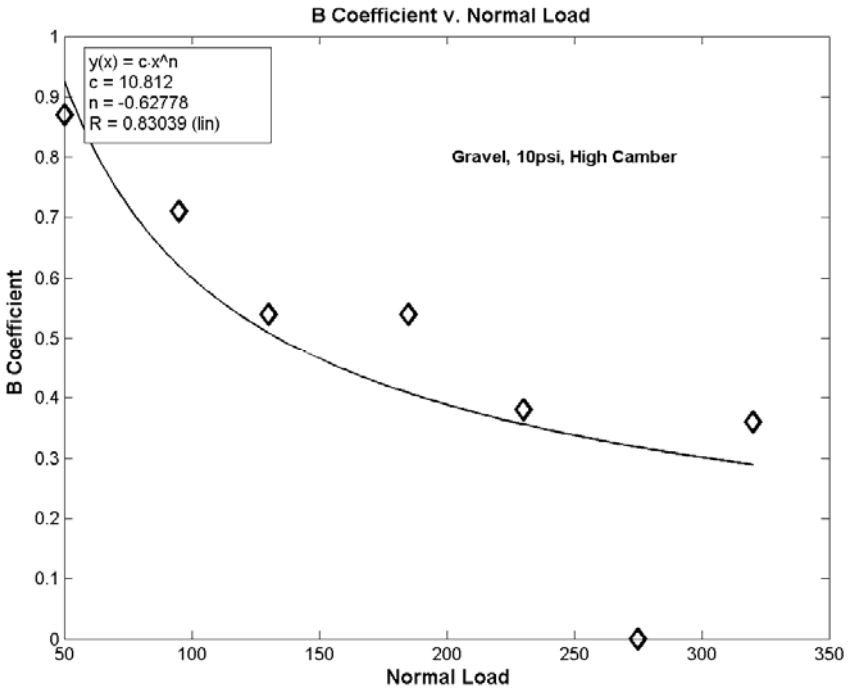

Figure 3.73 – Curve fit to B coefficient for Gravel, 10 psi, high camber

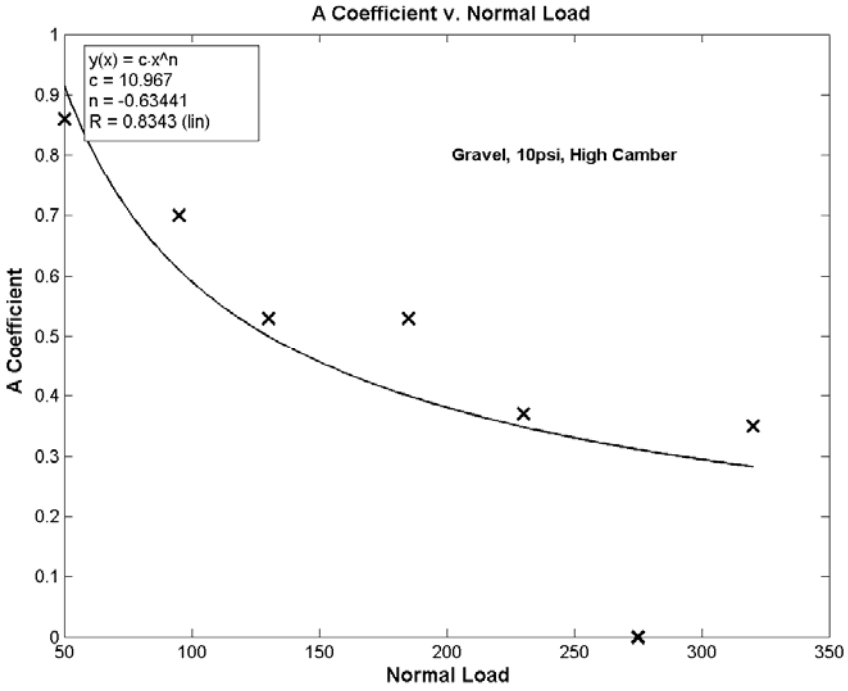

Figure 3.74 – Curve fit to A coefficient for Gravel, 10 psi, high camber

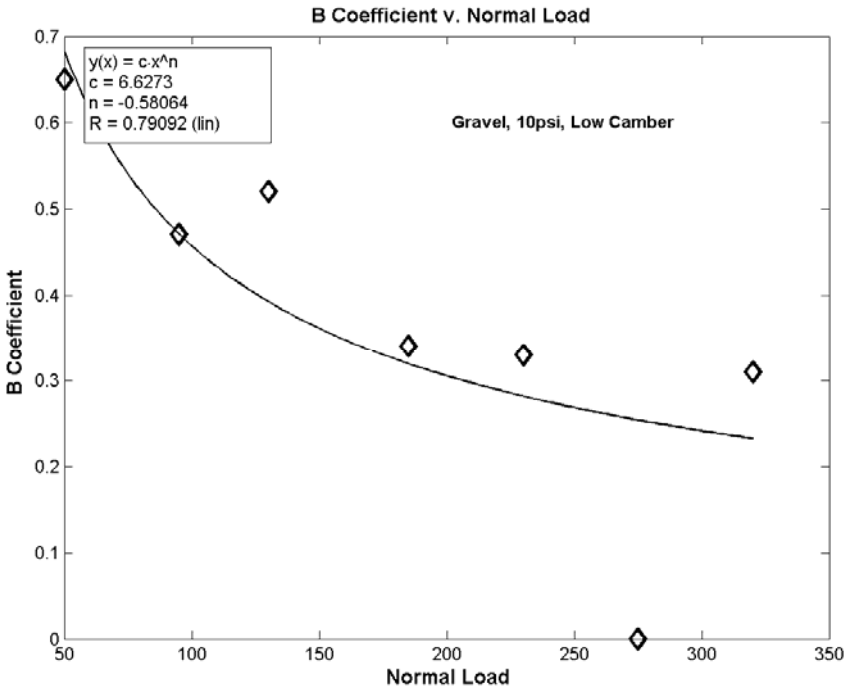

Figure 3.75 – Curve fit to B coefficient data for Gravel, 10 psi, low camber

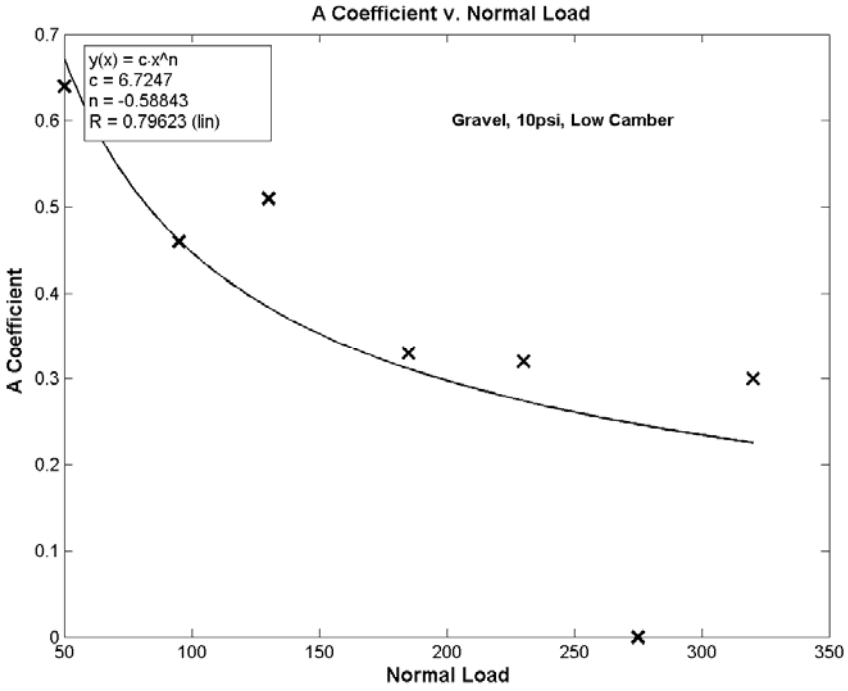

Figure 3.76 – Curve fit to A coefficient data for Gravel, 10 psi, low camber

Tabulated data for the coefficients shown in Figures 3.67 – 3.77 can be seen in Table 3.2. The values, *m*, and *C* are those which belong to Equation 3.2

Setup	For Model Coefficient	*m*	*C*	R^2
Clay, 10psi, Low Camber	B	-0.45	4.439	0.92
	A	-0.465	4.542	0.92
Gravel, 10psi, Low Camber	B	-0.58	6.627	0.79
	A	-0.58	6.727	0.80
Gravel, 10psi, High Camber	B	-0.627	10.812	0.83
	A	-0.634	10.967	0.83
Gravel, 5psi, Low Camber	B	-0.583	8.366	0.97
	A	-0.595	8.68	0.97
Gravel, 5psi, High Camber	B	-0.469	4.333	0.72
	A	-0.473	4.334	0.75

Table 3.6 – Exponential Tire Model Coefficient curve fit data

A quick glance at Table 3.2 will reveal *m*-values between 0.4 and 0.7. *C*-values spanned a range of 4.33 to 10.96. One may note that only one clay run is available on Table 3.6. In order to make the test matrix more digestible, the camber and pressure changes were evaluated on the gravel surface. This would save from having to make 252 extra runs.

Modification of the exponential tire model by Crolla [15] to accept the capability to change *A* and *B* values for changing normal loads would look like that of Equation 3.3.

$$F_y = F_z(CF_z{}^m)(1 - e^{-(CF_z{}^m)\alpha}) \tag{3.3}$$

To check Equation 3.3 and thus the effectiveness of the curve fits to *A* and *B* coefficient data, situations involving camber change, pressure change, and surface change are checked.

As shown in Figure 3.42, small additions of camber will result in a small increase in the amount of lateral force available. Changes in pressure between 5 and 10 psi do not seem to make noticeable changes as evidenced by the data in Figure 3.33. Surface changes in Figure 3.51 do not make an appreciable difference in lateral force either. The following figures depict how the tire model described by Equation 3.3 recognizes the differences between camber, surface, and inflation pressure.

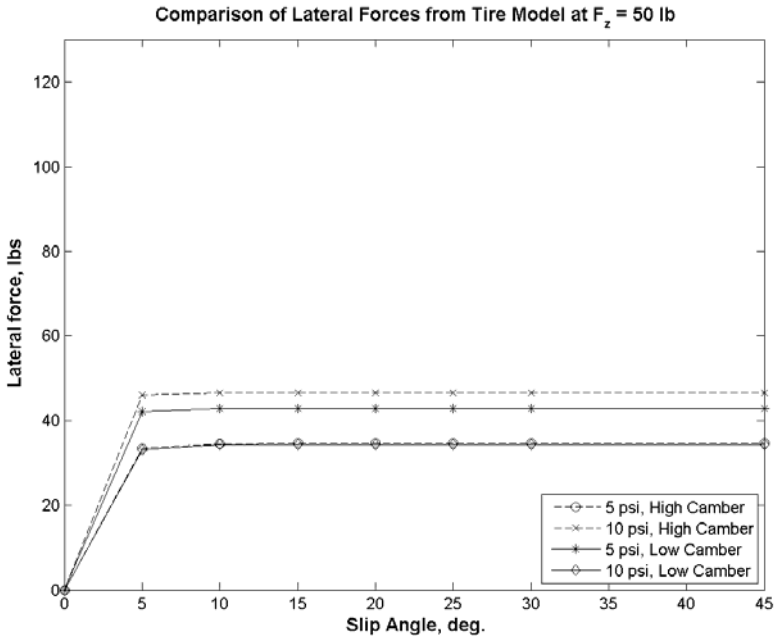

Figure 3.77 – Comparison of camber and pressure with Eq. 3.3 on gravel at 50 lbf

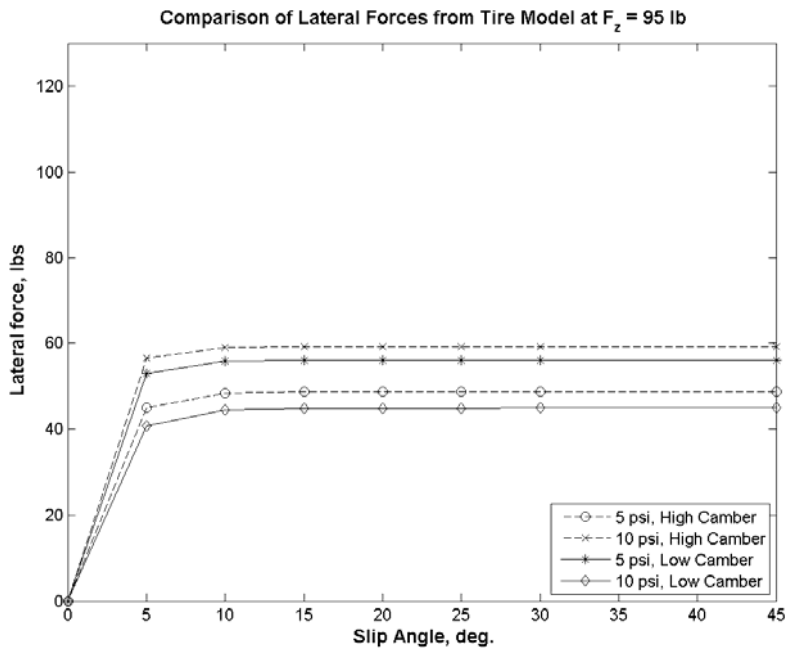

Figure 3.78 – Comparison of camber and pressure with Eq. 3.3 on gravel at 95 lbf

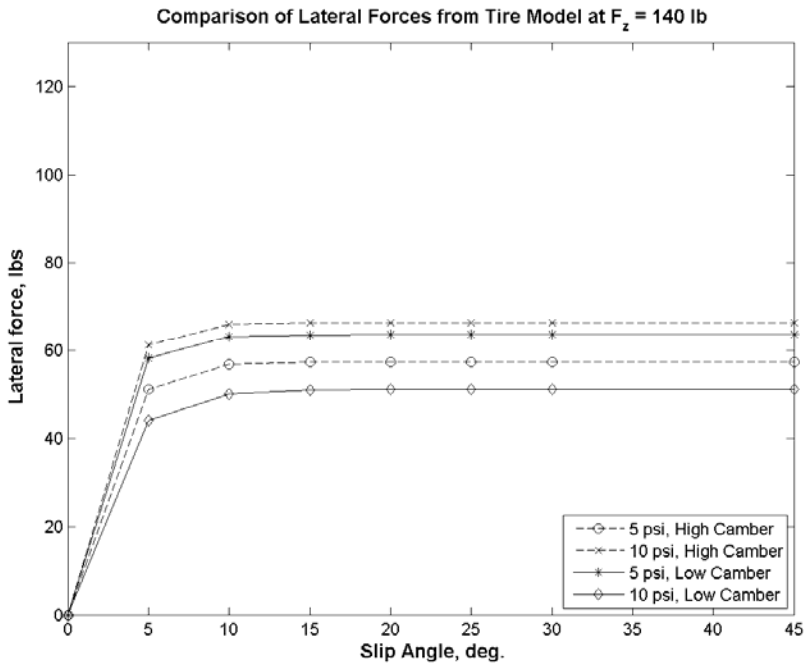

Figure 3.79 – Comparison of camber and pressure with Eq. 3.3 on gravel at 140 lbf

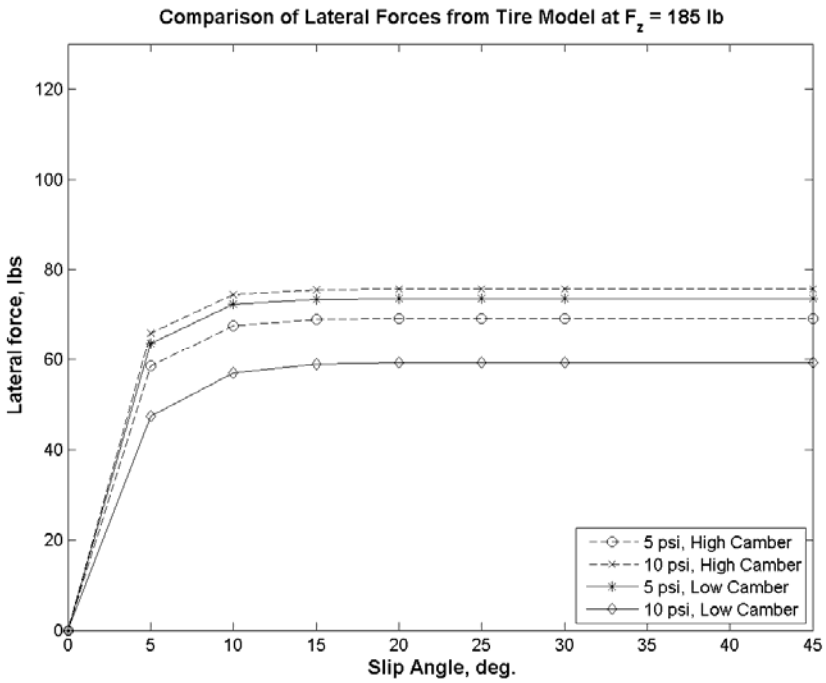

Figure 3.80 - Comparison of camber and pressure with Eq. 3.3 on gravel at 185 lbf

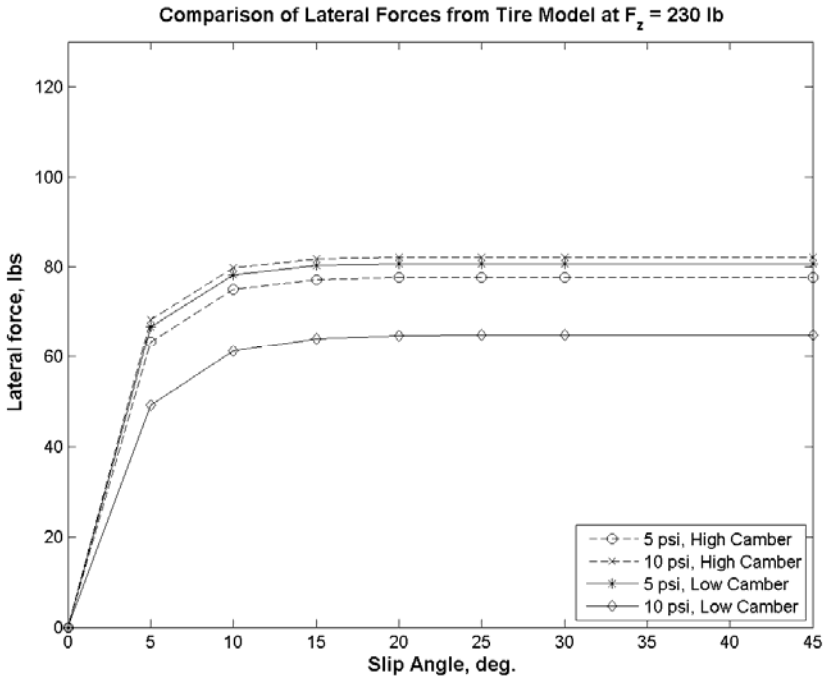

Figure 3.81 - Comparison of camber and pressure with Eq. 3.3 on gravel at 230 lbf

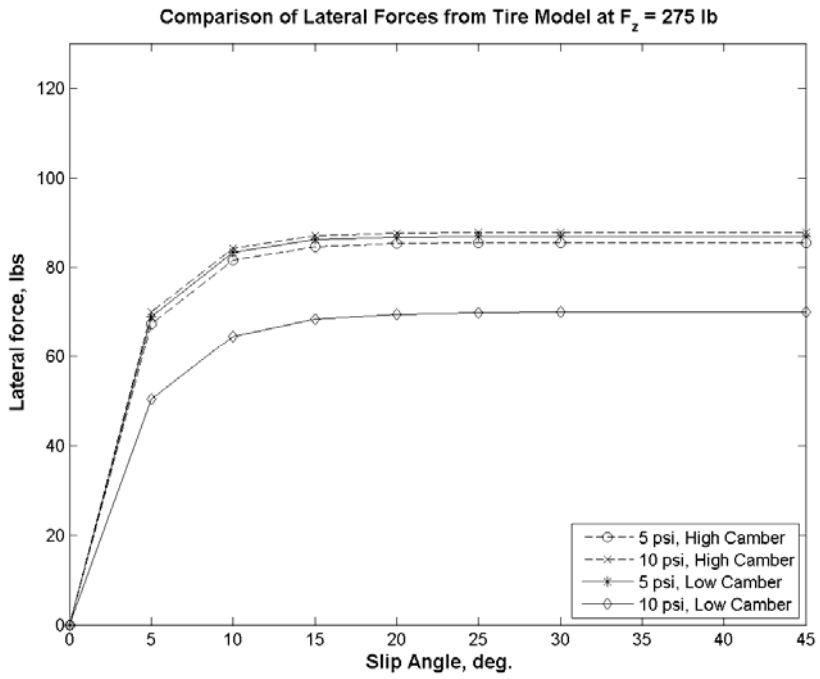

Figure 3.82 - Comparison of camber and pressure with Eq. 3.3 on gravel at 275 lbf

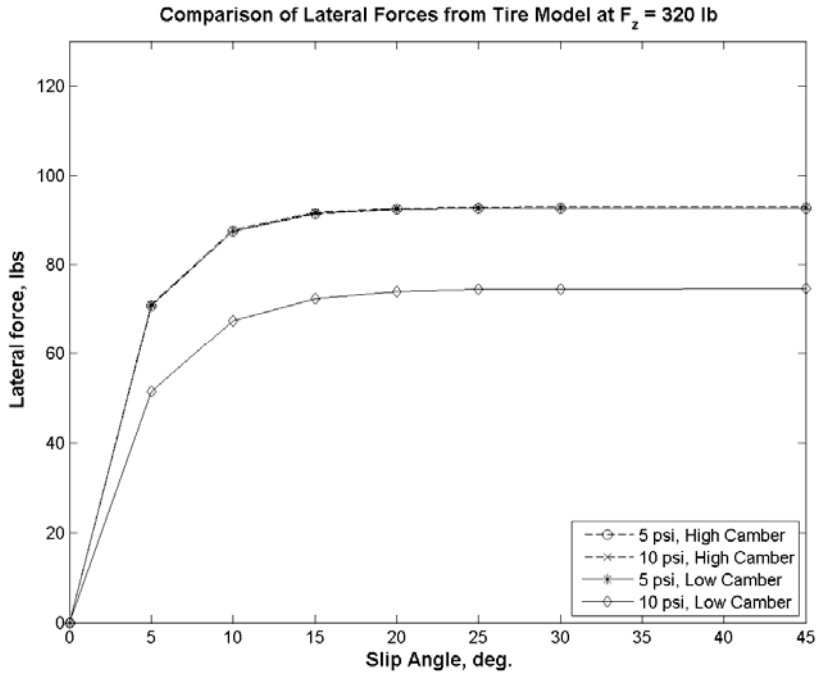

Figure 3.83 - Comparison of camber and pressure with Eq. 3.3 on gravel at 320 lbf

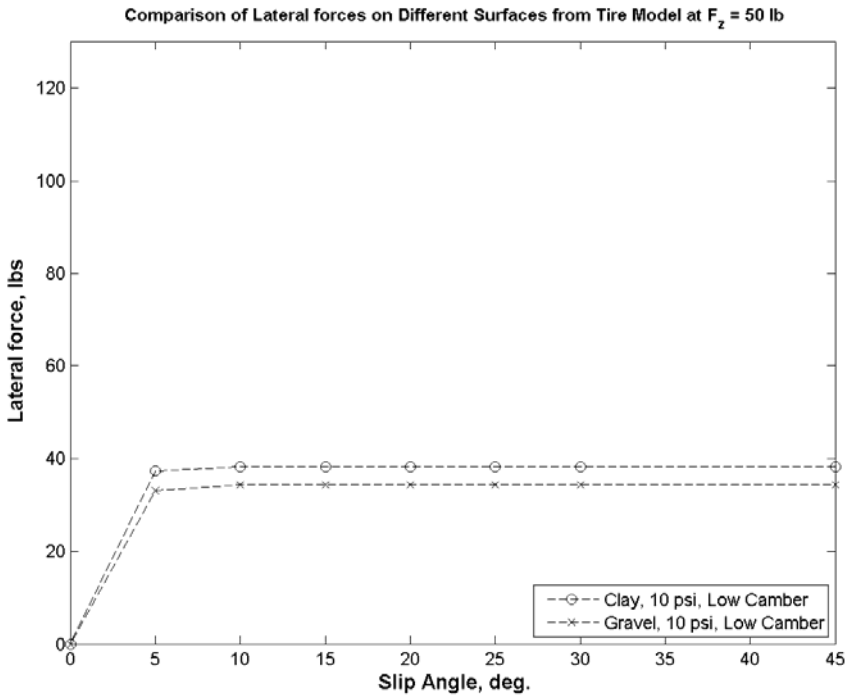

Figure 3.84 -Comparison of surface with Eq. 3.3 at 50 lbf

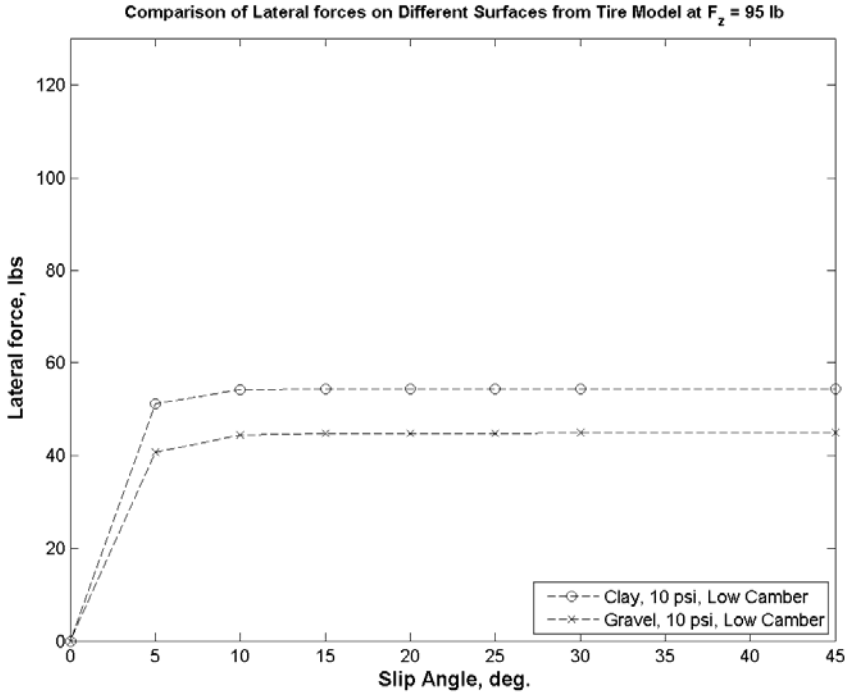

Figure 3.85 - Comparison of surface with Eq. 3.3 at 95 lbf

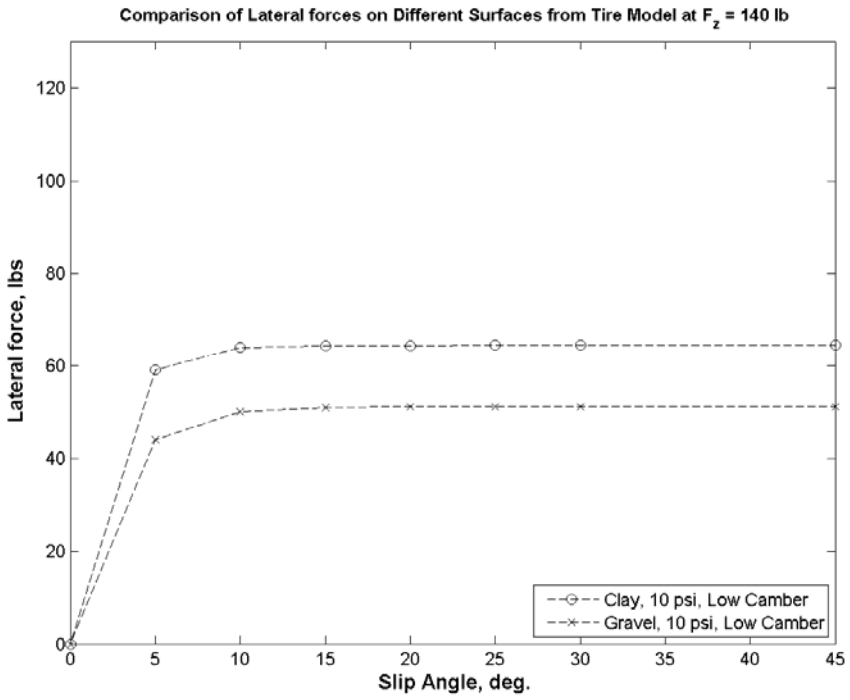

Figure 3.86 - Comparison of surface with Eq. 3.3 at 140 lbf

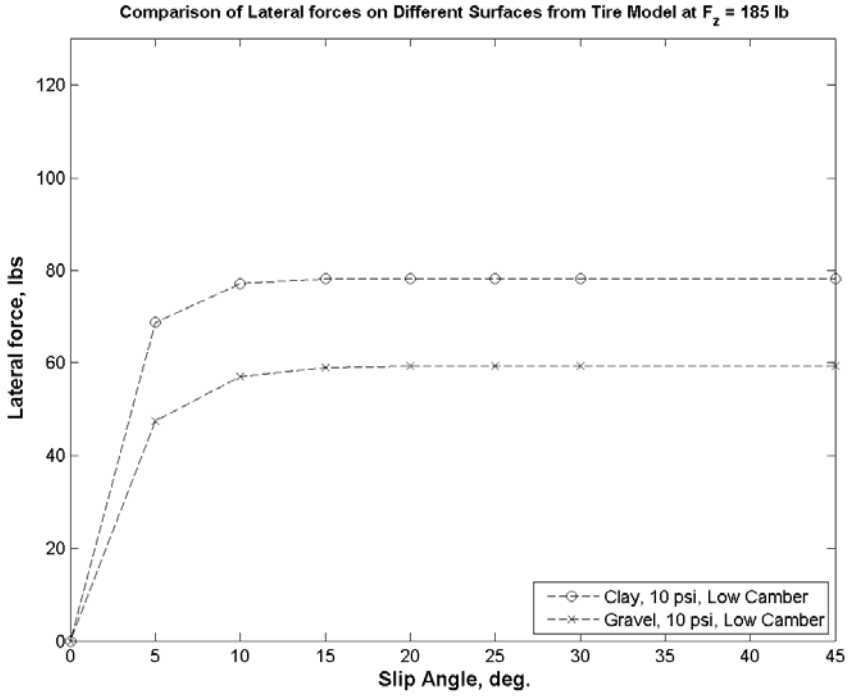

Figure 3.87 – Comparison of surface with Eq. 3.3 at 185 lbf

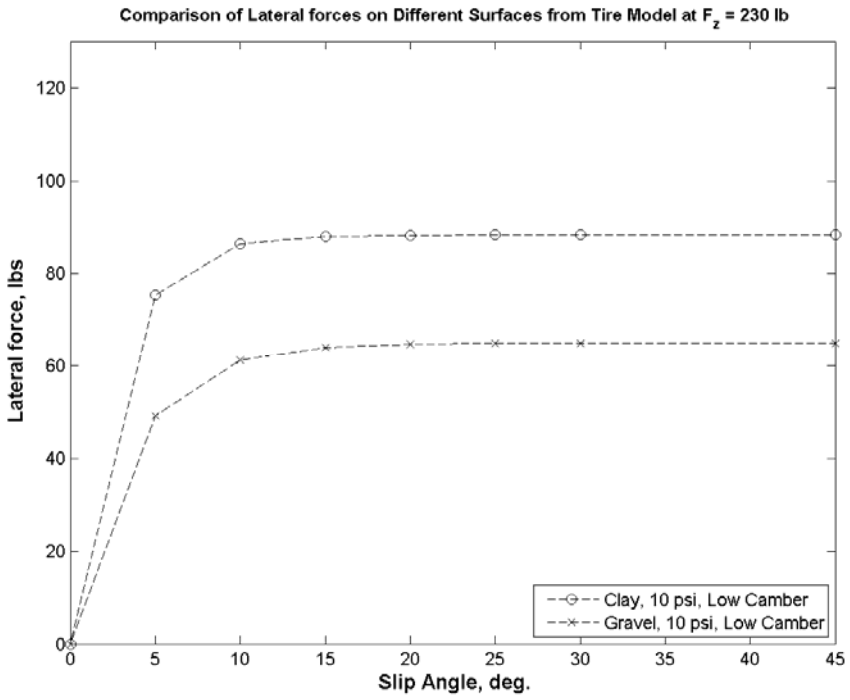

Figure 3.88 - Comparison of surface with Eq. 3.3 at 230 lbf

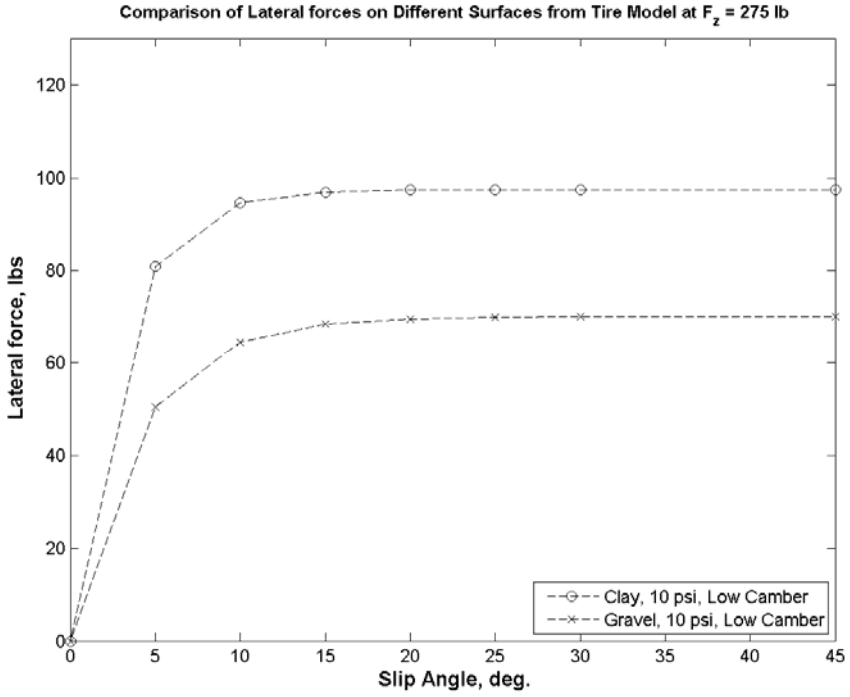

Figure 3.89 - Comparison of surface with Eq. 3.3 at 275 lbf

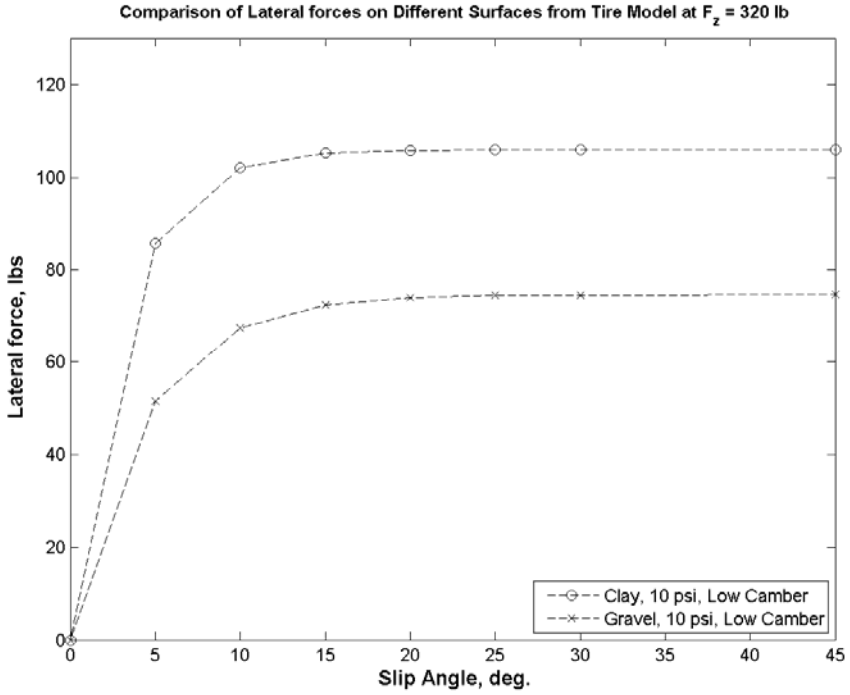

Figure 3.90 – Comparison of surface with Eq. 3.3 at 320 lbf

The clay and gravel surfaces in this study are again defined as having the properties in Table 3.7

	Clay (Cohesive Surface)	Gravel (Frictional Surface)
Sinkage exponent, n	2.89	6.08
Frictional sinkage coefficient, k_φ	39.33 lb/in^{n+2}	44.67 lb/in^{n+2}
Cohesive sinkage coefficient, k_c	14 lb/in^{n+1}	0 lb/in^{n+1}
Average friction angle, φ	6.13 deg.	10.68 deg.
Average cohesion, c	4.8 lb/in^2	0 lb/in^2
Soil-rubber shear modulus, k,	0.05 in.	0.06 in.

Table 3.7– Table of normal and shear properties for clay and gravel surfaces tested

Analysis of Figures 3.77 through 3.90, and Table 3.7 will show the following for the KT 821 tire:

1. At higher normal loads, cohesive surfaces will hold higher lateral loads than frictional soils.
2. At 10 psi, increasing the normal load on an uncambered tire will not generate as much as a cambered tire at the same pressure, or a tire at 5 psi, at high or low camber.
3. Camber effects are more significant at lower normal loads.
4. As inflation pressure increases, the addition of camber is advantageous in order to develop more lateral force.

5. A small difference in available lateral force is noticeable between 5 psi and 10 psi at low normal loads.
6. Dry frictional soils will produce less lateral force for increasing loads than a dry cohesive soil.
7. Soils with higher friction angles will produce less lateral force at increasing normal loads than a dry cohesive soil
8. Dry soils with elevated cohesion values will produce more lateral force than a dry soil with less cohesion
9. Shear deformation modulus seems to not be dependent on the type of surface (frictional or cohesive) but perhaps on the water content of the soil, where the build up of pore water pressure fails the surface faster than a soil which does not have any pore water pressure.
10. Normal load properties do not seem to have an effect on traction when the soil is very stiff. Had the soils been less stiff, the lugs of the tire would be able to penetrate and use the edges of the lugs for an extra bearing surface for generating more lateral traction.

These observations all make sense when considering the behavior of tires in general when working in concert with the mechanics of the soil-rubber interface. For the difference between surface effects, imagine a cylinder of gravel, with forces being applied to the top and bottom of the cylinder. What holds this gravel in a cylindrical shape? Since there are no molecular bonds between the stones, something must confine the gravel on the sides, as it is being loaded from the top and bottom. On a gravel surface, there is no confining stress, so the stones are free to shift laterally under the tire. At

higher normal loads, more gravel is forced out and away from the contact patch as these higher loads are increasing only in the vertical direction, and not the directions to confine the movement of the stones.

When increasing inflation pressure, especially on stiff surfaces, this can reduce the contact area that the tire has with the surface. A reduction in contact area will result in a reduced ability to generate lateral forces. Essentially, the setup tries to make less material to do more work, which it cannot do. Increasing negative camber on a tire will add to the amount of lateral force available, and counter the effects of a high tire pressure, as evidenced in Figure 3.82.

Significant amounts of data have been presented in the results chapter. Bevameter data for measuring the soil showed that the gravel (frictional) and cohesive (clay) exhibited trends that are expected to be found in those types of soil. Tire data from the tire rig provided insight into the noisy world of off-road testing. However, acceptable data could be generated, and thus verified the acceptance of the exponential tire model. Upon curve fitting with the exponential model, it was found that for the best fit, both model coefficients turned out to be the same value. Collecting this data for each run showed a consistent trend of the coefficients from test to test. The coefficients of the curve fit were then used to modify a tire model, which generated results that mimicked the expected behavior of tires on off-road surfaces, as evidenced by other researchers, and the data collected by this study.

CHAPTER 4

CONCLUSIONS AND SUGGESTIONS FOR FUTURE RESEARCH

Substantial amounts of data have been presented in the results chapter. Bevameter data describes the soil-rubber shearing behavior, and the vertical stiffness of the terrain. Tire rig data shows the lateral and longitudinal force data for a steered tire in various configurations. Finally the exponential tire model was fit to the data generated by the tire rig. Changes in the model coefficients versus changes in the tire configuration were recorded and analyzed. The data presented is of use to vehicle designers who employ ATV tires in their vehicle designs.

The bevameter data collected for this study matched trends found from other researchers. Shear behavior matched that of [3] and [30]. Normal loading trends were similar in the way of increasing sinkage for increasing pressure; however the soils tested in this work were substantially stiffer than the soils used for the works of [3] and [30].

The tire test rig generated acceptable data amidst the long and difficult process of collection. Tire data for the KT 821 tire used in this study showed behavior consistent with [19], [20], and especially [25] where ATV tires were specifically studied.

The use of the exponential tire model, chosen as the soil reacts in an exponential fashion, fit the tire data generated by the tire test rig with good results. Least squares methods were used to determine the best fit, and then the model coefficients were recorded. This was repeated for all various combinations of inflation pressure, nominal

camber angle, and surface. A note of interest is that the two coefficients of the tire model tended to become identical for the best fit. The coefficients are compared to the values of camber, pressure, and surface properties to determine basic correlations between the tire settings and model coefficients.

Upon the completion of this work, there is now a further understanding of the basics of lateral force generation of ATV tires and the effect of camber angle, inflation pressure, and surface properties. Further improvements to this work are within the capabilities of current technology and are highly encouraged.

While by no means this study is complete, there are several other paths to take from this point forward. There are two primary routes to take, one being centered on different surfaces or various aspects of the strength of surfaces. The remaining, and obvious, path is that of the tire. The tire is a complex and highly non-linear part of the vehicle, and to understand its operation, one must start from the most basic of models and move onward from there. Neither direction has more merit than the other and can generate equally weighted information towards solving problems of off-road mobility.

Researchers electing to investigate the operating surface may dive into problems with measuring the terrain. By no means is the method used in this study the most accurate or technologically advanced. The method used in this study borne out of the requirement for low cost and simplicity.

A person wishing to create a better bevameter could improve the methods for electronically collecting data through sensors. The displacement sensor for the shear test was connected to the rotating shaft by means of a pulley and belt. Certainly there could be some play in that system. Also, the actuation method of the bevameter, by human

power, could be improved with the addition of a servo motor system. Remembering to specify the motor such that shear rates match that of actual vehicles will save headache, and improve accuracy.

Furthermore, studies centered about the soil could be positioned to test several surfaces to varying degrees of accuracy. The soil tests for this study were not as substantial in number as was planned due to structural insufficiencies with the shear-head. Care must be taken to properly design the link between the rubber coating and the shear head body.

The route of further investigating the tire finds several opportunities available to researchers. While this study was conducted at zero longitudinal slip, Lateral forces can be investigated when the tire is subjected to traction (accelerative forces) or braking (decelerative forces). This would require retrofitting the hook on the current test rig to accept a traction motor, be it hydraulic or electric. The results of researching the traction/braking problem would result in an entire operational map of the tire on a particular surface.

Other studies could be conducted with different tires, comparing tread patterns. Even on one tire, various tread modifications could be studied, such as decreasing lug height, applying siping to the tire, or removing more material from the lugs by way of a tire grooving iron. These tread modifications change how the tire interacts with the surface, and thus changes the performance of the tire. The item of interest to the researcher is the magnitude of the change. Still in the tread modification category is the modification of the profile of the tire. Some tires have a squared profile, whereas some

have a very rounded profile, i.e. motorcycle tires. The interaction of profile and surface can have an effect on the way camber affects the performance of the tire.

Researchers building a similar test rig are advised to add a hydraulic damper between the vehicle and the triangle with a load cell on the end. This will tame some of the vertical oscillations of the tire that are excited by the ground at a steady speed. The equations to break down the lateral and longitudinal forces may be modified to accept the addition of a fourth load cell. The modification to the test rig to include a damper is not a significant investment and has the chance of improving the quality and accuracy of the data collected.

Finally, a problem of pure mathematics is the phenomenon observed in this study where the *A* and *B* coefficients of the exponential tire model were found to be the same value when run through software to check these parameters with the R-squared value to measure goodness of fit. In every case, the values for *A* and *B* became identical. No ill effects from this phenomenon were observed on the modification of the tire model to accept the curve fits to *A* and *B* coefficients.

REFERENCES

1. Bekker, M. G. “Off-the-Road Locomotion: Research and Development in Terramechanics”, University of Michigan Press, Ann Arbor, 1960.

2. Sloss, David; Alger, Russell; Osborne, Mark. “Re-design of the Bevameter” Proceedings of the 14th International Society of Terrain Vehicle Systems Conference, Vicksburg, Mississippi, U.S. 2002.

3. Wong, J.Y. “Terramechanics and Off-Road Vehicles,” Elsevier, Amsterdam, 1989.

4. Muro, T; O’Brien, J., “Terramechanics, Land Locomotion Mechanics,” A.A. Balkema Publishers, Tokyo, 2004.

5. Mulqueen, J, Stafford, J.V., Tanner, D.W., “Evaluation of Penetrometers for Measuring Soil Strength”, Journal of Terramechanics, 1977, V14, No.3, p137

6. Topp, G. Clarke, Lapen, David R., Cook, Freeman J., Morrison, Malcolm J. and Pillai-McGarry, Usha, “Facilitating Soil- and Plant-Water Research Through the Use of TDR", Proc. TDR 2006, Purdue University, West Lafayette, USA, Sept. 2006, Paper ID 39, 22p

7. Wong, J.Y. “Theory of Ground Vehicles,” John Wiley & Sons, Toronto, 2001.

8. Okello, J.A. “A Review of Soil Strength Measurement Techniques for Prediction of Terrain Vehicle Performance,” J. agric. eng. res., 1991, V50, No.2, p129

9. Kogure, K, Yamaguchi, K, Ohira, Y. “Comparison of Strength and Soil Thrust Characteristics Among Different Soil Shear Tests,” Journal of Terramechanics. 1988, V25, No.3, p201

10. Shoop, S.A. (Cold Regions Research and Engineering Laboratory, Department of the Army). *Comparison of Thawing Soil Strength Measurements for Predicting Vehicle Performance,* Washington, D.C.: U.S. Government Printing Office, 1992.

11. Karafiath, L.L., Nowatzki, E. A., “Soil Mechanics for Off-Road Vehicle Engineering.” Trans Tech Publications, Clausthal, Germany, 1978.

12. Baladi, G.Y. “Terrain Evaluation for Off-Road Mobility.” Journal of Terramechanics. 1987, V24, No.2, p127

13. Terzaghi, K. 1942. Theoretical soil mechanics. Wiley, New York.

14. Wong, J.Y. “Data Processing Methodology in the Characterization of the Mechanical Properties of Terrain”. Journal of Terramechanics, 1980, V17, No.1, p13

15. Crolla, D A; El-Razaz, A S A; Alstead, C J; Hockley, C. A model to predict the combined lateral and longitudinal forces on an off-road tyre : *Proceedings of the Ninth International Conference*, pp 362-372. New Hampshire, U.S.A., International Society for Terrain Vehicle Systems, 1987.

16. Freitag, D.R., A dimensional analysis of the performance of pneumatic tires on soft soils. *U.S. Army Waterways Experiment Station Technical Report* 3-688 (1965).

17. Turnage, G.W., Tyre selection and performance prediction for off-road wheeled-vehicle operations. *Proc. 4th Int. conf. Int. Soc. Terrain-Vehicle Systems*, Stockholm (1972).

18. Crolla, D.A. and El-Razaz, A.S.A., “A Review of the Combined Lateral and Longitudinal Force Generation of Tyres on Deformable Surfaces,” Journal of Terramechanics, Vol. 24, No. 3, 1987

19. Milliken, W. F. and Milliken, D. L., 1995, "Race Car Vehicle Dynamics," R-146, SAE International

20. Pacejka, H. B., *Tire and Vehicle Dynamics,* Society of Automotive Engineers and Butterworth-Heinemann, Oxford, 2002.

21. Bekker, M.G., “Parametric Analysis of Pneumatic Tires Update – Samples of Engineering Problems and Solutions in Off-Road Locomotion”, SAE Technical Paper 850536, 1985.

22. Golob, T.B., “Development of a Terrain Strength Measuring System.” Journal of Terramechanics, 1981, V18, No. 2, p109.

23. Okello, J.A., “A Review of Soil Strength Measurement Techniques for Prediction of Terrain Vehicle Performance.” Journal of Agric. Engr. Res. 50, p 129.

24. Krick, G. “Behaviour of Tyres Driven in Soft Ground with Side Slip”, ATZ 73, 1971 (7) p243-246

25. Holloway, D.C., Wilson, W.H., Drach, T.J. “Examination of ATV Tire Forces Generated on Clay, Grass, and Sand Surfaces.” SAE Paper 891106

26. Holtz, R.D., Kovacs, W.D. “An Introduction to Geotechnical Engineering”, Prentice Hall, Upper Saddle River, New Jersey, 1981.

27. M.G. Bekker. Introduction to Terrain-Vehicle Systems. The University of Michigan Press, Ann Arbor, 1969.

28. Weir, D.H., Zellner, J.W., “An Introduction to the Operational Characteristics of All-Terrain Vehicles” SAE Paper 860225

29. Shoop, S.A. (Cold Regions Research and Engineering Laboratory, Department of the Army). *Terrain Characterization for Trafficability,* Washington, D.C.: U.S. Government Printing Office, 1993

30. Yu, T. “The Tractive Performance of a Friction-Based Prototype Track”, PhD Dissertation, University of Pretoria, 2005.

31. Metz, L. D., “Dynamics of Four-Wheel-Steer Off-Highway Vehicles” SAE Paper 930765.

32. Gee-Clough, D., Sommer, M.S. “Steering Forces on Undrivern, Angled Wheels.” Journal of Terramechanics, 1981, V18, No.2, p25

33. Liang, C., Allen, R.W., Rosenthal, T.J., Chrstos, J.P., Nunez, P. “Tire Modeling for Off-Road Vehicle Simulation.” SAE Paper 2004-01-2058.

34. Bekker, M.G. “Parametric Analyses of Pneumatic Tires Update – Samples of Engineering Problems and Solutions in Off-Road Locomotion.” SAE Paper 850536

APPENDICES

A. Uncertainty Analysis

The uncertainty of the data presented in this study is addressed in this following section. Data processing methods and data analysis paired with structural deflections provide levels of uncertainty of the measurement required. Tire forces in three directions, lateral, vertical, and longitudinal are analyzed. Also, slip angle and camber are reviewed for the ranges they assume during a test.

As the test vehicle goes over an inherently uneven surface, the camber of a tire changes with position down the test track. The vertical perturbations in the terrain give rise to roll motions in the test vehicle, and these roll angles back and forth are directly seen at the test rig, as the mounting apparatus is very stiff.

For each surface, a slow-speed (>5 mph) was conducted with an inclinometer affixed to the hook, near where camber adjustments are made. Over 6,000 data points were collected, and analyzed. This was determined using the t-distribution tables and the following equations.

$$\sigma = \sqrt{\frac{1}{N}\sum_{i=1}^{N}(x_i - \bar{x})^2} \tag{6.1}$$

$$CL = \pm\frac{t\sigma}{\sqrt{N}} \tag{6.2}$$

Equation 6.1 is the standard deviation of a population of N samples. Equation 6.2 is the confidence limit for samples in the population. For the camber data, a confidence limit of 0.104 degrees was calculated at 99%. The standard deviation, which is a measure

of the spread of the values about a mean, was recorded to be 3.47 degrees. This spread is what gives rise to the selection of “high” and “low” cambers. Seeking an average value of zero degrees for “low” camber, one will see that this value can fluctuate about zero. The same goes for the “high” camber, where the nominal value is 8 degrees, however from the analysis, the spread of the values from a desired average of 8 degrees is around 3.5 degrees as well. This leaves the intermediate camber values to be shrouded in statistical shadows, as the effect of intermediate values cannot be discerned.

As camber angle has uncertainties, so does the slip angle. As indicated in the text, a simple FEA was conducted on the hook part of the tire test rig. A normal load of 600 lbf, and a lateral load of 300 lbf were applied. From the tire data generated in this study, there appears to be a factor of safety of two. The deflections recorded in the FEA showed a camber deflection of approximately one-half to three-quarters of a degree. Similarly, the slip angle had less deflection, on the order of one-half of a degree. By looking at the force diagram in Figure 3.20, one will see that addition of the lateral and longitudinal vectors will seek to decrease the slip angle.

Also a factor in the slip angle uncertainty is the ground-holding ability of the test vehicle. Even though the Yamaha Rhino weighs in excess of 1,000 lbf, at extreme normal loads (275 and 320 lbf) a yawing effect was noticed, and slight counter-steer was required to maintain a path parallel to the length of the test surface. The counter-steering effect to balance out the yaw effect would result in a slightly decreased slip angle than what was set on the test rig. A simple analysis was conducted to generate a yaw angle that would reduce the slip angle at extreme normal loads.

On both surfaces, tests were run at 320 lbf of normal load and 20 degrees of slip angle to generate significant lateral forces, creating the most pronounced yaw effect. A camera was placed at an elevated position in line with the direction of travel, which is capable of taking 3 frames per second. Marks on the roll cage of the vehicle were made to facilitate high contrast in the photographs. The photographs were compiled together in photo editing software, and by using the marks on the roll cage, each frame could be analyzed to trace the path of the center of the roll cage. Pixel measurements were manually taken from the images to calculate a rotation about the center of the roll cage. This rotation is assumed to be the yaw angle of the vehicle, as the center of the top of the roll cage is situated very near the yaw axis, as indicated by weight split calculations for the longitudinal position of the center of gravity. Figure 6.1 shows a trace of the movement of the vehicle. While more advanced image processing techniques could be employed at the cost of more analysis time, the manual analysis has generated an acceptable first cut for the uncertainty in slip angle, which turns out to be approximately 3.5 degrees at high normal loads and slip angles. This phenomenon could be assumed to be linearly varying with normal load and slip angle. Therefore the worst deflections occur at the highest normal loads and slip angles, and the insignificant deflections would be at zero slip angle, and the lowest normal load, 50 lbf.

Figure 6.1 – Composite photograph of yaw angle uncertainty

Tire force certainty is handled by software written in MATLAB. Once all testing is complete, all runs for a particular configuration are combined into one data file. Recall that the acceleration and deceleration portions are not part of the data, so combining the data does not have any ill effects. Three load cells and two accelerometers are read into the data acquisition system. Once adjusted through the calibration curves, lateral, longitudinal, and vertical forces can then be deduced.

Vertical load is determined through the accelerometer attached just below the dead weights. By knowing the acceleration and the mass, a vertical force can be calculated. As the terrain fluctuates greatly, this can cause wildly fluctuating normal loads. The software written for this study incorporates a filter that only processes lines of data where the normal load is within ten percent of nominal. This process manually sets the uncertainty of the vertical load. Brief experiments were conducted to reduce this tolerance, however further reductions in tolerance significantly limited the number of data points for analysis. As this is the first excursion into the uncertainty of ATV tire forces it was

determined that a ten percent tolerance was an acceptable starting point, as no analysis of this type has been conducted.

As data points are accepted by their meeting normal load tolerance, the program begins calculating lateral and longitudinal forces through the schematic of the tire rig, presented in Figure 3.20. Lateral and longitudinal forces are calculated as follows:

$$\begin{aligned} F_x &= f_{Ch.6}\sin(\alpha) + f_{Ch.7}\cos(\alpha) + f_{Ch.8}\cos(\alpha) \\ F_y &= -f_{Ch.6}\cos(\alpha) + f_{Ch.7}\sin(\alpha) + f_{Ch.8}\sin(\alpha) \end{aligned} \tag{6.3}$$

This process generates lateral and longitudinal force vectors that are associated with normal loads that are within ten percent of the nominal normal load for that run. As the vehicle has been driven over as a consistent and level surface as possible, the mean of these vectors is taken. This average value is then saved as the lateral and longitudinal forces for that particular run. Standard deviations are also computed for both vectors.

Given the standard deviation, and the number of samples, the standard error of the mean can be calculated for these mean values of lateral force.

$$S_E = \hat{\sigma} / \sqrt{n} \tag{6.4}$$

For most of the data presented in this paper, standard errors of the mean for lateral force and longitudinal force are approximately ±4 lbs.

All of these uncertainty values can be visualized graphically in Figure 6.2. In three dimensions, the box shows the levels of uncertainty for a given data point in a set of tire data.

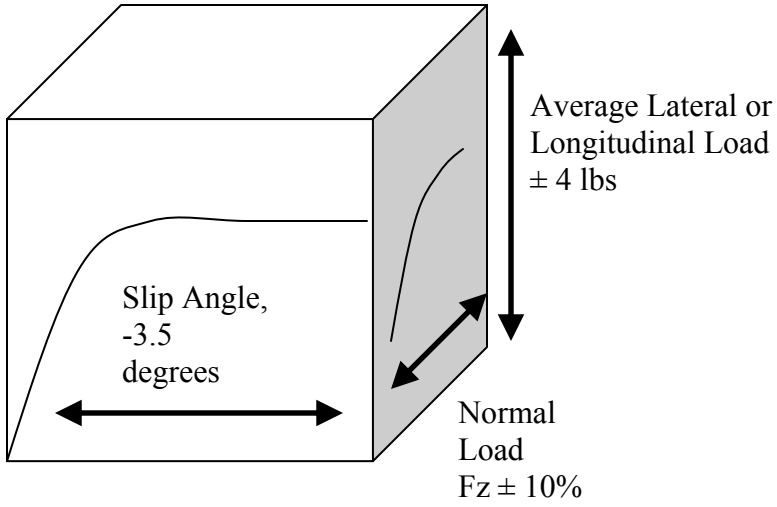

Figure 6.2 – Graphical Representation of Levels of Uncertainty

B. Analysis of Tire Spring Rates and Natural Frequencies

As a tire a flexible composite structure, this flexibility gives rise to varying deflections for varying loads. The proportion of load to deflection is viewed as a spring rate, in units of lb/in. A point raised in Chapter 2, was that the tire could be modeled as a spring-mass system in the vertical direction against the question that the tow speed excites the bounce frequency of the tire test rig. The basic system is described in Figure 6.3.

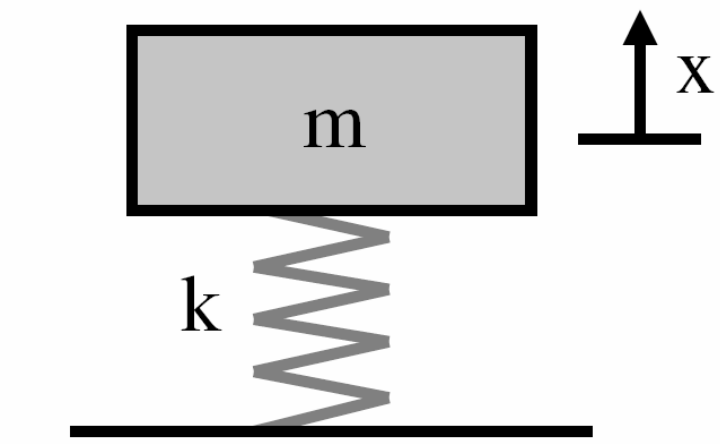

Figure 6.3 – Spring – Mass system

Equations associated with this one degree-of-freedom system are:

$$\begin{aligned} m\ddot{x} &= -kx \\ x(t) &= A\cos(2\pi f_{nat} t) \end{aligned} \tag{6.5}$$

Also noting that the natural frequency of this system in Hertz is:

$$f_{nat} = \frac{1}{2\pi}\sqrt{\frac{k}{m}} \tag{6.6}$$

Given the data in Figure 6.3 for spring rate versus pressure that was experimentally determined, natural frequencies for various pressure and mass combinations can be seen in Table 6.1.

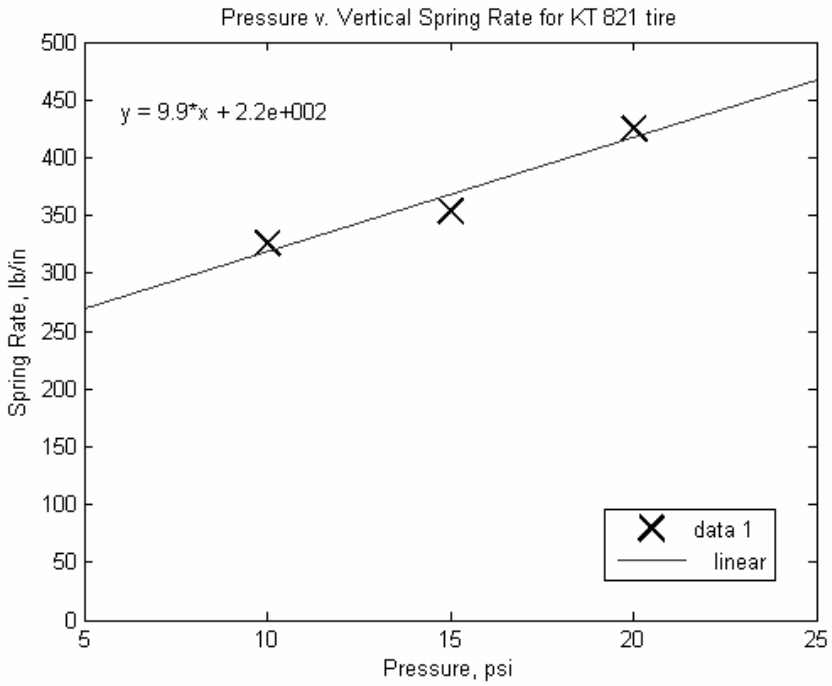

Figure 6.4 – Linear fit to Pressure v. Spring rate data for KT 821 tire

f_n, Hz	5 psi	6 psi	7 psi	8 psi	9 psi	10 psi
50 lb	0.369	0.372	0.382	0.389	0.395	0.402
95 lb	0.268	0.272	0.277	0.282	0.287	0.291
140 lb	0.220	0.225	0.228	0.232	0.236	0.240
185 lb	0.192	0.195	0.199	0.202	0.205	0.209
230 lb	0.172	0.175	0.178	0.181	0.184	0.187
275 lb	0.157	0.160	0.163	0.166	0.168	0.171
320 lb	0.146	0.148	0.151	0.153	0.156	0.158

Figure 6.1 – Table of natural frequencies in z-axis for KT 821 tire

One will notice that when Table 6.1's data is compared to the 2.0 Hz – 3.12 Hz range of excitation frequencies, that there is a significant difference. When observed from the perspective of wavelength, the wavelengths associated with the frequencies in Table 6.1 are on the range of 30 ft to 75 ft. This would suggest that certain undulations in the terrain or the acceleration period of the test run would have an impact on the excitation of the natural frequencies of the test rig. Another theory to the oscillations is that of a natural frequency in the lateral direction. As the carcass is flexible in the vertical direction, it is also flexible in a shearing sense, with lateral movement between the wheel and the surface. Coupled with the traction trends in the lateral direction, this phenomenon may be studied further yet is out of the scope of this work as no lateral spring rate measurements were taken.

C. Raw Data

Clay, 10psi, Low Camber

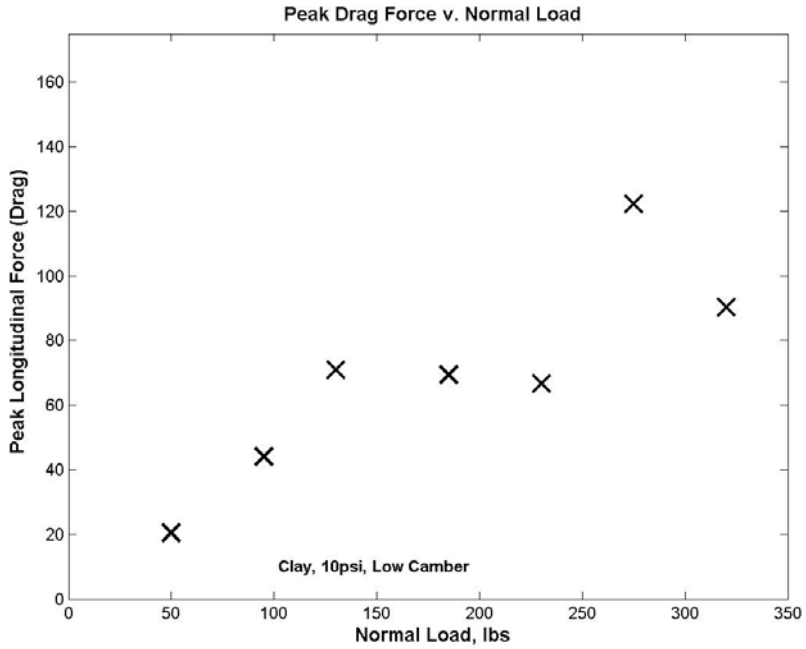

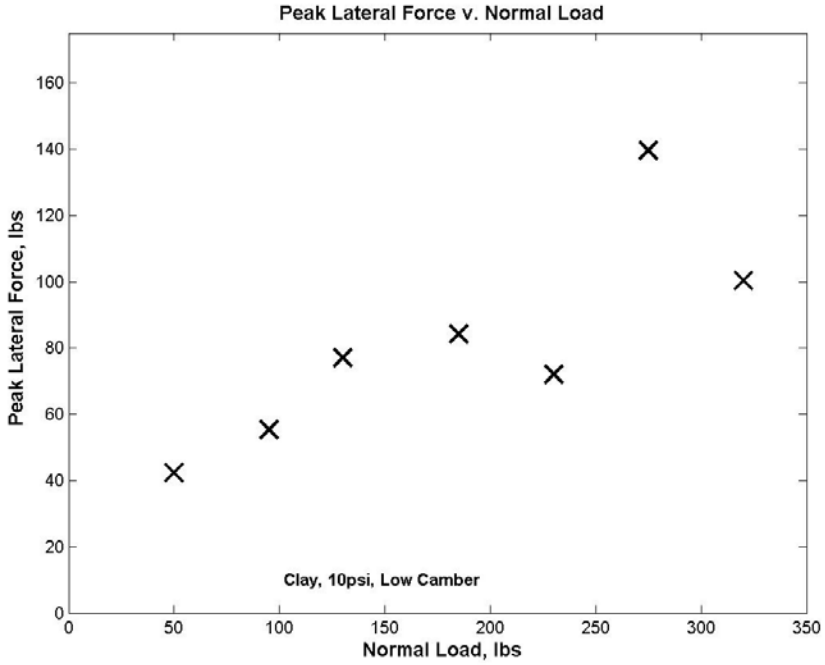

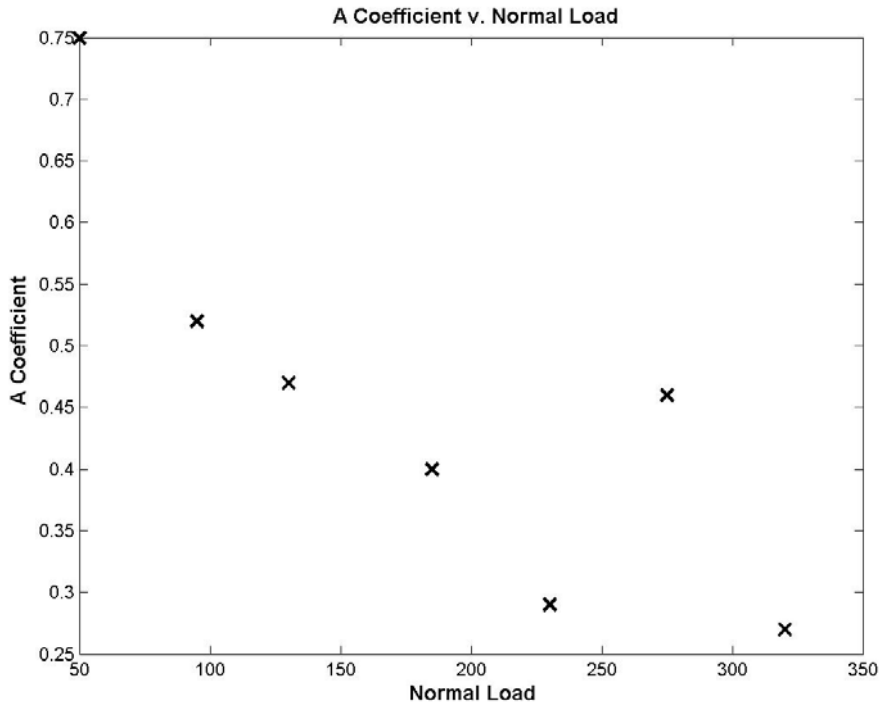
A Coefficient v. Normal Load
A Coefficient
Normal Load
0.75
0.7
0.65
0.6
0.55
0.5
0.45
0.4
0.35
0.3
0.25
50
100
150
200
250
300
350

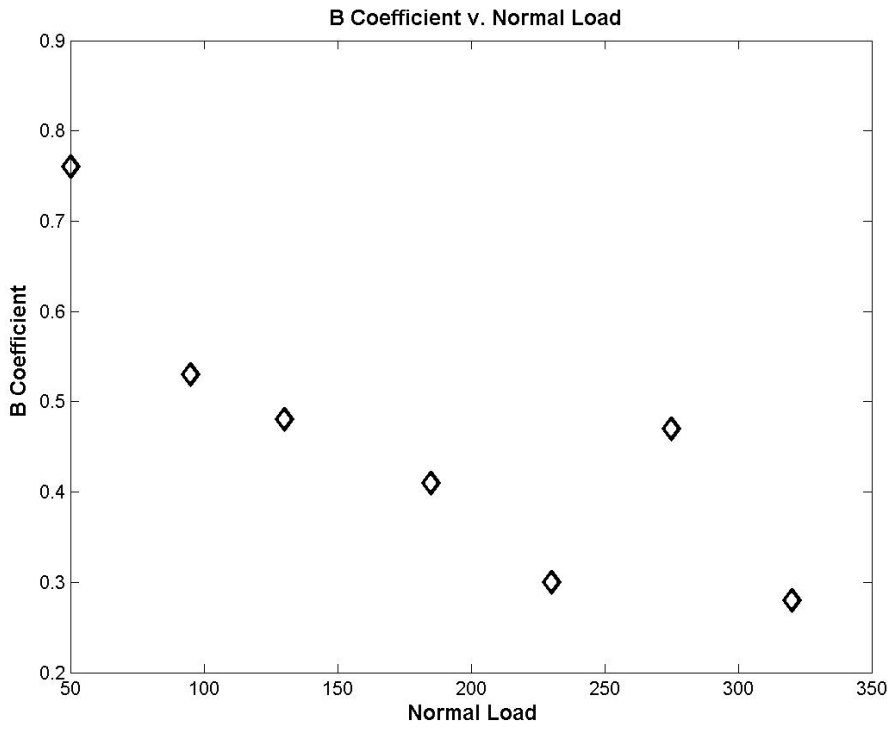
B Coefficient v. Normal Load
B Coefficient
Normal Load
0.9
0.8
0.7
0.6
0.5
0.4
0.3
0.2
50
100
150
200
250
300
350

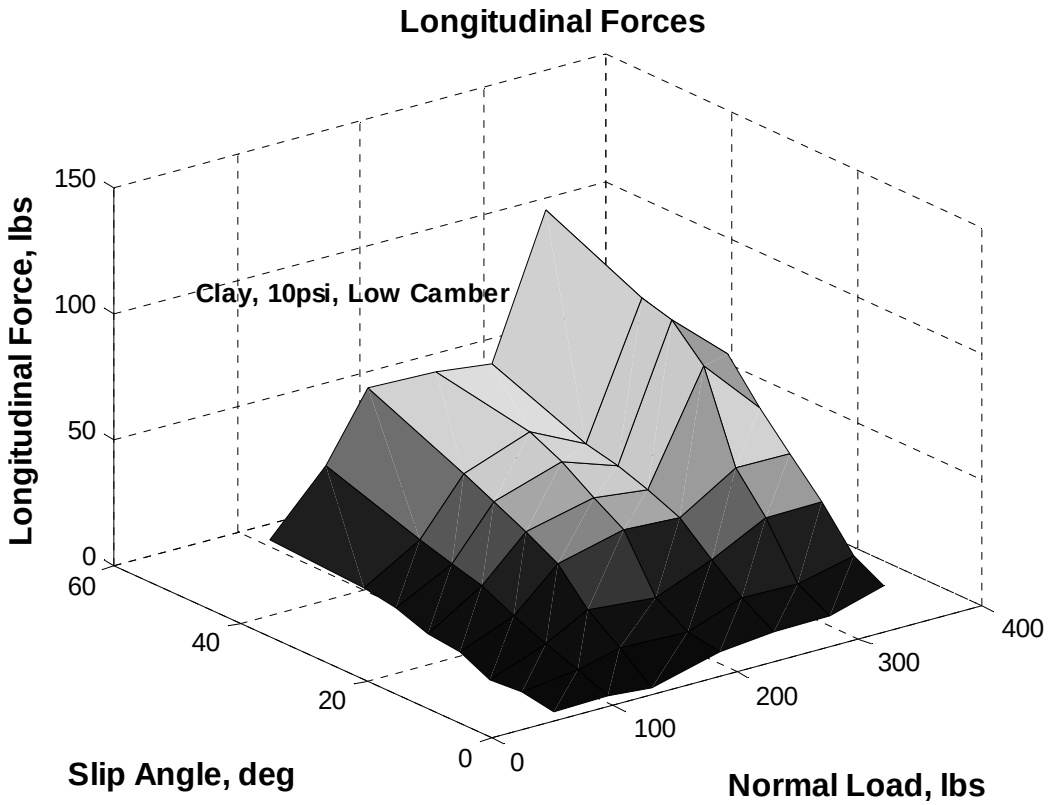
Longitudinal Forces
Clay, 10psi, Low Camber
Longitudinal Force, lbs
150
100
50
0
60
40
20
0
Slip Angle, deg
0
100
200
300
400
Normal Load, lbs

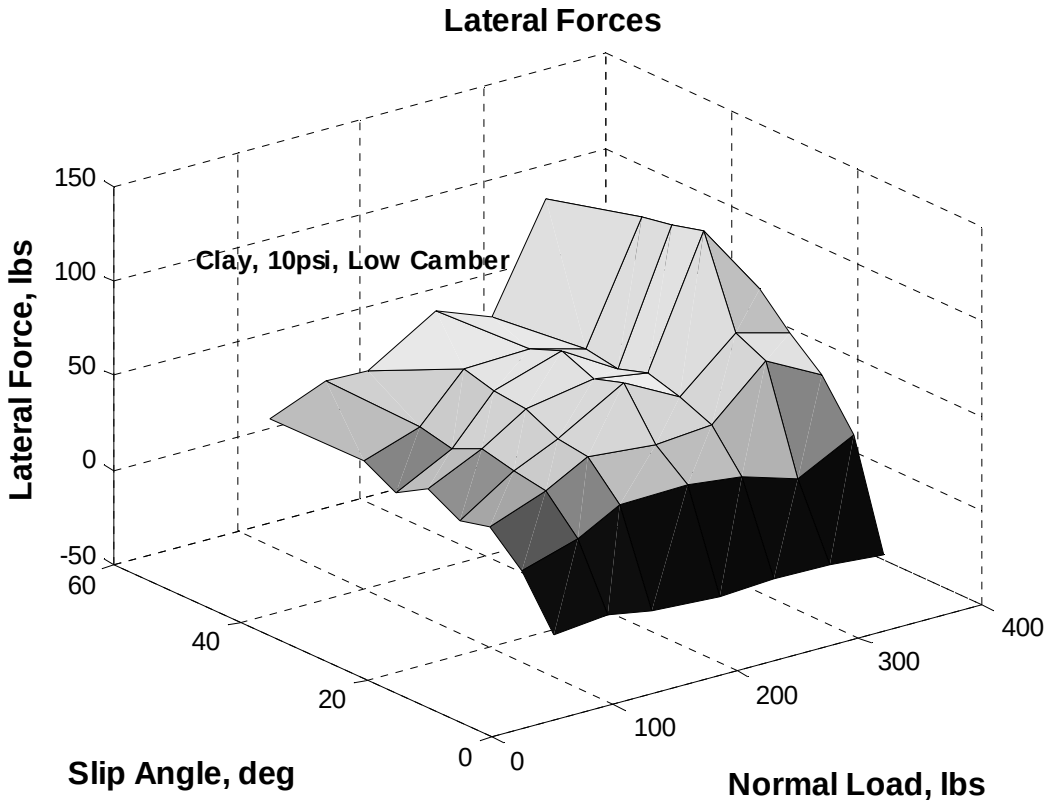
Lateral Forces
Clay, 10psi, Low Camber
Lateral Force, lbs
150
100
50
0
-50
60
40
20
0
Slip Angle, deg
0
100
200
300
400
Normal Load, lbs

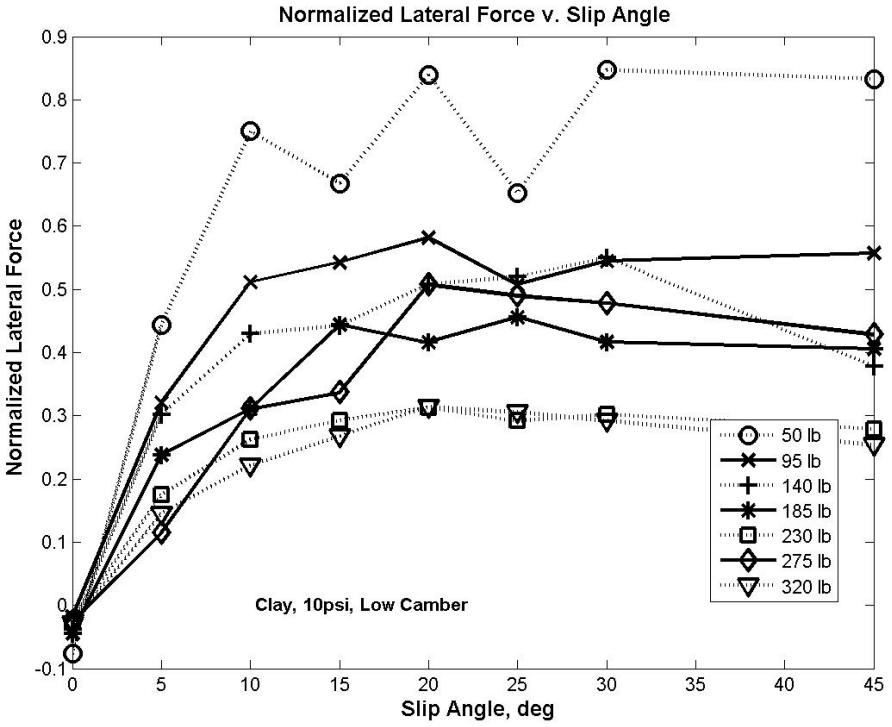
Normalized Lateral Force v. Slip Angle
Normalized Lateral Force
Slip Angle, deg
Clay, 10psi, Low Camber
50 lb
95 lb
140 lb
185 lb
230 lb
275 lb
320 lb

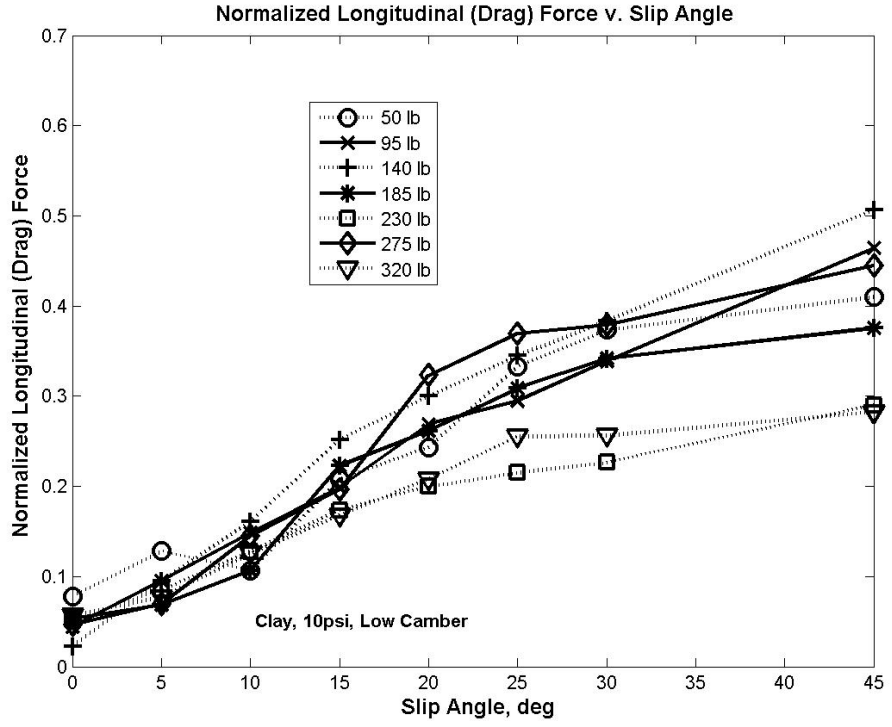
Normalized Longitudinal (Drag) Force v. Slip Angle
Normalized Longitudinal (Drag) Force
Slip Angle, deg
Clay, 10psi, Low Camber
50 lb
95 lb
140 lb
185 lb
230 lb
275 lb
320 lb

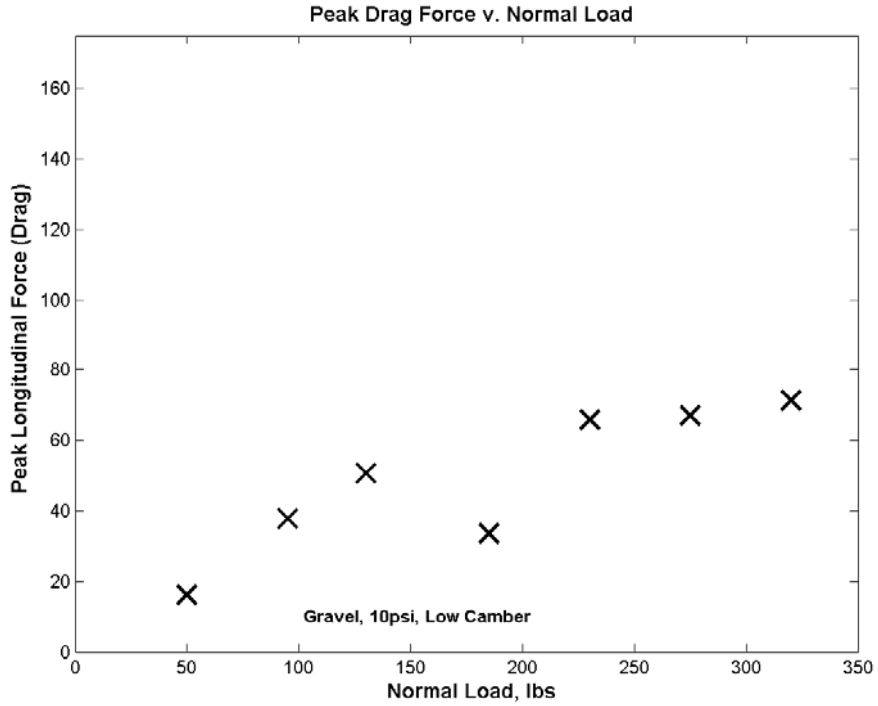
Peak Drag Force v. Normal Load
Peak Longitudinal Force (Drag)
Normal Load, lbs
Gravel, 10psi, Low Camber
0
20
40
60
80
100
120
140
160
0
50
100
150
200
250
300
350

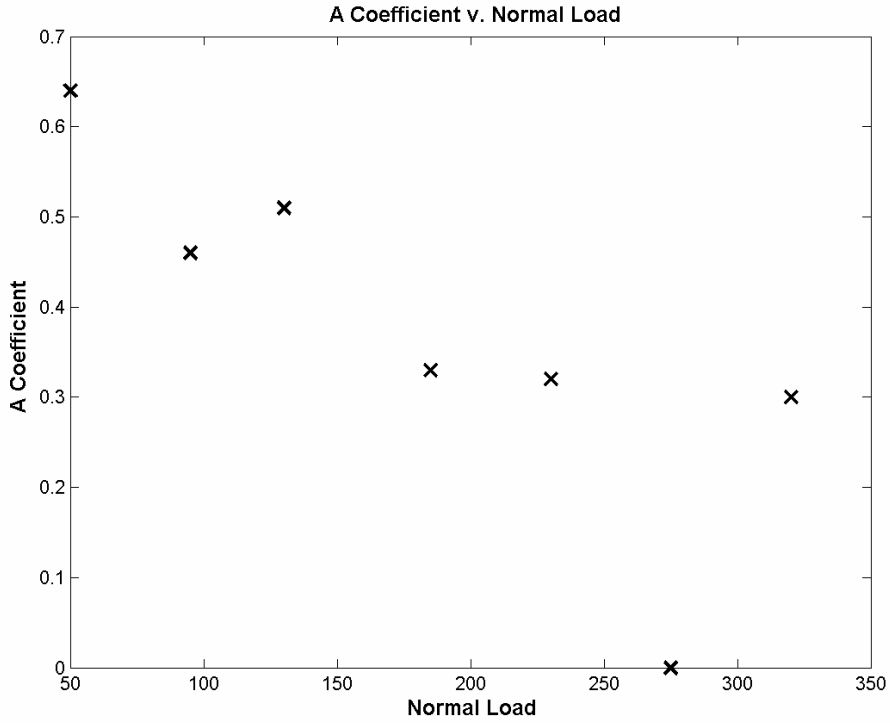
A Coefficient v. Normal Load
A Coefficient
Normal Load
0
0.1
0.2
0.3
0.4
0.5
0.6
0.7
50
100
150
200
250
300
350

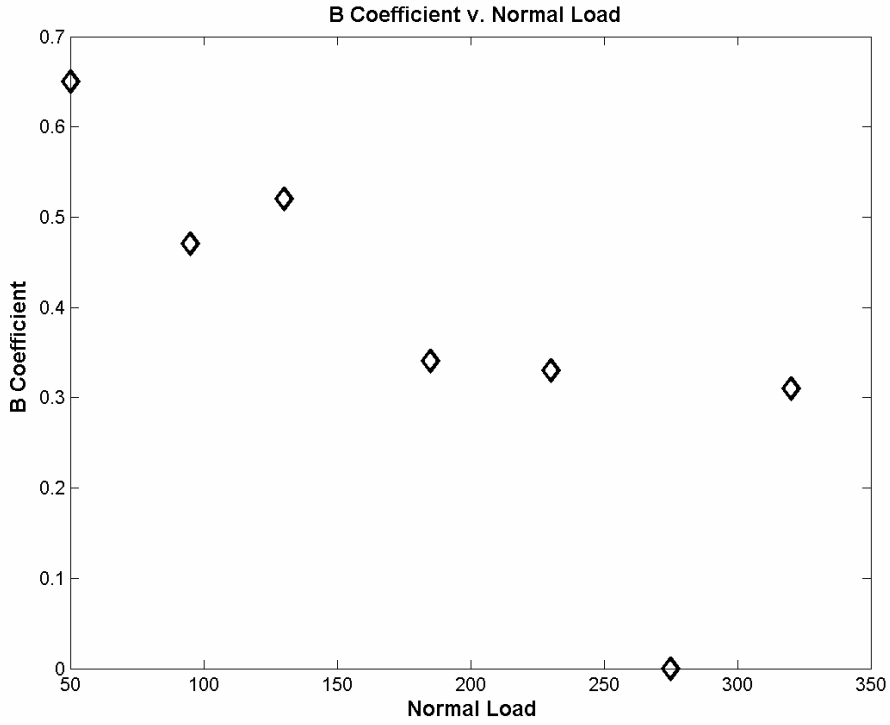
B Coefficient v. Normal Load
B Coefficient
Normal Load
0.7
0.6
0.5
0.4
0.3
0.2
0.1
0
50
100
150
200
250
300
350

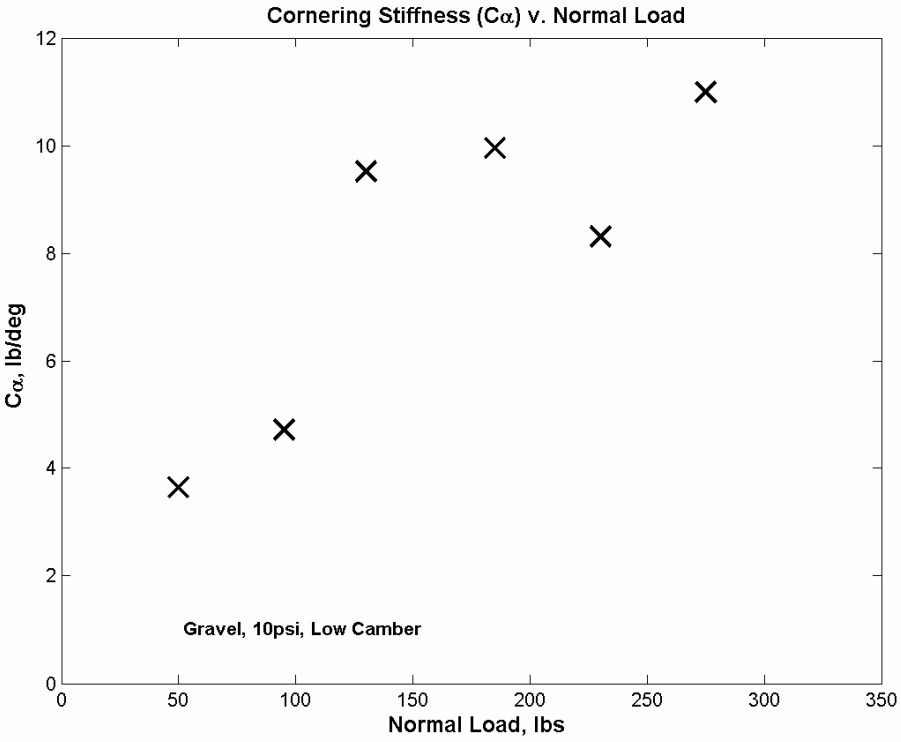
Cornering Stiffness (Cα) v. Normal Load
Cα, lb/deg
Normal Load, lbs
Gravel, 10psi, Low Camber
12
10
8
6
4
2
0
0
50
100
150
200
250
300
350

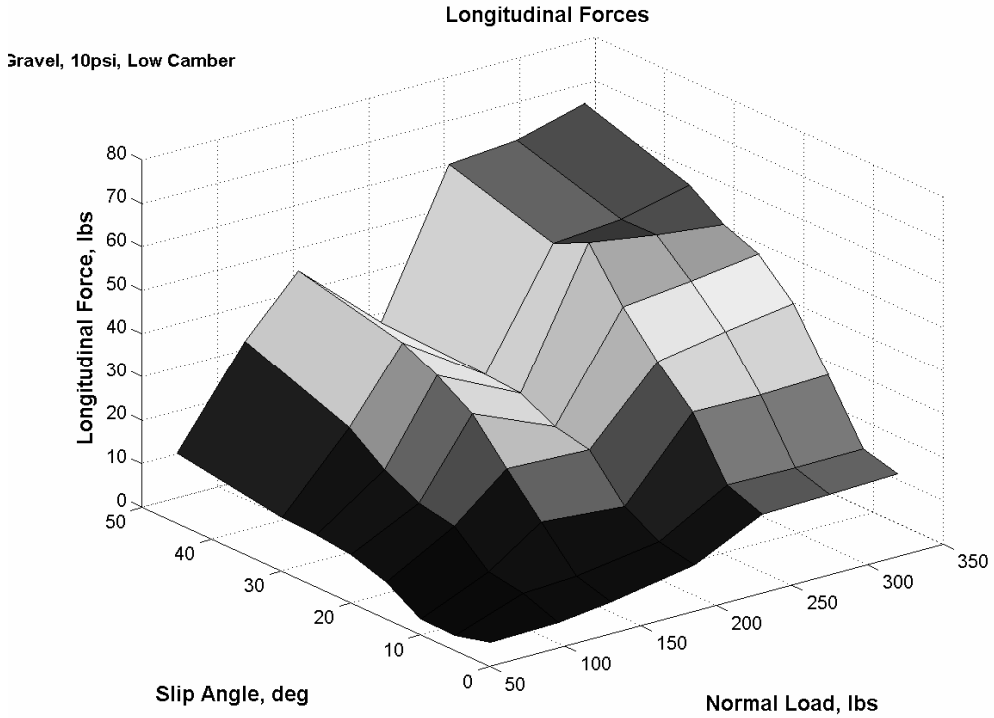
Longitudinal Forces
Gravel, 10psi, Low Camber
Longitudinal Force, lbs
80
70
60
50
40
30
20
10
0
50
40
30
20
10
0
Slip Angle, deg
50
100
150
200
250
300
350
Normal Load, lbs

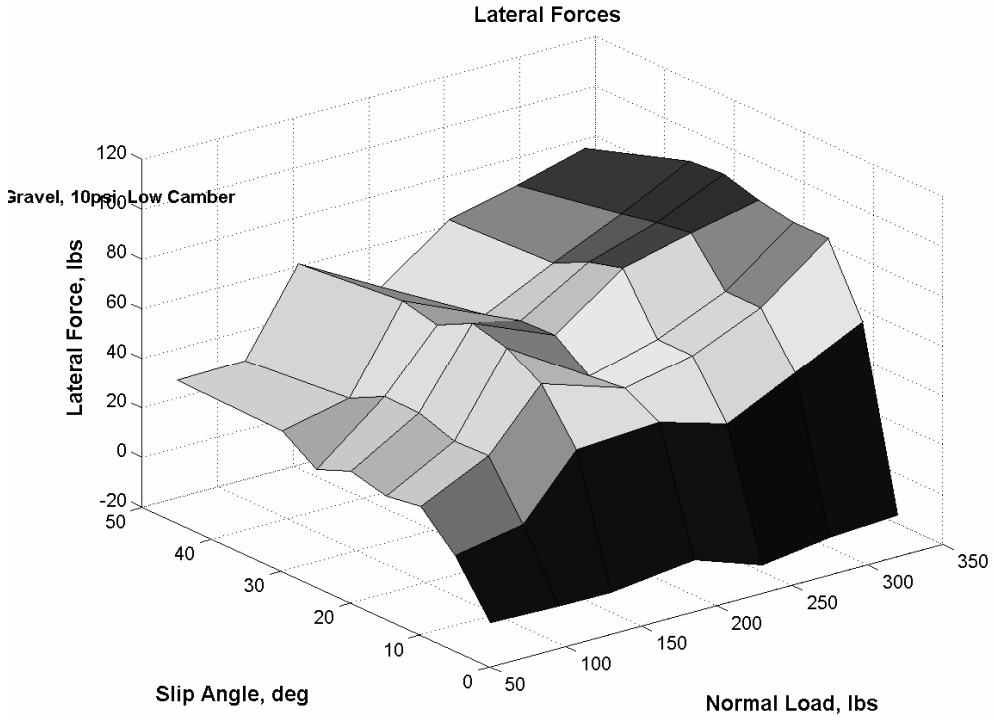
Lateral Forces
Gravel, 10psi, Low Camber
Lateral Force, lbs
120
100
80
60
40
20
0
-20
50
40
30
20
10
0
Slip Angle, deg
50
100
150
200
250
300
350
Normal Load, lbs

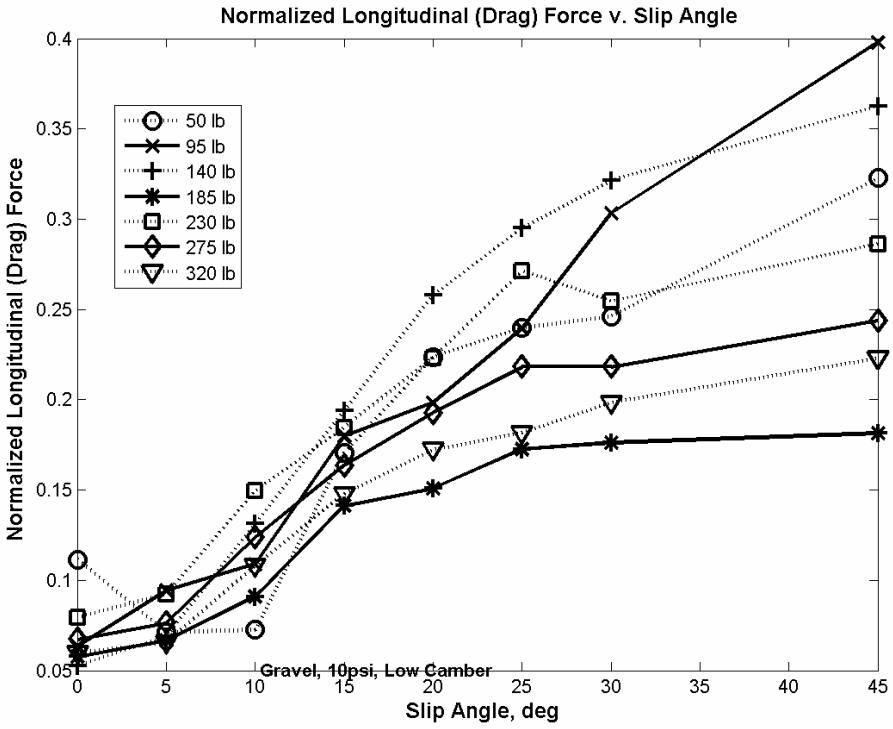
Normalized Longitudinal (Drag) Force v. Slip Angle
Normalized Longitudinal (Drag) Force
Slip Angle, deg
50 lb
95 lb
140 lb
185 lb
230 lb
275 lb
320 lb
Gravel, 10psi, Low Camber
0.4
0.35
0.3
0.25
0.2
0.15
0.1
0.05
0
5
10
15
20
25
30
35
40
45

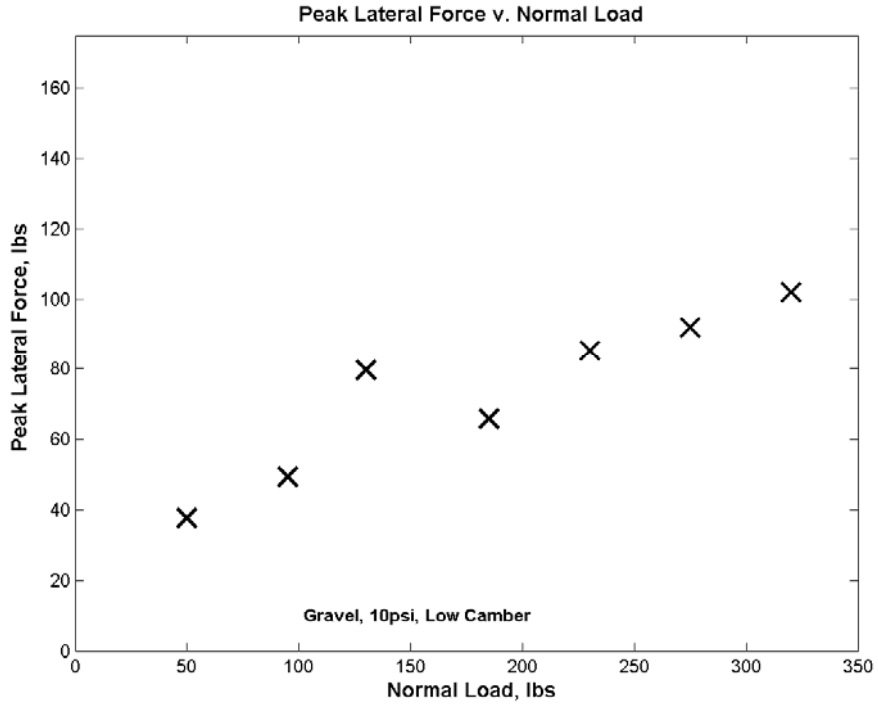
Peak Lateral Force v. Normal Load
Peak Lateral Force, lbs
Normal Load, lbs
Gravel, 10psi, Low Camber
160
140
120
100
80
60
40
20
0
0
50
100
150
200
250
300
350

Gravel, 5 psi, Low Camber

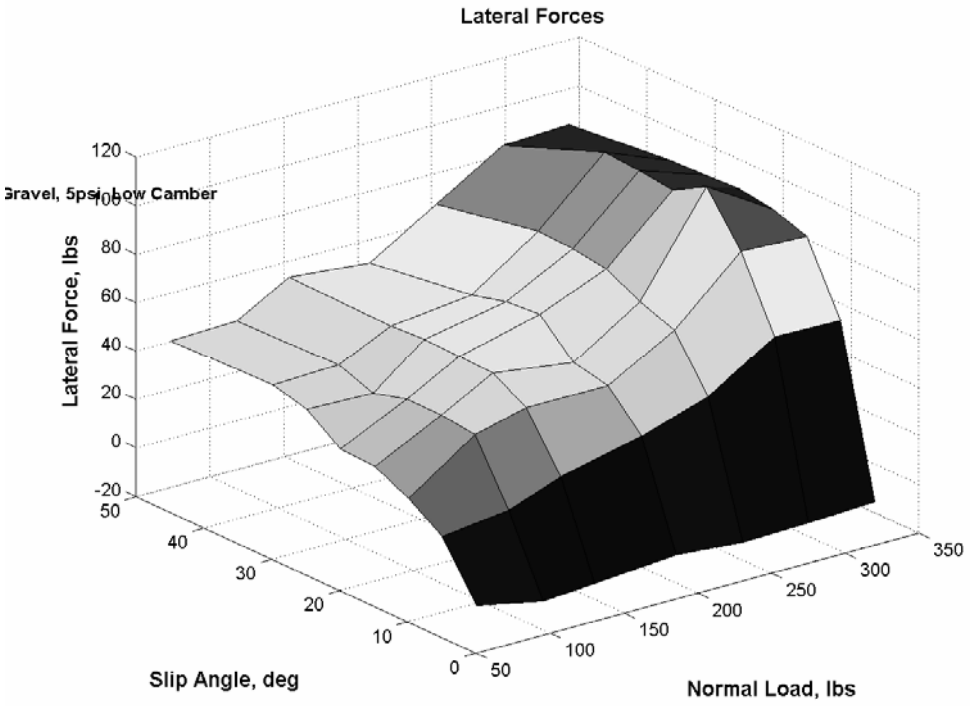

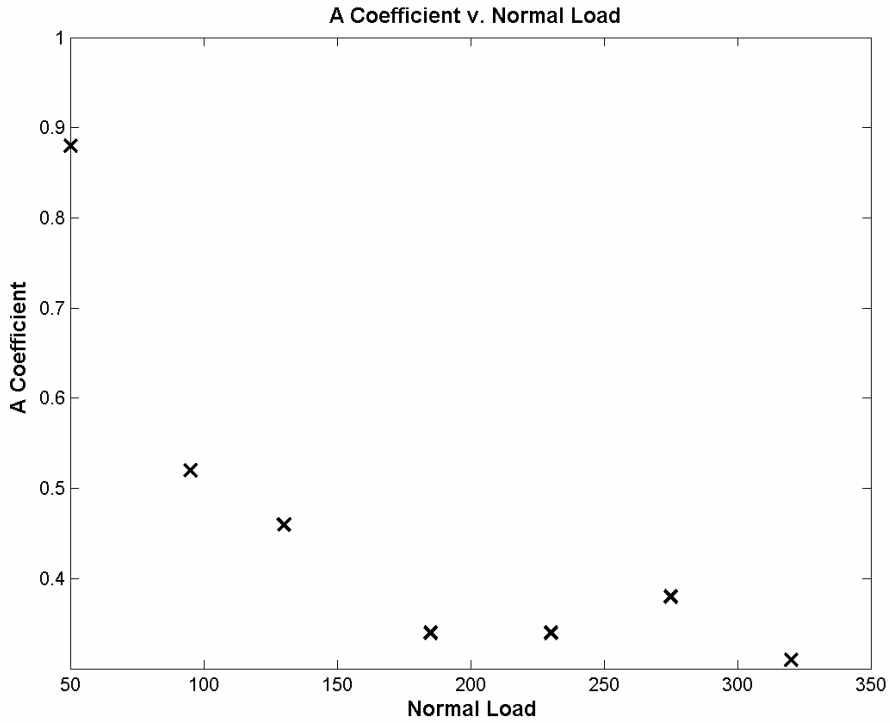

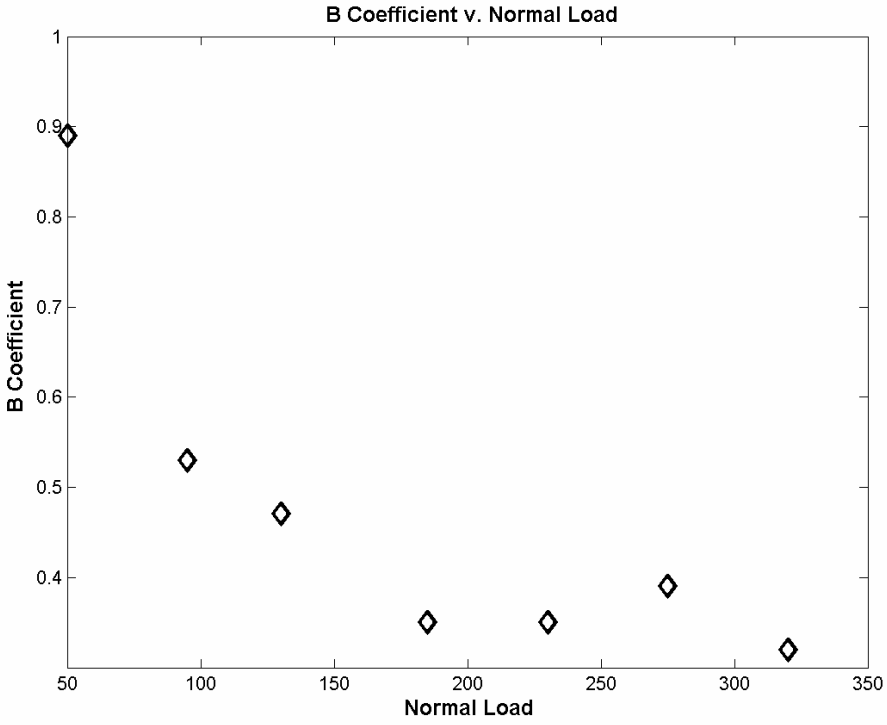
B Coefficient v. Normal Load
B Coefficient
Normal Load
1
0.9
0.8
0.7
0.6
0.5
0.4
50
100
150
200
250
300
350

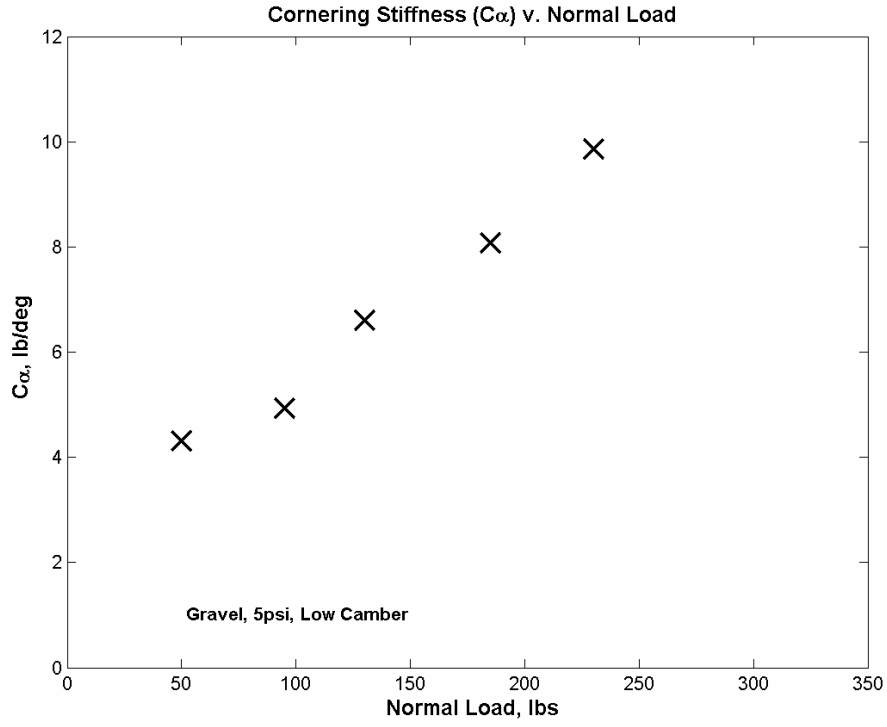
Cornering Stiffness (Cα) v. Normal Load
Cα, lb/deg
Normal Load, lbs
Gravel, 5psi, Low Camber
12
10
8
6
4
2
0
0
50
100
150
200
250
300
350

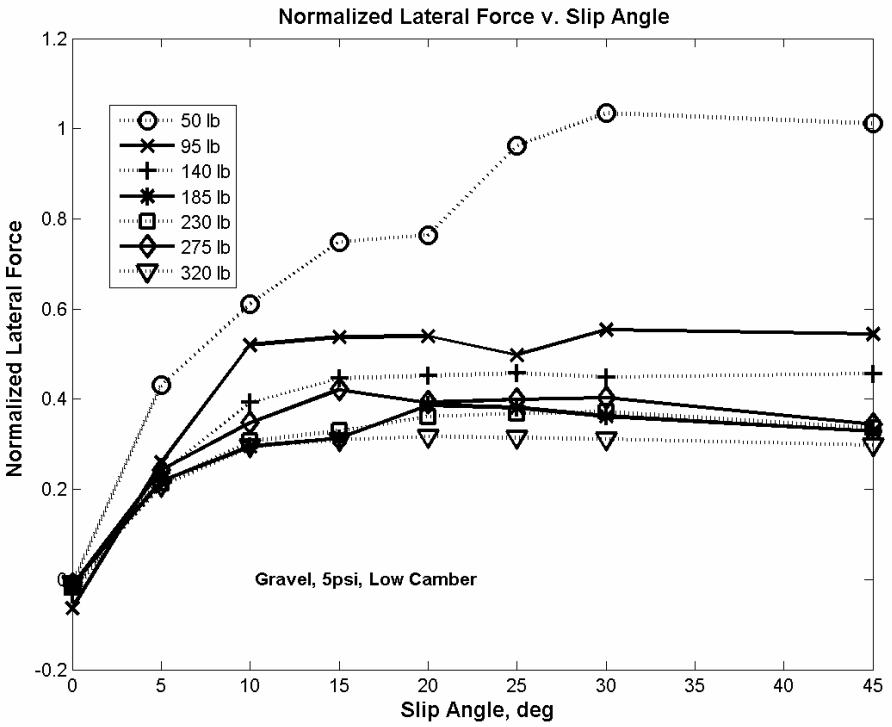
Normalized Lateral Force v. Slip Angle
Normalized Lateral Force
Slip Angle, deg
50 lb
95 lb
140 lb
185 lb
230 lb
275 lb
320 lb
Gravel, 5psi, Low Camber
1.2
1
0.8
0.6
0.4
0.2
0
-0.2
0
5
10
15
20
25
30
35
40
45

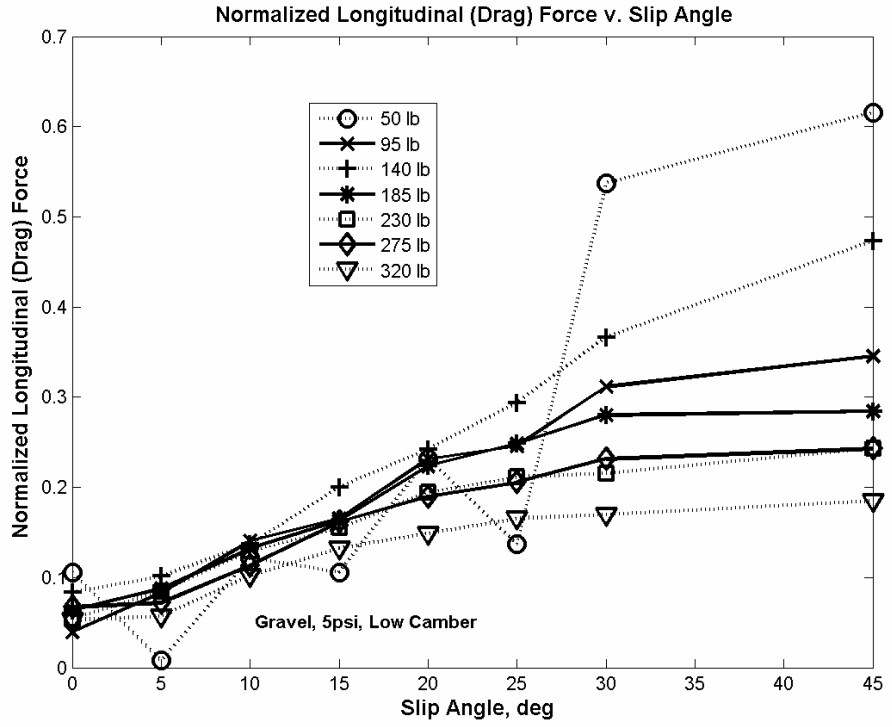
Normalized Longitudinal (Drag) Force v. Slip Angle
Normalized Longitudinal (Drag) Force
Slip Angle, deg
50 lb
95 lb
140 lb
185 lb
230 lb
275 lb
320 lb
Gravel, 5psi, Low Camber
0.7
0.6
0.5
0.4
0.3
0.2
0.1
0
0
5
10
15
20
25
30
35
40
45

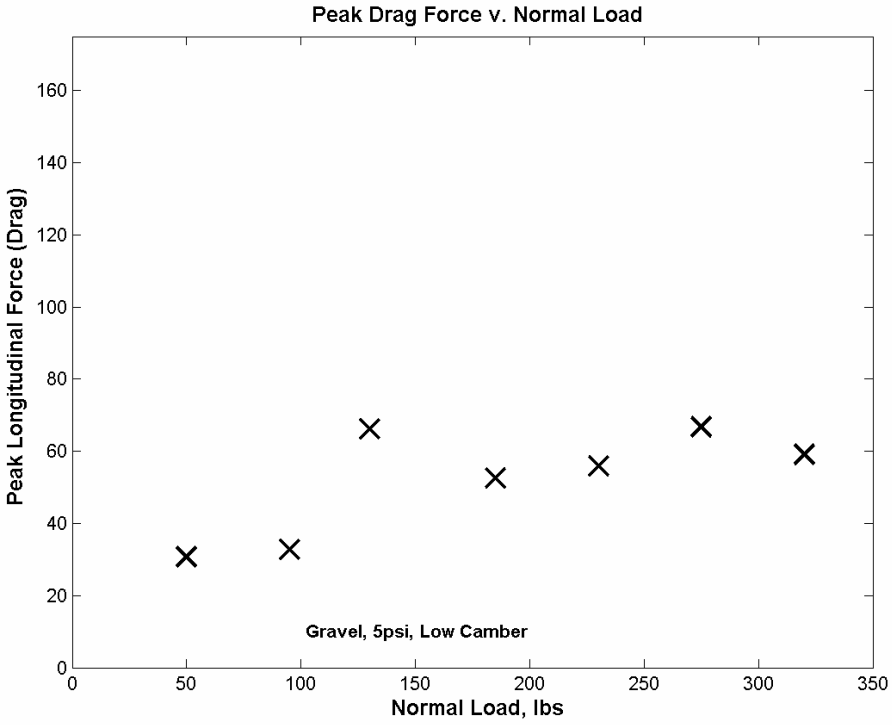
Peak Drag Force v. Normal Load
Peak Longitudinal Force (Drag)
Normal Load, lbs
Gravel, 5psi, Low Camber
0
20
40
60
80
100
120
140
160
0
50
100
150
200
250
300
350

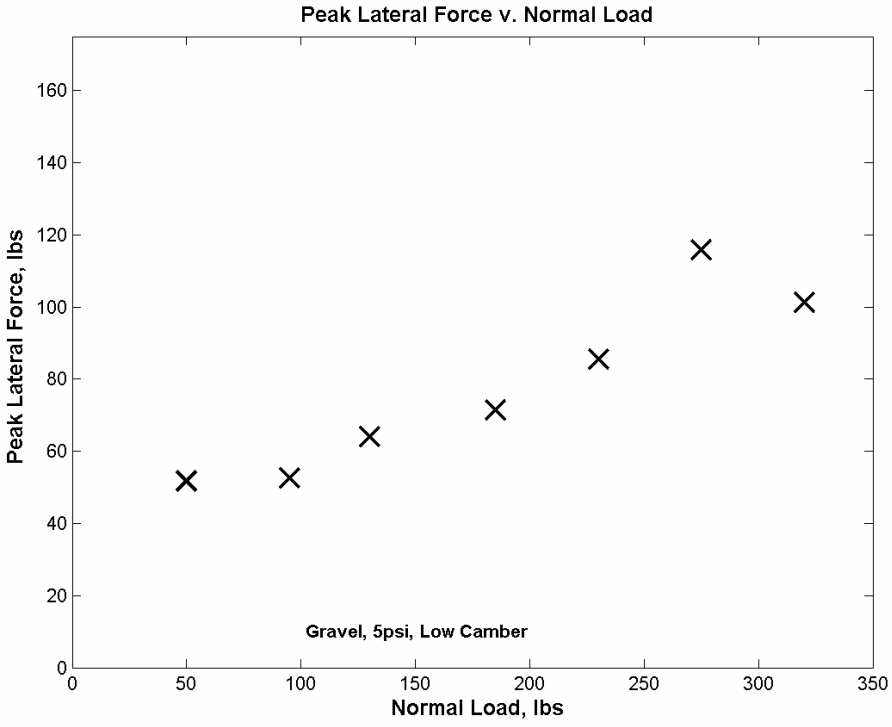
Peak Lateral Force v. Normal Load
Peak Lateral Force, lbs
Normal Load, lbs
Gravel, 5psi, Low Camber
0
20
40
60
80
100
120
140
160
0
50
100
150
200
250
300
350

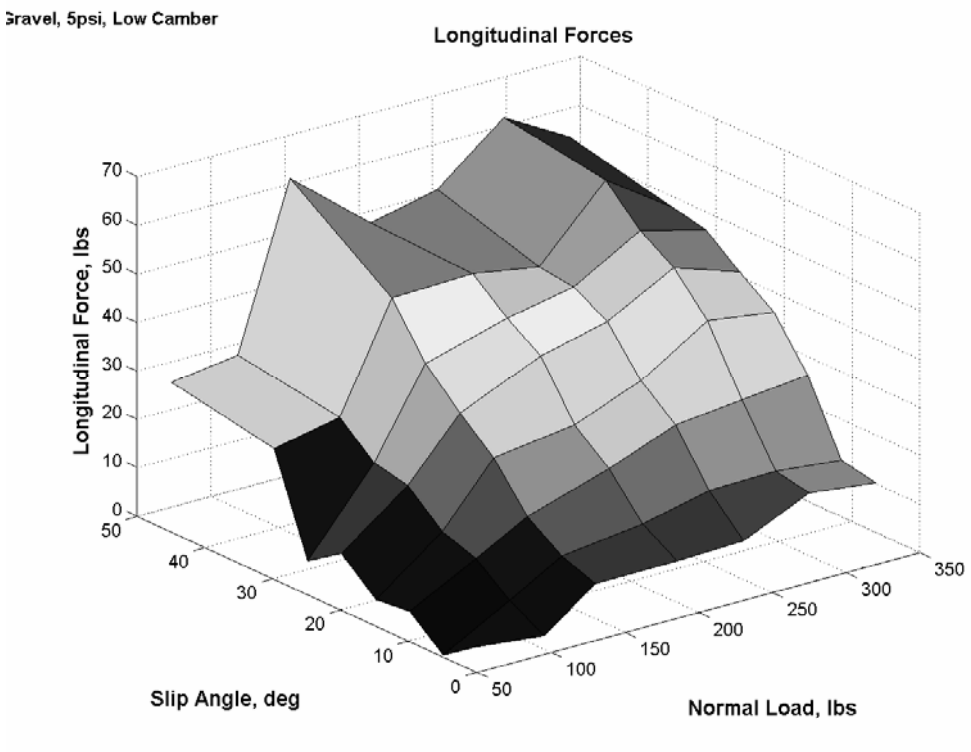
Gravel, 5psi, Low Camber
Longitudinal Forces
Longitudinal Force, lbs
70
60
50
40
30
20
10
0
50
40
30
20
10
0
Slip Angle, deg
50
100
150
200
250
300
350
Normal Load, lbs

Gravel, 5 psi, High Camber

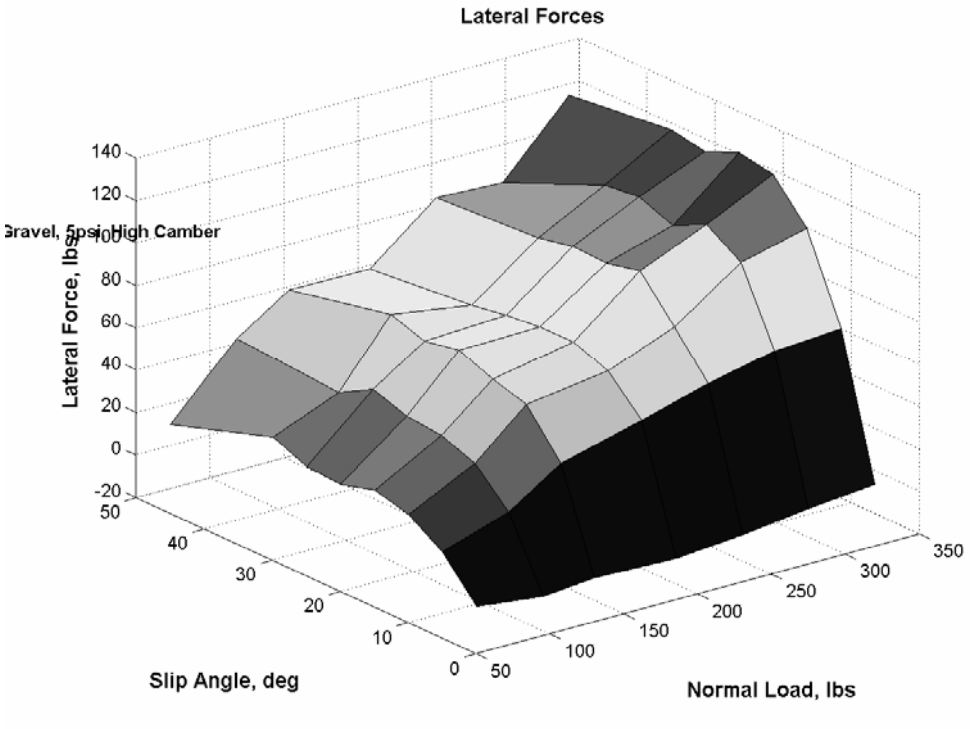

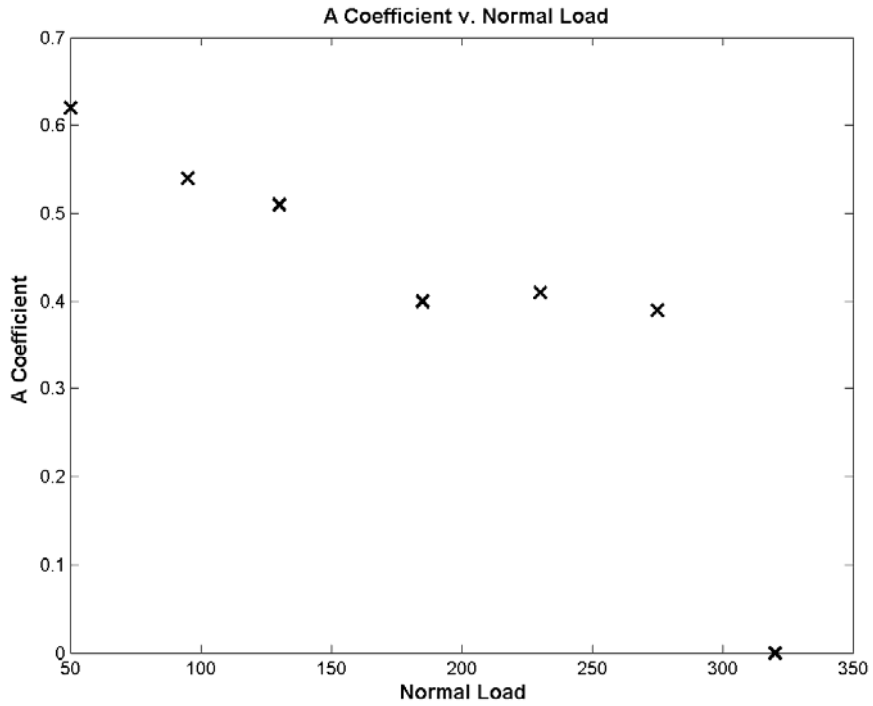

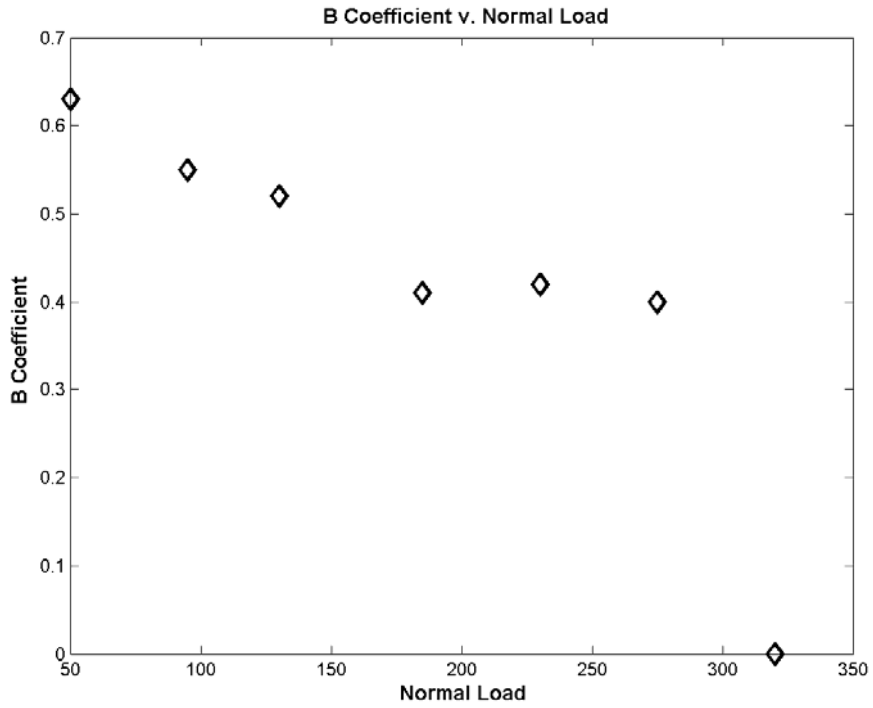
B Coefficient v. Normal Load
B Coefficient
Normal Load
0.7
0.6
0.5
0.4
0.3
0.2
0.1
0
50
100
150
200
250
300
350

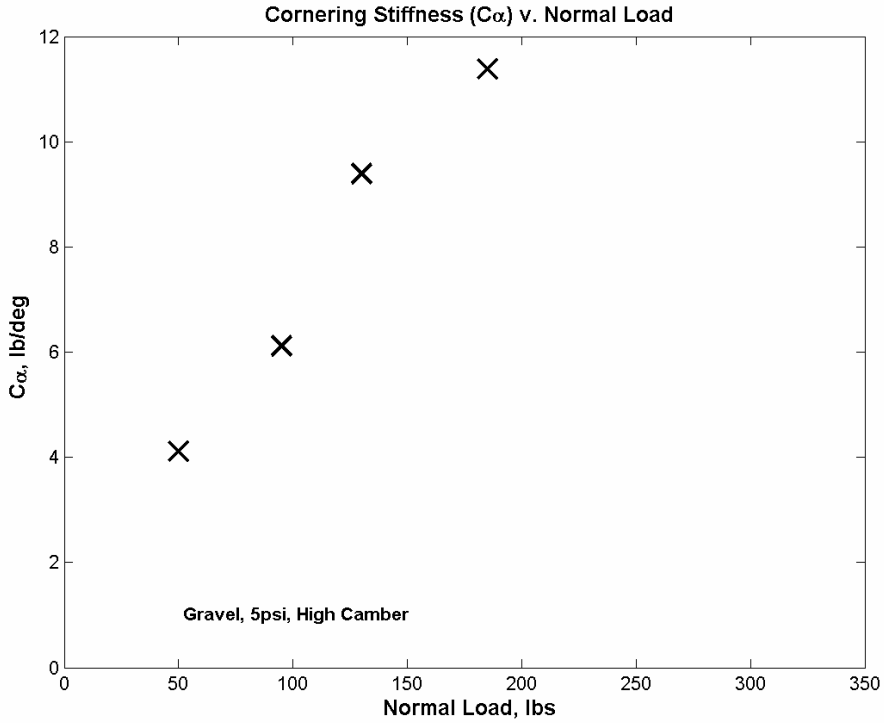
Cornering Stiffness (Cα) v. Normal Load
Cα, lb/deg
Normal Load, lbs
Gravel, 5psi, High Camber
12
10
8
6
4
2
0
0
50
100
150
200
250
300
350

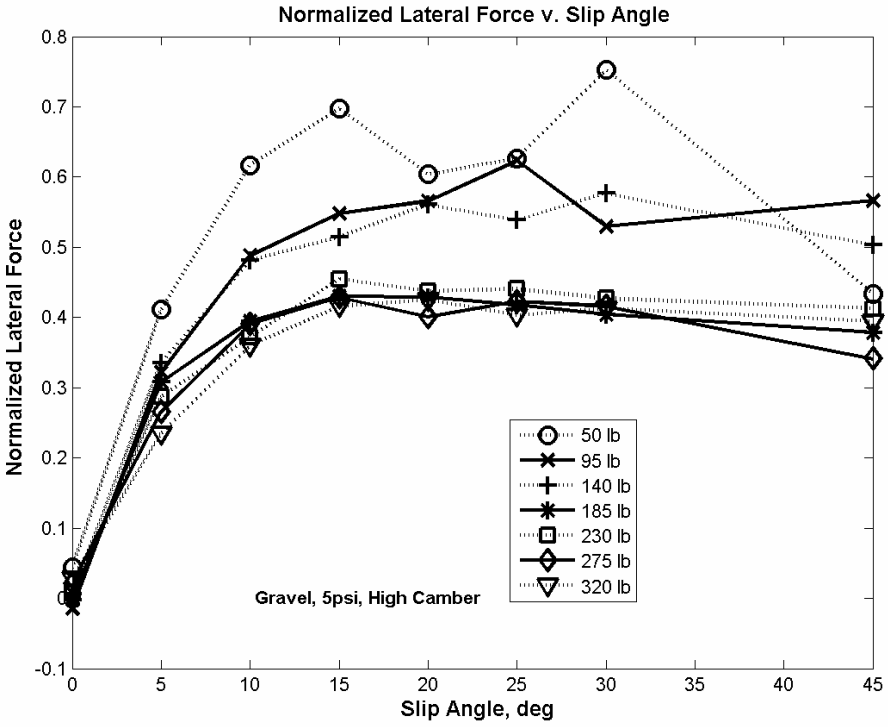
Normalized Lateral Force v. Slip Angle
Normalized Lateral Force
Slip Angle, deg
Gravel, 5psi, High Camber
50 lb
95 lb
140 lb
185 lb
230 lb
275 lb
320 lb

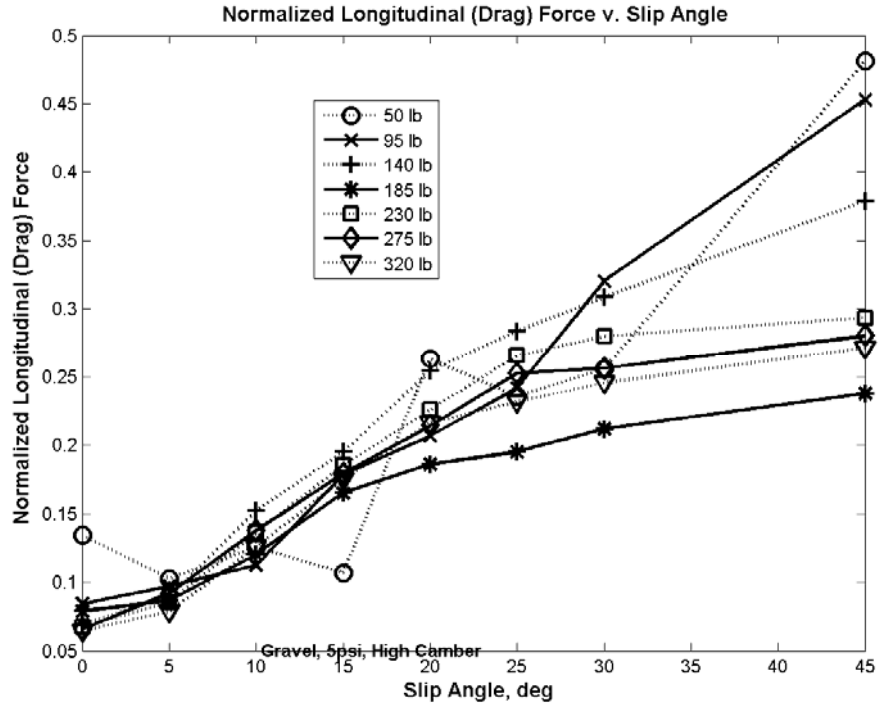
Normalized Longitudinal (Drag) Force v. Slip Angle
Normalized Longitudinal (Drag) Force
Slip Angle, deg
Gravel, 5psi, High Camber
50 lb
95 lb
140 lb
185 lb
230 lb
275 lb
320 lb

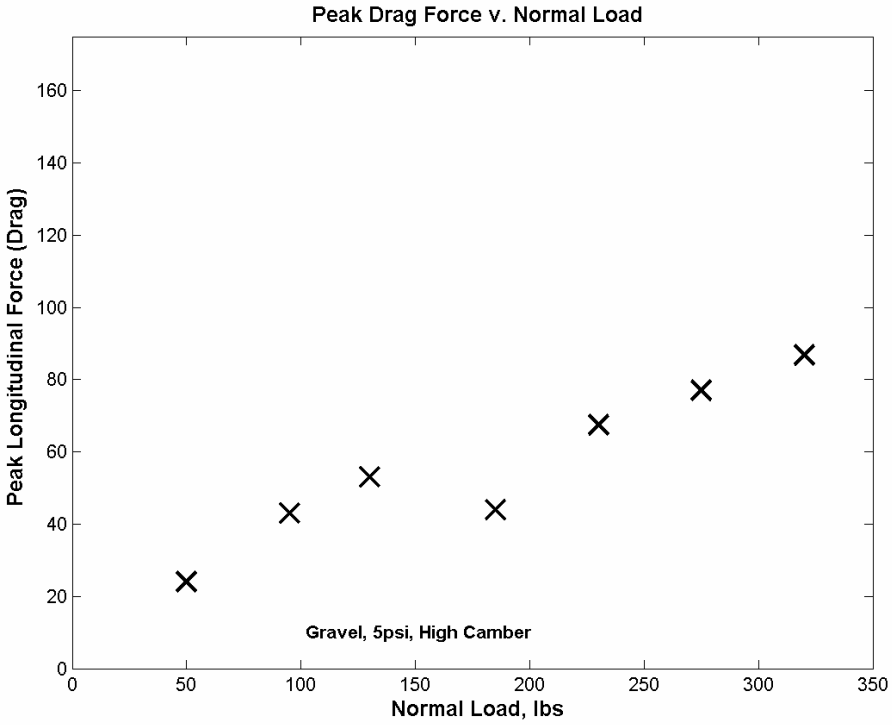
Peak Drag Force v. Normal Load
Peak Longitudinal Force (Drag)
Normal Load, lbs
Gravel, 5psi, High Camber
0
20
40
60
80
100
120
140
160
0
50
100
150
200
250
300
350

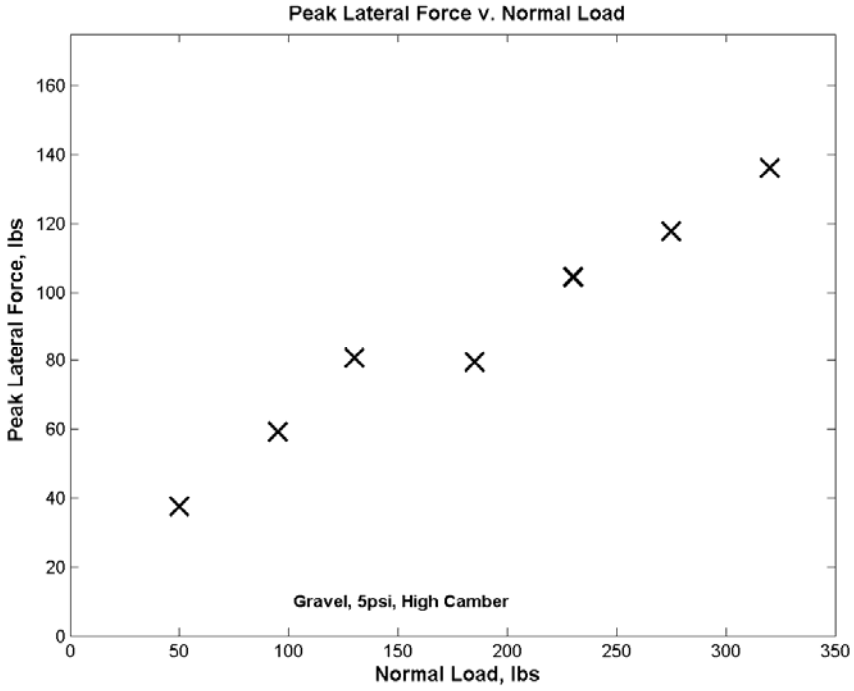
Peak Lateral Force v. Normal Load
Peak Lateral Force, lbs
Normal Load, lbs
Gravel, 5psi, High Camber
0
20
40
60
80
100
120
140
160
0
50
100
150
200
250
300
350

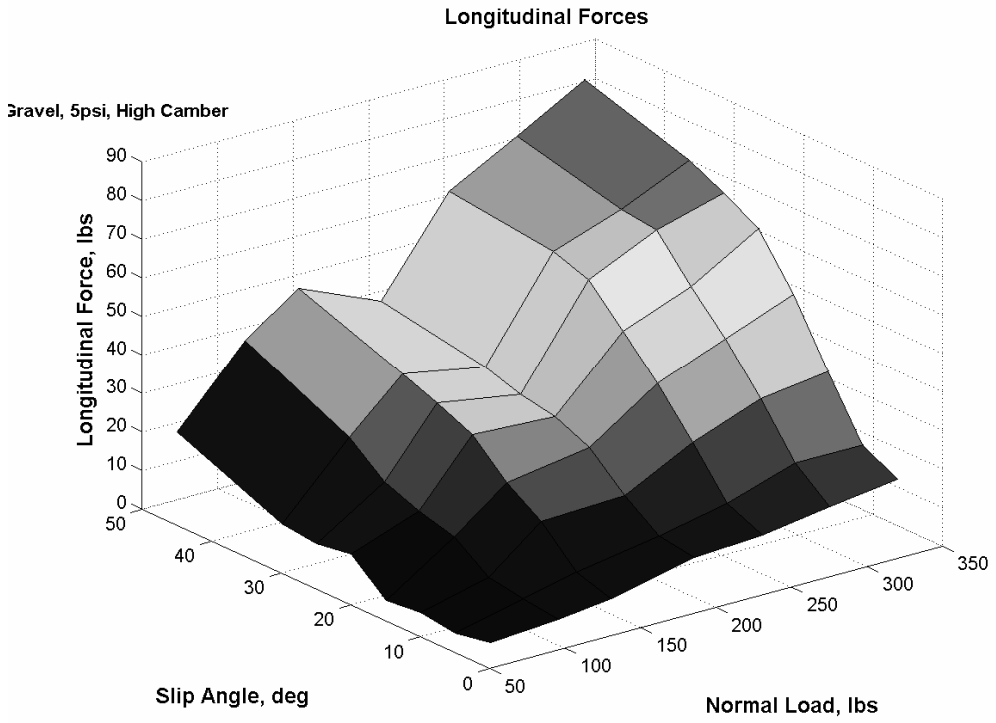
Longitudinal Forces
Gravel, 5psi, High Camber
Longitudinal Force, lbs
90
80
70
60
50
40
30
20
10
0
50
40
30
20
10
0
Slip Angle, deg
50
100
150
200
250
300
350
Normal Load, lbs

Gravel, 10 psi, High Camber

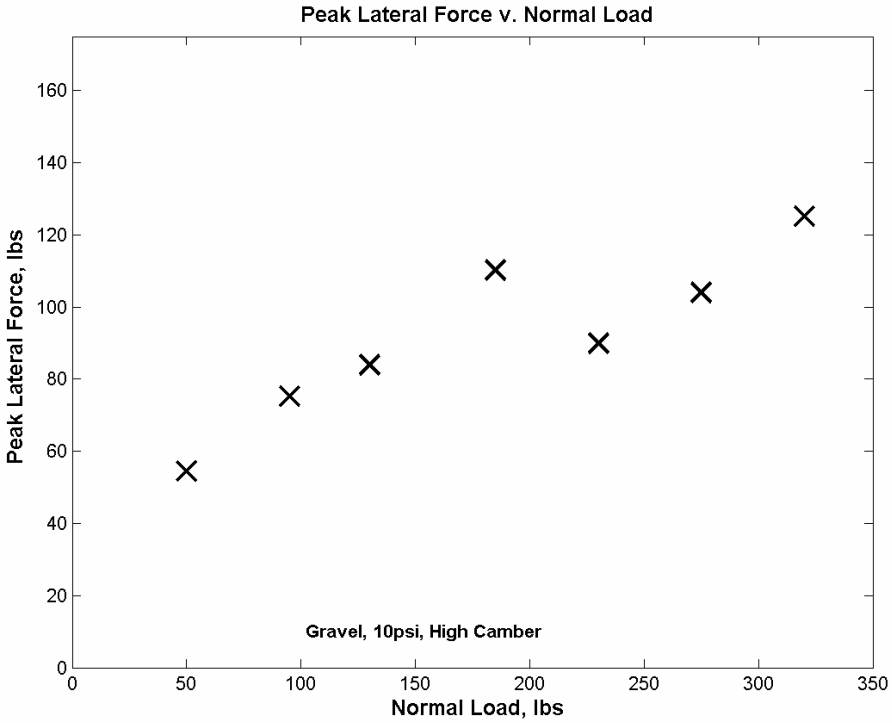

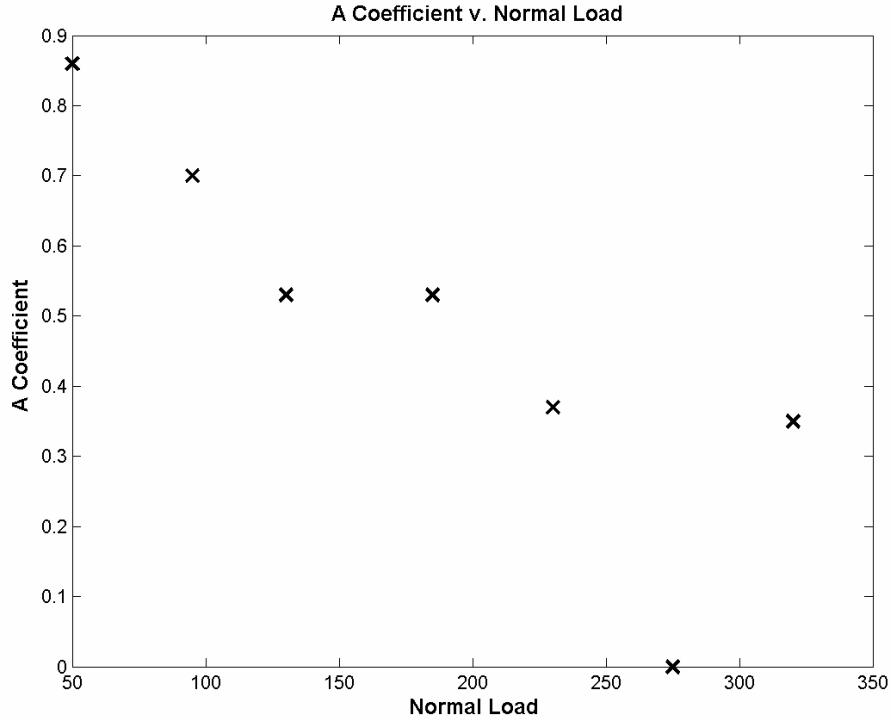

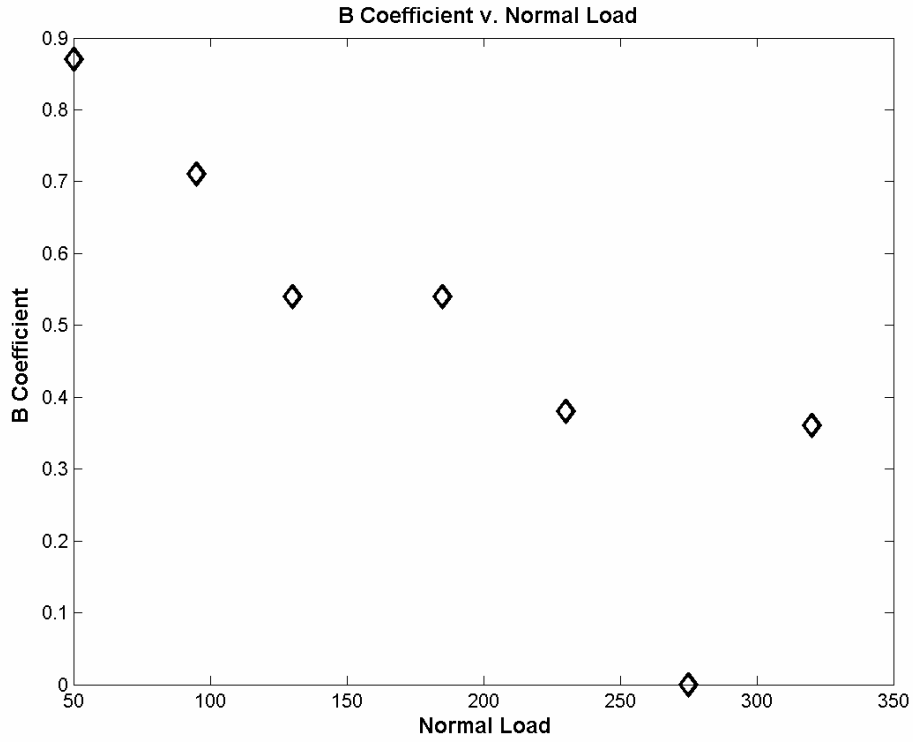
B Coefficient v. Normal Load
B Coefficient
Normal Load
0.9
0.8
0.7
0.6
0.5
0.4
0.3
0.2
0.1
0
50
100
150
200
250
300
350

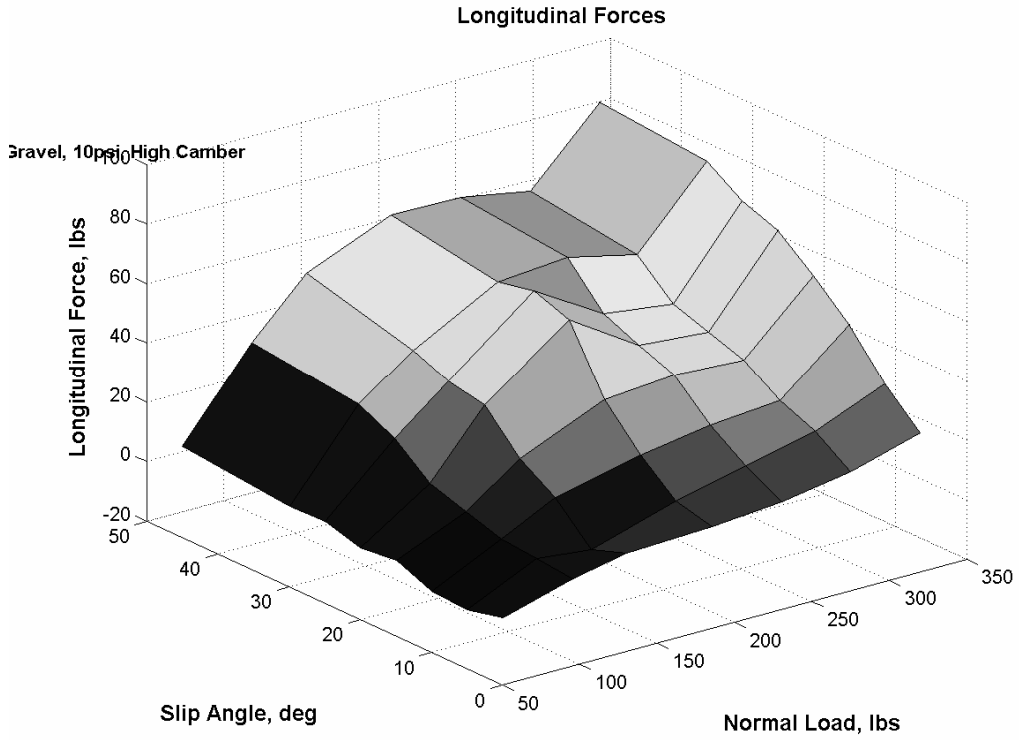
Longitudinal Forces
Gravel, 10psi, High Camber
Longitudinal Force, lbs
100
80
60
40
20
0
-20
50
40
30
20
10
0
Slip Angle, deg
50
100
150
200
250
300
350
Normal Load, lbs

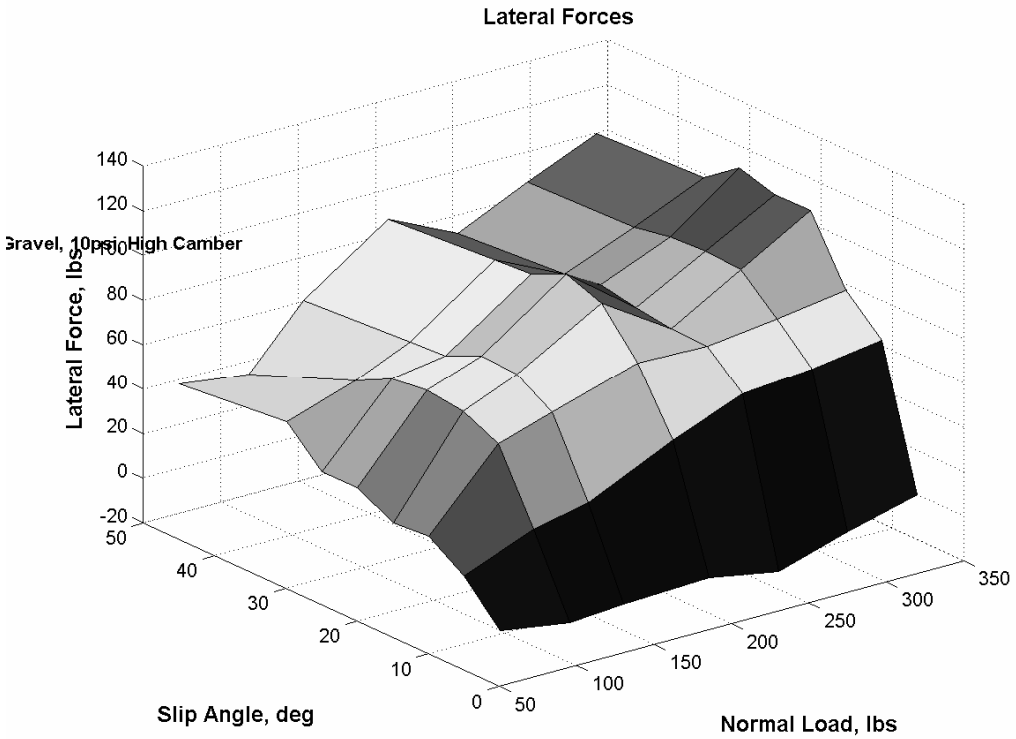
Lateral Forces
Gravel, 10psi, High Camber
Lateral Force, lbs
140
120
100
80
60
40
20
0
-20
50
40
30
20
10
0
Slip Angle, deg
50
100
150
200
250
300
350
Normal Load, lbs

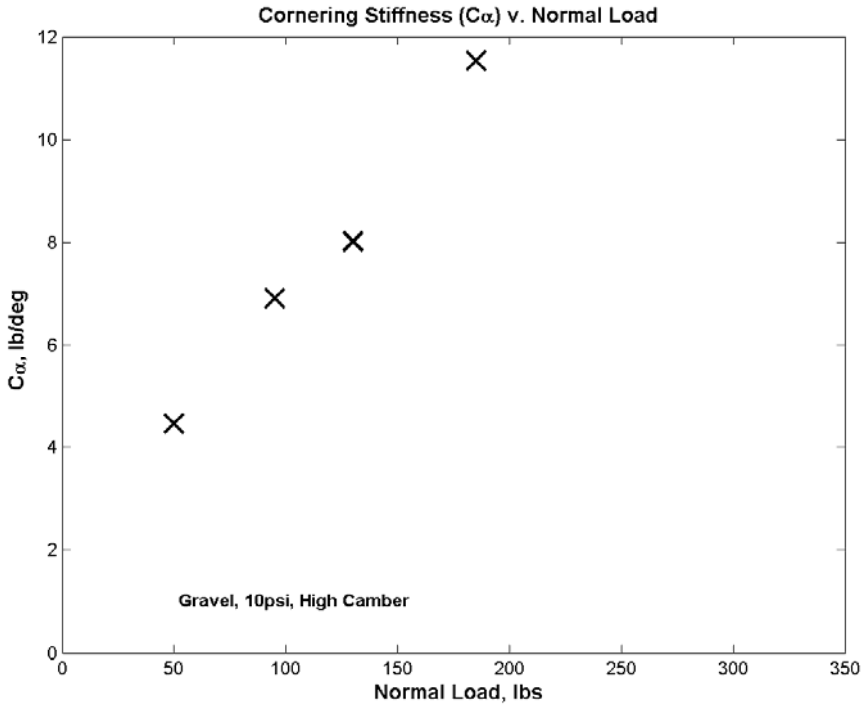
Cornering Stiffness (Cα) v. Normal Load
Cα, lb/deg
12
10
8
6
4
2
0
Gravel, 10psi, High Camber
0
50
100
150
200
250
300
350
Normal Load, lbs

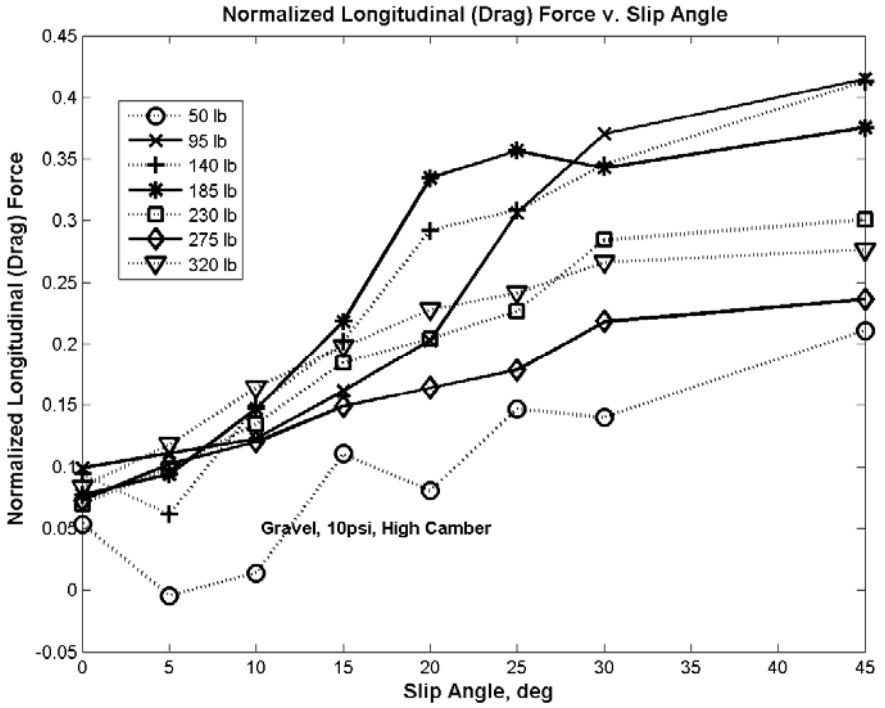
Normalized Longitudinal (Drag) Force v. Slip Angle
Normalized Longitudinal (Drag) Force
Slip Angle, deg
50 lb
95 lb
140 lb
185 lb
230 lb
275 lb
320 lb
Gravel, 10psi, High Camber

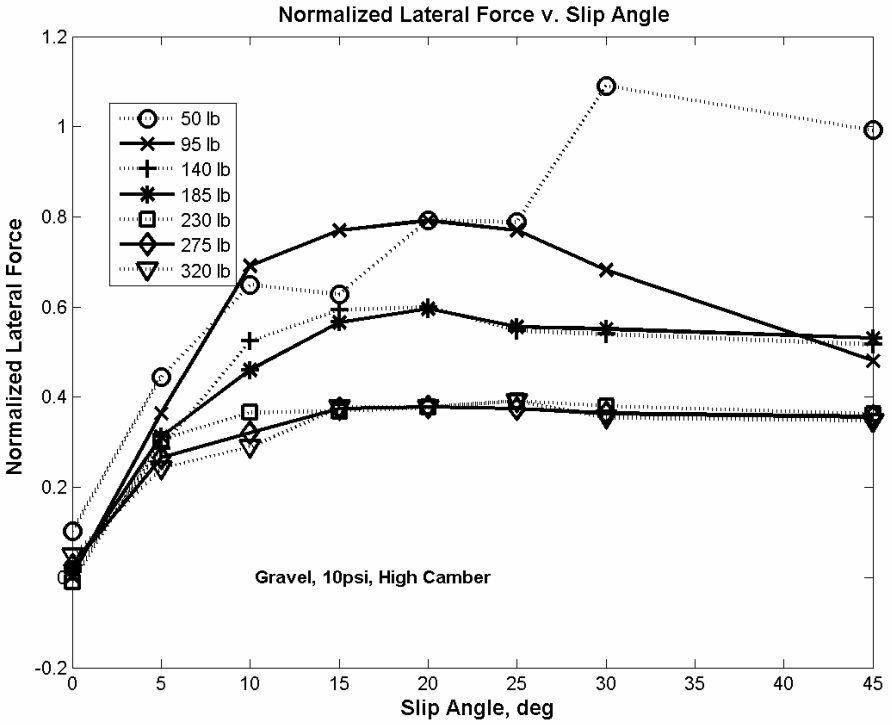
Normalized Lateral Force v. Slip Angle
Normalized Lateral Force
Slip Angle, deg
50 lb
95 lb
140 lb
185 lb
230 lb
275 lb
320 lb
Gravel, 10psi, High Camber

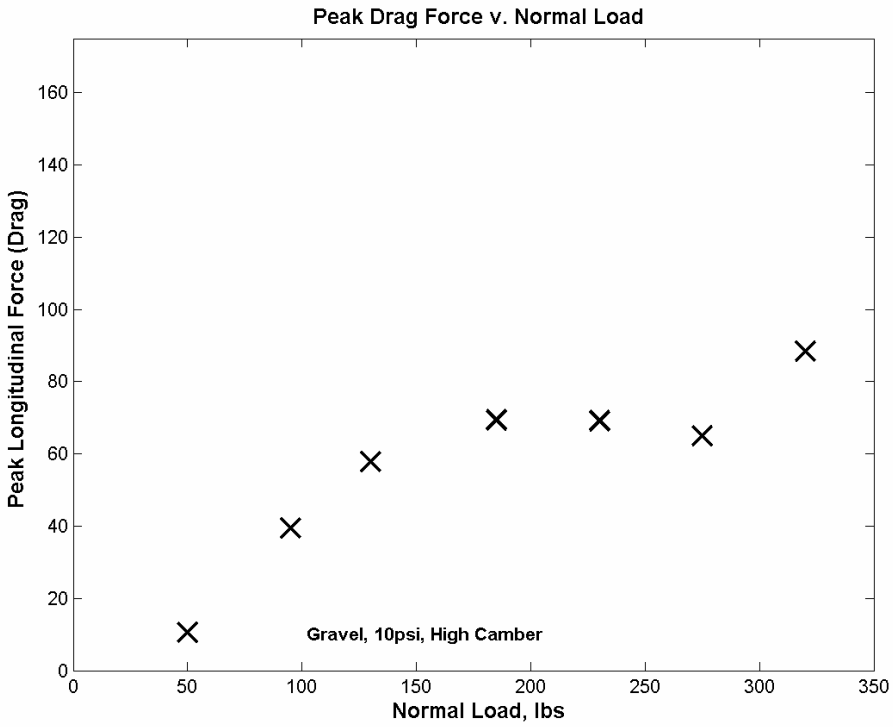
Peak Drag Force v. Normal Load
Peak Longitudinal Force (Drag)
Normal Load, lbs
Gravel, 10psi, High Camber
0
20
40
60
80
100
120
140
160
0
50
100
150
200
250
300
350

D. Computer Programs

Bevameter2.m – Bevameter data reduction program

```
clear
clc
clf
addpath('C:\DATAQMATLABExamples')

ring_od = 5; %Inches
ring_id = 3; %Inches
annulusarea = (pi*(ring_od/2)^2) - (pi*(ring_id/2)^2); %sq. in.
ringradius = 2/12; %ft
rval = 'R^2 = ';
mmkay = 'K = ';

%50psi
data = (ReadWinDaqFile('50psi.wdq',0,1800,1))'; % Read in Dataq file
shear50 = (((data(:,1)+.0004)/.0002)/ringradius)/annulusarea;
angle50 = (data(:,2)-data(1,2))/(5/360);
angle50(1168:1583) = angle50(1385:end)+34.63+685.2; % Adjusted because
pot ran over break point
angle50(1584:end) = angle50(1584:end)+104+658.7
% Adjusted because pot ran over break point
inch50 = angle50*((pi/180)*ringradius*12);
j=500;
k = 1;
while j <1800
    beaners50(k,1) = shear50(j);
    k = k+1;
    j= j+1;
end
residual50 = mean(beaners50);


%75psi
data = (ReadWinDaqFile('75psi.wdq',0,1800,1))'; % Read in Dataq file
shear75 = (((data(:,1)+.0004)/.0002)/ringradius)/annulusarea;
angle75 = (data(:,2)-data(1,2))/(5/360);
inch75 = angle75*((pi/180)*ringradius*12);
j=500;
k = 1;
while j <1800
    beaners75(k,1) = shear75(j);
    k = k+1;
    j= j+1;
end
residual75 = mean(beaners75);m

%100psi
data = (ReadWinDaqFile('100psi.wdq',0,1800,1))'; % Read in Dataq file
shear100 = (((data(:,1)+.0004)/.0002)/ringradius)/annulusarea;
```

```
angle100 = (data(:,2)-data(1,2))/(5/360);
inch100 = angle100*((pi/180)*ringradius*12);
j=500;
k = 1;
while j <1800
    beaners100(k,1) = shear100(j);
    k = k+1;
    j= j+1;
end
residual100 = mean(beaners100);

%125psi
data = (ReadWinDaqFile('125psi.wdq',0,1800,1))'; % Read in Dataq file
shear125 = (((data(:,1)+.0004)/.0002)/ringradius)/annulusarea;
angle125 = (data(:,2)-data(1,2))/(5/360);
inch125 = angle125*((pi/180)*ringradius*12);
j=500;
k = 1;
while j <1800
    beaners125(k,1) = shear125(j);
    k = k+1;
    j= j+1;
end
residual125 = mean(beaners125);


%Plot the shear displacement data
figure(1)
plot(inch50, shear50, '-k', 'linewidth',2)
hold on
plot(inch75, shear75, ':k', 'linewidth',2)
hold on
plot(inch100, shear100, '-k', 'linewidth',2)
hold on
plot(inch125, shear125, ':k', 'linewidth',2)
xlabel('\bf \fontsize{12}Displacement, in')
ylabel('\bf \fontsize{12}Shear Stress, psi')
title('\bf Shear Stress v. Displacement, Dirt Test 1')
legend('\sigma = 42.9 psi', '\sigma = 64.4 psi', '\sigma = 85.9 psi',
'\sigma = 107 psi')
print -djpeg dirt1raw
cylpress = [50;75;100;125];
cylinderarea =(pi*2^2)-(pi*.75^2); %2" OD, .75" ID on the pneu cyl
honeydew = cylpress.*cylinderarea;
normals = honeydew./annulusarea;
shears = [residual50;residual75;residual100;residual125];

fit = polyfit(normals, shears, 1);
fitting = polyval(fit,normals);

phi = atan(fit(1))*(180/pi)

%Plot Mohr-Coulomb Failure Envelope
figure(2)
```

```
plot(normals, shears, 'kx', 'linewidth', 2,'markersize', 15)
hold on
plot(normals, fitting, '-k', 'linewidth', 2)
title('\bf Mohr-Coulomb Failure Envelope, Dirt Test 2')
xlabel('\bf \fontsize{12}Normal Stress, psi')
ylabel('\bf \fontsize{12}Shear Stress, psi')
axis([30 120 0 20])
text(90, 18, '\bf \fontsize{12} \phi = 6.20 deg')
print -djpeg dirt1mohrcoulomb
% Shear Rate Plots
shish = [1:1:1800]';
sheartime = shish*.002084; % .002 is the time step
slopedy = sheartime(1000:1550); %indexes when sliding happened
figure(3)
plot(slopedy, inch100(1000:1550), '-k', 'linewidth',2)
hold on
plot(slopedy, inch75(1000:1550), ':k', 'linewidth',2)
hold on
plot(slopedy, inch125(1000:1550), '--k', 'linewidth',2)
title('\bf \fontsize{12} Shear Rate, Dirt Test 1')
xlabel('\bf \fontsize{12} Time, s')
ylabel('\bf \fontsize{12} Displacement, in')
legend('\sigma = 85.9 psi', '\sigma = 64.4 psi', '\sigma = 107 psi',
'Location','SouthEast')
axis([2 3.5 0 10])
print -djpeg dirt1shearrate

% Create plots to show fitting of shear stress data
%50 psi cylinder pressure
figure(4)
plot(inch50, shear50, '-k', 'linewidth',2)
K50=.01:.01:.99;
cheese = 1;
for cheese = 1:length(K50)
    shearfit50 = (((max(shear50)-residual50)/2)+residual50).*(1-exp(-
inch50./K50(cheese)));
    rsqd(cheese) = 1- sum((shearfit50-shear50).^2)/sum((shearfit50-
mean(shear50)).^2);
    if rsqd(cheese) >= max(rsqd)
        index50 = cheese;
    end
end
shearfit50 = (((max(shear50)-residual50)/2)+residual50).*(1-exp(-
inch50./K50(index50)));
hold on
plot(inch50, shearfit50, '--k')
title('\bf \fontsize{12}Exponential Shear Equation Fit, Dirt Test 1')
xlabel('\bf \fontsize{12} Displacement, in')
ylabel('\bf \fontsize{12} Shear Stress, psi')
legend('\sigma = 42.9 psi, Test 1', 'Exponential Curve Fit',
'location', 'southeast')
axis([-.5 6 0 15])
k50rsqd = num2str(rsqd(index50));
text(1,12, strcat(rval, k50rsqd))
mmkay50 = num2str(K50(index50));
```

```
stereoshift50 = strcat(mmkay, mmkay50);
text(1, 11, stereoshift50)
print -djpeg dirt1fit43

%75 psi cylinder pressure
figure(5)
plot(inch75, shear75, '-k', 'linewidth',2)
K75=.01:.01:.99;
cheese = 1;
for cheese = 1:length(K75)
    shearfit75 = (((max(shear75)-residual75)/2)+residual75).*(1-exp(-
inch75./K75(cheese)));
    rsqd(cheese) = 1- sum((shearfit75-shear75).^2)/sum((shearfit75-
mean(shear75)).^2);
    if rsqd(cheese) >= max(rsqd)
        index75 = cheese;
    end
end
shearfit75 = (((max(shear75)-residual75)/2)+residual75).*(1-exp(-
inch75./K75(index75)));
hold on
plot(inch75, shearfit75, '--k')
title('\bf \fontsize{12}Exponential Shear Equation Fit, Dirt Test 1')
xlabel('\bf \fontsize{12} Displacement, in')
ylabel('\bf \fontsize{12} Shear Stress, psi')
legend('\sigma = 64.4 psi, Test 1', 'Exponential Curve Fit',
'location', 'southeast')
axis([-.5 6 0 15])
k75rsqd = num2str(rsqd(index75));
text(1,11, strcat(rval, k75rsqd))
mmkay75 = num2str(K75(index75));
stereoshift75 = strcat(mmkay, mmkay75);
text(1, 10, stereoshift75)
print -djpeg dirt1fit64

%100 psi cylinder pressure
figure(6)
plot(inch100, shear100, '-k', 'linewidth',2)
K100=.01:.01:.99;
cheese = 1;
for cheese = 1:length(K100)
    shearfit100 = (((max(shear100)-residual100)/2)+residual100).*(1-
exp(-inch100./K100(cheese)));
    rsqd(cheese) = 1- sum((shearfit100-shear100).^2)/sum((shearfit100-
mean(shear100)).^2);
    if rsqd(cheese) >= max(rsqd)
        index100 = cheese;
    end
end

shearfit100 = (((max(shear100)-residual100)/2)+residual100).*(1-exp(-
inch100./K100(index100)));
hold on
plot(inch100, shearfit100, '--k')
title('\bf \fontsize{12}Exponential Shear Equation Fit, Dirt Test 1')
```

```
xlabel('\bf \fontsize{12} Displacement, in')
ylabel('\bf \fontsize{12} Shear Stress, psi')
legend('\sigma = 85.9 psi, Test 1', 'Exponential Curve Fit',
'location', 'southeast')
axis([-.5 6 0 20])
k100rsqd = num2str(rsqd(index100));
text(1,4, strcat(rval, k100rsqd))
mmkay100 = num2str(K100(index100));
stereoshift100 = strcat(mmkay, mmkay100);
text(1, 5, stereoshift100)
print -djpeg dirt1fit86

% %125 psi cylinder pressure
% figure(7)
% plot(inch125, shear125, '-b', 'linewidth',2)
% K125=.02;
% shearfit125 = (((max(shear125)-residual125)/2)+residual125).*(1-exp(-
inch125./K125));
% hold on
% plot(inch125, shearfit125, '-r')
% title('\bf \fontsize{12}Exponential Shear Equation Fit, Dirt Test 2')
% xlabel('\bf \fontsize{12} Displacement, in')
% ylabel('\bf \fontsize{12} Shear Stress, psi')
% legend('\sigma = 107 psi, Test 2', 'Exponential Curve Fit',
'location', 'southeast')
% axis([-.5 6 0 25])

% Shear modulus versus normal stress
shearmodulus = [K50(index50); K75(index75); K100(index100)];
figure(8)
plot(normals(1:3), shearmodulus, 'ko', 'linewidth', 2, 'markersize',
10')
title('\bf \fontsize{12} Shear Modulus v. Normal Stress, Gravel Test
1')
xlabel('\bf \fontsize{12} Normal Stress, psi')
ylabel('\bf \fontsize{12} Shear Modulus, in')
axis([40 110 0 .1])
print -djpeg dirt1shearmod

% See if the shear-displacement graph can collapse
normshear50 = shear50./42.9;
normshear75 = shear75./64.4;
normshear100 = shear100./85.9;
normshear125 = shear125./107;
norm_coeff_array =
[mean(normshear50(800:end));mean(normshear75(800:end));mean(normshear10
0(800:end));mean(normshear125(800:end))];
norm_coeff = mean(norm_coeff_array); % last half of data was analyzed,
average coeff for each data set was taken, then those were averaged

figure(9)
plot(inch50, normshear50, '-k', 'linewidth', 2)
hold on
plot(inch75, normshear75, '-.k', 'linewidth', 2)
hold on
```

```
plot(inch100, normshear100, ':k', 'linewidth', 2)
hold on
plot(inch125, normshear125, '--k', 'linewidth', 2)
title('\bf \fontsize{12} Normalized Shear Stress v. Displacement, Dirt
Test 2')
xlabel('\bf \fontsize{12} Displacement, in')
ylabel('\bf \fontsize{12} Normalized Shear Stress')
text( .5,.05, '\bf \fontsize{12} Mean Normalized Shear Stress = 0.185')
print -djpeg dirt1collapsed

dataout(:,1) = normals;
dataout(:,2) = shears;


csvwrite('dirt1.csv', dataout)
```

reduction.m – Tire rig data reduction program

```
clear
clc
clf
addpath('C:\DATAQMATLABExamples')
% 1 - vert accel
% 2 - lat accel
% 3 - hall effect
% 4 - clinometer
% 5 - f6 load cell
% 6 - f7 load cell
% 7 - f8 load cell



%Test Details
pressure = 5;   %PSI
fz = 140;       %lbs
surface = 1     %Gravel
info = zeros(8,1) %Generate blank vector
info(1,1) = pressure; %Add pressure to info vector
info(2,1) = fz;       %Add normal load to info vector
info(3,1) = surface;  %Add surface to info vector

tolerance = .1; % normal load tolerance
upperbound = fz+(fz*tolerance); %Set upper normal load bound
lowerbound = fz-(fz*tolerance); %Set lower normal load bound
%Setup slipangle vector
slipangle = [0;5;10;15;20;25;30;45]; %Generate slip angle vector

%Now, individually go through each file, and calculate appropriate data
% Alpha 0-----------------------------------------------------------------
---
data = (ReadWinDaqFile('alpha0.wdq',100,2000,1))'; % Read in Dataq file
fvert = fz*(1.0256*data(:,1)-2.5331); %take normal load voltage and
convert to lbs
n=1;
j=1;

while n <= length(data)
    if (fvert(n) >= lowerbound) & (fvert(n) <= upperbound)   %if the
normal load is within tolerance, save that index of data
        newdata(j,1) = data(n,1);
        newdata(j,2) = data(n,2);
        newdata(j,3) = data(n,3);
        newdata(j,4) = data(n,4);
        newdata(j,5) = data(n,5);
        newdata(j,6) = data(n,6);
        newdata(j,7) = data(n,7);
        j=j+1;
    end
    n=n+1;
```

```
end
glat = 1.0256*newdata(:,2)-2.5331;  % take lateral accel voltage and
convert to G
halleff = newdata(:,3);

f6 = newdata(:,5)/(7*10^-5);  %Load cell voltage and convert to lbs
f7 = newdata(:,6)/(7*10^-5);
f8 = newdata(:,7)/(7*10^-5);

fx0 =
f6*sin(slipangle(1,1)*(pi/180))+f7*cos(slipangle(1,1)*(pi/180))+f8*cos(
slipangle(1,1)*(pi/180)); %Longitudinal force
fy0 = -
f6*cos(slipangle(1,1)*(pi/180))+f7*sin(slipangle(1,1)*(pi/180))+f8*sin(
slipangle(1,1)*(pi/180)); %Lateral Force

avgfx(1,1) = mean(fx0)  %Average value of longitudinal force vector
stdfx(1,1) = std(fx0)/sqrt(length(fx0))   %Standard error
avgfy(1,1) = mean(fy0)  %Average value of lateral force vector
stdfy(1,1) = std(fy0)/sqrt(length(fx0))   %Standard error
%=====================================================================
==
%
% % Alpha 5 ------------------------------------------------------------
-----
data = (ReadWinDaqFile('alpha5.wdq',100,2000,1))';
fvert = fz*(1.0256*data(:,1)-2.5331);
n=1;
j=1;

while n <= length(data)
    if (fvert(n) >= lowerbound) & (fvert(n) <= upperbound)
        newdata(j,1) = data(n,1);
        newdata(j,2) = data(n,2);
        newdata(j,3) = data(n,3);
        newdata(j,4) = data(n,4);
        newdata(j,5) = data(n,5);
        newdata(j,6) = data(n,6);
        newdata(j,7) = data(n,7);
        j=j+1;
    end
    n=n+1;
end
glat = 1.0256*newdata(:,2)-2.5331;
halleff = newdata(:,3);


f6 = newdata(:,5)/(7*10^-5);
f7 = newdata(:,6)/(7*10^-5);
f8 = newdata(:,7)/(7*10^-5);

fx0 =
f6*sin(slipangle(1,1)*(pi/180))+f7*cos(slipangle(1,1)*(pi/180))+f8*cos(
slipangle(1,1)*(pi/180));
```

```
fy0 = -
f6*cos(slipangle(1,1)*(pi/180))+f7*sin(slipangle(1,1)*(pi/180))+f8*sin(
slipangle(1,1)*(pi/180));


avgfx(2,1) = mean(fx0)
stdfx(2,1) = std(fx0)/sqrt(length(fx0))
avgfy(2,1) = mean(fy0)
stdfy(2,1) = std(fy0)/sqrt(length(fx0))
%
%=========================================================================
===
%
% % Alpha 10 ---------------------------------------------------------------
-----
data = (ReadWinDaqFile('alpha10.wdq',100,2000,1))';
fvert = fz*(1.0256*data(:,1)-2.5331);
n=1;
j=1;

while n <= length(data)
    if (fvert(n) >= lowerbound) & (fvert(n) <= upperbound)
        newdata(j,1) = data(n,1);
        newdata(j,2) = data(n,2);
        newdata(j,3) = data(n,3);
        newdata(j,4) = data(n,4);
        newdata(j,5) = data(n,5);
        newdata(j,6) = data(n,6);
        newdata(j,7) = data(n,7);
        j=j+1;
    end
    n=n+1;
end
glat = 1.0256*newdata(:,2)-2.5331;
halleff = newdata(:,3);

f6 = newdata(:,5)/(7*10^-5);
f7 = newdata(:,6)/(7*10^-5);
f8 = newdata(:,7)/(7*10^-5);

fx0 =
f6*sin(slipangle(1,1)*(pi/180))+f7*cos(slipangle(1,1)*(pi/180))+f8*cos(
slipangle(1,1)*(pi/180));
fy0 = -
f6*cos(slipangle(1,1)*(pi/180))+f7*sin(slipangle(1,1)*(pi/180))+f8*sin(
slipangle(1,1)*(pi/180));


avgfx(3,1) = mean(fx0)
stdfx(3,1) = std(fx0)/sqrt(length(fx0))
avgfy(3,1) = mean(fy0)
stdfy(3,1) = std(fy0)/sqrt(length(fx0))
```

```
%
%=========================================================================
===
%
% % Alpha 15 ---------------------------------------------------------
-----
data = (ReadWinDaqFile('alpha15.wdq',100,2000,1))';
fvert = fz*(1.0256*data(:,1)-2.5331);
n=1;
j=1;

while n <= length(data)
    if (fvert(n) >= lowerbound) & (fvert(n) <= upperbound)
        newdata(j,1) = data(n,1);
        newdata(j,2) = data(n,2);
        newdata(j,3) = data(n,3);
        newdata(j,4) = data(n,4);
        newdata(j,5) = data(n,5);
        newdata(j,6) = data(n,6);
        newdata(j,7) = data(n,7);
        j=j+1;
    end
    n=n+1;
end
glat = 1.0256*newdata(:,2)-2.5331;
halleff = newdata(:,3);



f6 = newdata(:,5)/(7*10^-5);
f7 = newdata(:,6)/(7*10^-5);
f8 = newdata(:,7)/(7*10^-5);

fx0 =
f6*sin(slipangle(1,1)*(pi/180))+f7*cos(slipangle(1,1)*(pi/180))+f8*cos(
slipangle(1,1)*(pi/180));
fy0 = -
f6*cos(slipangle(1,1)*(pi/180))+f7*sin(slipangle(1,1)*(pi/180))+f8*sin(
slipangle(1,1)*(pi/180));



avgfx(4,1) = mean(fx0)
stdfx(4,1) = std(fx0)/sqrt(length(fx0))
avgfy(4,1) = mean(fy0)
stdfy(4,1) = std(fy0)/sqrt(length(fx0))
%
%=========================================================================
===
%
% % Alpha 20 ---------------------------------------------------------
-----
data = (ReadWinDaqFile('alpha20.wdq',100,2000,1))';
fvert = fz*(1.0256*data(:,1)-2.5331);
```

```
n=1;
j=1;

while n <= length(data)
    if (fvert(n) >= lowerbound) & (fvert(n) <= upperbound)
        newdata(j,1) = data(n,1);
        newdata(j,2) = data(n,2);
        newdata(j,3) = data(n,3);
        newdata(j,4) = data(n,4);
        newdata(j,5) = data(n,5);
        newdata(j,6) = data(n,6);
        newdata(j,7) = data(n,7);
        j=j+1;
    end
    n=n+1;
end
glat = 1.0256*newdata(:,2)-2.5331;
halleff = newdata(:,3);



f6 = newdata(:,5)/(7*10^-5);
f7 = newdata(:,6)/(7*10^-5);
f8 = newdata(:,7)/(7*10^-5);

fx0 =
f6*sin(slipangle(1,1)*(pi/180))+f7*cos(slipangle(1,1)*(pi/180))+f8*cos(
slipangle(1,1)*(pi/180));
fy0 = -
f6*cos(slipangle(1,1)*(pi/180))+f7*sin(slipangle(1,1)*(pi/180))+f8*sin(
slipangle(1,1)*(pi/180));



avgfx(5,1) = mean(fx0)
stdfx(5,1) = std(fx0)/sqrt(length(fx0))
avgfy(5,1) = mean(fy0)
stdfy(5,1) = std(fy0)/sqrt(length(fx0))
%
%=========================================================================
====
%
% Alpha 25 ---------------------------------------------------------------
----
data = (ReadWinDaqFile('alpha25.wdq',100,2000,1))';
fvert = fz*(1.0256*data(:,1)-2.5331);
n=1;
j=1;

while n <= length(data)
    if (fvert(n) >= lowerbound) & (fvert(n) <= upperbound)
        newdata(j,1) = data(n,1);
        newdata(j,2) = data(n,2);
        newdata(j,3) = data(n,3);
```

```
        newdata(j,4) = data(n,4);
        newdata(j,5) = data(n,5);
        newdata(j,6) = data(n,6);
        newdata(j,7) = data(n,7);
        j=j+1;
    end
    n=n+1;
end
glat = 1.0256*newdata(:,2)-2.5331;
halleff = newdata(:,3);


f6 = newdata(:,5)/(7*10^-5);
f7 = newdata(:,6)/(7*10^-5);
f8 = newdata(:,7)/(7*10^-5);

fx0 =
f6*sin(slipangle(1,1)*(pi/180))+f7*cos(slipangle(1,1)*(pi/180))+f8*cos(
slipangle(1,1)*(pi/180));
fy0 = -
f6*cos(slipangle(1,1)*(pi/180))+f7*sin(slipangle(1,1)*(pi/180))+f8*sin(
slipangle(1,1)*(pi/180));

avgfx(6,1) = mean(fx0)
stdfx(6,1) = std(fx0)/sqrt(length(fx0))
avgfy(6,1) = mean(fy0)
stdfy(6,1) = std(fy0)/sqrt(length(fx0))
%=========================================================================
====
%
% % Alpha 30 ---------------------------------------------------------
-----
data = (ReadWinDaqFile('alpha30.wdq',100,2000,1))';
fvert = fz*(1.0256*data(:,1)-2.5331);
n=1;
j=1;

while n <= length(data)
    if (fvert(n) >= lowerbound) & (fvert(n) <= upperbound)
        newdata(j,1) = data(n,1);
        newdata(j,2) = data(n,2);
        newdata(j,3) = data(n,3);
        newdata(j,4) = data(n,4);
        newdata(j,5) = data(n,5);
        newdata(j,6) = data(n,6);
        newdata(j,7) = data(n,7);
        j=j+1;
    end
    n=n+1;
end
glat = 1.0256*newdata(:,2)-2.5331;
halleff = newdata(:,3);

f6 = newdata(:,5)/(7*10^-5);
```

```
f7 = newdata(:,6)/(7*10^-5);
f8 = newdata(:,7)/(7*10^-5);

fx0 =
f6*sin(slipangle(1,1)*(pi/180))+f7*cos(slipangle(1,1)*(pi/180))+f8*cos(
slipangle(1,1)*(pi/180));
fy0 = -
f6*cos(slipangle(1,1)*(pi/180))+f7*sin(slipangle(1,1)*(pi/180))+f8*sin(
slipangle(1,1)*(pi/180));


avgfx(7,1) = mean(fx0)
stdfx(7,1) = std(fx0)/sqrt(length(fx0))
avgfy(7,1) = mean(fy0)
stdfy(7,1) = std(fy0)/sqrt(length(fx0))
%=========================================================================
====

% % Alpha 45 ------------------------------------------------------------
------
data = (ReadWinDaqFile('alpha45.wdq',100,2000,1))';
fvert = fz*(1.0256*data(:,1)-2.5331);
n=1;
j=1;

while n <= length(data)
    if (fvert(n) >= lowerbound) & (fvert(n) <= upperbound)
        newdata(j,1) = data(n,1);
        newdata(j,2) = data(n,2);
        newdata(j,3) = data(n,3);
        newdata(j,4) = data(n,4);
        newdata(j,5) = data(n,5);
        newdata(j,6) = data(n,6);
        newdata(j,7) = data(n,7);
        j=j+1;
    end
    n=n+1;
end
glat = 1.0256*newdata(:,2)-2.5331;
halleff = newdata(:,3);


f6 = newdata(:,5)/(7*10^-5);
f7 = newdata(:,6)/(7*10^-5);
f8 = newdata(:,7)/(7*10^-5);

fx0 =
f6*sin(slipangle(1,1)*(pi/180))+f7*cos(slipangle(1,1)*(pi/180))+f8*cos(
slipangle(1,1)*(pi/180));
fy0 = -
f6*cos(slipangle(1,1)*(pi/180))+f7*sin(slipangle(1,1)*(pi/180))+f8*sin(
slipangle(1,1)*(pi/180));
```

```
avgfx(8,1) = mean(fx0)
stdfx(8,1) = std(fx0)/sqrt(length(fx0))
avgfy(8,1) = mean(fy0)
stdfy(8,1) = std(fy0)/sqrt(length(fx0))
%=========================================================================
====
% "It doesn't hook up to the internet, it doesn't brush your teeth for
you,
% it just makes phone calls. Damnit I miss that phone."
% "Yep, ya cross them at Jaspermatater"
% JL Scott


clf

%Curve Fitting
%Seek to minimize the sum of absolute value of the errors
alphafit = [0;5;10;15;20;25;30;45];
%generate all the possible combinations
rickybobby = makecomb(100,2);
rickybobby = (rickybobby/100)';
% Check every possible combination and note the lowest error's index
% Yes, it's inefficient, but it's easy to program, and there's not that
% many numbers to go through.
for r=1:length(rickybobby)
    fyfit = fz*rickybobby(r,1)*(1-exp(-rickybobby(r,2)*alphafit));
    rsqd(r) = 1-(sum((fyfit-avgfy).^2)/sum((fyfit-mean(avgfy)).^2));
    if rsqd(r) >= max(rsqd)
        index = r;
    end
end
% Take calculated values for A and B and apply them to a curve fit.
A = rickybobby(index,1);
B = rickybobby(index,2);
fyfit = fz*A*(1-exp(-B*alphafit));
%Put A and B values into the information vector for transfer
info(4,1) = A;
info(5,1) = B;

%Put error value into info vector
%Recall the error figure here is the sum of the absolute value of the
errors
info(6,1) = rsqd(index);

figure(1)
errorbar(slipangle, avgfy, stdfy, '-kx')
hold on
errorbar(slipangle, avgfx, stdfx, '-.k*')
hold on
plot(alphafit,fyfit,'--k')
axis([0 45 -5 150]);
title('\bf \fontsize{12}Tire Forces')
xlabel('\bf \fontsize{12} Slip Angle, deg')
```

```
ylabel('\bf \fontsize{12} Force, lbs')
legend('Lateral Force', 'Drag Force', 'Lateral Force Fit','location',
'southeast')
turd = 'Fit R Squared = ';
dash9 = num2str(rsqd(index));
text(2,120, strcat(turd, dash9))
% title('Tire Forces');
% xlabel('Slip Angle, deg');
% ylabel('Force, lbs');
grid on
% figure(2)
% plot(slipangle, avgfy, '-r')
% hold on
% plot(alphafit, fyfit)
% axis([0 45 -5 150]);
% title('Tire Forces');
% xlabel('Slip Angle, deg');
% ylabel('Force, lbs');
% grid on

% Need to add camber angle certainty stuff
% Need to add vertical load certainty?

%Output Tire Data
tiredata = [slipangle,avgfy,stdfy,avgfx,stdfx,info]
csvwrite('C:\DATAQ\446CE22C\dunlop821\gravel\5psi\high\output140.csv',
tiredata)

figure(2)
plot(rsqd, 'k')
xlabel('Index number')
ylabel('R^2 Value')
title('Trace of R^2 values')
print -dtiff rsquared
```

compare.m – Program to compare results of camber, pressure, and surface tire data

```
% This file will be used to generate comparison plots for camber,
% inflation pressure and operating surface
clear
clc
clf
% The key plots to compare each situation will be:
% 1) Calpha v. Fz
% 2) Peak Fy v. Fz
% 3) Peak Fx v. Fz
% 4) Normalized Fy v. alpha


% Firstly, lets load everything

grav10highfz =
csvread('C:\DATAQ\446CE22C\dunlop821\gravel\10psi\high\grav10highfz');
grav10highfy =
csvread('C:\DATAQ\446CE22C\dunlop821\gravel\10psi\high\grav10highfy');

grav10lowfz =
csvread('C:\DATAQ\446CE22C\dunlop821\gravel\10psi\low\grav10lowfz');
grav10lowfy =
csvread('C:\DATAQ\446CE22C\dunlop821\gravel\10psi\low\grav10lowfy');

grav5highfz =
csvread('C:\DATAQ\446CE22C\dunlop821\gravel\5psi\high\grav5highfz');
grav5highfy =
csvread('C:\DATAQ\446CE22C\dunlop821\gravel\5psi\high\grav5highfy');

grav5lowfz =
csvread('C:\DATAQ\446CE22C\dunlop821\gravel\5psi\low\grav5lowfz');
grav5lowfy =
csvread('C:\DATAQ\446CE22C\dunlop821\gravel\5psi\low\grav5lowfy');

clay10lowfz =
csvread('C:\DATAQ\446CE22C\dunlop821\clay\10psi\low\clay10lowfz');
clay10lowfy =
csvread('C:\DATAQ\446CE22C\dunlop821\clay\10psi\low\clay10lowfy');
%=========================================================================
====
%Camber effects
%=========================================================================
====
%On Calpha
figure(1)
plot(grav10highfz(:,1), grav10highfz(:,2), 'k*', 'linewidth', 2,
'markersize',10) %High Camber
hold on
plot(grav10lowfz(:,1), grav10lowfz(:,2), 'kx', 'linewidth', 2,
'markersize',10) %Low Camber
title('\bf \fontsize{12} Cornering Stiffness v. Normal Load')
xlabel('\bf \fontsize{12} Normal Load, lbs')
```

```
ylabel('\bf \fontsize{12} Cornering Stiffness, C\alpha, lbs/deg')
legend('High Camber', 'Low Camber', 'location', 'southeast')
axis([0 350 0 20])
print -dtiff calphacamber

%On Peak Fx
figure(2)
plot(grav10highfz(:,1), grav10highfz(:,3), 'k*', 'linewidth', 2,
'markersize', 10) %High Camber
hold on
plot(grav10lowfz(:,1), grav10lowfz(:,3), 'kx', 'linewidth', 2,
'markersize', 10) %Low Camber
title('\bf\fontsize{12} Peak Longitudinal Force v. Normal Load')
xlabel('\bf\fontsize{12} Normal Load, lbs')
ylabel('\bf\fontsize{12} Peak Longitudinal Force, lbs')
legend('High Camber', 'Low Camber', 'location', 'southeast')
axis([0 350 0 150])
print -dtiff peakfxcamber

%on Peak Fy
figure(3)
plot(grav10highfz(:,1), grav10highfz(:,4), 'k*', 'linewidth', 2,
'markersize', 10) %High Camber
hold on
plot(grav10lowfz(:,1), grav10lowfz(:,4), 'kx', 'linewidth', 2,
'markersize', 10) %Low Camber
title('\bf\fontsize{12} Peak Lateral Force v. Normal Load')
xlabel('\bf\fontsize{12} Normal Load, lbs')
ylabel('\bf\fontsize{12} Peak Lateral Force, lbs')
legend('High Camber', 'Low Camber', 'location', 'southeast')
axis([0 350 0 150])
print -dtiff peakfycamber

%on normalized fy v. alpha
%split the first few normal loads to some graphs
figure(4)
plot(grav10highfy(1:8,1), grav10highfy(9:16,1), '-k', 'markersize', 10,
'linewidth', 1.5)
hold on
plot(grav10lowfy(1:8,1), grav10lowfy(9:16,1), '--k', 'markersize', 10,
'linewidth', 1.5)
title('\bf\fontsize{12} Normalized Lateral Force v. Slip Angle')
xlabel('\bf\fontsize{12} Slip Angle, deg')
ylabel('\bf\fontsize{12} Normalized Lateral Force, lbs')
axis([0 45 -.01 .8])
legend('95 lbs, High Camber', '95 lbs, Low Camber','location',
'southeast')
print -dtiff fyValpha95camber

figure(5)
plot(grav10highfy(1:8,2), grav10highfy(9:16,2), '-k', 'markersize', 10,
'linewidth', 1.5)
hold on
plot(grav10lowfy(1:8,2), grav10lowfy(9:16,2), '--k', 'markersize', 10,
'linewidth', 1.5)
```

```
title('\bf\fontsize{12} Normalized Lateral Force v. Slip Angle')
xlabel('\bf\fontsize{12} Slip Angle, deg')
ylabel('\bf\fontsize{12} Normalized Lateral Force, lbs')
axis([0 45 -.01 .8])
legend('140 lbs, High Camber', '140 lbs, Low Camber','location',
'southeast')
print -dtiff fyValpha140camber

figure(6)
plot(grav10highfy(1:8,3), grav10highfy(9:16,3), '-k', 'markersize', 10,
'linewidth', 1.5)
hold on
plot(grav10lowfy(1:8,3), grav10lowfy(9:16,3), '--k', 'markersize', 10,
'linewidth', 1.5)
title('\bf\fontsize{12} Normalized Lateral Force v. Slip Angle')
xlabel('\bf\fontsize{12} Slip Angle, deg')
ylabel('\bf\fontsize{12} Normalized Lateral Force, lbs')
axis([0 45 -.01 .8])
legend('185 lbs, High Camber', '185 lbs, Low Camber','location',
'southeast')
print -dtiff fyValpha185camber

%now do the remaining normal loads
figure(7)
plot(grav10highfy(1:8,4), grav10highfy(9:16,4), '-k', 'markersize', 10,
'linewidth', 1.5)
hold on
plot(grav10lowfy(1:8,4), grav10lowfy(9:16,4), '--k', 'markersize', 10,
'linewidth', 1.5)
title('\bf\fontsize{12} Normalized Lateral Force v. Slip Angle')
xlabel('\bf\fontsize{12} Slip Angle, deg')
ylabel('\bf\fontsize{12} Normalized Lateral Force, lbs')
legend('230 lbs, High Camber', '230 lbs, High
Camber','location','southeast')
axis([0 45 -.01 .8])
print -dtiff fyValpha230camber

figure(8)
plot(grav10highfy(1:8,5), grav10highfy(9:16,5), '-k', 'markersize', 10,
'linewidth', 1.5)
hold on
plot(grav10lowfy(1:8,5), grav10lowfy(9:16,5), '--k', 'markersize', 10,
'linewidth', 1.5)
title('\bf\fontsize{12} Normalized Lateral Force v. Slip Angle')
xlabel('\bf\fontsize{12} Slip Angle, deg')
ylabel('\bf\fontsize{12} Normalized Lateral Force, lbs')
legend('275 lbs, High Camber', '275 lbs, Low
Camber','location','southeast')
axis([0 45 -.01 .8])
print -dtiff fyValpha275camber

figure(9)
plot(grav10highfy(1:8,6), grav10highfy(9:16,6), '-k', 'markersize', 10,
'linewidth', 1.5)
hold on
```

```
plot(grav10lowfy(1:8,6), grav10lowfy(9:16,6), '--k', 'markersize', 10,
'linewidth', 1.5)
title('\bf\fontsize{12} Normalized Lateral Force v. Slip Angle')
xlabel('\bf\fontsize{12} Slip Angle, deg')
ylabel('\bf\fontsize{12} Normalized Lateral Force, lbs')
legend('320 lbs, High Camber','320 lbs, Low
Camber','location','southeast')
axis([0 45 -.01 .8])
print -dtiff fyValpha320camber

%=========================================================================
====
%Pressure Effects
%=========================================================================
====
%On Calpha
figure(10)
plot(grav10lowfz(:,1), grav10lowfz(:,2), 'k*', 'linewidth', 2,
'markersize',10) %High pressure
hold on
plot(grav5lowfz(:,1), grav5lowfz(:,2), 'kx', 'linewidth', 2,
'markersize',10) %Low pressure
title('\bf \fontsize{12} Cornering Stiffness v. Normal Load')
xlabel('\bf \fontsize{12} Normal Load, lbs')
ylabel('\bf \fontsize{12} Cornering Stiffness, C\alpha, lbs/deg')
legend('10 psi', '5 psi', 'location', 'southeast')
axis([0 350 0 20])
print -dtiff calphapressure

%On Peak Fx
figure(11)
plot(grav10lowfz(:,1), grav10lowfz(:,3), 'k*', 'linewidth', 2,
'markersize', 10) %High pressure
hold on
plot(grav5lowfz(:,1), grav5lowfz(:,3), 'kx', 'linewidth', 2,
'markersize', 10) %Low pressure
title('\bf\fontsize{12} Peak Longitudinal Force v. Normal Load')
xlabel('\bf\fontsize{12} Normal Load, lbs')
ylabel('\bf\fontsize{12} Peak Longitudinal Force, lbs')
legend('10 psi', '5 psi', 'location', 'southeast')
axis([0 350 0 150])
print -dtiff peakfxpressure

%on Peak Fy
figure(12)
plot(grav10lowfz(:,1), grav10lowfz(:,4), 'k*', 'linewidth', 2,
'markersize', 10) %High pressure
hold on
plot(grav5lowfz(:,1), grav5lowfz(:,4), 'kx', 'linewidth', 2,
'markersize', 10) %Low pressure
title('\bf\fontsize{12} Peak Lateral Force v. Normal Load')
xlabel('\bf\fontsize{12} Normal Load, lbs')
ylabel('\bf\fontsize{12} Peak Lateral Force, lbs')
legend('10 psi', '5 psi', 'location', 'southeast')
axis([0 350 0 150])
```

```
print -dtiff peakfypressure

%on normalized fy v. alpha
figure(13)
plot(grav10lowfy(1:8,1), grav10lowfy(9:16,1), '-k', 'markersize', 10,
'linewidth', 1.5)
hold on
plot(grav5lowfy(1:8,1), grav5lowfy(9:16,1), '--k', 'markersize', 10,
'linewidth', 1.5)
title('\bf\fontsize{12} Normalized Lateral Force v. Slip Angle')
xlabel('\bf\fontsize{12} Slip Angle, deg')
ylabel('\bf\fontsize{12} Normalized Lateral Force, lbs')
legend('95 lbs, 10 psi', '95 lbs, 5 psi','location', 'southeast')
axis([0 45 -.01 .8])
print -dtiff fyValpha95pressure

figure(14)
plot(grav10lowfy(1:8,2), grav10lowfy(9:16,2), '-k', 'markersize', 10,
'linewidth', 1.5)
hold on
plot(grav5lowfy(1:8,2), grav5lowfy(9:16,2), '--k', 'markersize', 10,
'linewidth', 1.5)
title('\bf\fontsize{12} Normalized Lateral Force v. Slip Angle')
xlabel('\bf\fontsize{12} Slip Angle, deg')
ylabel('\bf\fontsize{12} Normalized Lateral Force, lbs')
legend('140 lbs, 10 psi', '140 lbs, 5 psi','location', 'southeast')
axis([0 45 -.01 .8])
print -dtiff fyValpha140pressure

figure(15)
plot(grav10lowfy(1:8,3), grav10lowfy(9:16,3), '-k', 'markersize', 10,
'linewidth', 1.5)
hold on
plot(grav5lowfy(1:8,3), grav5lowfy(9:16,3), '--k', 'markersize', 10,
'linewidth', 1.5)
title('\bf\fontsize{12} Normalized Lateral Force v. Slip Angle')
xlabel('\bf\fontsize{12} Slip Angle, deg')
ylabel('\bf\fontsize{12} Normalized Lateral Force, lbs')
legend('185 lbs, 10psi', '185 lbs, 5 psi','location', 'southeast')
axis([0 45 -.01 .8])
print -dtiff fyValpha185pressure

figure(16)
plot(grav10lowfy(1:8,4), grav10lowfy(9:16,4), '-k', 'markersize', 10,
'linewidth', 1.5)
hold on
plot(grav5lowfy(1:8,4), grav5lowfy(9:16,3), '--k', 'markersize', 10,
'linewidth', 1.5)
title('\bf\fontsize{12} Normalized Lateral Force v. Slip Angle')
xlabel('\bf\fontsize{12} Slip Angle, deg')
ylabel('\bf\fontsize{12} Normalized Lateral Force, lbs')
legend('230 lbs, 10 psi', '230 lbs, 5 psi', 'location', 'southeast')
axis([0 45 -.01 .8])
print -dtiff fyValpha230pressure
```

```
figure(17)
plot(grav10lowfy(1:8,5), grav10lowfy(9:16,5), '-k', 'markersize', 10,
'linewidth', 1.5)
hold on
plot(grav5lowfy(1:8,5), grav5lowfy(9:16,5), '--k', 'markersize', 10,
'linewidth', 1.5)
title('\bf\fontsize{12} Normalized Lateral Force v. Slip Angle')
xlabel('\bf\fontsize{12} Slip Angle, deg')
ylabel('\bf\fontsize{12} Normalized Lateral Force, lbs')
legend('275 lbs, 10 psi', '275 lbs, 5 psi', 'location', 'southeast')
axis([0 45 -.01 .8])
print -dtiff fyValpha275pressure

figure(18)
plot(grav10lowfy(1:8,6), grav10lowfy(9:16,6), '-k', 'markersize', 10,
'linewidth', 1.5)
hold on
plot(grav5lowfy(1:8,6), grav5lowfy(9:16,6), '--k', 'markersize', 10,
'linewidth', 1.5)
title('\bf\fontsize{12} Normalized Lateral Force v. Slip Angle')
xlabel('\bf\fontsize{12} Slip Angle, deg')
ylabel('\bf\fontsize{12} Normalized Lateral Force, lbs')
legend('320 lbs, 10 psi', '320 lbs, 5 psi','location', 'southeast')
axis([0 45 -.01 .8])
print -dtiff fyValpha320pressure

%=========================================================================
====
%Suface Effects
%=========================================================================
====
%On Calpha
figure(19)
plot(grav10lowfz(:,1), grav10lowfz(:,2), 'k*', 'linewidth', 2,
'markersize',10) %High Camber
hold on
plot(clay10lowfz(:,1), clay10lowfz(:,2), 'kx', 'linewidth', 2,
'markersize',10) %Low Camber
title('\bf \fontsize{12} Cornering Stiffness v. Normal Load')
xlabel('\bf \fontsize{12} Normal Load, lbs')
ylabel('\bf \fontsize{12} Cornering Stiffness, C\alpha, lbs/deg')
legend('Gravel', 'Clay', 'location', 'southeast')
axis([0 350 0 20])
print -dtiff calphasurface

%On Peak Fx
figure(20)
plot(grav10lowfz(:,1), grav10lowfz(:,3), 'k*', 'linewidth', 2,
'markersize', 10) %High Camber
hold on
plot(clay10lowfz(:,1), clay10lowfz(:,3), 'kx', 'linewidth', 2,
'markersize', 10) %Low Camber
title('\bf\fontsize{12} Peak Longitudinal Force v. Normal Load')
xlabel('\bf\fontsize{12} Normal Load, lbs')
```

```
ylabel('\bf\fontsize{12} Peak Longitudinal Force, lbs')
legend('Gravel', 'Clay', 'location', 'southeast')
axis([0 350 0 150])
print -dtiff peakfxsurface

%on Peak Fy
figure(21)
plot(grav10lowfz(:,1), grav10lowfz(:,4), 'k*', 'linewidth', 2,
'markersize', 10) %High Camber
hold on
plot(clay10lowfz(:,1), clay10lowfz(:,4), 'kx', 'linewidth', 2,
'markersize', 10) %Low Camber
title('\bf\fontsize{12} Peak Lateral Force v. Normal Load')
xlabel('\bf\fontsize{12} Normal Load, lbs')
ylabel('\bf\fontsize{12} Peak Lateral Force, lbs')
legend('Gravel', 'Clay', 'location', 'southeast')
axis([0 350 0 150])
print -dtiff peakfysurface

%on normalized fy v. alpha
figure(22)
plot(grav10lowfy(1:8,1), grav10lowfy(9:16,1), '-k', 'markersize', 10,
'linewidth', 1.5)
hold on
plot(clay10lowfy(1:8,1), clay10lowfy(9:16,1), '--k', 'markersize', 10,
'linewidth', 1.5)
title('\bf\fontsize{12} Normalized Lateral Force v. Slip Angle')
xlabel('\bf\fontsize{12} Slip Angle, deg')
ylabel('\bf\fontsize{12} Normalized Lateral Force, lbs')
axis([0 45 -.01 .8])
legend('95 lbs, Gravel', '95 lbs, Clay','location', 'southeast')
print -dtiff fyValpha95surface

figure(23)
plot(grav10lowfy(1:8,2), grav10lowfy(9:16,2), '-k', 'markersize', 10,
'linewidth', 1.5)
hold on
plot(clay10lowfy(1:8,2), clay10lowfy(9:16,2), '--k', 'markersize', 10,
'linewidth', 1.5)
title('\bf\fontsize{12} Normalized Lateral Force v. Slip Angle')
xlabel('\bf\fontsize{12} Slip Angle, deg')
ylabel('\bf\fontsize{12} Normalized Lateral Force, lbs')
axis([0 45 -.01 .8])
legend('140 lbs, Gravel','140 lbs, Clay', 'location', 'southeast')
print -dtiff fyValpha140surface

figure(24)
plot(grav10lowfy(1:8,3), grav10lowfy(9:16,3), '-k', 'markersize', 10,
'linewidth', 1.5)
hold on
plot(clay10lowfy(1:8,3), clay10lowfy(9:16,3), '--k', 'markersize', 10,
'linewidth', 1.5)
title('\bf\fontsize{12} Normalized Lateral Force v. Slip Angle')
xlabel('\bf\fontsize{12} Slip Angle, deg')
ylabel('\bf\fontsize{12} Normalized Lateral Force, lbs')
```

```
axis([0 45 -.01 .8])
legend('185 lbs, Gravel', '185 lbs, Clay', 'location', 'southeast')
print -dtiff fyValpha185surface

%other normal loads
figure(25)
plot(grav10lowfy(1:8,4), grav10lowfy(9:16,4), '-k', 'markersize', 10,
'linewidth', 1.5)
hold on
plot(clay10lowfy(1:8,4), clay10lowfy(9:16,3), '--k', 'markersize', 10,
'linewidth', 1.5)
title('\bf\fontsize{12} Normalized Lateral Force v. Slip Angle')
xlabel('\bf\fontsize{12} Slip Angle, deg')
ylabel('\bf\fontsize{12} Normalized Lateral Force, lbs')
legend('230 lbs, Gravel','230 lbs, Clay', 'location', 'southeast')
axis([0 45 -.01 .8])
print -dtiff fyValpha230surface

figure(26)
plot(grav10lowfy(1:8,5), grav10lowfy(9:16,5), '-k', 'markersize', 10,
'linewidth', 1.5)
hold on
plot(clay10lowfy(1:8,5), clay10lowfy(9:16,5), '--k', 'markersize', 10,
'linewidth', 1.5)
title('\bf\fontsize{12} Normalized Lateral Force v. Slip Angle')
xlabel('\bf\fontsize{12} Slip Angle, deg')
ylabel('\bf\fontsize{12} Normalized Lateral Force, lbs')
legend('275 lbs, Gravel','275 lbs, Clay', 'location', 'southeast')
axis([0 45 -.01 .8])
print -dtiff fyValpha275surface

figure(27)
plot(grav10lowfy(1:8,6), grav10lowfy(9:16,6), '-k', 'markersize', 10,
'linewidth', 1.5)
hold on
plot(clay10lowfy(1:8,6), clay10lowfy(9:16,6), '--k', 'markersize', 10,
'linewidth', 1.5)

title('\bf\fontsize{12} Normalized Lateral Force v. Slip Angle')
xlabel('\bf\fontsize{12} Slip Angle, deg')
ylabel('\bf\fontsize{12} Normalized Lateral Force, lbs')
legend('320 lbs, Gravel', '320 lbs, Clay', 'location', 'southeast')
axis([0 45 -.01 .8])
print -dtiff fyValpha320surface
```

norm_dirt.m – Program to process data from normal load tests on the bevameter

```
% Bevameter Normal Load Tests
% Dirt Surface
clear
clc
clf

% Small Penetration Plate is 3 inches diameter
% Large Penetration Plate is 4 inches diameter
b1 = 3.0/2;
b2 = 4.0/2;

load big1.csv;
load big2.csv;
load big3.csv;

load small1.csv;
load small2.csv;
load small3.csv;


kphi(1) = (b2*big1(1,2) - b1*small1(1,2))/(b2-b1);
kphi(2) = (b2*big2(1,2) - b1*small2(1,2))/(b2-b1);
kphi(3) = (b2*big3(1,2) - b1*small3(1,2))/(b2-b1);

kc(1) = ((small1(1,2)-big3(1,2))*(b1*b2))/(b2-b1);
kc(2) = ((small2(1,2)-big3(1,2))*(b1*b2))/(b2-b1);
kc(3) = ((small3(1,2)-big3(1,2))*(b1*b2))/(b2-b1);

keq = (mean(kc)/b1)+mean(kphi);

n(1) = log((small1(3,2)*1000)/keq)/(log(small1(3,1)*1000));
n(2) = log((small2(3,2)*1000)/keq)/(log(small2(3,1)*1000));
n(3) = log((small2(3,2)*1000)/keq)/(log(small3(3,1)*1000));

mean(kphi)
mean(kc)
mean(n)

figure(1)
plot(big1(:,1), big1(:,2).*.3125, '-kx', 'linewidth', 2, 'markersize',
10)
hold on
plot(big2(:,1), big2(:,2).*.3125, ':kx', 'linewidth', 2, 'markersize',
10)
hold on
plot(big3(:,1), big3(:,2).*.3125, '-.kx', 'linewidth', 2, 'markersize',
10)
title('\bf \fontsize{12}Dirt Penetration Test, 4" Plate')
xlabel('\bf \fontsize{12}Sinkage, in.')
ylabel('\bf \fontsize{12}Pressure, psi')
```

```
figure(2)
plot(small1(:,1), small1(:,2).*.21, '-kx', 'linewidth', 2,
'markersize', 10)
hold on
plot(small2(:,1), small2(:,2).*.21, ':kx', 'linewidth', 2,
'markersize', 10)
hold on
plot(small3(:,1), small3(:,2).*.21, '-.kx', 'linewidth', 2,
'markersize', 10)
title('\bf \fontsize{12}Dirt Penetration Test, 3" Plate')
xlabel('\bf \fontsize{12}Sinkage, in.')
ylabel('\bf \fontsize{12}Pressure, psi')
```

nicedata.m – Program to compile all data from various normal loads for a given setup

```
clear
 clc
 clf

 ident = '\bf Gravel, 10psi, High Camber';
 %Define vectors for z-plane in surface plot
 normal = [50;95;130;185;230;275;320];
 slip = [0; 5; 10; 15; 20; 25; 30; 45];


  load('output50.csv');
 load('output95.csv');
 load('output140.csv');
 load('output185.csv');
 load('output230.csv');
 load('output275.csv');
 load('output320.csv');

 fy50 = output50(:,2);
 fx50 = output50(:,4);

 fy95 = output95(:,2);
 fx95 = output95(:,4);

 fy140 = output140(:,2);
 fx140 = output140(:,4);

 fy185 = output185(:,2);
 fx185 = output185(:,4);

 fy230 = output230(:,2);
 fx230 = output230(:,4);

 fy275 = output275(:,2);
 fx275 = output275(:,4);

 fy320 = output320(:,2);
 fx320 = output320(:,4);

 fy = [fy50 fy95 fy140 fy185 fy230 fy275 fy320];
 fx = [fx50 fx95 fx140 fx185 fx230 fx275 fx320];


figure(1)
surf(normal, slip,fy )
title('\bf \fontsize{12} Lateral Forces')
xlabel('\bf \fontsize{12} Normal Load, lbs')
ylabel('\bf \fontsize{12} Slip Angle, deg')
```

```
zlabel('\bf \fontsize{12} Lateral Force, lbs')
text(0, 60, 100, ident)
print -dtiff grav10highfysurf

figure(2)
surf(normal, slip,fx)
title('\bf \fontsize{12} Longitudinal Forces')
xlabel('\bf \fontsize{12} Normal Load, lbs')
ylabel('\bf \fontsize{12} Slip Angle, deg')
zlabel('\bf \fontsize{12} Longitudinal Force, lbs')
text(0, 60, 100, ident)
print -dtiff grav10highfxsurf

% Peak Fx vs Fz
figure(3)
peakfx = [max(fx50); max(fx95); max(fx140); max(fx185); max(fx230);
max(fx275); max(fx320)];
plot(normal, peakfx, 'kx', 'linewidth', 2, 'markersize', 15)
axis([0 350 0 175])
xlabel('\bf \fontsize{12} Normal Load, lbs')
ylabel('\bf \fontsize{12} Peak Longitudinal Force (Drag)')
title('\bf \fontsize{12} Peak Drag Force v. Normal Load')
text(100,10, ident)
print -dtiff peakfxfy

% Peak Fy vs Fz
figure(4)
peakfy = [max(fy50); max(fy95); max(fy140); max(fy185); max(fy230);
max(fy275); max(fy320)];
plot(normal, peakfy, 'kx', 'linewidth', 2, 'markersize', 15)
axis([0 350 0 175])
xlabel('\bf \fontsize{12} Normal Load, lbs')
ylabel('\bf \fontsize{12} Peak Lateral Force, lbs')
title('\bf \fontsize{12} Peak Lateral Force v. Normal Load')
text(100,10, ident)
print -dtiff peakfyfz

% C_alpha vs Fz - use 0,0, and the 5degree fy value for C alpha
calpha = [fy50(2)/5; fy95(2)/5; fy140(2)/5; fy185(2)/5; fy230(2)/5;
fy275(2)/5; fy320(2)/5];
figure(5)
plot(normal, calpha, 'kx', 'linewidth', 2, 'markersize', 15)
axis([0 350 0 12])
title('\bf \fontsize{12} Cornering Stiffness (C\alpha) v. Normal Load')
xlabel('\bf \fontsize{12} Normal Load, lbs')
ylabel('\bf \fontsize{12} C\alpha, lb/deg')
text(50, 1,ident)
print -dtiff normalcalpha

% Normalized Lateral Force Coefficient v. Alpha
;
figure(6)
plot(slip, fy50./50, ':ko', 'linewidth', 2, 'markersize', 10)
hold on
```

```
plot(slip, fy95./95, '-kx', 'linewidth', 2, 'markersize', 10)
hold on
plot(slip, fy140./140, ':k+', 'linewidth',2,'markersize', 10)
hold on
plot(slip, fy185./185, '-k*', 'linewidth',2,'markersize', 10)
hold on
plot(slip, fy230./230, ':ks', 'linewidth',2,'markersize',10)
hold on
plot(slip, fy275./275, '-kd', 'linewidth',2,'markersize',10)
hold on
plot(slip, fy320./320, ':kv', 'linewidth', 2,'markersize',10)
legend('50 lb', '95 lb', '140 lb', '185 lb', '230 lb', '275 lb', '320
lb', 'location', 'best')
title('\bf \fontsize{12}Normalized Lateral Force v. Slip Angle')
xlabel('\bf \fontsize{12} Slip Angle, deg')
ylabel('\bf \fontsize{12} Normalized Lateral Force')
text(10, 0, ident)
print -dtiff normlatalpha

% Normalized Longitudinal Force Coefficient v. Alpha

figure(7)
plot(slip, fx50./50, ':ko', 'linewidth', 2, 'markersize', 10)
hold on
plot(slip, fx95./95, '-kx', 'linewidth', 2, 'markersize', 10)
hold on
plot(slip, fx140./140, ':k+', 'linewidth',2,'markersize', 10)
hold on
plot(slip, fx185./185, '-k*', 'linewidth',2,'markersize', 10)
hold on
plot(slip, fx230./230, ':ks', 'linewidth',2,'markersize',10)
hold on
plot(slip, fx275./275, '-kd', 'linewidth',2,'markersize',10)
hold on
plot(slip, fx320./320, ':kv', 'linewidth', 2,'markersize',10)
legend('50 lb', '95 lb', '140 lb', '185 lb', '230 lb', '275 lb', '320
lb', 'location', 'best')
title('\bf \fontsize{12}Normalized Longitudinal (Drag) Force v. Slip
Angle')
xlabel('\bf \fontsize{12} Slip Angle, deg')
ylabel('\bf \fontsize{12} Normalized Longitudinal (Drag) Force')
text(10, .05, ident)
print -dtiff normdlongalpha

%Get the tire coefficient data together
A = [output50(4,6), output95(4,6), output140(4,6), output185(4,6),
output230(4,6), output275(4,6), output320(4,6)];
B = [output50(5,6), output95(5,6), output140(5,6), output185(5,6),
output230(5,6), output275(5,6), output320(5,6)];
rsqd = [output50(6,6), output95(6,6), output140(6,6), output185(6,6),
output230(6,6), output275(6,6), output320(6,6)];

figure(8)
plot(normal, A, 'xk', 'linewidth',2,'markersize', 10)
title('\bf \fontsize{12} A Coefficient v. Normal Load')
```

```
xlabel('\bf \fontsize{12}Normal Load')
ylabel('\bf \fontsize{12} A Coefficient')
print -dtiff coeffA

figure(9)
plot(normal, B, 'dk', 'linewidth',2,'markersize', 10)
title('\bf \fontsize{12} B Coefficient v. Normal Load')
xlabel('\bf \fontsize{12}Normal Load')
ylabel('\bf \fontsize{12} B Coefficient')
print -dtiff coeffB

normlat95 = [slip;fy95./95];
normlat140 = [slip;fy140./140];
normlat185 = [slip;fy185./185];
normlat230 = [slip;fy230./230];
normlat275 = [slip;fy275./275];
normlat320 = [slip;fy320./320];
comparefzdata = [normal, calpha, peakfx, peakfy];
comparefydata = [normlat95, normlat140, normlat185, normlat230,
normlat275, normlat320];
csvwrite('grav10highfz', comparefzdata)
csvwrite('grav10highfy', comparefydata)
```

E. Photographs

Photograph depicting yaw motion at high normal loads and high slip angles.

Photograph of test rig operating on clay surface.

Photograph detailing the camber adjustment

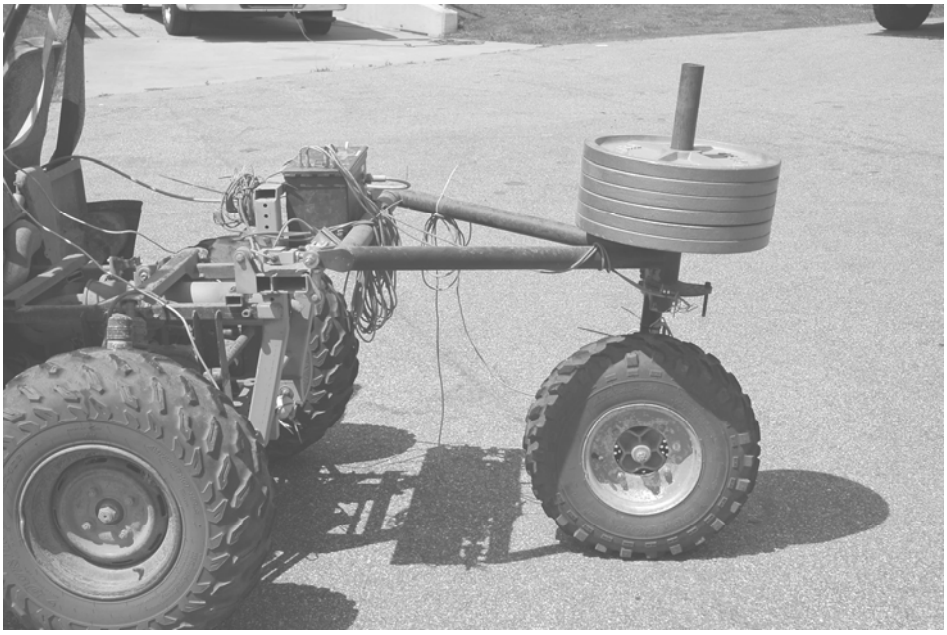

Left side view of test rig.

Right side view of test rig and tow vehicle.

Detail view of mounting frame and data acquisition box. Note video camera mounted within trailer hitch.

1987